Bangor University

DOCTOR OF PHILOSOPHY

Electrorotation analysis on artificial particles.

Chan, Ka Lok

Award date:
1996

Awarding institution:
Bangor University

A Thesis submitted to University of Wales
in candidature for the degree of
Doctor of Philosophy

Electrorotation Analysis on Artificial Particles

by

Ka Lok Chan B.Sc.

School of Electronic Engineering & Computer Systems,
University of Wales,
Bangor, Gwynedd.

September 1996

ACKNOWLEDGEMENTS

I would like to take this opportunity of thanking all my friends and members university staff, both academic and technical, who have given invaluable assistance during the course of this work.

I am particularly grateful to my supervisor Professor Ron Pethig for his constant enthusiasm, advice, encouragement, continuous guidance, support and supervision throughout the theoretical, experimental and manuscript preparation stages of this work.

I am also indebt to my co-supervisor Dr. Peter Gascoyne for his help and encouragement and guidance during my visit to the M.D. Anderson Cancer Center, Houston, Texas, USA and for making the time I spent there so rewarding and enjoyable. Also, I am grateful to Professor Alan Schroit of M.D. Anderson Cancer Center, in whom has shared with me the precious knowledge and expertise of making synthetic vesicles.

Many thanks also go to my colleagues, Drs. Julian Burt, Mark Talary, Gerard Markx, Xiao-Feng Zhou, Xiao-Bo Wang, Ying Huang, Michael Hughes, Juliette Rousselet, Andy Goater, Clare Hodgson and John Kerslake, for their friendship, invaluable assistance and useful discussions during the course of this work.

Finally, I am grateful for the financial support of the Advanced Technology Program of the State of Texas Higher Educational Co-ordinating Board (USA), the National Foundation of Cancer Research (USA) and the award of a CVCP ORS research studentship (UK).

SUMMARY

Dielectrophoresis and electrorotation are receiving increasing attention as useful phenomena for the characterisation and physical manipulation of cells. The primarily concern of this investigation was to determine whether these techniques can interpret accurately the dielectric properties of biological cells with an appropriate dielectric shell model. In this study, synthetic vesicles have been used as the testing samples in electrorotation experiments to verify the reliability of these techniques. By using the electrorotation technique with the dielectric shell models, dielectric properties of vesicles could be analysed very accurately and the results were in agreements with the observed morphology and membrane properties. The physical structure of the vesicles varied from a simple one such as unilamellar vesicle, to a more complex structure such as the oligolamellar and multilamellar form. The morphology and membrane structure of the vesicles were also characterised by fluorescence microscopy, flow cytometry and electron spin resonance using spin probes. This allowed this validification of the application of the dielectric shell theory for analysis of simple cellular systems.

The second objective of this work was to extend the potential used of the electrorotation technique, and not only for the analysis of cellular systems. Electrorotation was also performed on single stranded DNA oligonucleotides, covalently bound onto the surface of microscopic-sized latex beads. Different types of the DNA oligonucleotides exhibited different electrorotation responses according to their different base sequences. This has shown that the electrorotation technique can be used as an analytic tool to identify different sequences of DNA oligonucleotide.

CONTENTS

Chapter 1

Introduction

1.1 Introduction

The study of AC dielectric properties of cells and biological suspensions has been of scientific interest over the century increasing our understanding of biological systems. Höber (1913) [1] was the first person to measure the electrical impedance of suspensions of erythrocytes up to frequencies of 10MHz. He found that the resistance of the cell suspensions decreased with increasing frequency, which led him to conclude that the erythrocytes consisted of a poorly conducting envelope enclosing a conducting electrolyte. Fricke (1925) [2] conducted a similar experiment with erythrocytes, based on the theory of energy transfer and reported that energy stored in the suspension at low frequency should be equal to that stored in the cell membrane. He concluded that a membrane thickness was 3.3nm and a membrane capacitance was $0.81\mu F.cm^{-2}$. Later on, the observation of inductive properties of squid axons by Cole and Baker (1941) [3] directly led Hodgkin and Huxley (1952) [4] to discover the concept of voltage-gate membrane pores that eventually led to the award of a Nobel prize.

Since then, the dielectric theories of analysing cell suspension have been further improved by Schwan in 1957 [5], Pauly and Schwan in 1959 [6], Hanai in 1960 [7], Schwarz in 1962 [8], Grant *et al* in 1978 [9], Irimajiri *et al* in 1979 [10], Pethig in 1979 [11] and Pethig and Kell in 1987 [12].

During the same period, Hatsckek and Thorne in 1923 [13] had observed that particles had induced motion in non-uniform electric fields. The phenomenon was named as dielectrophoresis (DEP) by Pohl in 1951 [14]. Dielectrophoresis was defined as "the translational motion of neutral matter caused by polarisation effects in a non-uniform electric field", where the most polar matter moves towards the region of greatest electric field intensity. In corporation with the dielectric theory, Pohl had established the fundamental theory of describing the dielectrophoresis phenomenon in 1978 [15]. Then theoretical work of dielectrophoresis was further improved by Jones and Kallio in 1979 [16], followed by Benguigui and Lin in 1982 [17], then by Sauer in 1985 [18], Wang *et al* in 1992 [19] and more recently by Washizu and Jones in 1994 [20].

Another AC electrokinetic effect involving the physical rotational motion of particles under the influence of rotating electric field was called electrorotation (ROT). This phenomenon was first discovered by Hertz in 1881 [21] and Quincke in 1896 [22] who described the theoretical and experimental works of the electric field-induced rotation on solids. However, the first report of biological cells electrorotation was by Teixeira-Pinto *et al* in 1960 [23]. Later on, the electrorotation of erythrocytes and yeast cells were reported by Füredi and Ohad in 1964 [24] and Pohl in 1978 [15]. Pohl had interpreted electrorotation as an interaction between internal oscillations of cells and the applied electric field. Unfortunately, their experimental methods were not precise and the results were difficult to interpret. In 1982, Arnold and Zimmermann [25] and Mischel *et al* [26] made a major advance in the experimental methods by applying phase shifted AC voltages to needle shaped electrodes to create rotating electric fields that induced rotation motion of a cell. They had also improved the theory of electrorotation by describing this phenomenon with the dipole theory rather than the explanation that was given by Pohl. By 1985, Fuhr developed the theory of interpreting the electrorotation torque by using the effective dipole moment method.

Since then, both dielectrophoresis and electrorotation methods have further been investigated. Dielectrophoresis techniques have been used in cell analysis by Jones since 1979 [16]. Also, dielectrophoresis has been employed as an advanced technique for cells separation which has potential in clinical usage, as demonstrated by Gascoyne *et al* in 1992 [27], Markx and Pethig in 1994 [28] and Talary *et al* in 1995 [29]. Electrorotation offers a new non-invasive qualitative technique for cells analysis enabling the viability of biological cells to be accurately determined, as shown by Huang *et al* in 1992 [30] and Zhou *et al* in 1995 [31].

1.2 Objective of this investigation

Both dielectrophoresis and electrorotation techniques have been used increasingly and have been developed over the last two decades.

Unfortunately, experimental proof was lacking for using electrorotation techniques to determine the accuracy and the reliability of the interpretation for the dielectric properties of cells using the dielectric shell model. Although this experimental proof had been attempted by Fuhr in 1982 [32], he had performed the experiments on solid objects rather than on cell-sized biological materials. In this present investigation, synthetic vesicles have been created of the size of biological cells, with phospholipids and aqueous ionic medium of known dielectric properties. Experiments were performed with these synthetic vesicles the using electrorotation technique. The dielectric variables that were interpreted from the results of electrorotation by using the dielectric shell model were then compared with the known dielectric properties values of the sample to determine the accuracy and the reliability of this technique (Chapter 4). The accuracy analysis was also performed on computer programmes that analysed the electrorotation data (Chapter 3). Furthermore, the electrorotation technique was used to analyse biological materials such as DNA oligonucleotides. DNA oligonucleotides were covalently bound to the surface of latex beads. Due to the different binding sequence of different oligonucleotides, electrorotation would hopefully be able to identify different types of oligonucleotides depending on their base sequence (Chapter 5).

1.3 Reference

1. R. Höber (1913) Messungen der inneren leitfähigkeit von Zellen, *Pfl. Physiol. Archiv. Mensch. Tiere.*, **150** 15-45

2. H. Fricke (1925) The dielectric capacity of suspensions of red corpuscles of a dog, *Phys. Rev.,* **26** 682-687

3. K. S. Cole and R. F. Baker (1941) Longitudinal impedance of the squid giant axon, *J. Gen. Physiol.,* **19** 771-788

4. A. L. Hodgkin and A. F. Huxley (1952) A quantitative description of membrane current and its application to conductance and excitation in nerve, *J. Physiol.,* **117** 500-544

5. H. P. Schwan (1957) Electrical properties of tissue and cell suspension, *Adv. Biol. Med. Phy.* **5** 147-209

6. H. Pauly and H. P. Schwan (1959) *Z. Naturf.,* **146** 125-131

7. T. Hanai (1960) *Kolloid Z,* **171** 23-31

8. G. Schwarz (1962) A theory the low-frequency dielectric dispersion of colloidal particles in electrolyte solution, *J. Phys. Chem.* **66** 2636-2642

9. E. H. Grant, R. J. Sheppard and G. P. South (1978) Dielectric Behaviour of Biological Molecules in Solution (Oxford: Clarendon)

10. A. Irimajiri, T. Hanai and A. Inouye (1979) A dielectric theory of "multi-stratified shell" model with its application to a lymphoma cell, *J. Theor. Biol.* **78** 251-269

11. R. Pethig (1979) Dielectric and Electronic properties of Biological materials, J. Wiley, Chichester

12. R. Pethig and D. B. Kell (1987) The passive electrical properties of biological systems: their significane in physiology, Biophysics and Biotechnology. *Phys. Med. Biol.,* **32** 933-970

13. E. Hatsckek and P. C. L. Thorne (1923) Metal sols in non-dissociating liquids. Part1 : Nickel in toluene and benzene. *Roy. Soc. Proc.,* **103** 276-284

14. H. A. Pohl (1951) The motion and precipitation of suspensioids in divergent electric fields, *J. Appl. Phys.,* **22** 869-871

15. H. A. Pohl (1978) Dielectrophoresis, Cambridge: Cambridge University Press

16. T. B. Jones and G. A. Kallio (1979) Dielectrophoresis levitation of spheres and shells, *J. Electrostat.,* **33** 199-212

17. L. Benguigui and I. J. Lin (1982) More about the dielectrophoretic force, *J. Appl. Phys.* **53** 1141-1143

18. F. A. Sauer and R. W. Schögl (1985) Torques exerted on cylinders and spheres by external electromagnetic field: A contribution to the theory of field induced cell rotation. Interactions Between Electromagnetic Fields and Cells, (A Chiabrera ed.) New York: Plenum pp203-251.

19. X-B. Wang, R. Pethig and T. B. Jones (1992) Relationship of dielectrophoretic and electrorortation behaviour exhibited by polarised particles, *J. Phys. D: Appl. Phys.,* **25** 905-912

20. T. B. Jones and M. Washizu (1994) Equilibria and dynamics of DEP levitated particles: Multipolar theory, *J. Electrostat.,* **33** 199-212.

21. H. R. Hertz (1881) Über die Verteilung der Electricität auf der Oberfläche bewgter Leiter., *Wied. Ann.,* **13** 266-275

22. G. Quincke (1896) Über Rotationen im constanten elektrischen Felde, *Wied. Ann.,* **59** 417-486

23. A. A. Teixeira-Pinto, L. L. Nejelski, J. L. Cutler and J. H. Heller (1960) The behaviour of unicellular organisms in an electromagnetic field, *Exp. Cell. Res.,* **20** 548-564

24. A. A. Füredi and I. Ohad (1964) Effects of high-frequency electric field on the living cell. I: Behaviour of human erythrocytes in high-frequency electric field and its relation to their age, *Biochim. Biophys. Acta,* **78** 1-8

25. W. M. Arnold and U. Zimmermann (1982) Rotating-field induced rotation and measurement of the membrane capacitance of single mesophyll cells, *Z. Naturforsch.,* **37c** 908-915

26. M. Mischel, A. Voss and H. A. Pohl (1982) Cellular spin resonance in rotating electric fields, *J. Biol. Phys.,* **10** 223-226

27. P. R. C. Gascoyne, Y. Huang, R. Pethig, J. Vykoukal and F.F. Becker (1992) Dielectrophoretic separation of mammalian cells studies by computerized image analysis, *Meas. Sci. Technol.* **3** 439-445

28. G. H. Markx and R. Pethig (1995) Dielectrophoretic Separation of Cells: Continuous Separation, *Biotechnology and Bioengineering*, **45** 337-343

29. M. S. Talary, K. I. Mills, T. Hoy, A. K. Burnett and R. Pethig (1995) Dielectrophoretic separation and enrichment of CD34+ cell subpopulation from bone marrow and peripheral blood stem cells, *Medical & Biological Engineering & Computing,* **33**

30. Y. Huang, R. Hölzel, R. Pethig and X-B. Wang (1992) Differences in the AC electrodynamics of viable and non-viable yeasts cells determined through combined dielectrophoresis and electrorotation studies, *Phys. Med. Biol.* **37** 1499-1517

31. X-F. Zhou, G, H. Markx, R. Pethig and I. M. Eastwood (1995) Differentiation of viable and non-viable bacterial biofilms using electrorotation, **1245** 85-93

32. G. Fuhr, R. Glaser and R. Hagedorn (1986) Rotation of dielectrics in a rotating electric high-frequency field, *Biophys. J.,* **49** 395-402

Chapter 2

Theory

2.1 Introduction

The dielectric properties of matter have been investigated by physicists and electrical engineers since the 19th century. The results have led clearly to expansion in the electronic world, in particular the semiconductor industries. The studies of dielectric materials are also important in the chemical and biological sciences. This chapter presents the necessary dielectric theory and information on the dielectric properties of materials, theory on dielectrophoresis and electrorotation that will be used in chapter 3 to 5. Furthermore, the chemical structure of phospholipids, the membrane fluidity analysis by electron spin resonance (ESR) technique and membrane thickness determined by the membrane capacitance will also be described in this chapter. The chemical structure of DNA nitrogenous bases will be described in this chapter as well.

2.2 Dielectric Theory

Consider a pair of parallel metal plates of area A separated by a vacuum at a distance d (Figure 2.1). There is an applied potential difference V, across the facing surface of the parallel plates.

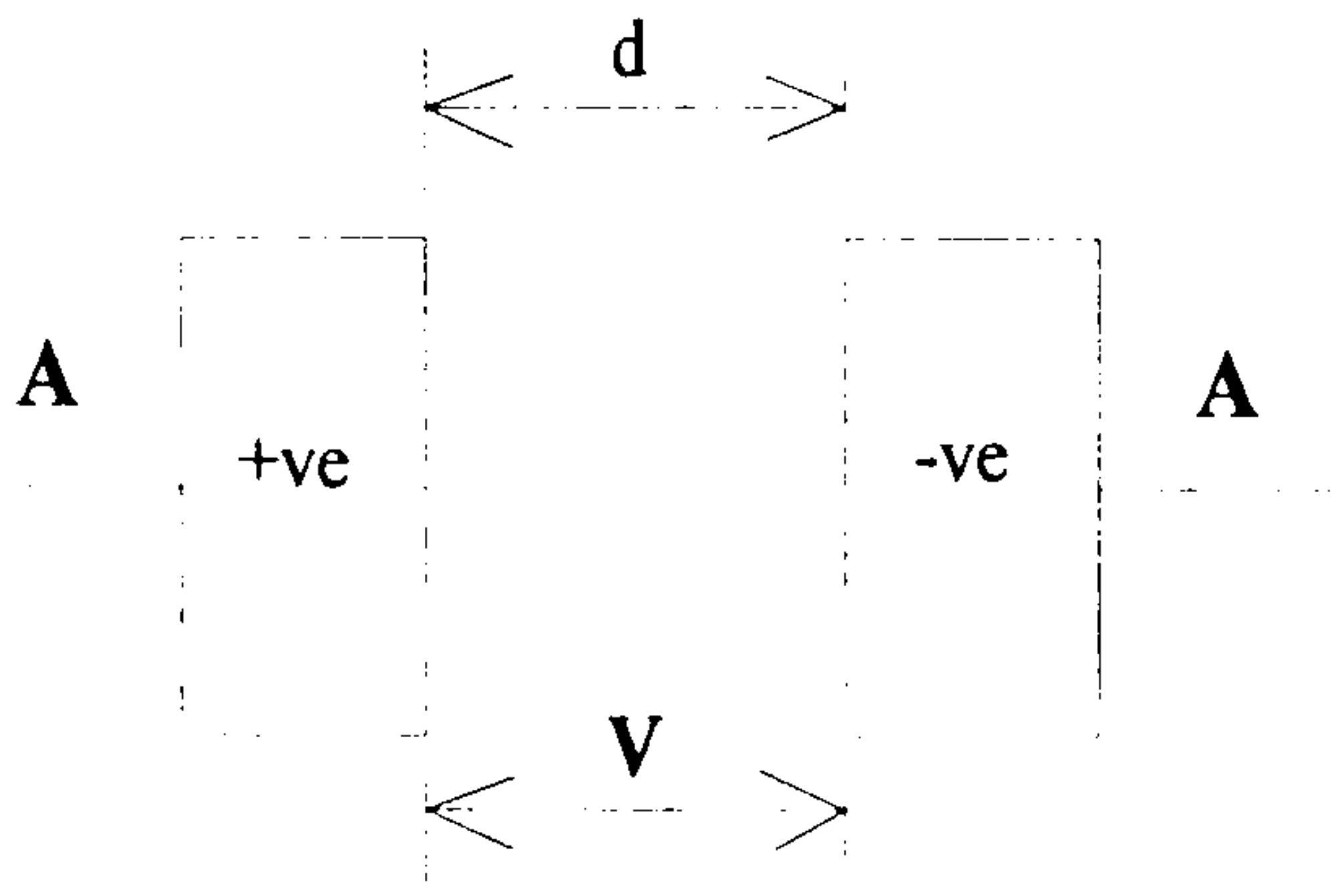

Figure 2.1 A parallel plate capacitor with two plates of area A that is separated by distance d with an applied potential difference V across it.

This relationship is governed by Gauss's Law such that :

$$Q_0 = C_0 . V \qquad (2.1)$$

where C_0 is the capacitance of the plates. The electric field between the plates must be proportional to the charge density on the plates, such that

$$E \propto \frac{Q_0}{A} \qquad (2.2)$$

On the other hand, the electric field strength E of a parallel plate system can be expressed as follows:

$$E = \frac{V}{d} \qquad (2.3)$$

By substituting equation 2.2 and 2.3 into equation 2.1, an expression for the capacitance of the plates in terms of their area and separation will be obtained.

$$C_0 = \varepsilon_0 \frac{A}{d} \tag{2.4}$$

where ε_0 is the constant that known as the permittivity of free space ($\varepsilon_0 = 8.854 \times 10^{-12}\ Fm^{-1}$).

Now consider an identical system with a homogenous dielectric material that is inserted between the plates (Figure 2.2).

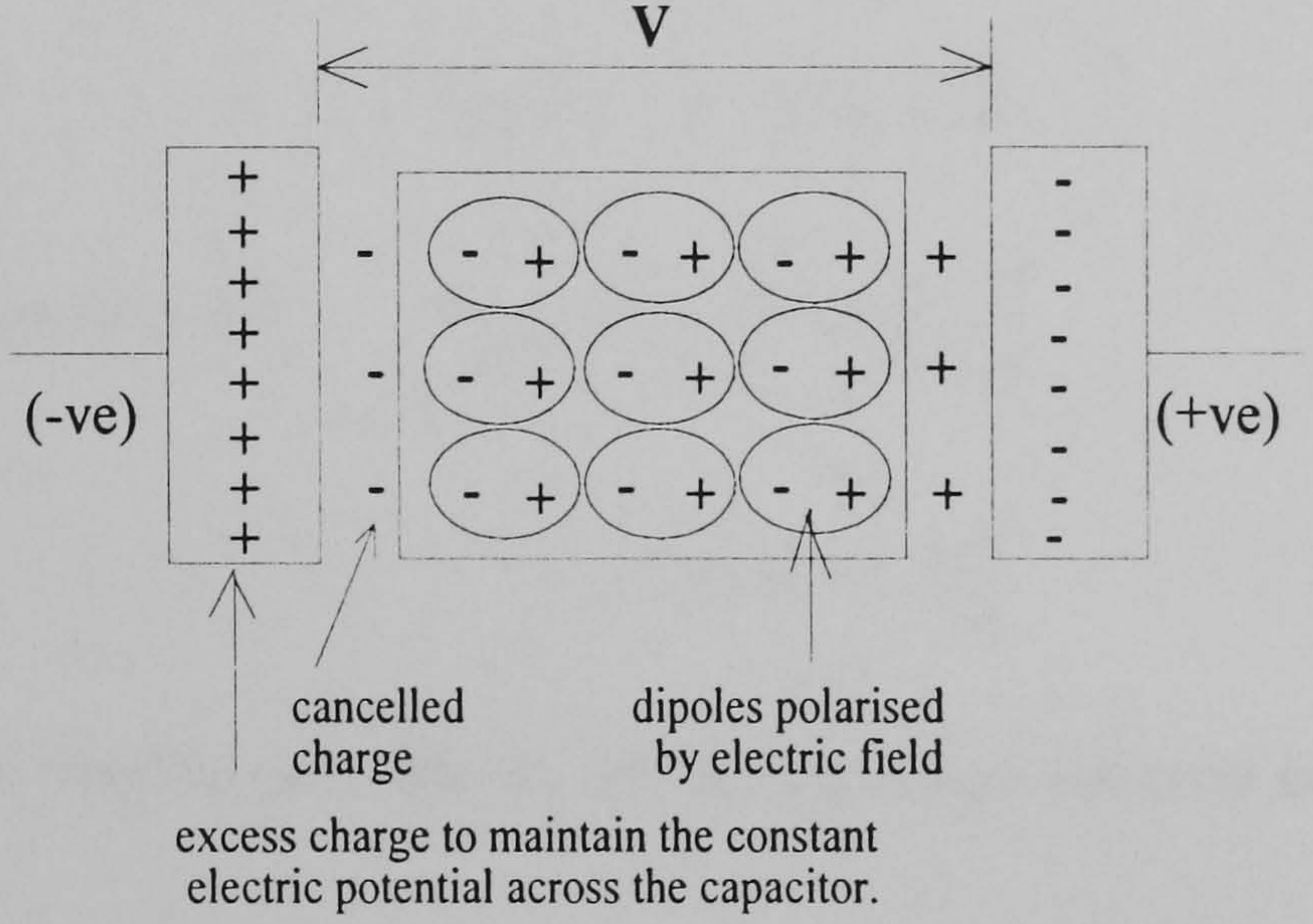

Figure 2.2 Dielectric material was inserted between the parallel plates of capacitor. The dielectric material was polarised by electric field.

The charge on the surfaces of the metal plates attracts the opposite charges within the dielectric material. As the result, the positive charges (nuclei) are shifted slightly to the plate with negative polarity and the negative charges (electrons) are shifted slightly towards the opposite direction. The dielectric material is polarised. This effect will induce an amount of net charge to build upon the facing surface of the dielectric to the metal plate with opposite charge polarity. The amount of net charge that is induced by the applied electric field within the dielectric will cancel some charges on the plates of the capacitor.

This will allow more charge to flow onto the plates of the capacitor in order to maintain a constant potential difference across the plates. Therefore, the presence of dielectric increases the amount of charge that is stored in the capacitor. The amount of stored charge is equal to the degree of polarisation of the dielectric.

$$Q_{Total} = Q_0 + Q_{polarisation}$$

Therefore for a constant applied voltage (equation 2.1)

$$C_{Total} = C_0 + C_{polarisation}$$

Hence from equation 2.4: $$C_{Total} = \varepsilon_0 \frac{A}{d} + \varepsilon_0 \varepsilon_r \frac{A}{d}$$

$$\Rightarrow \varepsilon_0 (1 + \varepsilon_r) \frac{A}{d}$$

where ε_r is the relative permittivity of the dielectric material compared to that of free space.

2.2.1 *Relationship between polarisation and permittivity*

It is important to establish the relationship between the polarisation of a dielectric and its relative permittivity, since the former is a function of its atomic structure while the latter determines the electrical properties of the bulk material.

When a dielectric material is subjected to an external applied electric field, it becomes polarised. The total dipole moment μ_{tot} of the polarised particles can be described as:

$$\mu_{tot} = \alpha_{tot} E_{loc} \tag{2.5}$$

where α_{tot} is the total polarisation and E_{loc} is the local electric field induced by the total dipole moments of the dielectric material. The polarisation α_{tot} includes the electronic α_e, atomic α_a and orientational α_o polarisation effects. The orientational polarisation α_o is the relaxation of permanent dipole.

$$\alpha_{tot} = \alpha_e + \alpha_a + \alpha_0$$

For a material such as water, it possesses a permanent dipole μ with the value of 1.8 debye units. When it is subjected to a DC or AC electric fields of frequency less than 10^9 Hz, water exhibits a relative permittivity of $\varepsilon_r \approx 80$ at 25°C. However ε_r value falls to about 4.5 when the frequency of the AC field raises higher than 10^{11}Hz, because the orientational polarisation is absent in the ultra-high frequencies region.

In general, the polarisation vector P (or the charge density) [1] of a dielectric material is an induced dipole moment per unit volume:

$$P = N\mu_{tot} \quad \text{or} \quad P = N\alpha_{tot} E_{loc} \tag{2.6}$$

where N is the number of dipoles per unit volume and μ_{tot} is the total dipole moment. This polarisation vector P can also be described in terms of an electric flux density D [1]. For the polarisation vector P is equal to the total charge density D_{tot} on the plate of a capacitor with dielectric material ε_r minus the charge density D_{vac} on the plate of the capacitor with a vacuum cavity.

$$P = D_{tot} - D_{vac} \tag{2.7}$$

Since the term of electric flux density can be described as the product of the permittivity of the dielectric and the applied electric field E [1]

$$D = \varepsilon_0 \varepsilon_r . E \tag{2.8}$$

Therefore equation 2.7 can be written as:

$$\begin{aligned} P &= \varepsilon_0 \varepsilon_r E - \varepsilon_0 E \\ P &= \varepsilon_0 (\varepsilon_r - 1) E \end{aligned} \tag{2.9}$$

The applied electric field E and the polarisation vector P are related by the relative dielectric susceptibility χ by the definition:

$$P = \varepsilon_0 \chi . E \qquad \text{where } \chi = \varepsilon_r - 1$$

$$\chi = \frac{P}{\varepsilon_0 . E} \tag{2.10}$$

by substituting equation 2.5 and 2.6 into equation 2.10, the relative dielectric susceptibility χ can relate to the local field E_{loc} that is induced by the total dipole moment of the dielectric:

$$\chi = \frac{N \alpha_{tot} E_{loc}}{\varepsilon_0 . E}$$

Therefore the relative permittivity of a dielectric material can be written as:

$$\varepsilon_r = 1 + \frac{N \alpha_{tot} E_{loc}}{\varepsilon_0 . E} \tag{2.11}$$

In order to relate the relative permittivity ε_r of a dielectric material to its polarisability α_{tot}, the ratio between the induced electric field E_{loc} within the dielectric and the external applied electric E is required. In dense material such as liquids and solids, E_{loc} is not equal to the applied electric field E, because the polarisability P is large and the resultant electric field that is applied to the dielectric is the contribution between the external applied field and the induced field amongst the polarised molecules. The relationship has been simplified for materials with high degrees of crystal symmetry or complex molecular disorder [1, 2, 3, 4] to arrive at the Clausius Mossotti equation:

$$\frac{\varepsilon_r - 1}{\varepsilon_r + 2} = \frac{N\alpha}{3\varepsilon_0} \tag{2.12}$$

2.3 Dielectric Relaxation

In a dielectric material, the rates of polarisation can be limited, so that as the frequency of the applied electric field is increased, some polarisations will no longer be able to attain their DC or low frequency values. Since the total dipole moment α_{tot} of any dielectric material can be contributed by three main polarisations which are orientational α_0, atomic α_a, and electronic polarisation α_e. The orientational polarisation is normally the first to disappear because it has the slowest polarisation mechanism that is contributed by the a permanent dipole reorientation. Therefore the dipoles are no longer able to orient fast enough to keep in alignment with the applied electric field with increasing frequency and the total polarisability falls from α_{tot} to (α_{tot} -α_0). This fall of polarisability that is associated with the reduction in permittivity of material, and energy absorption is referred to as dielectric relaxation or dispersion. This mechanism can be described as complex permittivity or complex conductivity of the materials.

2.3.1 Complex permittivity

The total polarisation of a dielectric material can be described in terms of a mathematical model. The total polarisation vector P_{tot} of the dielectric consists of two parts P_1 and P_2.

$$P_{tot} = P_1 + P_2 \qquad (2.13)$$

P_1 arises from the atomic and electronic polarisation and P_2 is from the displacement of a permanent dipole, the orientational polarisation. As the frequency of the external applied electric field increases up to 10^{14}Hz, P_1 should align with external field instantly, and has a constant value of $P_1 = \varepsilon_0\chi_1 E$ (by equation 2.10). Meanwhile the polarisation vector P_2 lags behind the field E in such a way that at any instant , P_2 approaches its final value of $P_2 = \varepsilon_0\chi_2 E$ at a rate proportional to $(\varepsilon_0\chi_2 E - P_2)$, so that:

$$\frac{dP_2}{dt} = \frac{1}{\tau}\left(\varepsilon_0\chi_2 E - P_2\right) \qquad (2.14)$$

where τ is the constant of proportionality. E and P_2 are time dependent, they are influenced by the rise time of the applied voltage and the reorientation rate of the dipole respectively. Solving equation 2.14 using the integration factor $e^{t/\tau}$ the following relationship is obtained:

$$P_2 e^{t/\tau} = \varepsilon_0\chi_2 E e^{t/\tau} + C \qquad (2.15)$$

where C is the integration constant, and the field is applied as a step-function at t=0 when P_2 is zero. The value of constant C is:

$$C = -\varepsilon_0 \chi_2 E$$

Therefore polarisation vector P_2 can be described as:

$$P_2 = \varepsilon_0 \chi_2 E(1 - e^{-t/\tau}) \qquad (2.16)$$

And the total polarisation vector of the dielectric from equation 2.13 can be described as:

$$P_{tot} = \varepsilon_0 \chi_1 E + \varepsilon_0 \chi_2 E\left(1 - e^{-t/\tau}\right)$$

$$= \varepsilon_0 E\left[\chi_1 + \chi_2\left(1 - e^{-t/\tau}\right)\right] \qquad (2.17)$$

Equation 2.17 indicates that the total polarisation vector P_{tot} reaches its maximum value exponentially at a rate determined by τ. Therefore the dielectric material will reach its maximum dipole moment when time t is significantly greater than the characteristic time constant τ of the dipole moment.

In the situation where a sinusoidal electric field is applied to the dielectric material:

$$E = E_0 e^{j\omega\tau}$$

where ω is the angular frequency of the applied field. The orientational polarisation vector P_2 of the dielectric that is subjected to a sinusoidal field can be expressed as:

$$\frac{dP_2}{dt} = \frac{1}{\tau}\left(\varepsilon_0 \chi_2 E_0 e^{j\omega\tau} - P_2\right)$$

After integration: $$P_2 e^{t/\tau} = \frac{\varepsilon_0 \chi_2 E_0 e^{t/\tau}}{1 + j\omega\tau} + C$$

For steady condition when $\omega = 0$, $P_2 = \varepsilon_0\chi_2 E$, and the integral constant C will be zero. Therefore orientational polarisation vector P_2 can be described as:

$$P_2 = \frac{\varepsilon_0 \chi_2 E_0}{1 + j\omega\tau} \tag{2.18}$$

By equation 2.13 and 2.18, the total polarisation vector for the dielectric can be expressed as:

$$P_{tot} = \varepsilon_0 E_0 \left(\chi_1 + \frac{\chi_2}{1 + j\omega\tau} \right) \tag{2.19}$$

ε_s is defined as the relative permittivity measured at the static electric field condition. Here, the total polarisation vector P_{tot} is at its maximum. ε_∞ is the permittivity measured at a sufficiently high frequency where the orientational polarisation disappears. From equation 2.10 that describes dielectric susceptibility:

$$\begin{aligned} \chi &= \chi_1 + \chi_2 = \varepsilon_s - 1 \\ \chi_1 &= \varepsilon_\infty - 1 \\ \chi_2 &= \varepsilon_s - \varepsilon_\infty \end{aligned}$$

Therefore total polarisation can be expressed in terms of permittivities:

$$P_{tot} = \varepsilon_0 E_0 \left[\left(\varepsilon_\infty + \frac{\varepsilon_s - \varepsilon_\infty}{1 + j\omega\tau} \right) - 1 \right] \tag{2.20}$$

$$P_{tot} = \varepsilon_0 E_0 \left(\varepsilon^* - 1 \right)$$

where ε^* is the complex permittivity, consisting of a real (ε') and an imaginary (ε'') component:

$$\varepsilon^{*} = \varepsilon' - j\varepsilon'' = \varepsilon_{\infty} + \frac{\varepsilon_{s} - \varepsilon_{\infty}}{1 + j\omega\tau} \tag{2.21}$$

The complex permittivity is described by Debye formulations [5] as:

$$\varepsilon' = \varepsilon_{\infty} + \frac{\varepsilon_{0}(\varepsilon_{s} - \varepsilon_{\infty})}{1 + \omega^{2}\tau^{2}} \tag{2.22}$$

$$\varepsilon'' = \frac{\omega\tau\varepsilon_{0}(\varepsilon_{s} - \varepsilon_{\infty})}{1 + \omega^{2}\tau^{2}} \tag{2.23}$$

and the relationship between the real (ε') and imaginary (ε") parts of the complex permittivity is shown in figure 2.3.

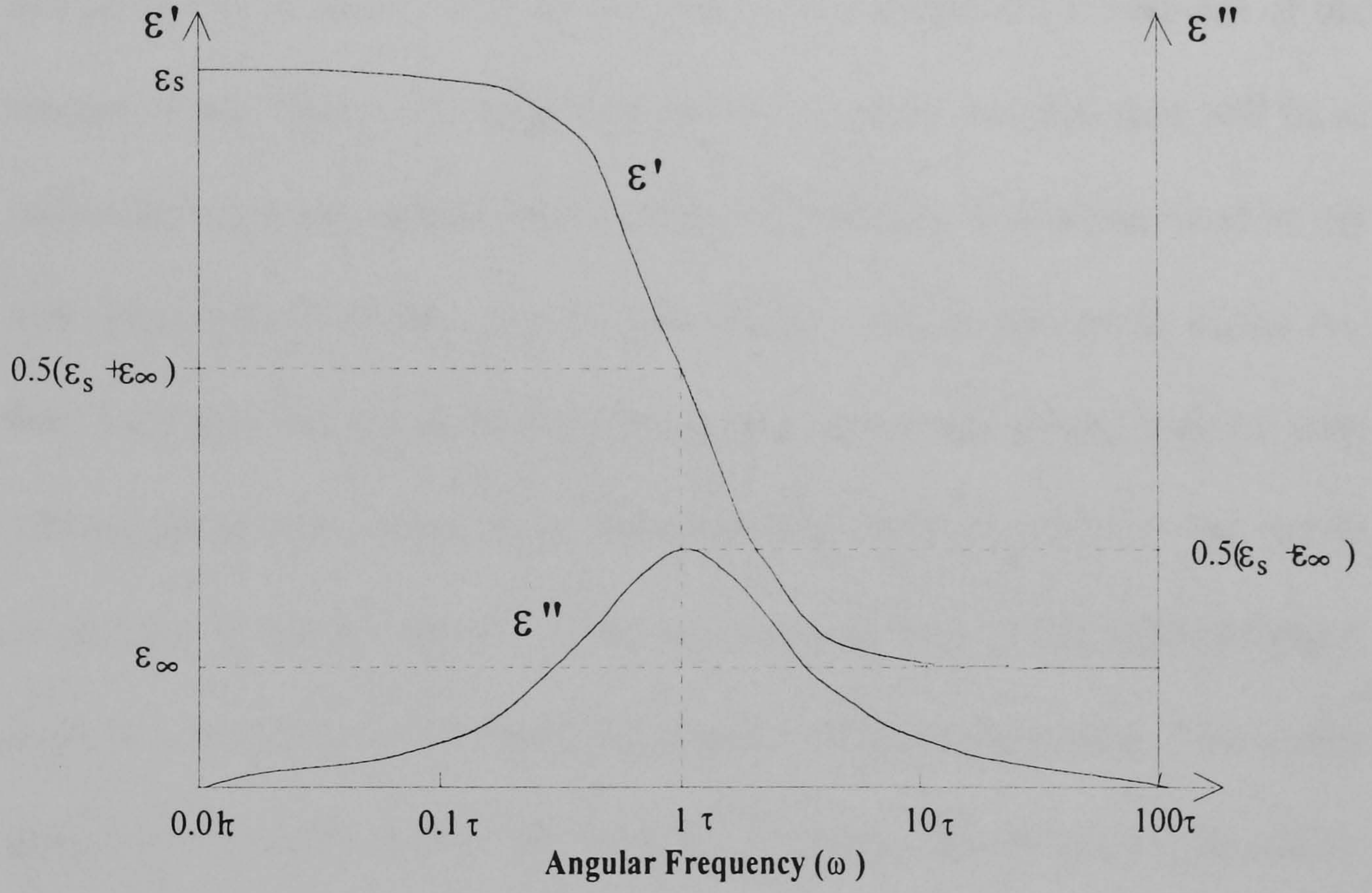

Figure 2.3 Variation of the real ε' and imaginary ε" components of the complex permittivity of the Debye equation (equation 2.21, 2.22).

The Debye equation reveals that the real part of the complex permittivity ε' describes energy storage from the applied electric field. Energy loss (per cycle) due to reorientation of the dipoles occurs as the frequency of the AC applied field increases. This energy lost factor is described as the imaginary part ε" of the complex permittivity. This mechanism of energy transfer and energy loss can be explained in terms of the first law of thermodynamics (conservation of energy) [4].

Let us consider that the characteristic time constant τ of the dipoles within a dielectric to align with the applied electric field is 1 second, whilst the applied AC electric field has a period of 100 seconds. Then 99% of the energy from the applied field with be stored within the dielectric. At the same time, 1 second or 1% of energy will be lost due to the orientation movement of the dipoles. From figure 2.3, the energy that is stored by the dielectric will be at maximum when the applied field is in static condition. It is represented by the real component ε' of the complex permittivity. As the frequency of the AC field increases, the dipole aligns for a greater percentage of the periodic time causing the energy storage to be decreased (shown in ε') whilst giving rise to an increase in energy lost ε". When the periodic time of the applied field is equal to τ, the dipole will orientate in phase with the applied field. The energy storage of the dipole will be the same as the energy that is lost by the dipole. This frequency is referred to as the relaxation frequency of the dielectric. It is the maximum frequency at which the dipole can fully align with the applied field. When the frequency of the applied field is larger than the relaxation frequency value, the dipole can no longer orientate fully with the field. Therefore both the stored energy and lost energy of the dipole begin to fall until the periodic time of the applied field is very much smaller than time τ, when the dipole can no longer orientate itself with the applied field to any degree. The dipole will not contribute to the overall polarisation process.

2.3.2 *Complex Conductivity*

The complex conductivity of a material can be represented similar as the complex permittivity. It also processes a single relaxation time.

$$
\begin{aligned}
\sigma^* &= \sigma' + \sigma'' \\
&= \omega\varepsilon'' + j\omega\varepsilon' \\
&= \sigma_\infty + \frac{\sigma_s - \sigma_\infty}{1 + j\omega\tau_\sigma} \\
&= \left(\sigma_\infty + \frac{\sigma_s - \sigma_\infty}{1 + \omega^2\tau_\sigma^2}\right) - j\frac{\omega\tau_\sigma(\sigma_s - \sigma_\infty)}{1 + \omega^2\tau_\sigma^2}
\end{aligned}
$$

where the real and imaginary parts are:

$$
\sigma' = \sigma_\infty + \frac{\sigma_s - \sigma_\infty}{1 + \omega^2\tau_\sigma^2} \tag{2.24}
$$

$$
\sigma'' = \frac{\omega\tau_\sigma(\sigma_s - \sigma_\infty)}{1 + \omega^2\tau_\sigma^2} \tag{2.25}
$$

where σ_s and σ_∞ refer to the static and high frequency conductivity values respectively, and τ_σ is the relaxation time associated with the conduction process.

2.4 Polarisation

In general, the dielectric materials are polarised under the influence of the external applied electric field. The polarisation processes within a dielectric consist of the electronic α_e , atomic α_a and orientational α_0 polarisations. If the dielectric material is a heterogeneous system, a polarisation mechanism that is called the interfacial polarisation α_i also takes place in the macroscopic scale. Each different polarisation process consists of their own characteristic time constant, and can be seen as dielectric relaxations occuring in different frequency regions.

2.4.1 *Electronic Polarisation*

This electronic polarisation can take place in both polar and non-polar materials. The electronic polarisation takes place when an applied field causes the nucleus and electrons to experience oppositely directed forces and the electrons orbitals are distorted in such a way that the centre of gravity of electrons no longer coincides with the nucleus. This distortion is small since the applied fields, in the order of $10^6 Vm^{-1}$, are considerably smaller than those within the atom that are about $10^{11} Vm^{-1}$. The displacement of the charges is therefore only in the order of 10Å. The frequency region of this polarisation is above 10^{14}Hz.

2.4.2 *Atomic Polarisation*

The atomic polarisation occurs from the displacement of differently charged ions in the crystal lattice. Atomic polarisation process can contribute greatly to the total polarisation in inorganic compounds, but polarisation only makes a small contribution to the total in organic solvents where ions are absent. For ionic solid compounds such as sodium chloride, the sodium ions move relative to the negative charged chloride ions when subjected to an external electric field. A dipole moment will be induced within the solid.

2.4.3 *Orientational Polarisation*

The orientational polarisation occurs only in polar molecules which contain permanent dipoles in their chemical structure. The permanent molecular dipoles in these material can rotate about their axis of symmetry to align with an applied field which exerts a torque in them. Also, the orientational polarisation is temperature dependent, since the higher the temperature the greater is the thermal agitation and the lower is the polarisation α_0.

2.4.4 *Interfacial Polarisation*

When a heterogeneous system is subjected to an applied electric field, there is an accumulation of charges at the structural interfaces between dissimilar phases within the dielectric. This gives rise to the formation of charge double layers at the boundaries. In 1892, Maxwell was the first person to describe this phenomena, followed by Wagner in 1924. The phenomena is thus called the Maxwell-Wagner interfacial polarisation [6, 7, 8]. The simplest form of the Maxwell-Wagner interfacial polarisation is a parallel plate capacitor with two dielectrics of differing thickness (d_1, d_2), permittivities (ε_1, ε_2) and conductivites (σ_1, σ_2) as shown in figure 2.4.

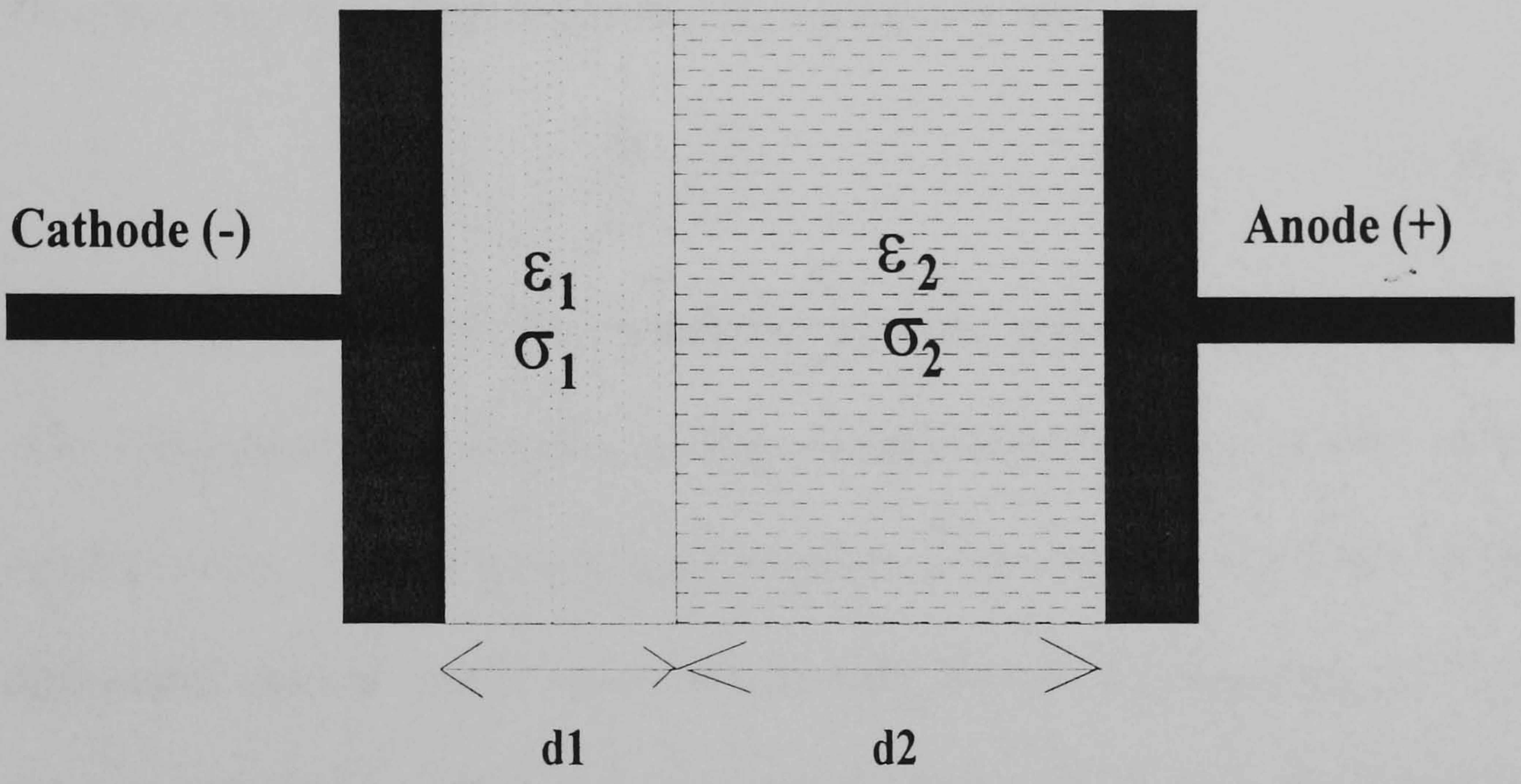

Figure 2.4 A parallel plate capacitor consisting of two differing dielectrics.

On application of a static field, the electric flux density that flow through the dielectrics d_1 and d_2 will be the same.

$$D_1 = D_2 \tag{2.26}$$

where by equation 2.8 ($D = \varepsilon . E$)

$$\varepsilon_1 E_1 = \varepsilon_2 E_2 \tag{2.27}$$

The ratio of the field distribution will be:

$$\frac{E_1}{E_2} = \frac{\varepsilon_2}{\varepsilon_1} \tag{2.28}$$

The final field distribution, arising after a certain time is determined by the condition of current continuity through the material J.

$$J_1 = J_2 \tag{2.29}$$

where $J = \sigma . E$ $$\sigma_1 E_1 = \sigma_2 E_2 \tag{2.30}$$

Therefore the ratio of the field intensity distribution will be:

$$\frac{E_1}{E_2} = \frac{\sigma_2}{\sigma_1} \tag{2.31}$$

The electric field distribution changes from that initially determined by the ratio of the dielectric constants, to be eventually determined by the ratio of the conductivities. This is seen as a polarisation of the material and is due to the differential rates of charge movement through the two dielectric regions. The response of this dielectric to an alternating field can be analysed using the equivalent circuit shown in figure 2.5.

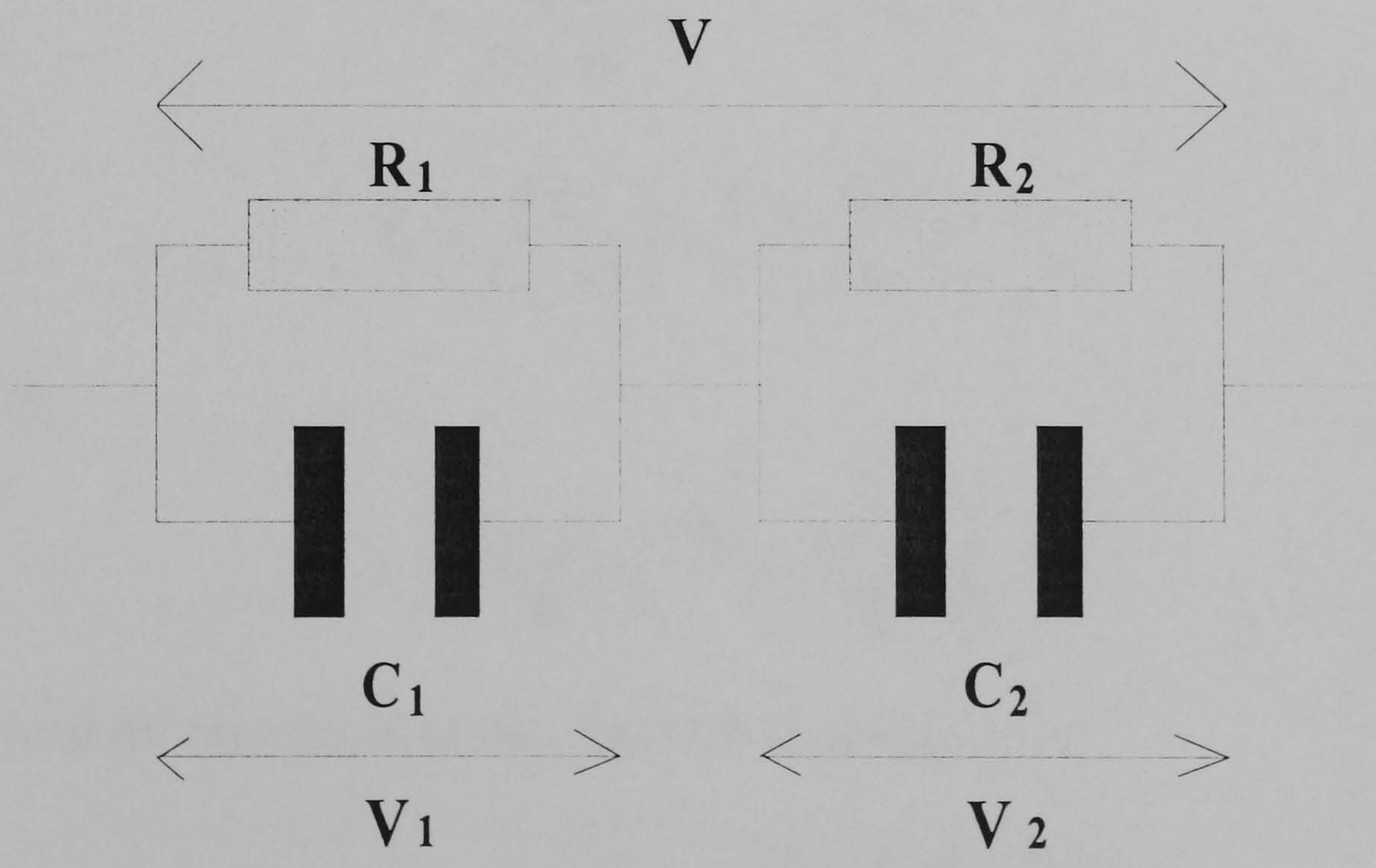

Figure 2.5 Equivalent electric circuit of a parallel plate capacitor consisting of two differing dielectrics.

The parallel plate capacitor with two differing dielectrics can be described as two capacitors in series where the capacitance and the resistance of the component in the equivalent circuit are given by:

$$C_1 = \varepsilon_0 \varepsilon_1 \frac{A}{d_1} \qquad C_2 = \varepsilon_0 \varepsilon_2 \frac{A}{d_2}$$

$$R_1 = \frac{d_1}{\sigma_1 A_1} \qquad R_2 = \frac{d_2}{\sigma_2 A_2}$$

$$\tau_1 = R_1 C_1 \qquad \tau_2 = R_2 C_2$$

The current that flows through the circuit can be described by the following differential equations:

$$I = C_1 \frac{dV_1}{dt} + \frac{V_1}{R_1} = C_2 \frac{dV_2}{dt} + \frac{V_2}{R_2} \tag{2.32}$$

The solution of these equations reveals that, on the application of a step voltage V_1 and V_2 increase exponentially to their maximum value with a time constant τ as described below:

$$V_1 = \frac{VR_1}{R_1 + R_2}\left[1 - \left(\frac{\tau - R_2 C_2}{\tau}\right) e^{-t/\tau}\right]$$

$$V_2 = \frac{VR_2}{R_1 + R_2}\left[1 - \left(\frac{\tau - R_1 C_1}{\tau}\right) e^{-t/\tau}\right]$$

where:

$$\tau = \frac{R_1 R_2 (C_1 + C_2)}{R_1 + R_2} = \frac{R_2 \tau_1 + R_1 \tau_2}{R_1 + R_2}$$

The total AC impedance of the circuit can be calculated as:

$$Z_{total} = Z_1 + Z_2 = \frac{(R_1 + R_2)(1 + j\omega\tau)}{(1 + j\omega\tau_1)(1 + j\omega\tau_2)}$$

The total impedance can be written in terms of a capacitance with a complex permittivity:

$$\frac{1}{Z} = j\omega\varepsilon_0\varepsilon^* \frac{d}{A}$$

Solving for ε^* reveals the following expression for the effective permittivity of the capacitor:

$$\varepsilon^* = \varepsilon' - j\varepsilon''$$

where:
$$\varepsilon' = \frac{d\left(\tau_1 + \tau_2 - \tau + \omega^2\tau_1\tau_2\tau\right)}{\varepsilon_0 A\left(R_1 + R_2\right)\left(1 + \omega^2\tau^2\right)}$$

$$\varepsilon'' = \frac{d - d\left(\omega^2\tau_1\tau_2 + \omega^2\tau\left(\tau_1 + \tau_2\right)\right)}{\omega\varepsilon_0 A\left(R_1 + R_2\right)\left(1 + \omega^2\tau^2\right)}$$

These equation are the same form as the Debye equation 2.22 and 2.23. At very low frequencies, the complex permittivity tends to the DC or maximum permittivity ε_s:

$$\varepsilon_s = \frac{d\left(\tau_1 + \tau_2 - \tau\right)}{\varepsilon_0 A\left(R_1 + R_2\right)}$$

As the frequency of the applied field is increased, the complex permittivity approaches the high frequency or minimum permittivity ε_∞ given by:

$$\varepsilon_\infty = \frac{d\tau_1\tau_2}{\varepsilon_0 A\left(R_1 + R_2\right)\tau}$$

These equations show that at the interface between the two dielectrics, a Debye relaxation process occurs where the relaxation time and complex permittivity is dependent on the properties and dimensions of each dielectric. In addition to the Debye-type of dispersion caused by interfacial polarisation, an extra frequency-dependent conductance occurs through the interface giving an effective interfacial permittivity ε_{int} of:

$$\varepsilon_{int} = \varepsilon_{\infty} + \frac{\varepsilon_s - \varepsilon_{\infty}}{1 + j\omega\tau} - j\frac{\sigma}{\omega} \qquad (2.33)$$

where: $$\sigma = \frac{d}{(R_1 + R_2)A}$$

The effects of the interfacial polarisation can extend from 1Hz to 100MHz depending on the nature of the interface. The overall effect of each of these polarisation processes is to produce a number of dispersions in the dielectric permittivity. As the applied field frequency is increased from the steady state, the permittivity changes from ε_s to the high frequency value ε_∞ as shown in figure 2.6.

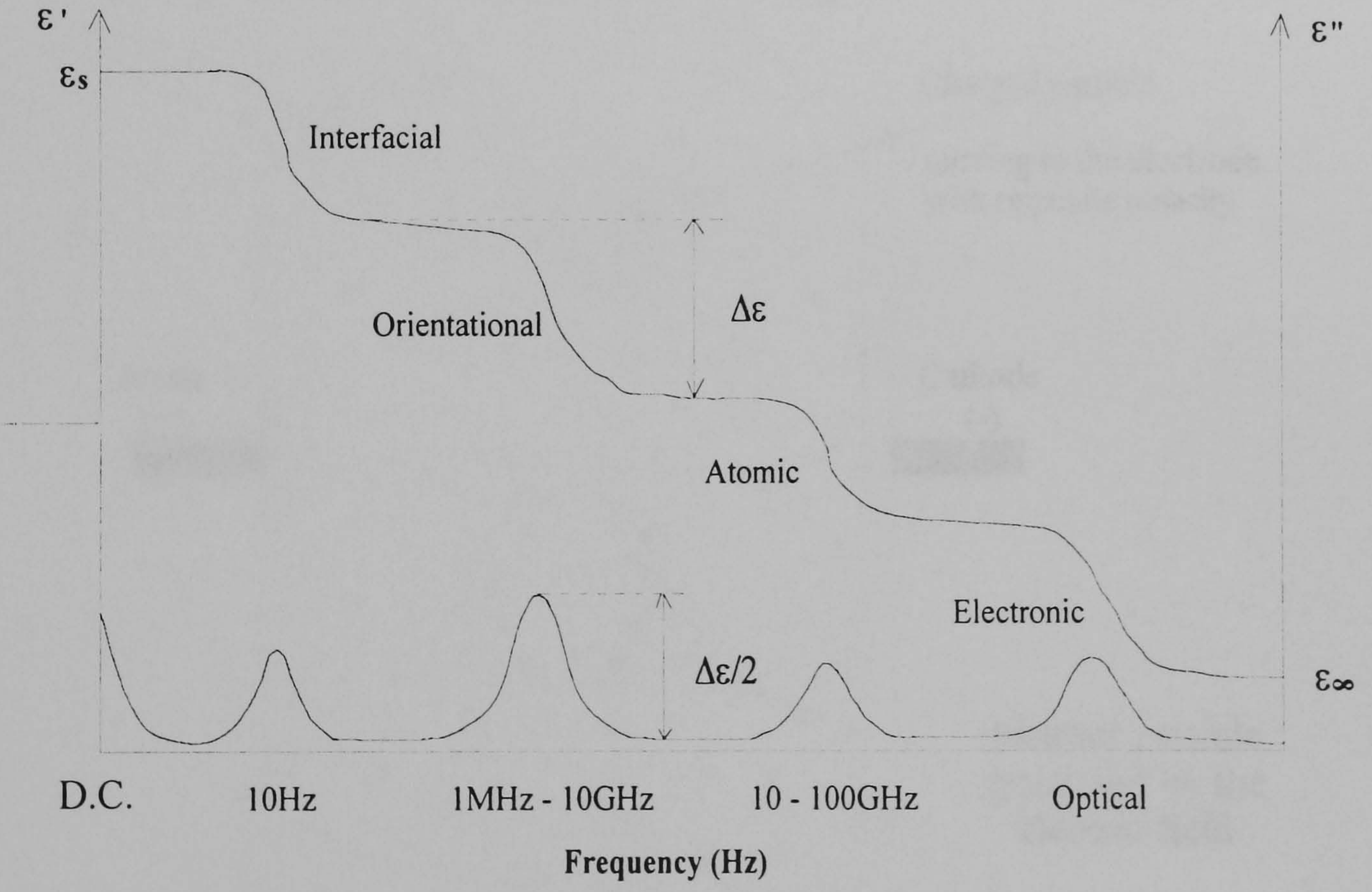

Figure 2.6 Variations of the real and imaginary parts of the complex permittivity for a dielectric exhibiting a number of relaxation processes.

2.5 Dielectrophoresis and Electrorotation

2.5.1 *The Dielectrophoretic Force*

Dielectrophoresis is the translation motion of neutral matter caused by polarisation effects in a nonuniform electric field [3, 9, 10]. It is different from the phenomenon of electrophoresis that describes motion caused by the response to free charge on a body in an electric field. In electrophoresis effects, a charged particle with a net positive charge +Q will be subject to a force from an uniform electric field F = Q.E. The charged particle will move towards the electrode with an opposite polarity to the charged particle (Figure 2.7), while a neutral particle will be polarised to form a dipole by the electric field. There will be no net physical motion applied to this neutral particle.

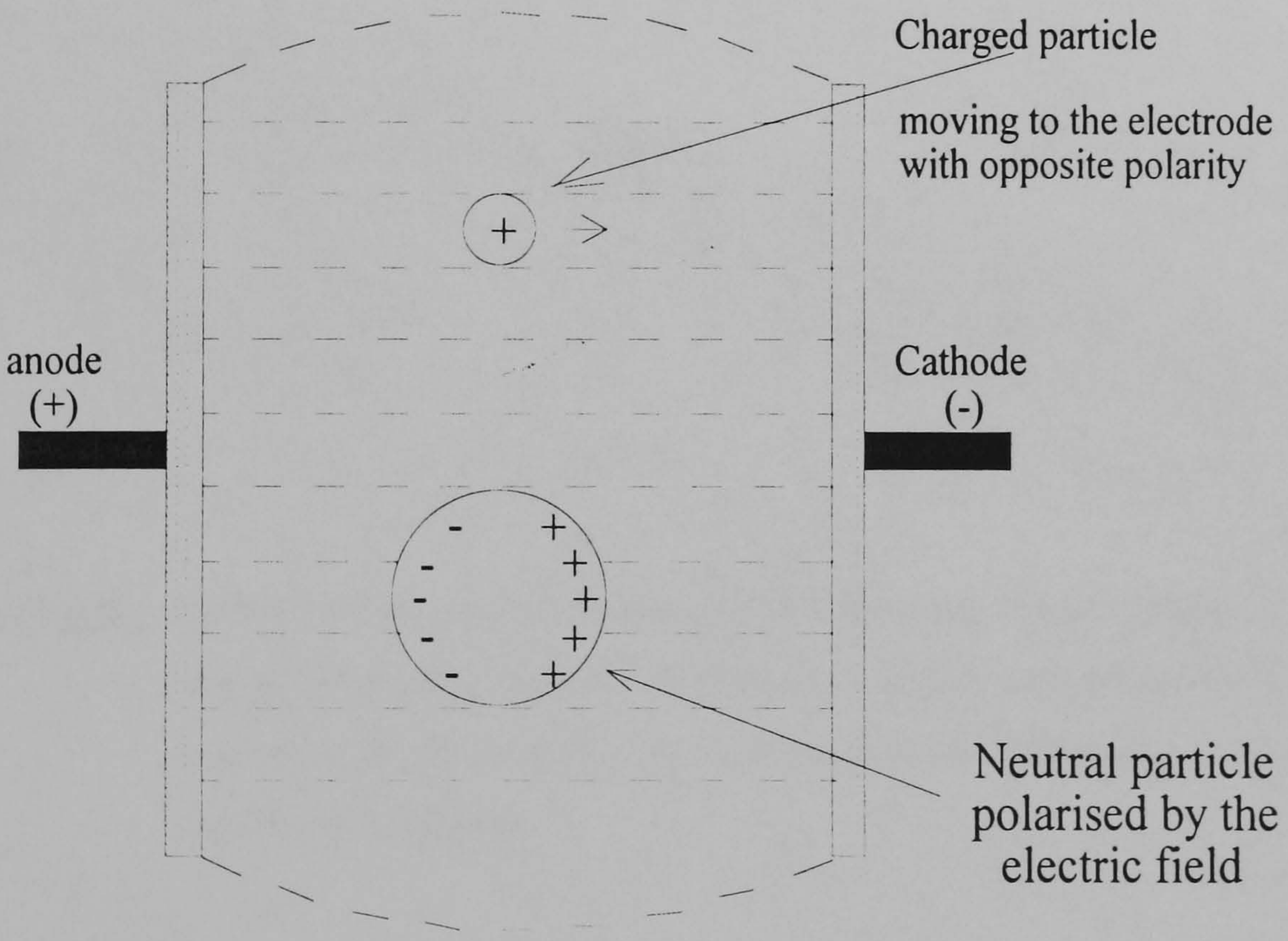

Figure 2.7 The behaviour of neutral and charged particles in a uniform electric field. There is no net force applied to the neutral particle.

In the dielectrophoresis effects with DC fields, the charged particles will behave in the same was as for electrophoresis. The charged particle will move towards to the electrode with opposite charge polarity, while the neutral particle will experience a net translation force. First, the neutral particle will be polarised by the field. The amount of positive ions on the side nearer the negative electrode will be the same as the amount of negative ions upon the side nearer the positive electrode. However, the field operating on the two regions are unequal. This will give rise to a net force. If the neutral polarised particle is more polarised than the surrounding medium, the neutral particle will moved along the electric field line towards the electrode with higher field intensity (Figure 2.8).

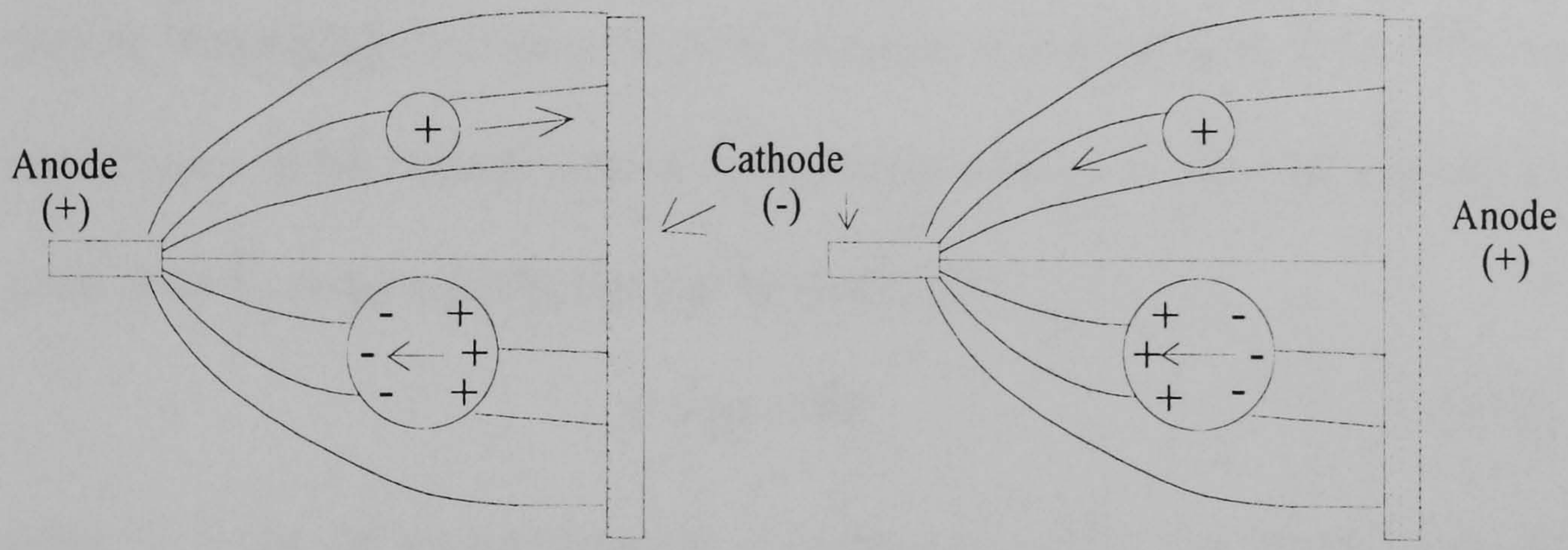

Figure 2.8 Neutral particle is polarised by the field and there is net translation force that causes the particle to move towards the electrode with higher field intensity regardless of the polarity. The charged particle will move to the electrode with opposite polarity.

In an AC condition, the polarised neutral particle will move to the area with the higher field intensity no matter what the polarity of the electrodes, while the charged particle will move to the electrode with the opposite polarity at the low frequency region. As the frequency of the electric field increases, the effect of dielectrophoresis begins to dominate over the electrophoresis effect. Eventually, as the frequency of the applied field increases further, the dielectrophoresis effect will completely dominate the charged particle and the particle will move towards the regions of highest field intensities.

The polarisation of a dielectric material has been shown to be frequency dependent with the characteristic dispersions of these polarisations occuring at different frequencies. Materials exhibit different dielectrophoretic spectra because of their different dielectric properties. The rate of dielectrophoretic motion of a particle is related to the dielectric dispersions. In 1978, Pohl provided a simplified theory for the force exerted upon an electrically neutral particle suspended in a fluid medium when in a non-uniform field. The net force F on a small neutral particle with dipole moment μ per unit volume in a static field E_0 at the equilibrium can be shown as:

$$F = (\mu \cdot \nabla) E_0 \qquad (2.34)$$

where ∇ is the del vector operator. For the case where the neutral dielectric particle is homogeneously, isotropically and linearly polarisable:

$$\mu = \alpha . v E_0 \qquad (2.35)$$

where α and v are the polarisability and the volume of the particle respectively. The net force will be:

$$F = (\alpha . v E_0 \nabla) E_0 = \frac{1}{2} \alpha . v \nabla |E_0|^2 \qquad (2.36)$$

The factor E^2 is independent of the field direction, thus to maximise the magnitude of the dielectrophoretic force, the divergence of the non-uniform field should also be maximised.

Consider a sphere of radius r, composed of an ideal dielectric, with zero conductivity, of relative permittivity ε_p suspended in an ideal dielectric fluid medium with a relative permittivity of ε_m and subjected to a homogeneous electric field E. The field in the fluid medium is uniform before the insertion of the sphere. The sphere distorts this field to give a field E_{in} interior to the sphere boundary [11] of:

$$E_{in} = \left(\frac{3\varepsilon_m}{\varepsilon_p + 2\varepsilon_m} \right) E \tag{2.37}$$

The induced polarisation per unit volume is:

$$P = \varepsilon_0 (\varepsilon_p - \varepsilon_m) E_{in} \tag{2.38}$$

Whilst the induced dipole moment (μ) is given by:

$$\mu = vP = \alpha . vE$$

The polarisability (α) per unit volume can therefore be given as:

$$\alpha = \frac{P}{E} = \varepsilon_0 (\varepsilon_p - \varepsilon_m) \frac{E_{in}}{E}$$

$$\alpha = 3\varepsilon_0 \varepsilon_m \left(\frac{\varepsilon_p - \varepsilon_m}{\varepsilon_p + 2\varepsilon_m} \right) \tag{2.39}$$

Therefore by substituting equation 2.39 to 2.36, the total dielectrophoretic force F acting on a small sphere of volume $v = \frac{4}{3}\pi . r^3$ is:

$$F = \frac{1}{2}\alpha.v\nabla|E_0|^2$$

$$= \frac{3}{2}v\varepsilon_0\varepsilon_m\left(\frac{\varepsilon_p - \varepsilon_m}{\varepsilon_p + 2\varepsilon_m}\right)\nabla|E_0|^2$$

$$= 2\pi.r^3\varepsilon_0\varepsilon_m\left(\frac{\varepsilon_p - \varepsilon_m}{\varepsilon_p + 2\varepsilon_m}\right)\nabla|E_0|^2 \qquad (2.40)$$

In complex permittivity term, the dielectrophoretic force can be described as the real part of the of the Clausius-Mossotti factor [12]:

$$F = 2\pi.r^3\varepsilon_0\varepsilon_m \operatorname{Re}\left(\frac{\varepsilon_p^* - \varepsilon_m^*}{\varepsilon_p^* + 2\varepsilon_m^*}\right)\nabla|E_0|^2 \qquad (2.41)$$

2.5.2 *Positive Dielectrophoresis*

When the permittivity of the particle is greater than the permittivity of the suspending medium, the neutral particle becomes polarised when placed in an electric field, and a dipole moment is induced on the particle. This dipole moment is in the same direction as the applied field, as the permittivity of the particle is greater than that of its suspending medium giving a positive dielectric polarisability factor (by equation 2.40). Since the applied field is non-uniform there is a greater field intensity on one side of the particle than the other. The force on the particle in the high field region is greater than that on the other side of the particle so the net translation force on the particle is directed towards the high field region. This translation motion in a non-uniform electric field towards the high field region is called positive dielectrophoresis (Figure 2.9a).

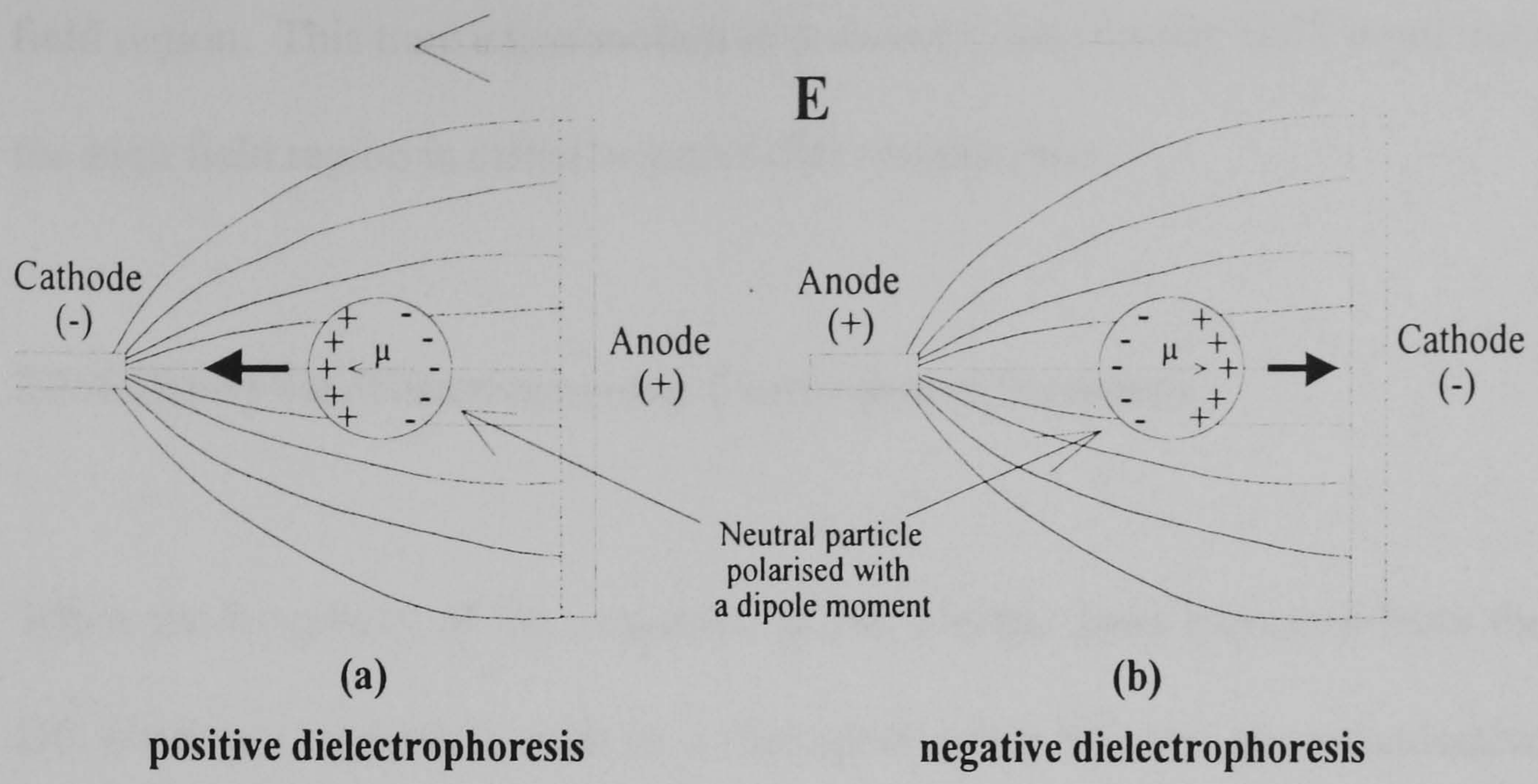

Figure 2.9 (a): Positive dielectrophoresis: permittivity of the polarised neutral particle is larger than that of the suspending medium. (b): Negative dielectrophoresis: permittivity of the particle is less than that of the medium. Particle moves to the low field region.

2.5.3 *Negative Dielectrophoresis*

When the permittivity of the particle is less than that of the suspending medium, the net translation motion of the particle is towards the low field region (Figure 2.9b). The neutral particle becomes polarised when placed in an electric field, and a dipole moment is induced on the particle. This induced dipole moment is in the opposite direction to the applied field, as the permittivity of the suspending medium is greater than that of the particle, giving a negative dielectric polarisability factor (equation 2.40). Since the applied field is non-uniform there is a greater field intensity on one side of the particle than the other. The force on the particle in the high field region is greater than that on the other side of the particle but, since the dipole moment opposes the field, the net translation force on the particle is towards the low field region. This translation motion in a non-uniform electric field away from the high field region is called negative dielectrophoresis.

2.5.4 *Theory on Dielectrophoresis Crossing-over frequency*

When the frequency of the non-uniform AC electric field increases from the DC condition, a particle such as a biological cell with very poor conductive membrane experiences a translation force to pull the cell to the low field intensity region. It experiences the negative dielectrophoresis because the permittivity and conductivity (complex permittivity) of the cell membrane is less than the complex permittivity of the suspending medium. When the frequency of the applied electric field is sufficiently high to penetrate through the cell membrane into the interior of the cell, the cytoplasm, the complex permittivity of the cytoplasm can become higher than that of the suspending medium. Then, the translational force will move the cell towards the high field intensity region [13, 14]. When the translational force changes from negative dielectrophoresis to positive dielectrophoresis, there is a transition period when is no net force acts on the cell. This is because the complex permittivities of the biological cell and the suspending medium behave the same and the net translation force is cancelled (Equation 2.40). This transition period is called the dielectrophoresis crossing-over frequency point. If this transition frequency point (dielectrophoresis crossing-over frequency point) of a biological cell is measured and identified, the value of the membrane capacitance of the cell can be analysed. The theoretical background to this analysis is given by Gascoyne in 1994 [15] and is as follows:

When there is no net translational force applied to a cell, the permittivity of the cell and the suspending medium are equal. Therefore the real part of the Clausius-Mossotti factor form equation 2.41 will be equal to zero.

$$0 = \mathrm{Re}\left[\frac{\left(\varepsilon_p^* - \varepsilon_m^*\right)}{\left(\varepsilon_p^* + 2\varepsilon_m^*\right)}\right] \tag{2.42}$$

where $\varepsilon^*_{\mathrm{p}}$ is the complex permittivity of a biological cell and $\varepsilon^*_{\mathrm{m}}$ is the complex permittivity of the suspending medium. Since $\varepsilon^* = \varepsilon_0\varepsilon_r - j\frac{\sigma}{\omega}$, equation 2.42 become:

$$0 = \mathrm{Re}\left[\frac{\left(\varepsilon_0\varepsilon_{rp} - j\frac{\sigma_p}{\omega}\right) - \left(\varepsilon_0\varepsilon_{rm} - j\frac{\sigma_m}{\omega}\right)}{\left(\varepsilon_0\varepsilon_{rp} - j\frac{\sigma_p}{\omega}\right) + 2\left(\varepsilon_0\varepsilon_{rm} - j\frac{\sigma_m}{\omega}\right)}\right]$$

where ε_{rp} and σ_p is the relative permittivity and conductivity of the biological particle, respectively. The factor ε_{rm} and σ_m are the relative permittivity and the conductivity of the suspending medium, respectively. The angular frequency of the dielectrophoresis crossing-over frequency can be derived as:

$$\omega = \left[\frac{\left(\sigma_m - \sigma_p\right)\left(\sigma_p + 2\sigma_m\right)}{\left(\varepsilon_0\varepsilon_{rp} - \varepsilon_0\varepsilon_{rm}\right)\left(\varepsilon_0\varepsilon_{rp} + 2\varepsilon_0\varepsilon_{rm}\right)}\right]^{1/2}$$

for the dielectrophoresis cross-over frequency $f_{co} = \frac{\omega}{2\pi}$:

$$f_{co} = \frac{1}{2\pi}\left[\frac{(\sigma_m - \sigma_p)(\sigma_p + 2\sigma_m)}{(\varepsilon_0\varepsilon_{rp} - \varepsilon_0\varepsilon_{rm})(\varepsilon_0\varepsilon_{rp} + 2\varepsilon_0\varepsilon_{rm})}\right]^{1/2} \qquad (2.43)$$

By using the generalised dielectric shell model [16]:

$$\varepsilon_p^* = \varepsilon_{mem}^*\left[\frac{\left(\frac{R}{R-d}\right)^3 + 2\left(\frac{\varepsilon_{in}^* - \varepsilon_{mem}^*}{\varepsilon_{in}^* + 2\varepsilon_{mem}^*}\right)}{\left(\frac{R}{R-d}\right)^3 - \left(\frac{\varepsilon_{in}^* - \varepsilon_{mem}^*}{\varepsilon_{in}^* + 2\varepsilon_{mem}^*}\right)}\right] \qquad (2.44)$$

where ε^*_{in} and ε^*_{mem} are the complex permittivities of the interior of cell (cytoplasm) and cell membrane respectively. R and d are the radius of the cell and the membrane thickness respectively. The cell membrane is a thin and poorly conductive layer comparing with the cell interior (cytoplasm). Also, the relative permittivity of the cell membrane is small in comparion with the interior of the cell. At a frequency well below the Maxwell-Wagner relaxation frequency (below 1MHz).

$$1 \approx \left(\frac{\varepsilon_{in}^* - \varepsilon_{mem}^*}{\varepsilon_{in}^* + 2\varepsilon_{mem}^*}\right)$$

Equation 2.44 can be written as:

$$\varepsilon_p^* = \varepsilon_{mem}^*\left[\frac{\left(\frac{R}{R-d}\right)^3 + 2}{\left(\frac{R}{R-d}\right)^3 - 1}\right]$$

$$\varepsilon_p^* = \varepsilon_{mem}^*\left[\frac{\left(\frac{1}{1-d/R}\right)^3 + 2}{\left(\frac{1}{1-d/R}\right)^3 - 1}\right] \qquad (2.45)$$

By using the Binomial series:

$$(1-x)^n = 1 - nx + \frac{n(n-1)}{2!}x^2 - \frac{n(n-1)(n-2)}{3!}x^3 + \cdots$$

The complex permittivity of the biological particle can be expressed as:

$$\varepsilon_p^* = \varepsilon_{mem}^* \left[\frac{\left(1 + {}^{3d}\!/_{R}\right) + 2}{\left(1 + {}^{3d}\!/_{R}\right) - 1} \right]$$

$$\varepsilon_p^* = \varepsilon_{mem}^* \left(\frac{R+d}{d} \right) \tag{2.46}$$

Since the radius R of the cell is very much larger than the thickness d of the membrane:

$$R >> d \qquad \varepsilon_p^* = \varepsilon_{mem}^* \left(\frac{R}{d} \right) \tag{2.47}$$

The membrane capacitance equation: $C_{mem} = \frac{\varepsilon_{mem} . A}{d}$

The specific membrane capacitance $C_{mem.sp}$ (in unit $F.m^{-2}$) can be known as:

$$C_{mem.sp} = \frac{\varepsilon_{mem}}{d} \tag{2.48}$$

By substituting equation 2.48 into equation 2.47, the permittivity of the biological particle ε_p can be described in terms of the specific membrane capacitance.

$$\varepsilon_p = R.C_{mem.sp} \tag{2.49}$$

If the medium conductivity is very high compared with the membrane conductivity, equation 2.43 describing the dielectrophoresis cross-over frequency can be simplified as follows:

Assume that $\sigma_p \approx 0$, $\sigma_m >> \sigma_p$, and $\varepsilon_p >> \varepsilon_m$

Then:

$$f_{co} \equiv \frac{1}{\pi\sqrt{2}} \cdot \frac{\sigma_m}{\varepsilon_p} \tag{2.50}$$

By eventually substituting equation 2.49 into equation 2.50, the membrane capacitance of the biological cell can be expressed as:

$$C_{mem.sp} = \frac{\sigma_m}{\pi\sqrt{2} \cdot R \cdot f_{co}} \tag{2.51}$$

Therefore the specific membrane capacitance of any biological cell can be known from the values of the suspending medium conductivity, the radius of the cell and the measurement of the dielectrophoresis cross-over frequency f_{co}.

2.6 Electrorotation Theory

Electrorotation is a phenomena that occurs as a result of a rotational torque exerted on a polarised particle subjected to a rotating electric field [16]. When an electric field is applied to a system consisting of particles suspended in a liquid medium, an electric dipole moment μ is induced in each particle as a result of electrical polarisation at the interfaces that define their structure. This induced moment interacts with the rotating field to produce a torque on the particle which is dependent on the geometry and dielectric properties of the particle. A spherical particle of radius r in an applied electric field E of angular frequency ω has a dipole moment μ induced as the particle becomes polarised. This can be expressed as:

$$\mu = 4\pi\varepsilon_0\varepsilon_m \cdot r^3 \left(\frac{\varepsilon_p^* - \varepsilon_m^*}{\varepsilon_p^* + 2\varepsilon_m^*} \right) E \qquad (2.52)$$

where ε_m and ε^*_m are the relative permittivity and complex permittivity of the suspending medium, respectively and the ε^*_p is the complex permittivity of the particle.

In general, a quadrature rotating electric field can be generated by electrodes with four sets of sinusoidal voltage that are separated by a 90° phase shift.

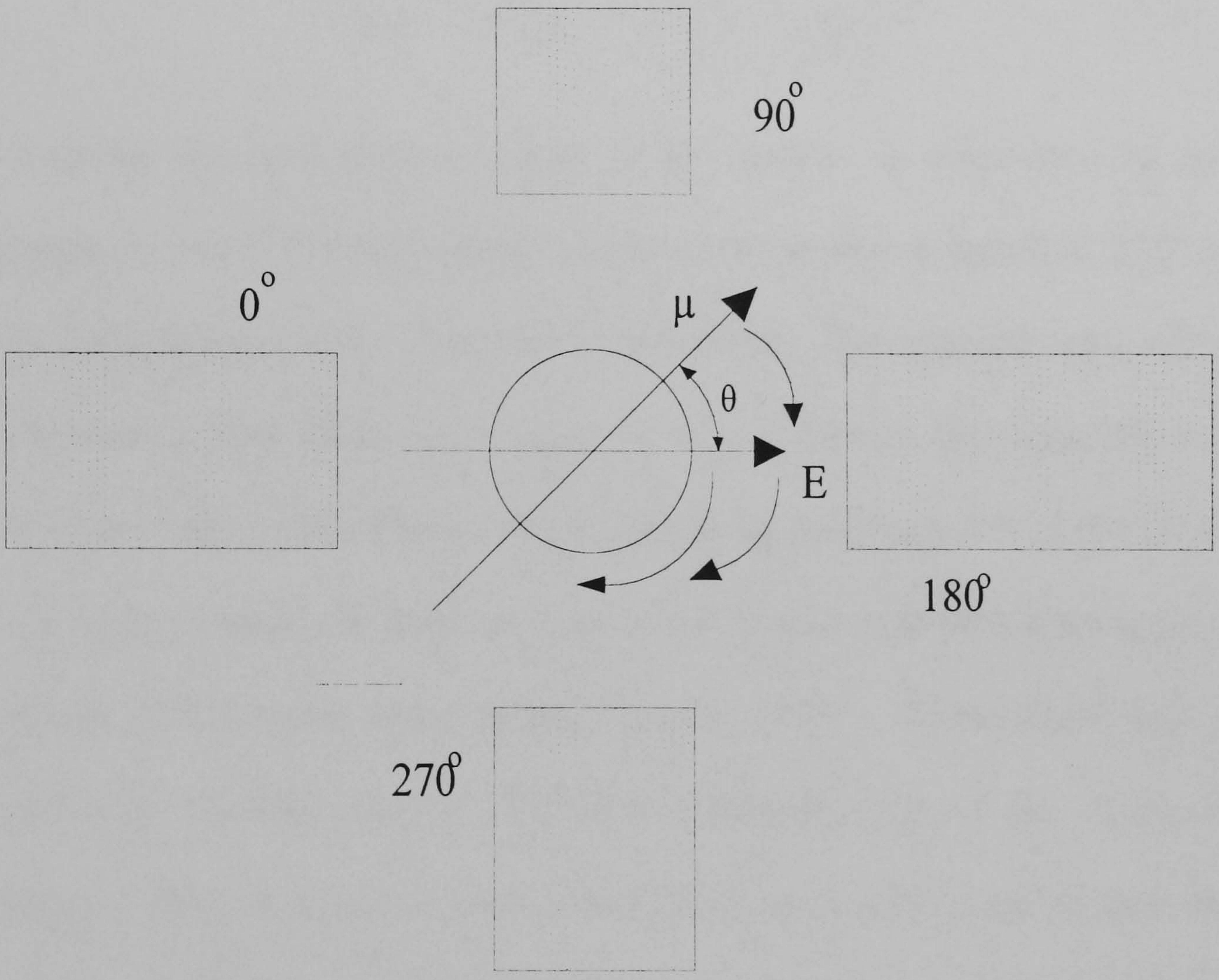

Figure 2.10 A particle undergoing electrorotation. The induced dipole moment μ is following the movement of the electric field and it has a phase angle of θ.

Since the induced dipole moment may either lead or lag behind the applied electric field, the phase angle θ between the applied field (Figure 2.10) and the dipole moment can be described as:

$$\theta = \frac{\mathrm{Im}(\mu)}{\mathrm{Re}(\mu)} \qquad (2.53)$$

where Re(μ)and Im(μ) are the real and imaginary parts of the induced dipole moment of the particle respectively. The electrorotation torque that is experience by a spherical particle can be expressed as [17, 18]:

$$\Gamma(\omega) = -4\pi\varepsilon_0\varepsilon_m \cdot r^3 \,\mathrm{Im}\left(\frac{\varepsilon_p^* - \varepsilon_m^*}{\varepsilon_p^* + 2\varepsilon_m^*}\right) E^2 \qquad (2.54)$$

Therefore the electrorotation torque of the particle is determined by the imaginary part of the induced dipole moment of the particle (equation 2.52) or the imaginary part of the Clausius-Mossotti factor. This imaginary part of the Clausius-Mossotti factor is the major factor to determine the magnitude and the phase angle of the dipole moment. When the imaginary part of this factor is a negative value, the dipole moment of the particle lags behind the applied electric field E by the angles ranging from 0° to 180° . In this situation, it is called the Co-field rotation. When the imaginary part of this Clausius-Mossotti factor is a positive value, the dipole moment of the particle leads the applied field by the angles ranging from 0° to 180°. This is called the anti-field rotation.

When the rotational torque is balanced by the frictional force due to the opposing viscous drag of the medium and the frictional contact between the particle and the glass surface, a stationary electrorotation velocity can be reached. It has been derived by Arnold and Zimmermann [19] as:

$$V(\omega) = -\frac{\varepsilon_0 \varepsilon_m}{2R} \mathrm{Im}\left(\frac{\varepsilon_p^* - \varepsilon_m^*}{\varepsilon_p^* + 2\varepsilon_m^*} \right) E^2 \qquad (2.55)$$

where R is the friction coefficient that depends on the viscosity of the suspending medium and on the geometry and the surface frictional properties of the particle [20].

2.7 Dielectric Shell Model

Cells are not homogeneous in their electrical and physical properties. In 1913, Höber [21] showed that red blood cells could be represented as a conducting sphere surrounded by a resistive membrane. In 1891, Maxwell demonstrated that such a concentric system could be replaced by a homogeneous sphere of the same external radius with an effective resistance r_p. [6]. The "smeared-out" sphere can substitute a heterogeneous sphere without altering the external applied electric field. Later on in 1914 Wagner, based on the work of Maxwell derived the effective complex permittivity of a system composed of particles dispersed in a dielectric medium [7]. This means that the interfacial charging effect that occurs for a homogeneous particle is reflected in the overall dielectric properties of the heterogeneous mixture. Then more recently, the theory of multishell model for cells was further developed by Fricke in 1924 [22], Hanai in 1960 [23], Irimajiri *et al* in 1979 [24] and followed by Huang *et al* in 1992 [16]. An ellipsoidal multishell model has also been improved by Kakutani *et al* in 1993 [20].

2.7.1 *Spherical Multishell Model Theory*

The spherical multishell model [16] can be used to describe the dielectric properties of the heterogeneous parts within the cell (such as cell membrane and cytoplasm). The geometry of the cell sample is spherical. The equation of this spherical multishell model is as follows:

$$\varepsilon^*_{peff} = \varepsilon^*_{Neff} = \varepsilon^*_{N+1}\left[\frac{\left(\frac{R_{N+1}}{R_N}\right)^3 + 2\left(\frac{\varepsilon^*_{N-1eff} - \varepsilon^*_{N+1}}{\varepsilon^*_{N-1eff} + 2\varepsilon^*_{N+1}}\right)}{\left(\frac{R_{N+1}}{R_N}\right)^3 - \left(\frac{\varepsilon^*_{N-1eff} - \varepsilon^*_{N+1}}{\varepsilon^*_{N-1eff} + 2\varepsilon^*_{N+1}}\right)}\right] \qquad (2.56)$$

where $\varepsilon^*_{\text{p eff}}$ or $\varepsilon^*_{\text{N eff}}$ is the effective complex permittivity of the N-shelled sphere model. R_N and R_{N+1} are the radius of Nth-shell and N+1th shell respectively. $\varepsilon^*_{\text{N-1 eff}}$ is the effective complex permittivity of the N-1th shell that starts from the innermost shell of the model. ε^*_{N+1} is the effective complex permittivity of the N+1th shell (see figure 2.11).

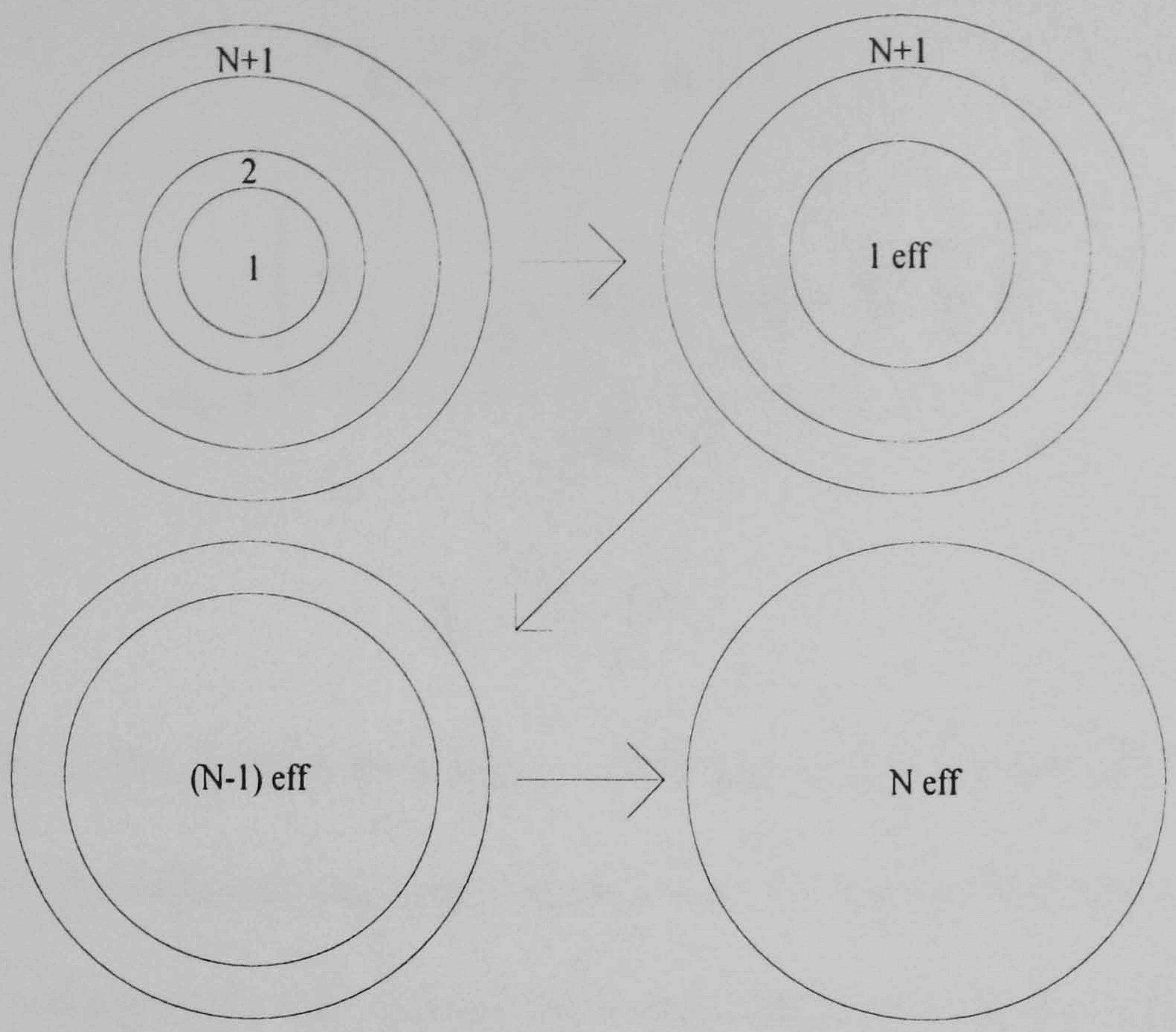

Figure 2.11 Smeared-out sphere approach for determining the effective permittivity of a N-shell sphere, showing the progressive simplification to a simple, homogeneous sphere having an effective, complex permittivity (equation 3.1) that mimics the dielectric properties of the multi-shell model sphere.

2.7.2 *Ellipsoidal Multishell Model Theory*

If the geometry of a particle (such as red blood cell) is in the shape of an ellipse, an ellipsoidal multishell model is more appropriate to be used in the analysis. The ellipsoidal multi-shell model [20] consists of five sets of equations to analyse the ROT data of any ellipsoidal particles. First, there are depolarising factors along the x and y axis of the ellipsoidal particle (Figure 2.12). This depolarising factor is dependent on the shape of the sample. In the latex bead ROT experiments (Chapter 5), the shapes of the samples are prolate spheroids ($a_o > b_0 = c_0$) (Figure 2.12: c_0 is a radius in the z-axis). The equations for the depolarising factors of prolate spheroids are given by equations 2.57, 2.58 (for x-axis) and 2.59 (for z and y-axis).

$$q_i = {a_i}/{b_i} \quad \text{for} \quad q_i > 1 \tag{2.57}$$

$$A_{ix} = \frac{\left[\dfrac{q_i}{\left(q_i^2 - 1\right)^{1/2}} \right] \ln\left[q_i + \left(q_i^2 - 1\right)^{1/2} \right] - 1}{\left(q_i^2 - 1\right)} \tag{2.58}$$

$$A_{iy} = \frac{\left(1 - A_{ix}\right)}{2} \tag{2.59}$$

where A_{ix} is the depolarising factor in the x-axis for each shell ($i = 0, 1, \ldots, n-1$). A_{iy} is the depolarising factor in the y-axis for each i shell layer. The factor a_i is the radius of the *ith* shell in the x-axis direction; b_i is the radius of the *ith* shell in the y-axis direction.

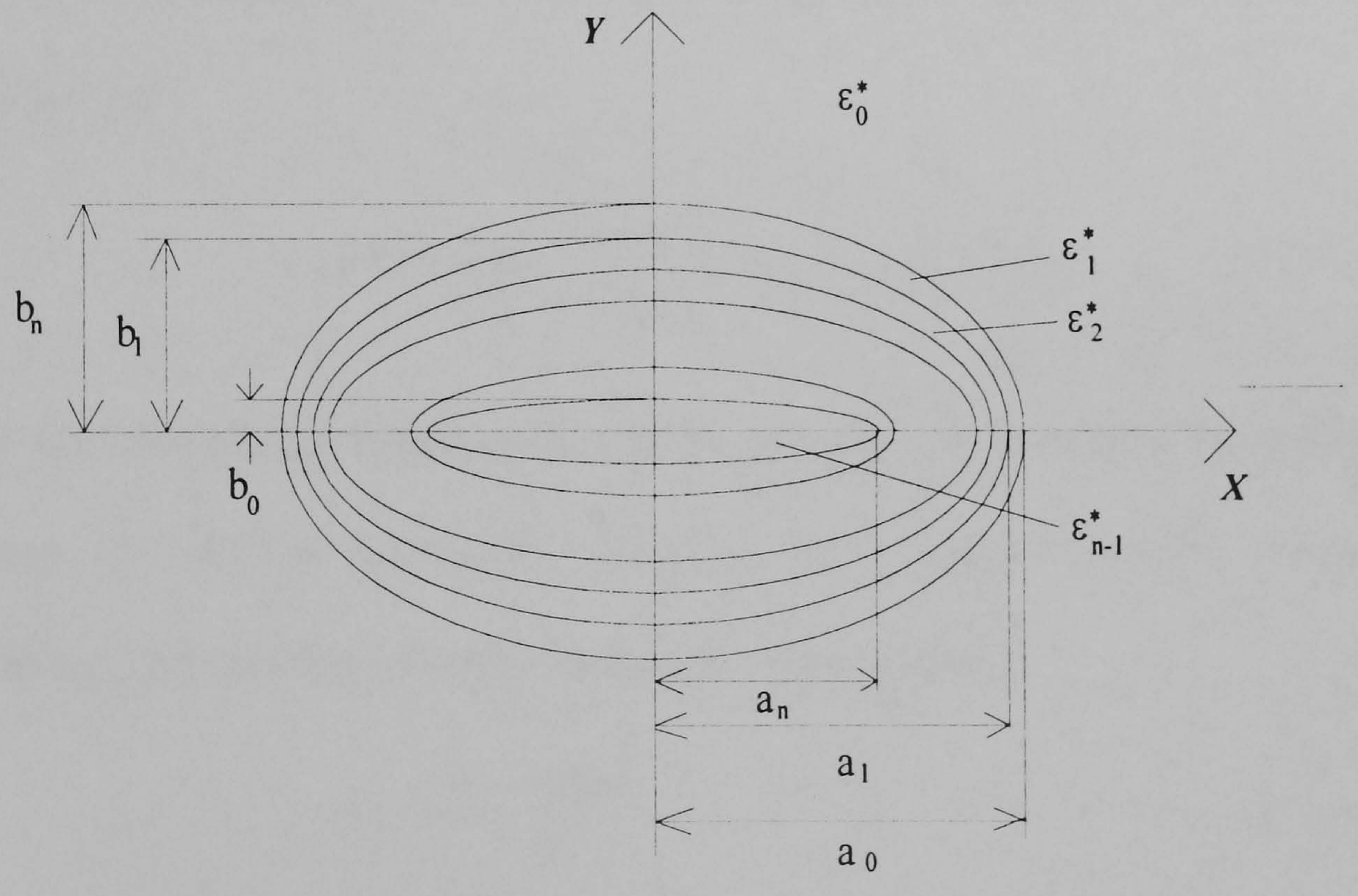

Figure 2.12 Cross-section of an ellipsoidal multishell model in the *x-y* plane

The ratio v_i between the outer shell and the immediate inner shell required for the ellipsoidal multishell model is given by

$$v_i = \frac{a_i b_i c_i}{a_{i-1} b_{i-1} c_{i-1}} \qquad i = 1, 2, \ldots\ldots, n\text{-}1 \tag{2.60}$$

where a_i, b_i and c_i are the radii of the ith shell in the x, y and z-axis direction. Also

$$\bar{\varepsilon}^*_{i-1,\alpha} = \varepsilon^*_{i-1} \frac{\varepsilon^*_{i-1} + \left(\varepsilon^*_i - \varepsilon^*_{i-1}\right)\left[A_{i-1,\alpha} + v_{i-1}\left(1 - A_{i-2,\alpha}\right)\right]}{\varepsilon^*_{i-1} + \left(\varepsilon^*_i - \varepsilon^*_{i-1}\right)\left(A_{i-1,\alpha} - v_{i-1} A_{i-2,\alpha}\right)} \tag{2.61}$$

where $i = 2, \ldots., n\text{-}2$; and variables $A_{i-1,\alpha}$ and $A_{i-2,\alpha}$ are defined by equation 2.58 and 2.59.

Having obtained the effective permittivity $\bar{\varepsilon}^*_{i-1,\alpha}$, the induced dipole moment $\chi_\alpha(\omega)$ could be calculated by substituting the effective permittivity value into equation 2.62.

$$\chi_\alpha(\omega) = \frac{\overline{\varepsilon^*_{1\alpha}} - \varepsilon^*_0}{\left(\overline{\varepsilon^*_{1\alpha}} - \varepsilon^*_0\right) A_{0\alpha} + \varepsilon^*_0} \qquad \alpha = x, y \tag{2.62}$$

After the induced dipole moment of the model is known, the stationary angular velocity of rotation about the z-axis for the ellipsoidal model can be calculated. The procedure of this calculation is as follows:

$$V_c = \frac{4\pi \cdot a_0 b_0 c_0}{3} \tag{2.63}$$

where V_c is the volume of the multishell ellipsoid, a_0, b_0 and c_0 are the outermost shell radii of the model.

$$R_f = 2V_c\eta\left[\frac{\left(a_0^2 + b_0^2\right)}{\left(a_0^2 A_{0x} + b_0^2 A_{0y}\right)}\right] \tag{2.64}$$

where η was the viscosity of the external medium; A_{0x} and A_{0y} are defined by equation 2.58 and 2.59.

$$\omega_c = 0.5\varepsilon_0\left(\frac{V_c}{R_f}\right)\left\{\mathrm{Im}\left[\chi_x(\omega) + \chi_y(\omega)\right]\right\}E_0^2 \tag{2.65}$$

where ω_c is the stationary angular velocity of rotation about the z-axis. E_0 is the external applied electric field. $\chi_x(\omega)$ and $\chi_y(\omega)$ are the induced dipole moments of the ellipsoidal model (equation 2.62).

2.8 Vesicles structure

A vesicle is a synthetic particle that contains an aqueous volume enclosed by a membrane composed of lipids molecules (usually phospholipids) [25]. They form spontaneously when lipids are dispersed in aqueous media, giving rise to a population of vesicles which may range from tens of nanometers to tens of micrometers in diameter. The membrane structure of vesicles are very similar to the structure of normal biological cells, except that there are no proteins ions channels and sugar molecules in the membrane structure. Therefore the membrane conductivity of the vesicle is small compared with the conductivity of the cell membrane, which has a more complex ionic structure. The interior of the vesicles simply consist of an aqueous medium rather than the complex structure of the cytoplasm of cells. Therefore, vesicles can provide model samples with very simple physical and electrical structures to be analysed by the dielectrophoresis or electrorotation technique.

In this investigation, the membrane of the vesicle only consists of the phospholipids (DOPC: 1-2-Dioleoyl-sn-Glycero-3-Phosphocholine) and cholesterol molecules. Their chemical structures are shown in figure 2.13.

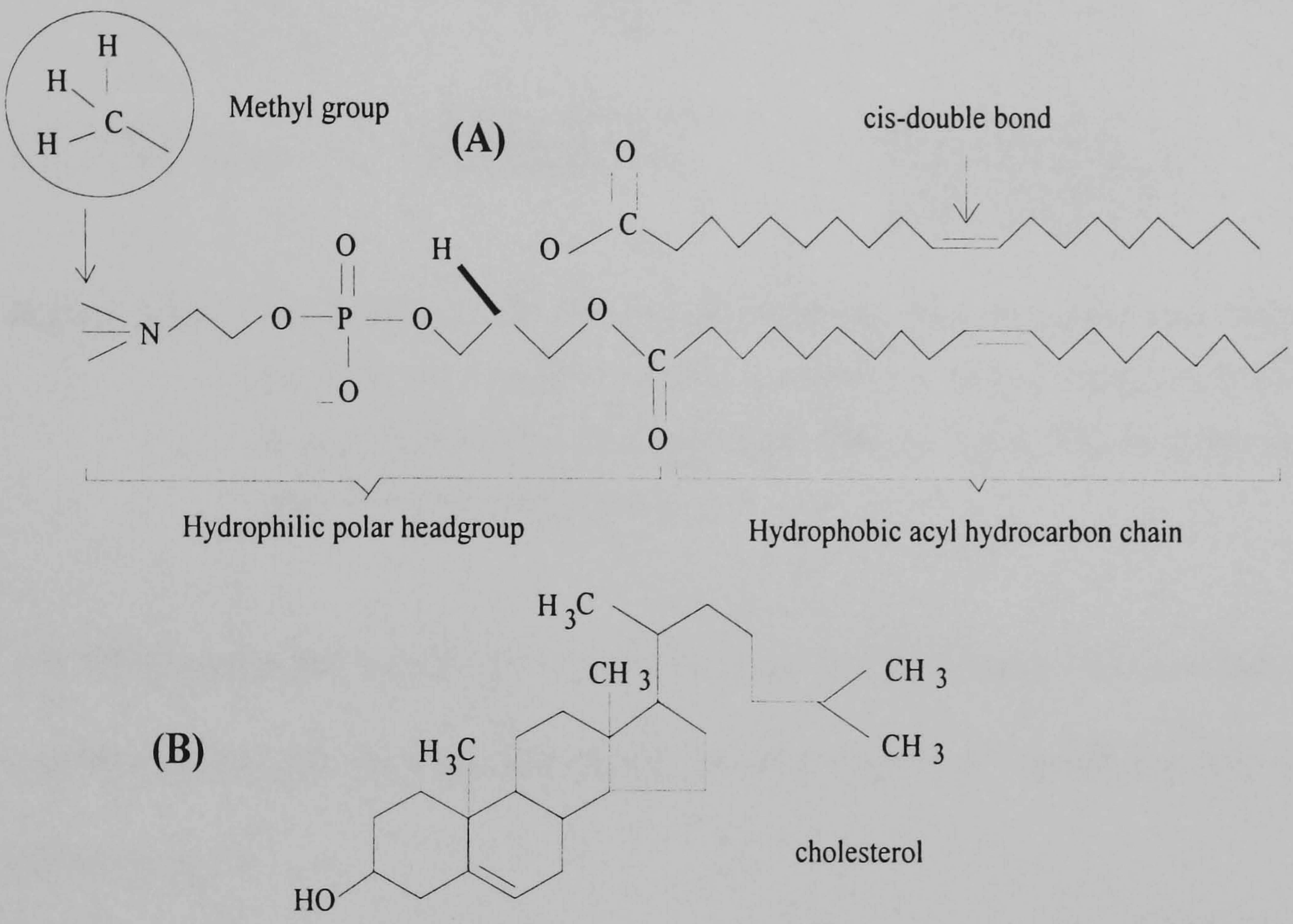

Figure 2.13 (A): Phospholipid DOPC: 1-2-dioleoyl-sn-glycero-3-phosphocholine.
(B): Cholesterol

The dielectric and physical properties of the vesicles' membrane can be altered by the variation of temperature. This is because different types of lipids molecules have different phase transition temperatures [25]. The most consistently observed of these phase transitions is the one occurring at the highest temperature, in which the membrane passes from a tightly ordered 'gel' or 'solid' phase, to a liquid-crystal phase at raised temperatures where the freedom of movement of individual molecules is higher. This mechanism of transformation is shown in figure 2.14.

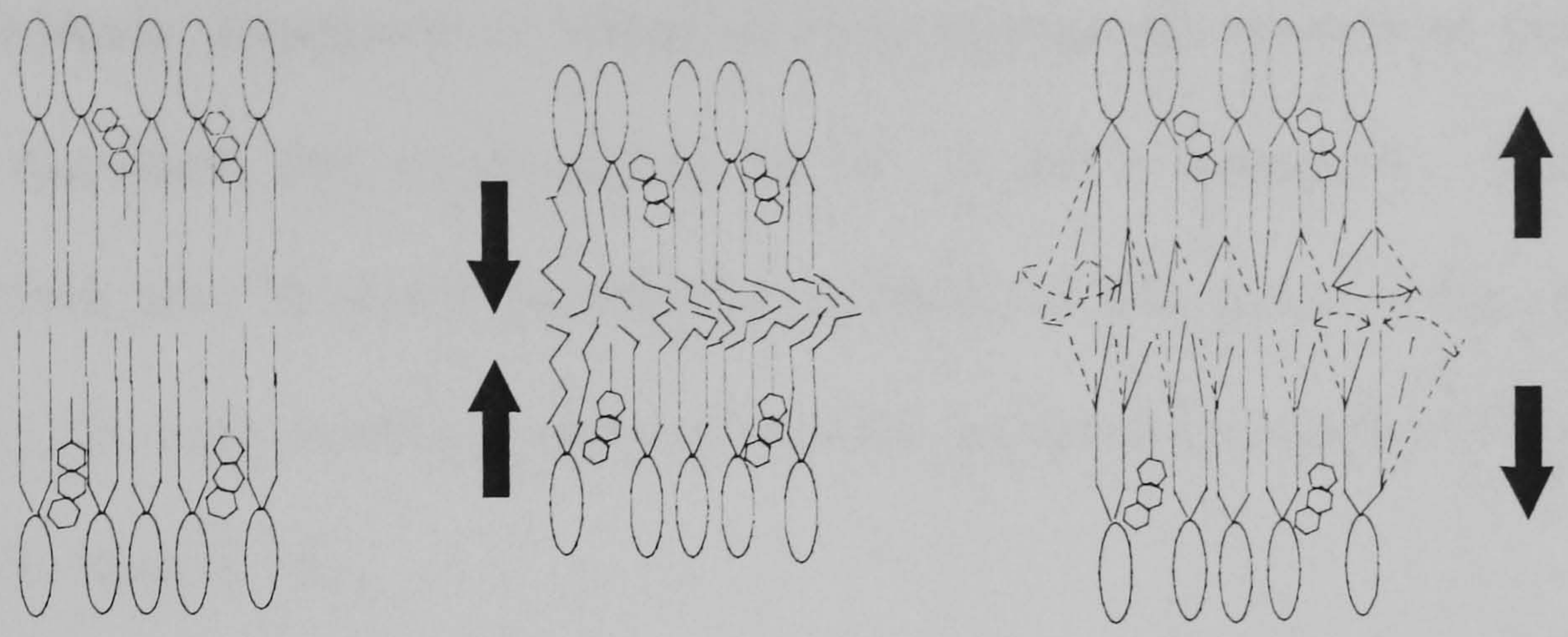

"Solid" Gel Phase state
Below Transition Temperature

Gel to Liquid crystalline transition
At Transition temperture
Membrane thickness decreases

"Fluid" Liquid crystalline state
above transition temperature
Membrane swells up by fluctration movement of hydrocarbon chains
Membrane thickness increases

Figure 2.14 As temperature rises, membrane goes through phase transition from "solid" gel phase state (below transition temperature), Gel to Liquid crystalline state (at the transition temperature) and lastly to "Fluid" liquid crystal state (above transition temperature).

The thickness of the membrane will be changed by these temperature induced variations [26], and the dielectric properties of the vesicles' membrane will be altered as well.

The α-dispersion of biological cells occurs in the frequency region of 100Hz to 10kHz. It is considered to be associated with the relaxation of an ionic layer at the surface of the cells. The surface of cells consists of negatively charged head groups of phospholipids, proteins ions channel and sugar molecules attached to the membrane surface. The membrane of the vesicles has neither proteins ion channels nor the sugar molecules which contribute to the large amount of surface charge to the cells' surface. Therefore, the amount of ionic molecules at the interfaces of vesicles will be very small, and the α dispersion can be expected to be relatively small.

The β-dispersion of the cells occurs in the frequency range of 1MHz to 10MHz and is considered to be associated with the resistive properties of the cell membrane that acts as an insulating barrier between the suspending medium and conductive cytoplasm. The relaxation mechanisms that arise are associated with the interfacial polarisation processes. The membrane of the vesicles also behaves as an insulating barrier between the suspending medium and the conductive encapsulating medium that is inside the vesicles. Therefore the interfacial polarisation also takes place in the vesicles. The membrane interface between the suspending media and the charge build-up on the outer surface of the cells are identical to the interfacial Maxwell-Wagner relaxation effects described earlier. If the conductivity of the encapsulating medium of the vesicles are either higher or lower than the conductivity of the suspending medium, the interfacial Maxwell-Wagner relaxation can be observed. This relaxation becomes more magnified if the difference between the conductivity of the suspending medium and the encapsulating medium increases. On the contrary, the Maxwell-Wagner interfacial relaxation is minimal if the conductivities of both the suspending medium and the encapsulating medium are the same.

Finally the γ-dispersion of the biological cells appears at high frequencies and is associated with the relaxation of water molecules within the cytoplasm [27]. Since the interior of vesicles contain only the aqueous ionic solution, the γ-dispersions of vesicles are similar to that of biological cells.

2.10 Electron Spin Resonance Labelling Technique

Since the electrical and physical properties of vesicle membranes and biological cells are very sensitive to temperature variations in the experimental environment, it is appropriate to understand the phase transitions of the membrane in a fixed temperature region. The technique of electron spin resonance (ESR) [29] is used to study the motion and organisation of the biological membranes, and in this work ESR was used to investigate the vesicle membrane. Membrane ESR spectroscopy uses a paramagnetic reporter group (probe or label molecules) to elucidate the topology and dynamic state of membrane components. Probe molecules may be non-covalently, non-specifically intercalated into the membranes, noncovalently bound to membrane proteins through specific interactions (e.g., receptor binding to tagged ligands), or covalently attached to integral or peripheral proteins.

Analysis of the ESR spectra of membranes "spin-labelled" in this manner yields information not only on the mobility and polarity of the label, but also the proximity of labels to one another.

Electron spin resonance absorption of energy occurs because the intrinsic magnetic moment of an unpaired electron interacts with an applied magnetic field. In spin-label studies on biological membranes, this unpaired electron is usually that of an oxazolidine ring (Figure 2.16). The alkyl side chains (R_1 and R_2) stabilise the free radical, and these may be used to attach the label either to intrinsic membrane components such as proteins and glycolipids, or to extrinsic probes that may be incorporated into the membrane.

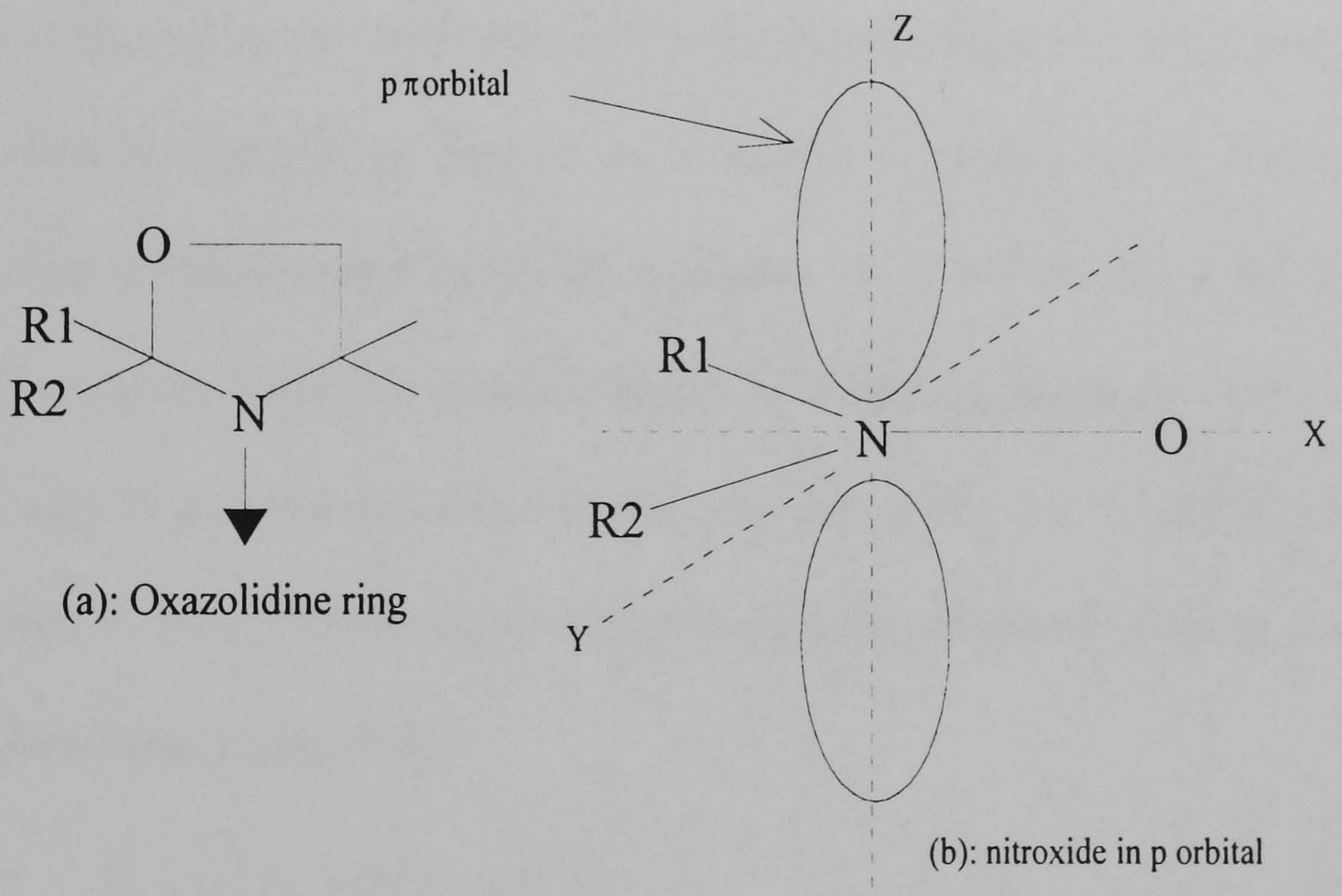

Figure 2.16 (a): The stable free radical, oxazolidine ring typically used to label model and biological membranes in ESR studies.
(b): The nitroxide group showing the nitrogen pπ orbital direction of the unpaired electron in relation to the x, y and z principal axes. N, nitrogen; O, oxygen; R1 and R2 are alkyl chains.

This label has been frequently used in ESR studies and has a simple spectrum (Figure 2.17) that is characteristically perturbed by the rapid motional states typical of the biological membranes. This spectrum is used to determine the position of the absorption bands in the magnetic-field plot, and a coupling constant "T", the nuclear hyperfine tensor [29] which is equal to the spacing between components of the hyperfine spectrum. The hyperfine spectrum is created by the interaction of the nitroxide nitrogen nucleus with the unpaired electron. Because the unpaired electron occupies an almost pure (80-90%) 2pπ molecular orbital on the nitrogen nucleus, the nitrogen 14 atom splits the absorption band into three bands of equal intensity.

If the label undergoes rapid rotational and segmented motion in the membrane such that the z'-axis is defined as a unique symmetry axis, the nuclear hyperfine splitting tensor T|| which is parallel to the unique symmetry z'-axis, and the nuclear hyperfine splitting tensor T⊥ which is perpendicular to the z'-axis, may be expressed in terms of the elements of T. T_{xx}, T_{yy} and T_{zz} are the elements of the hyperfine tensor which have been measured in the x, y and z-axis directions, respectively.

$$T_{\|} = \overline{\alpha^2} T_{xx} + \overline{\beta^2} T_{yy} + \overline{\gamma^2} T_{zz} \tag{2.66}$$

$$T\perp = \tfrac{1}{2}\left(1-\overline{\alpha^2}\right)T_{xx} + \tfrac{1}{2}\left(1-\overline{\beta^2}\right)T_{yy} + \tfrac{1}{2}\left(1-\overline{\gamma^2}\right)T_{zz} \tag{2.67}$$

where $\overline{\alpha^2}$, $\overline{\beta^2}$ and $\overline{\gamma^2}$ are the time averages of the squares of the direction consines of the unique symmetry z'-axis in the x, y and z axis system. The isotropic hyperfine coupling constant a_N (in gauss) for the nitroxide molecule in the crystal state is given as [29]:

$$a_N = \frac{1}{3}\left(T_{zz} + T_{xx}\right) \ gauss \tag{2.68}$$

and the isotropic hyperfine coupling constant for the probe in the membrane a_N' is given as[29]:

$$a_N' = \frac{1}{3}\left(T_{\|} + T\perp\right) \ gauss \tag{2.69}$$

Therefore the membrane fluidity of a sample can be expressed in terms of Seelig order parameter [29, 30]:

$$S\left(T_{\|}\right) = \frac{1}{2}\left[\frac{3\left(T_{\|} - T_{xx}\right)}{\left(T_{zz} - T_{xx}\right)} - 1\right] \tag{2.70}$$

If $a_N' = a_N$, then $T_{\|}$ can be expressed as a function of $T_{\perp}$:

$$T_{\|} = \left(T_{zz} + 2T_{xx}\right) - 2T_{\perp} \tag{2.71}$$

This eventually gives rise to the polarity-corrected order parameter S [31]:

$$S = \frac{\left(T_{\|} - T_{\perp}\right)\left(a_N\right)}{\left(T_{zz} - T_{xx}\right)\left(a_N'\right)} \tag{2.72}$$

If the value of S increases, the fluidity of the membrane becomes more rigid. On the contrary, the membrane fluidity becomes less rigid if the value of S decreases.

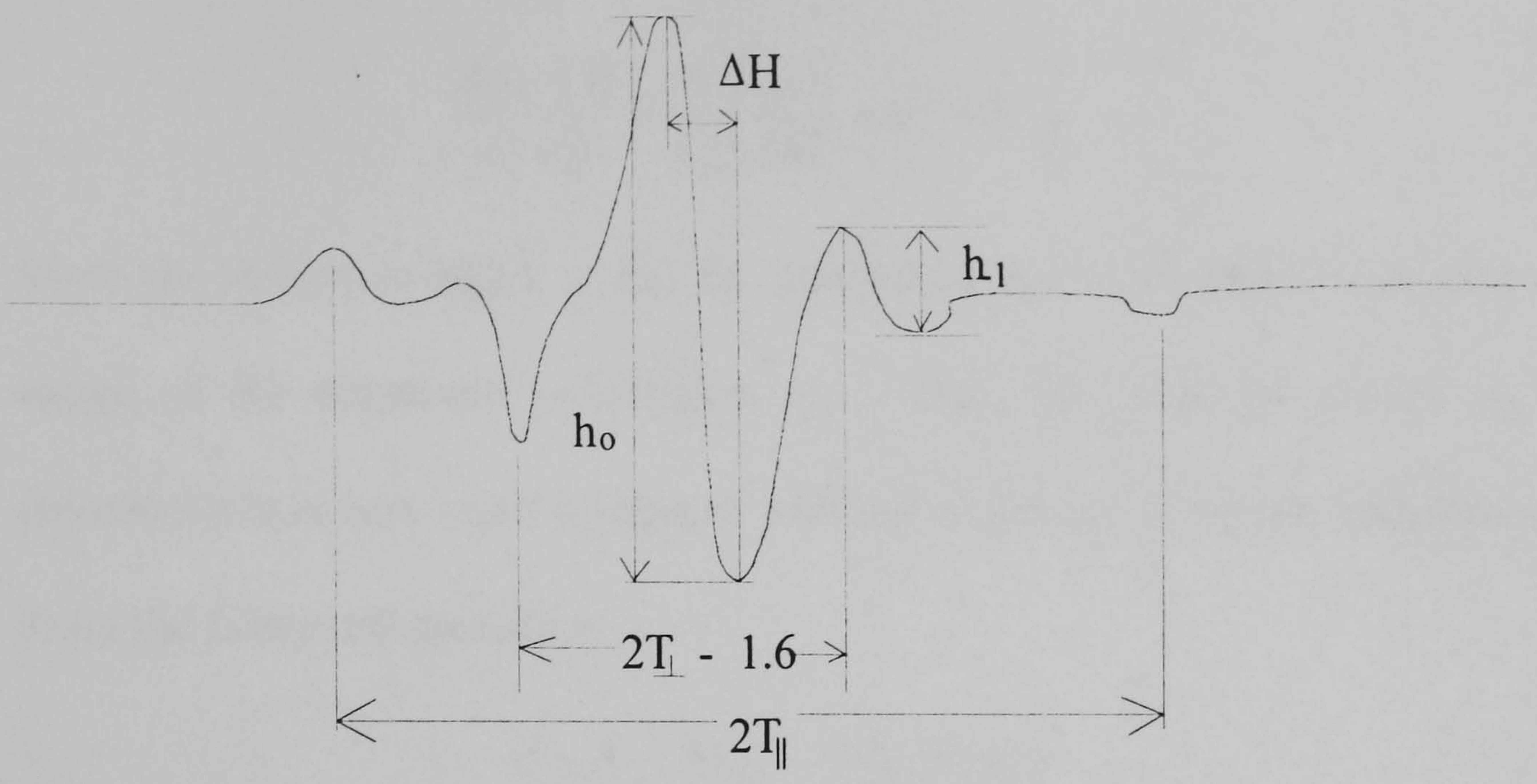

Figure 2.17 A typical ESR spectrum from a membrane of a human red blood cell. The outer and inner hyperfine splitting $2T_{\parallel}$ and $2T_{\perp}$ can be measured as shown. Respective heights of the central line (h_0) and the high-field peak of the inner hyperfine doublet (h_{-1}) are shown.

2.11 Membrane Thickness Determined by Lorentz Formulation

The membrane capacitance of vesicles and biological cells can be determined by using the dielectric shell model in conjugation with the dielectrophoresis or electrorotation technique. However the true value of the membrane thickness might not be certain. It is because both the thickness value and the relative permittivity of a bilayer membrane will be changed with different temperature. In this section, a possible solution has been presented to calculate the membrane thickness of the vesicles or biological cells. It is as follows:

From the Lorentz formulation [3] the static condition permittivity εs is given by:

$$\frac{3(\varepsilon_s - 1)}{\varepsilon_s + 2} = \frac{N}{\varepsilon_o}\left(\frac{\mu^2}{3kT} + \alpha_e + \alpha_a\right)$$

Since the refractive index n can be interpreted the as dielectric relaxation values of the electronic polarisation α_e. Also, the value of atomic α_a polarisation's is very small compared with the electronic dielectric relaxation. From the Lorentz formulation:

$$\frac{n^2 - 1}{n^2 + 2} = \frac{N\alpha_e}{3\varepsilon_o} \approx \frac{N(\alpha_e + \alpha_a)}{3\varepsilon_o}$$

$$\frac{3(n^2 - 1)}{(n^2 + 2)} = \frac{N}{\varepsilon_o}(\alpha_e + \alpha_a) \tag{2.73}$$

by comparing with the Lorentz formulation at high frequencies:

$$\frac{3(\varepsilon_\infty - 1)}{(\varepsilon_\infty + 2)} = \frac{N}{\varepsilon_o}(\alpha_e + \alpha_a) \tag{2.74}$$

Therefore equation 2.73 can substitute into equation 2.74 and expressed as:

$$\frac{3(\varepsilon_\infty - 1)}{(\varepsilon_\infty + 2)} = \frac{3(n^2 - 1)}{(n^2 + 2)}$$

$$n^2 = \varepsilon_\infty$$

The refractive index n of phospholipids bilayer membrane can be measured by the optical reflectivity technique and n is taken as 1.438 [31]:

$$\varepsilon_\infty = 2.0678$$

Combine with the Lorentz formulation and equation 2.74:

$$\frac{3(\varepsilon_s - 1)}{(\varepsilon_s + 2)} = \frac{N\mu^2}{3\varepsilon_o kT} + \frac{3N(\varepsilon_\infty - 1)}{(\varepsilon_\infty + 2)} \tag{2.75}$$

$$N\mu^2 = 9\varepsilon_o kT\left[\left(\frac{\varepsilon_s - 1}{\varepsilon_s + 2}\right) - \left(\frac{\varepsilon_\infty - 1}{\varepsilon_\infty + 2}\right)\right] \tag{2.76}$$

and the relative permittivity at static condition:

$$\varepsilon_s = \frac{9kT\varepsilon_o + 2\left[N\mu^2 + 9\varepsilon_0 kT\left(\frac{\varepsilon_o - 1}{\varepsilon_o + 1}\right)\right]}{9kT\varepsilon_o - \left[N\mu^2 - 9\varepsilon_0 kT\left(\frac{\varepsilon_o - 1}{\varepsilon_o + 1}\right)\right]} \tag{2.77}$$

From the parallel plate capacitor equation, the effective capacitance is given by:

$$C = \frac{\varepsilon_o \varepsilon_s}{d} \Rightarrow \varepsilon_s = \frac{Cd}{\varepsilon_o} \tag{2.78}$$

From (2.77) and (2.78) the membrane thickness d is given by:

$$d = \frac{\varepsilon_o}{C}\left\{\frac{9kT\varepsilon_o + 2\left[N\mu^2 + 9\varepsilon_o kT\left(\frac{\varepsilon_o - 1}{\varepsilon_o + 1}\right)\right]}{9kT\varepsilon_o - \left[N\mu^2 - 9\varepsilon_o kT\left(\frac{\varepsilon_o - 1}{\varepsilon_o + 1}\right)\right]}\right\} \tag{2.79}$$

At any specific reference temperature T_{sp}, from (2.76) and (2.78):

$$N\mu_{sp}^2 = 9\varepsilon_o kT_{sp}\left[\left(\frac{{C_{sp}d}/{\varepsilon_o} - 1}{{C_{sp}d}/{\varepsilon_o} + 2}\right) - \left(\frac{\varepsilon_\infty - 1}{\varepsilon_\infty + 2}\right)\right] \tag{2.80}$$

The polarisation factor of the membrane at any specific temperature T_{sp} can be calculated. From(2.80) and (2.77):

$$\varepsilon_s = \frac{T + 2\left[T_{sp}\left(\frac{C_{sp}d/\varepsilon_o - 1}{C_{sp}d/\varepsilon_o + 2}\right) + \left(T - T_{sp}\right)\left(\frac{\varepsilon_\infty - 1}{\varepsilon_\infty + 2}\right)\right]}{T - \left[T_{sp}\left(\frac{C_{sp}d/\varepsilon_o - 1}{C_{sp}d/\varepsilon_o + 2}\right) + \left(T - T_{sp}\right)\left(\frac{\varepsilon_\infty - 1}{\varepsilon_\infty + 2}\right)\right]} \tag{2.81}$$

Therefore the relative permittivity of the bilayer membrane of a vesicle at different temperatures can be calculated using parameters of the membrane at $21°C$. From (2.74) and (2.78):

$$d = \frac{\varepsilon_o}{C}\left\{\frac{T + 2\left[T_{sp}\left(\frac{C_{sp}d/\varepsilon_o - 1}{C_{sp}d/\varepsilon_o + 2}\right) + \left(T - T_{sp}\right)\left(\frac{\varepsilon_\infty - 1}{\varepsilon_\infty + 2}\right)\right]}{T - \left[T_{sp}\left(\frac{C_{sp}d/\varepsilon_o - 1}{C_{sp}d/\varepsilon_o + 2}\right) + \left(T - T_{sp}\right)\left(\frac{\varepsilon_\infty - 1}{\varepsilon_\infty + 2}\right)\right]}\right\} \tag{2.82}$$

We obtain the expression for the membrane thickness d. The calculation for the membrane thickness of vesicles is presented in the appendix for this chapter.

2.11 Structure of DNA molecules

The electrorotation technique is not only performed on cell sized vesicles in this investigation, it is also used in the identification of DNA oligonucleotides of different nitrogenous bases sequences. Therefore it is essential to have a basic knowledge of the chemical structure and the electrical properties of DNA oligonucleotides.

Each nucleotide of the DNA oligonucleotide consists of three components: a carbohydrate molecules, a phosphate group and a nitrogenous base [32] (Figure 2.18). The carbohydrate is a deoxyribose compound. The phosphate group is an organic ion formed by the loss of hydrogen ions from phosphoric acid. The nitrogenous bases are any of four nitrogen-containing compounds that have excessive numbers of amino groups and therefore act as bases. In DNA, these bases are adenine, guanine, cytosine and thymine. The deoxyribose compounds are joined by covalent bonds with the phosphate group to form the backbone of the nucleotides. Then the backbone of the nucleotide bond covalently with the nitrogenous bases to form the single stranded oligonucleotide.

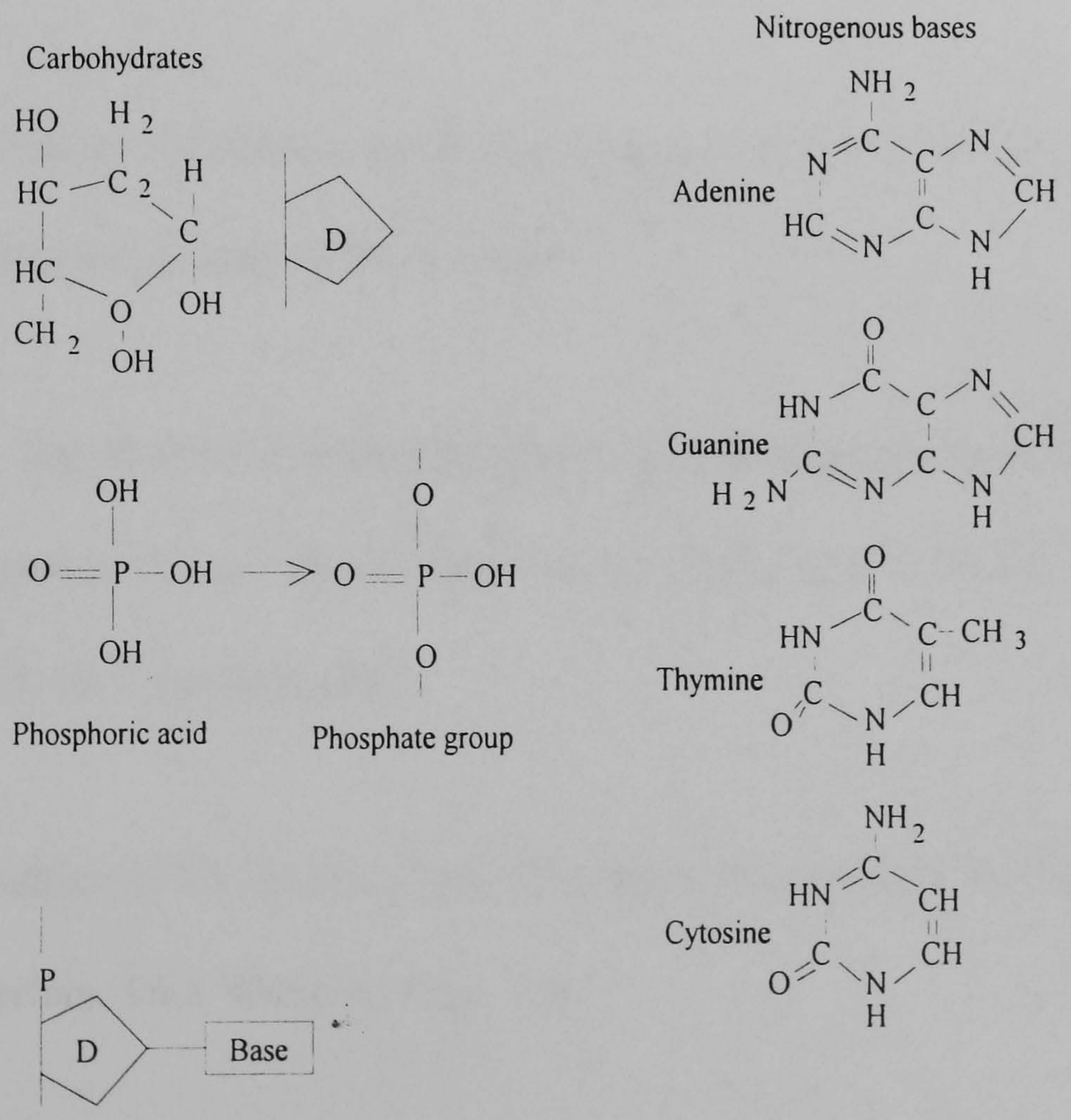

Figure 2.18 The carbohydrate in nucleotide is deoxyribose. They are the basic building blocks of the deoxyribonucleic acid (DNA).

The backbone structure of the oligonucleotide is quite conductive because it contains phosphate ionic group compounds that is capable of attracting ions from the surrounding medium. The nitrogenous bases are separated into two main groups. The first group contains adenine and thymine, these bases have two hydrogen bonding sites which are available to interact with ions from the medium. The second base groups are guanine and cytosine, this group of bases contains three hydrogen bonding sites. Therefore the second base group should be more conductive than the first base group.

2.13 Reference

1. J Allison (1971) Electronic engineering materials and devices, McGraw-Hill Book Company (UK) Limited

2. C. P. Smyth (1955) Dielectric behaviour and structure: *Dielectric Constant and Loss, Dipole Moment and Molecular Structure,* McGraw-Hill Book Company, INC.

3. R. Pethig (1979) Dielectric and Electronic Properties of Biological Materials, John Wiley & Sons, Ltd.

4. H. Fröhlich (1958) Theory of Dielectrics: *Dielectric constant and Dielectric Loss,* Oxford University Press

5. P. Debye (1929) Polar molecules, Chemical Book Company, New York

6. J. C. Maxwell (1892) A Treatise on Electricity and Magnetism, 3rd ed., Vol 1, Clarendon Press, Oxford

7. K. W. Wagner (1914) Erklarung der dielectrischen Nachwirkungsvorgange auf grund Maxwellsher Forstellungen, *Archiv. Electrotechnik.,* **2** 371-389.

8. K. W. Wagner (1924) Die Isolierstoffe der Electrotechnik, ed. Schering, Springer, Berlin. (as cited by H. A. Pohl, 1978)

9. H. A. Pohl (1978) Dielectrophoresis: The behaviour of neutral matter in nonuniform electric fields, Cambridge University Press (Cambridge)

10. T. B. Jones (1995) Electromechanics of particles, Cambridge University Press

11. A. R. von Hippel (1995) Dielectrics and waves: Artech House Microwaves Library, Originally published: New York, Wiley, c1954

12. X-B. Wang, Y. Huang, R. Hölzel, J. P. H. Burt and R. Pethig (1993) Theoretical and experimental investigations of the interdependence of the dielectric, dielectrophoretic and electrorotational behaviour of colloidal particles, *J. Phys. D: Appl. Phys.*, **26** 312-322

13. R. Pethig, Y. Huang, X-B. Wang and J. P. H. Burt (1991) Positive and negative dielectrophoretic collection of colloidal particles using interdigitated castellated microelectrodes, *J. Phys. D: Appl. Phys.*, **24** 881-888

14. P. R. C. Gascoyne, Y. Huang, R. Pethig, J. Vykoukal and F. F. Becker (1992) Dielectrophoretic separation of mammalian cells studied by computerized image analysis, *Meas. Sci. Technol.*, **3** 439-445

15. P. R. C. Gascoyne, J. Noshari and F. F. Becker (1994) Use of dielectrophoretic collection spectra for characterizing differences between normal and cancerous cells, *IEEE Transactions on Industry Applications,* **30,** 4, 829-834

16. Y. Huang, R. Hölzel, R. Pethig and X-B. Wang (1992) Differences in the AC electrodynamics of viable and non-viable yeast cells determined through combined dielectrophoresis and electrorotation studies, *Phys. Med. Biol.* **37,** Vol 7, 1499-1517

17. G. Fuhr (1985) Über die Rotation dielektrischer Körper in rotierenden Feldern, PhD Dissertation, Humboldt-Universität, Berlin

18. F. A. Sauer and R. W. Schlögl (1985) Torque exerted on cylinders and spheres by external electromagnetic field: A contribution to theory of field induced cell rotation interactions between electromagnetic fields and cells (A Chiabrera ed.) New York: Plenum, Pp 203-251

19. W. M. Arnold and U. Zimmermann (1988) Electro-rotation: development of a technique for dielectric measurements on individual cell and particles, *J. Electrostat.*, **21** 151-191

20. T. Kakutani, S. Shibatani and M. Sugai (1993) Electrorotation of non-spherical cells: theory for ellipsoidal cells with an arbitrary number of shells. *Bioelectrochem. Bioenerg.*, **31** 131-145

21. R. Höber (1913) Messungen der inneren Leitfähigkeit von Zellen, *Pfl. Physiol. Archiv. Mensch. Tiere.*, **150** 15-45

22. H. Fricke (1924) A mathematical treatment of the electric conductivity and capacity of disperse system, *Phys. Rev.*, **24** 575-587

23. T. Hanai (1960) Theory of the dielectric dispersion due to the interfacial polarisation and its application to emulsion, *Kolloid Z.*, **171** 23-31

24. A. Irimajiri, T. Hanai and A. Inouye (1979) A dielectric theory of "multi-stratified shell" model with its application to a lymphoma cell, *J. Theor. Biol.,* **78** 251-269

25. R. R. C. New (1990) Liposomes: a practical approach, IRL Press, Oxford University Press, Oxford

26. B. A. Lewis and D. M. Engelman (1983) Lipid bilayer thickness linearly with Acyl chain length in fluid phosphatidylcholine vesicles, *J. Mol. Biol.,* **166** 211-217

27. E. H. Grant, R. J. Sheppard and G. P. South (1978) Dielectric behaviour of Biological Molecules in solution, Clarendon Press, Oxford

28. H. P. Schwan (1957) Electrical properties of tissue and cell suspensions, *Adv. Biol. Med. Phy.,* **5** 147-209

29. L. M. Gordon and C. C. Curtain (1988) *Methods for Studying Membrane Fluidity:* Electron Spin Resonance Analysis of Model and Biological Membranes, Pp 25-88, Alan R. Liss, Inc

30. J. Seelig (1970) Spin label studies of oriented smectic liquid crystals (a model system for bilayer membranes), *J. Am. Chem. Soc.,* **92** 3881-3887

31. R. E. Pagano, R. J. Cherry and D. Chapman (1973) Phase Transitions and Heterogeneity in Lipids Bilayers, *Science,* **181** 557-559

32. I. E. Alcamo (1994) Fundamentals of microbiology (Fourth edition), The Benjamin/Cummings Publishing Company, Inc.

33. G. E. Crawford and J. C. Earnshaw (1989) Phase transitions in monoglyceride bilayers: A Light Scattering Study, *Biophysical Journal* **49** 869-889

34. Robert C. Weast and Melvin J. Astle (1982) *Handbook of Chemistry and Physics 62nd Edition 1981-1982* CRC Press

35. Benz R., Frohlich O., Lauger P. and Montal M. (1975) Electrical capacity of black films and of lipid bilayers made frim monolayers, *Biochim. Biophys. Acta* **394** 323-334

2.12 Appendix A

Caculation for vesicle membrane thickness in chapter 4:

The effective membrane capacitance C_m of 1, 2 Dioleoyl phosphatidyl choline can be represented as the capacitance of the hydrocarbon region C_{hc} in series with the capacitance of phosphate head group C_{phg}:

$$\frac{1}{C_m} = \frac{1}{C_{phg}} + \frac{1}{C_{hc}} \qquad \text{A(1)}$$

From reference [33]:

phosphate peak spacing (total membrane thickness)(d_m) = $3.8 \pm 0.1 nm$

Thickness of hydrocarbon region (d_{hc}) = $2.7 \pm 0.1 nm$

From reference [34]:

relative permittivity of hydrocarbon region at $23° C$ = 2.25

From equation 2.81, relative permittivity of hydrocarbon region at (ε_{hc}) = 2.25

From reference [35]:

membrane capacitance [di-(18:1)-lecithin] (C_m) = $7.21 mFm^{-2}$

relative permittivity of membrane (ε_m):

$$\varepsilon_m = \frac{C_m d_m}{\varepsilon_o} = 3.09 \qquad \text{A(2)}$$

From A(1), relative permittivity of phosphate head group ε_{phg}:

$$\varepsilon_{phg} = \frac{d_{phg}}{\left(\frac{d_m}{\varepsilon_m} - \frac{d_{hc}}{\varepsilon_{hc}}\right)} = 38.26 \qquad \text{A(3)}$$

From A(1), the thickness of hydrocarbon region can be calculated, assuming that the thickness of the phosphate head group is constant at $1.1nm$ as the temperature of experimental condition varies.

$$\frac{1}{C_m} = \frac{1}{C_{phg}} + \frac{1}{C_{hc}} \Rightarrow \frac{nd_{phg}}{\varepsilon_o \varepsilon_{phg}} + \frac{nd_{hc}}{\varepsilon_o \varepsilon_{hc}} \qquad \text{A(4)}$$

where n is the number of bilayers present in the vesicle membrane. The values of ε_{phg} and ε_{hc} can be calculated from equation 2.81 for different tempertures. The value of membrane capacitance C_m are from the ROT and DEP experiments which are related to the same temperature of ε_{phg} and ε_{hc}.

The thickness of hydrocarbon region d_{hc}:

$$d_{hc} = \frac{\varepsilon_o \varepsilon_{hc}}{nC_m} - \frac{d_{phg}\varepsilon_{hc}}{\varepsilon_{phg}} \qquad \text{C(5)}$$

Therefore the total membrane thickness d_m of vesicle at different temperature can be known:

$$d_m = n(d_{hc} + d_{phg}) \qquad \text{C(6)}$$

The relative permittivity of the phosphate head group is the dominant factor contributing to the capacitance value of the phosphate head group. Therefore, the thickness of the phosphate head group is presumed to be unchanged throughout the range of temperature in this analysis .

Chapter 3

Computer-aided analysis on Multishell Model of Spherical Bioparticles and Ellipsoidal Particles

3.1 Introduction

Conventional methods for interpreting dielectric properties of any biological cells use existing dielectric shell models [1, 2, 3] with guessed variables to fit the electrorotation (ROT) experimental data. However, the interpreted dielectric variables may not be accurate using this method, since more than one combined solution might be able to fit the ROT experimental data.

In this investigation, computing programs (see appendix 3.1-3.2) were written to interpret the dielectric variables of bioparticles that were examined by ROT experiments. These computing programs used the Nelder and Mead simplex method for function minimisation [4, 5], which was an aid for the dielectric shell models [1, 2, 3] to find the correct values of dielectric variables from any tested bioparticle sample. Computer programs were also written to test the accuracy limitation provided by this Nelder-Mead minimisation routine (see appendix's 3.3-3.4). Various tests were carried out with different conditions. The effect of superimposed noise on the ROT data was first examined. Then, the different characteristic of variables were examined to determine their true values. Also, ROT data was examined using the dielectric shell models with and without the inclusion of dielectrophoresis "cross-over" frequency data [6]. Lastly, the number of shells incorporated into the model were varied. From the results of all these analyses, the accuracy of determining the true values of the dielectric variables by these analytic programs was determined for the different conditions. In turn, these results were used to establish the best method of analysing the ROT data using the computer-aided program, and to ensure that the analysed dielectric variables from the ROT data were as close as possible to the true values of the dielectric properties of the tested bioparticle.

3.2 Experimental methods, Instrumentation and Algorithm

In all the computing analysis, the analytic computing programs used to analyse the experimental ROT data were written in the MATLAB computing language [The Math Works, Inc] [7]. All the experimental ROT data were stored in the TEXT format as spread sheet programs. Each different set of experimental ROT data was stored into different set of data, so each set of ROT results could be identified with its own predicted dielectric variables and be analysed separately.

3.2.1 *Data programs for the spherical dielectric multi-shell model*

In each set of the ROT data program, it contained a standard matrix format to store the experimental ROT data and the DEP crossing over frequency data, and a set of predicted dielectric variables (Table 3.1). The predicted dielectric variables were used in the ROT analysis to generate a best theoretical fit. This set of the predicted dielectric variables included the permittivity and conductivity values of each shell layer of the model, such as the permittivity and conductivity values of a cell's cytoplasm and the cell's membrane.

Table 3.1 A ROT data file that is stored in the matrix format that is shown as below for ROT analysis. This ROT data file is used to represent the spherical dielectric multi-shell model.

nr: (no. of radii)	Temperature	DEP Crossover frequency
r2: innermost membrane shell radius	d2: innermost membrane thickness	Applied voltage: Vrms
r4	d4	Scaling factor: EL
..	..	0
r(nr): outermost membrane shell radius	d(nr): outermost membrane thickness	0
maxlimit	minlimit	0
e1: innermost shell permittivity	s1: innermost shell conductivity	(0,1,2,3)
e2	s2	(0,1,2,3)
..	..	..
e(nr)	s(nr)	(0,1,2,3)
f1	s1	rot1
f2	s2	rot2
..	..	..
fn	sn	rotn

The first row of the data sheet (Table 3.1) contains the physical dimension of the model and the environmental condition of the experiment. The first row of the first column of the matrix determines what kind of shell model would be used in the analysis. If the number was 2, then the single shell model was used, i.e.,

(Number of radii (nr) = Number of shells in the model + 1).

If the number was 4, it would be a three shell model, etc. The matrix in the second column of the first row gives the value of the experimental temperature (°C). The third column gives the measured DEP "cross-over" frequency point of the sample.

In the second row of the matrix is described the physical dimensions of the measured sample. The first column gives the radius of the innermost membrane (r2); the second column gives the membrane thickness of the innermost membrane (d2). The third column is the root mean square value of the applied voltage (E). If this data sheet represented a complex system such as, for example, a three shell model, then the third row of the matrix would contain the values for the radius and the thickness of the outermost membrane of the sample. The third column of the third row in this matrix contained the value of the scaling factor that was used in the calculation for theoretical fitting to the experimental data. After the physical dimensions of the sample were described, the next row of matrix gives the maximum (maxlimit) and minimum (minlimit) boundaries of the medium permittivity. The medium that was inside the shell model would be self-iterated when the Nelder-Mead simplex algorithm was employed in the calculation. The number of this row was described as: (number of shell + 2). However, the variables "maxlimit" and "minlimit" were no longer required to be used in the calculation.

The next section of the matrix shows the predicted dielectric variables for the shell model. The first column of the first row in this section described the innermost permittivity of the sample. The second row showed the innermost conductivity. The number of this row was described as: (number of shell + 3). The first column of next row, (number of shell + 4)th row, would show the membrane permittivity and the second column the membrane conductivity. If it was a three shell model, the permittivity and conductivity of the outer shell would be described further into the next row of the matrix. The third row of these columns of this section determined the dielectric variables that were obtained with or without self-iteration using the Nelder-Mead simplex algorithm. If the value of this column was zero, both the permittivity and the conductivity of this shell would not be subjected to the self-iteration process. If the value was one, only the permittivity of this shell would be passed through the self-iteration process. If the value was two, the self-iteration process would only be applied to the conductivity value of this shell. If the value was three, both the permittivity and the conductivity values of this shell would be subjected to the self-iteration using the Nelder-Mead simplex algorithm.

The remaining part of the spread sheet contained the experimental ROT data as a function of frequency. The frequency values were recorded in the first column, and the measured ROT data was recorded in the third column of this part of the matrix. Lastly, the experimentally measured medium conductivity was recorded in the second column.

3.2.2 *Computer program for the spherical dielectric multi-shell model*

This program contained mainly the spherical dielectric multi-shell model [1] (equation 3.1) and the Nelder-Mead simplex minimisation algorithm [4, 5]. The flow chart diagram of this program is shown at figure 3.1.

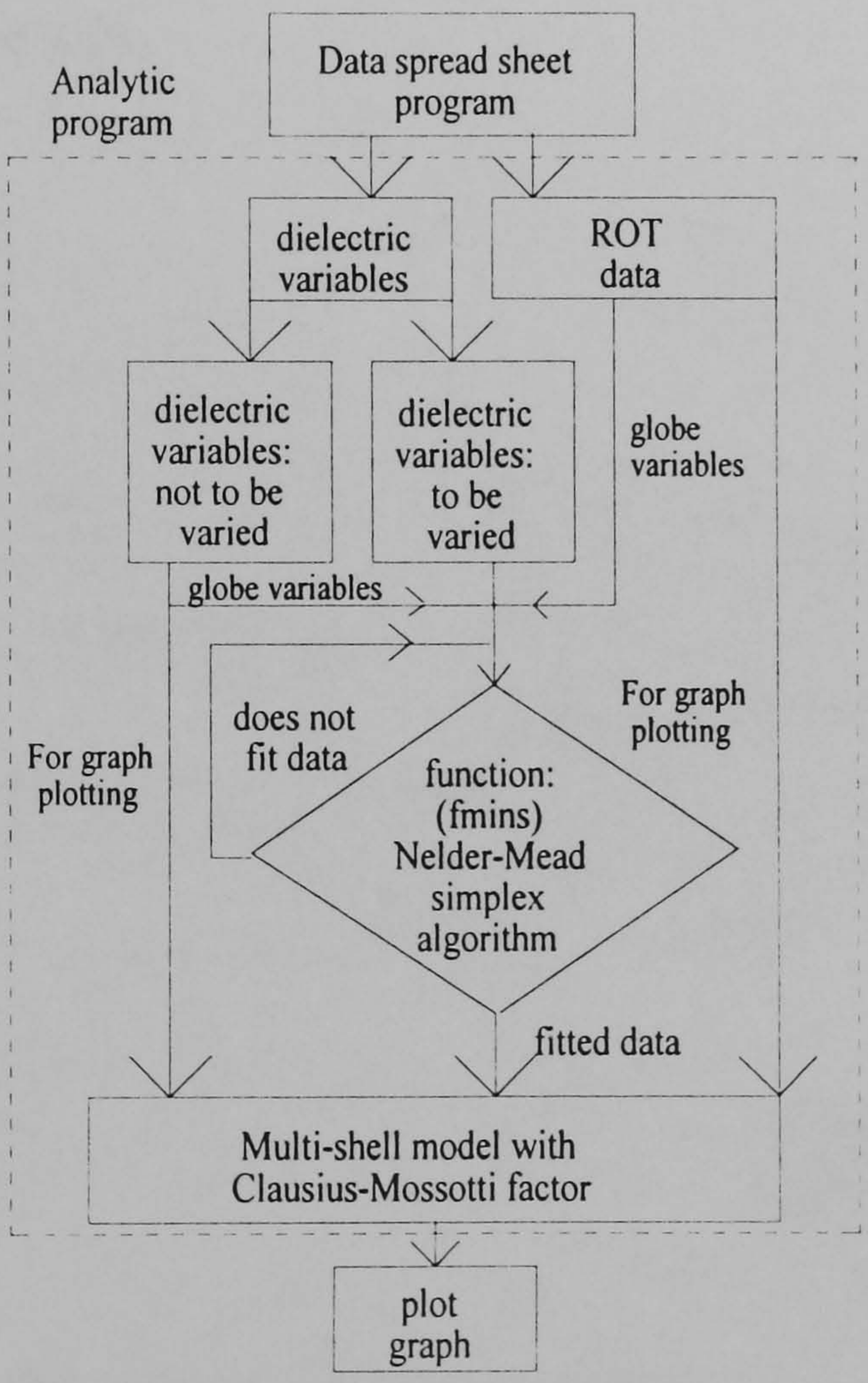

Figure 3.1 Flow chart diagram for the spherical dielectric multi-shell analytic program

All the initial predicted dielectric variables for the shell model were inserted into the analytic spherical shell model with the experimental ROT data as a spread sheet data program (Table 3.1). Once the data program was loaded into the analytic program, the dielectric variables that were passed into the Nelder-Mead simplex algorithm were separated into two groups of variables by using the "if" statement. One group of these variables behaved as a constant value during the analysis. This group of variables were kept as GLOBE VARIABLES [7]. The value of the second group was altered to fit the experimental data when they were corrected by the Nelder-Mead simplex algorithm. The separation method was briefly described in the previous section 3.2.1 (Figure 3.2).

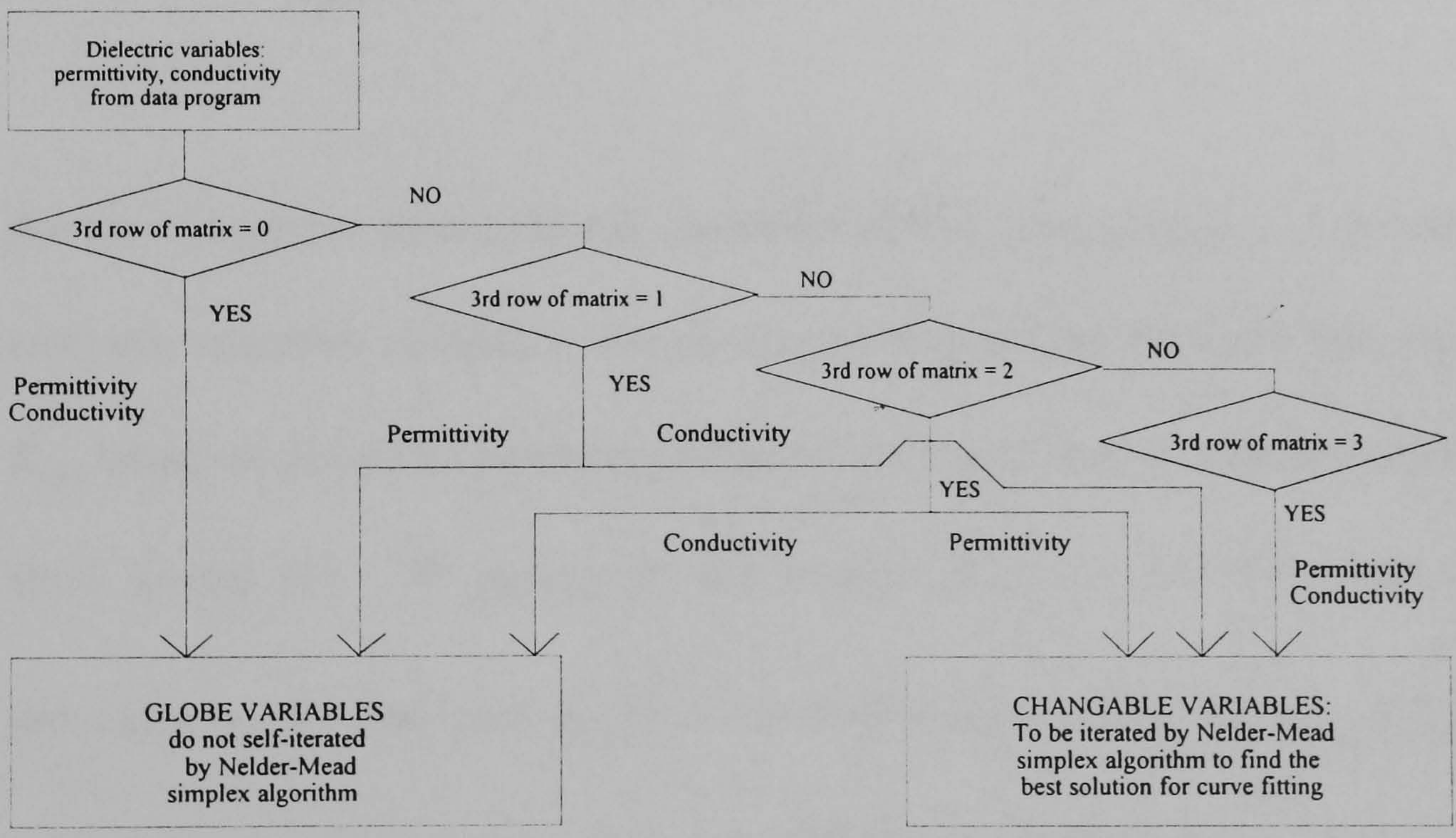

Figure 3.2 Using "If "statement to separate the permittivity and conductivity values of each shell into two groups of variable, GLOBE VARIABLES and CHANGEABLE VARIABLES. The globe variables [6] were used as constants during the calculation for the best curve fitting. The variables were self-iterated to give the best possible to fit to the experimental data by using the Nelder-Mead simplex algorithm.

In the MATLAB program language, the Nelder-Mead simplex algorithm is provided by the program's library as the FUNCTION of "FMINS" [7]. Both the globe variables [7] and the changeable variables were passed into this "FMINS" function. Then a theoretical curve was generated by these variables with the multi-shell model equation (equation 3.2 that will be discussed later) and the Clausius-Mossotti factor.

Once the theoretical curve was calculated, the curve could be compared with the experimental data by a minimisation procedure (equation 3.1) based on the Nelder-Mead simplex algorithm [4, 5].

$$Min\left\{\sum_i \left[R_{sim}(f_i) - R_{\exp}(f_i)\right]^2 + W * \mathrm{Re}^2\left(f_{CM_{fitted}}\left(f_c\right)\right)\right\} \tag{3.1}$$

for the i frequency points f in the experimental ROT spectrum R_{exp}. A general purpose, recursive algorithm was developed to generate the ROT spectrum R_{sim} based on dielectric parameter estimates for the spherical dielectric multi-shell model [1]. W represents the weight given in the minimisation procedure to the real part of the Clausius-Mossotti factor $\mathrm{Re}\left(f_{CM_{fitted}}\left(f_c\right)\right)$ (which has a value of zero when the DEP force vanishes at the crossover frequency f_c) calculated from the dielectric parameters used to simulate R_{sim}.

The general purpose, recursive algorithm was based on the spherical dielectric multi-shell model (equation 3.2).

$$\varepsilon^*_{peff} = \varepsilon^*_{Neff} = \varepsilon^*_{N+1}\left[\frac{\left(\frac{R_{N+1}}{R_N}\right)^3 + 2\left(\frac{\varepsilon^*_{N-1eff} - \varepsilon^*_{N+1}}{\varepsilon^*_{N-1eff} + 2\varepsilon^*_{N+1}}\right)}{\left(\frac{R_{N+1}}{R_N}\right)^3 - \left(\frac{\varepsilon^*_{N-1eff} - \varepsilon^*_{N+1}}{\varepsilon^*_{N-1eff} + 2\varepsilon^*_{N+1}}\right)}\right] \qquad (3.2)$$

where $\varepsilon^*_{\mathrm{p\ eff}}$ or $\varepsilon^*_{\mathrm{N\ eff}}$ is the effective complex permittivity of the N-shelled sphere model. R_N and R_{N+1} are the radius of Nth-shell and N+1th shell respectively. $\varepsilon^*_{\mathrm{N-1\ eff}}$ is the effective complex permittivity of the N-1th shell that starts from the innermost shell of the model. $\varepsilon^*_{\mathrm{N+1}}$ is the effective complex permittivity of the N+1th shell (see figure 3.1).

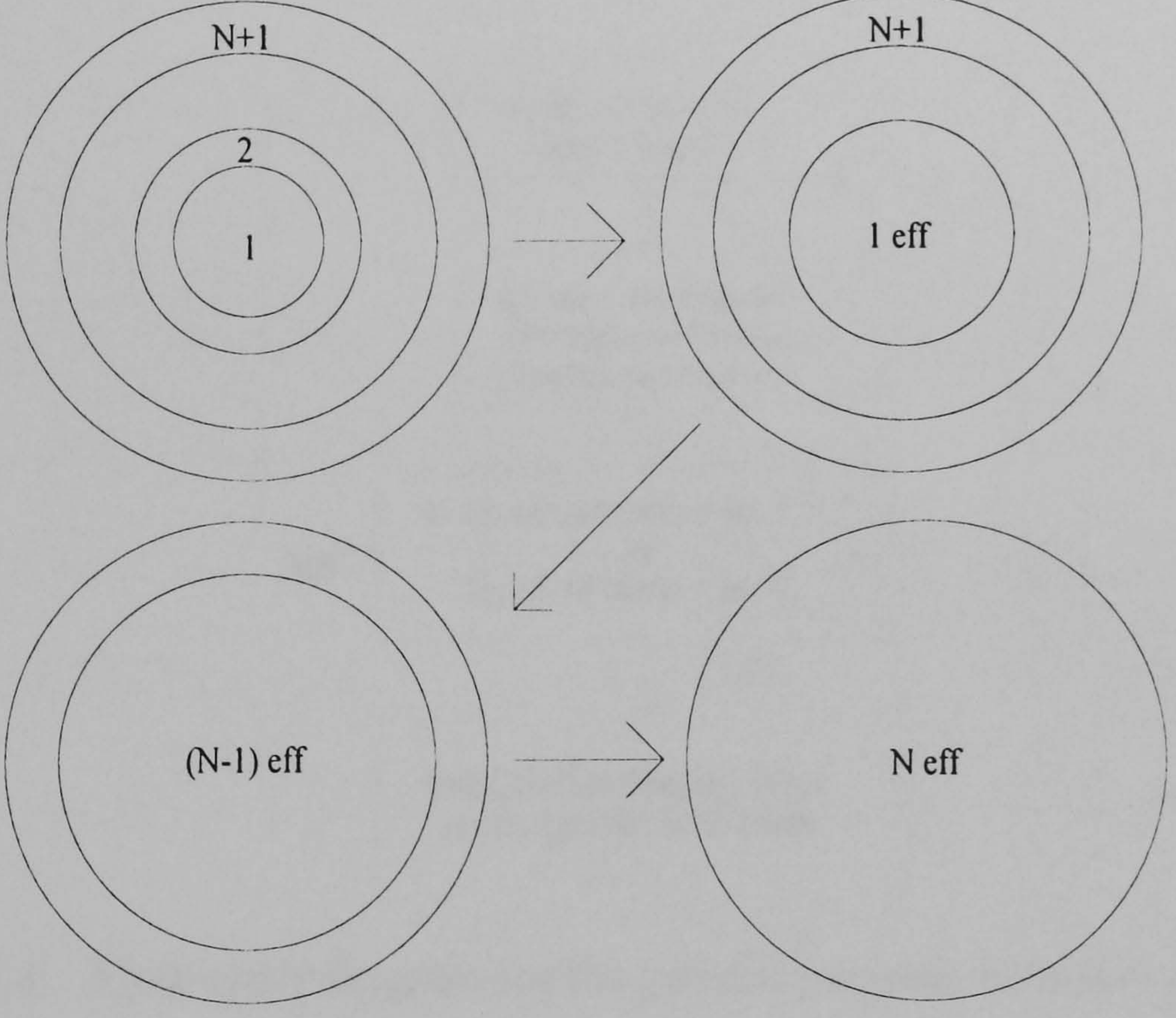

Figure 3.3 Smeared-out sphere approach for determining the effective permittivity of a N-shell sphere, showing the progressive simplification to a simple, homogeneous sphere having an effective complex permittivity (equation 3.2) that mimics the dielectric properties of the multi-shell model sphere.

The general recursive algorithm of this multi-shell model was created by the "for" loop routine (Figure 3.4). The amount of shell that was required by the model for data analysis had been described by the number nr (number of radii) from the data program. The effective complex permittivity of each shell could be calculated systematically from the innermost part to the outermost part of the shell model. Eventually, the effective complex permittivity of the whole model could be calculated. This general purpose, recursive algorithm of the spherical multi-shell model was used in the Nelder-Mead simplex algorithm and in the plotting of the theoretical curve. The analytical program is shown in appendix 3.1.

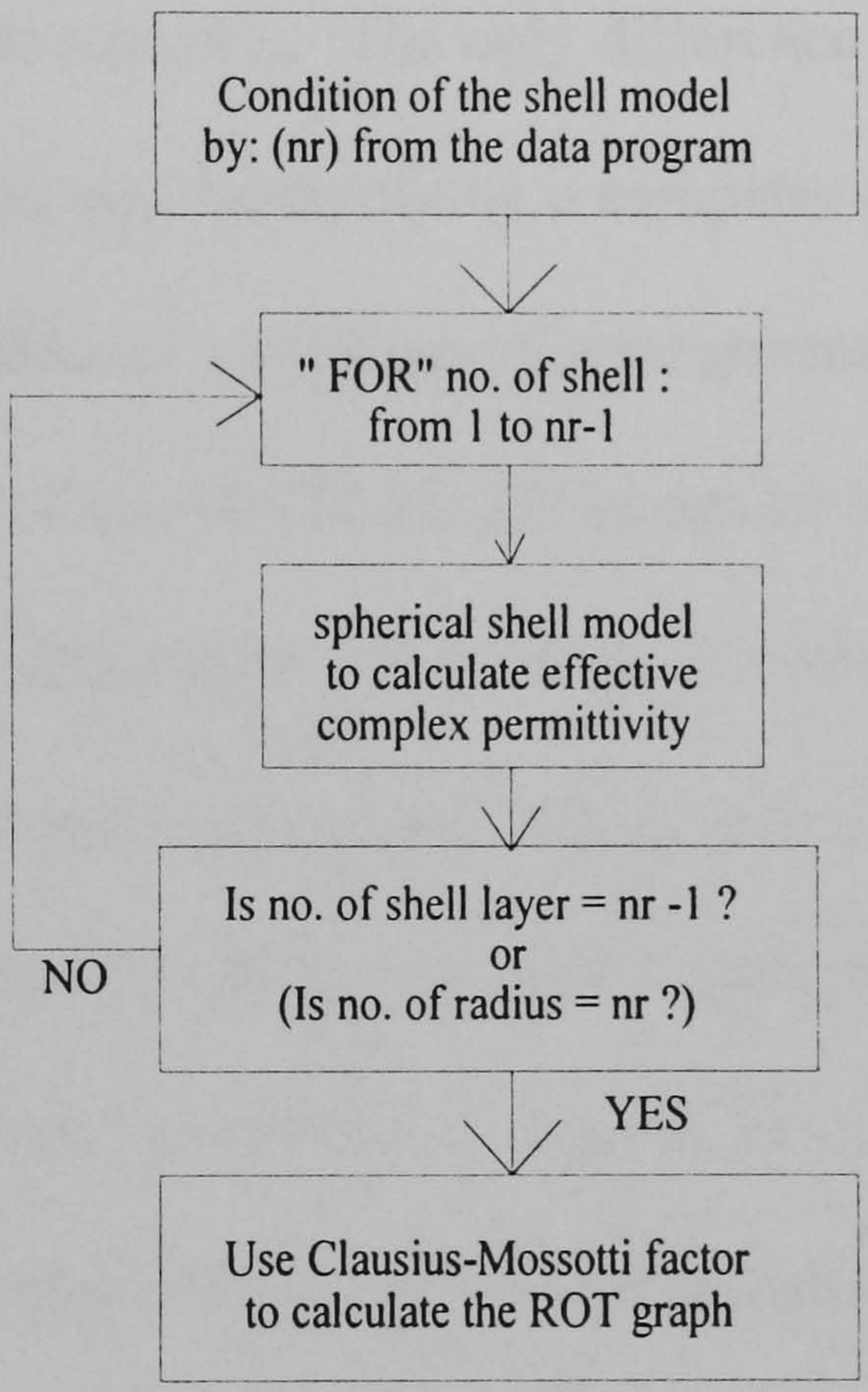

Figure 3.4 Flow-chart diagram for the general purpose, recursive algorithm

3.2.3 *The testing program for the Nelder-Mead simplex algorithm in the spherical dielectric multi-shell model*

The purpose of this testing program was to determine the reliability and the accuracy of the spherical multi-shell model to find the true values of dielectric variables by the Nelder-Mead simplex algorithm. In this program, the analytical part that included the spherical multi-shell model and the Nelder-Mead simplex algorithm was completely identical to the computer program of the previous section. The only difference was that input data of this program was generated randomly by a computer (Appendix 3.3). First, all the dielectric variables of a shell model were generated randomly by using a function "random" of the MATLAB [7] computer language. Second, the simulated ROT data (Appendix 3.3a) and a simulated DEP crossing over frequency point (Appendix 3.3b) would be generated by the spherical shell model with this group of random variables. Third, this group of generated variables would be stored as a data file. Fourth, the simulated ROT data and the DEP data would pass into the analytic program (already described in the previous section) with a group of prefixed dielectric variables to be analysed. After the analysis, the resultant dielectric variables would be stored in the same file that had stored the generated variables. Thus, the resultant variables could be compared with the original simulated variables to investigate differences between these two groups of data. If the difference was large, the Nelder-Mead simplex algorithm had failed to find the correct solution. If the difference was small or minimal, the Nelder-Mead simplex algorithm was successful in achieving the true values of the dielectric variables. Thus, the computer-aided analysis was an accurate method for data analysis. The flow-chart diagram of this program was shown in figure 3.5.

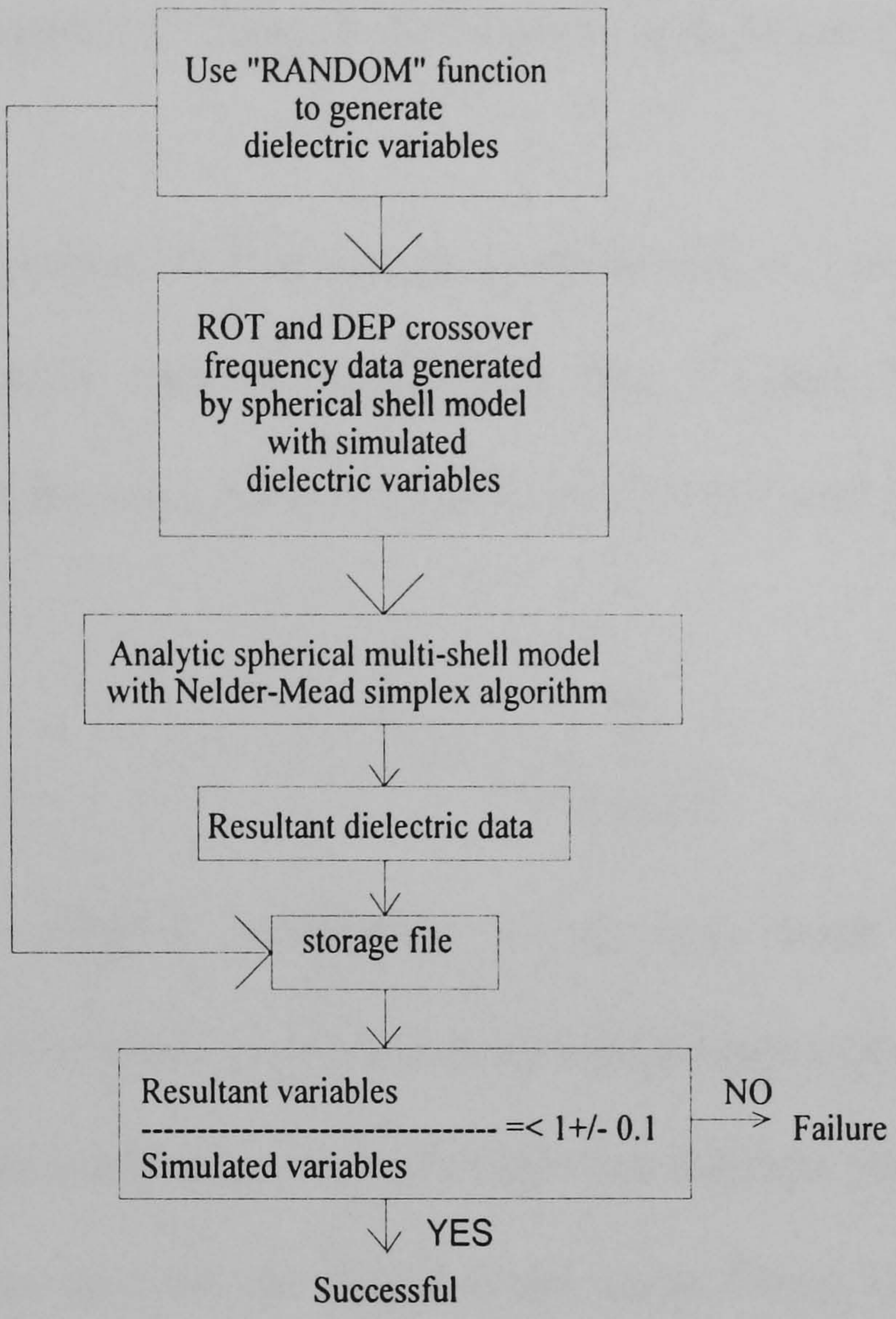

Figure 3.5 Flow-chart diagram for testing the accuracy of the Nelder-Mead simplex algorithm program (Spherical dielectric multi-shell model)

3.2.4 *Computer program for the ellipsoidal dielectric shell model*

This analytic program mainly consisted of the ellipsoidal multi-shell model [2] and the equation (equation 3.3) that described the effective surface conductivity of a latex particle [3] with the Nelder-Mead simplex algorithm [4, 5] as the analytic tool. The flow-chart diagram and the layout structure of this program were the same as the spherical shell model program that had used the Nelder-Mead simplex algorithm. The only difference of this program was the use of an ellipsoidal model [3, 4] with the effective surface conductivity equation [3] instead of the spherical shell model equation [1].

Since the ellipsoidal shell model program would be used to analyse the experimental ROT data of latex beads (see Chapter 5), equation 3.3 describing the effective conductivity of the latex beads was required.

$$\sigma_p = \sigma_b + \frac{2K_s}{r} + \frac{A}{1+(j\omega T)^{\alpha}} \tag{3.3}$$

where σ_p is effective conductivity of the latex bead, σ_b is the bulk conductivity of the bead. K_s is the surface conductance of the bead. A and T are the magnitude and mean characteristic time constant respectively, and α is a variable to describe the experimental curve fitting [3]. The effective conductivity of the latex bead σ_p is substituted into the conductivity value of the outermost shell of the ellipsoidal model (equation 3.4).

$$\varepsilon_1^* = \varepsilon_1 - j\frac{\sigma_p}{\omega} \tag{3.4}$$

where ε_1^* is the effective permittivity of the latex bead within the ellipsoidal model. The factor ε_1 is the permittivity of the latex bead and σ_p is the effective conductivity of the latex bead (equation 3.3). Because beads are homogeneous in structure, the ellipsoidal multishell model is not required to analyse in the experimental ROT data. Thus, equation 3.4 represents the effective permittivity of the latex beads in ROT data analysis.

The ellipsoidal multi-shell model consists of five sets of equations to analyse the ROT data of any ellipsoidal particle. First, there are the depolarising factors along the x and y axis of the particle (Figure 3.6). This depolarising factor was dependent on the shape of the sample. The latex beads were prolate spheroids ($a_0 > b_0 = c_0$) (Figure 3.6: c_0 is the radius along the z-axis). The depolarising factors of a prolate spheroid are given by equations 3.6 and 3.7 (for x-axis) and 3.8 (for z and y-axes).

$$q_i = {}^{a_i}\!/_{b_i} \quad \text{for } q_i > 1 \tag{3.6}$$

$$A_{ix} = \frac{\left[\dfrac{q_i}{\left(q_i^2 - 1\right)^{1/2}}\right] \ln\left[q_i + \left(q_i^2 - 1\right)^{1/2}\right] - 1}{\left(q_i^2 - 1\right)} \tag{3.7}$$

$$A_{iy} = \frac{\left(1 - A_{ix}\right)}{2} \tag{3.8}$$

where A_{ix} is the depolarising factor in the x-axis for each shell ($i = 0, 1, \ldots, n-1$). A_{iy} is the depolarising factor in the y-axis for each i shell layer. The a_i is the radius of the *ith* shell in the x-axis direction; b_i is the radius of the *ith* shell in the y-axis direction.

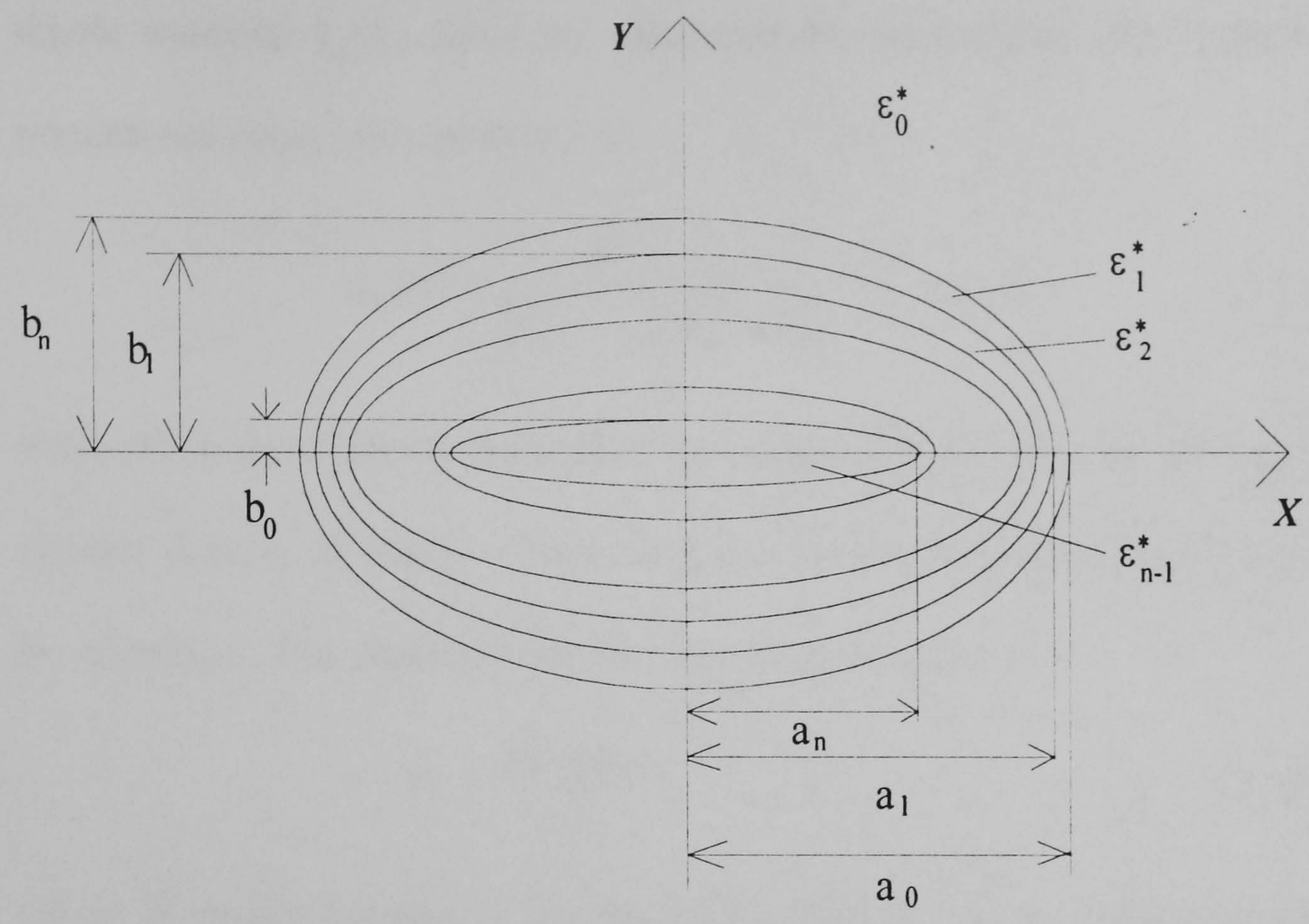

Figure 3.6 Cross-section of an ellipsoidal multishell model in the *x-y* plane

The ratio v_i between the outer shell and the immediate inner shell required for the ellipsoidal multishell model is given by

$$v_i = \frac{a_i b_i c_i}{a_{i-1} b_{i-1} c_{i-1}} \qquad i = 1, 2, \ldots\ldots, n\text{-}1 \tag{3.9}$$

where a_i, b_i and c_i are the radii of the ith shell in the x, y and z-axis directions.

Also

$$\bar{\varepsilon}^{*}_{i-1,\alpha} = \varepsilon^{*}_{i-1} \frac{\varepsilon^{*}_{i-1} + \left(\varepsilon^{*}_{i} - \varepsilon^{*}_{i-1}\right)\left[A_{i-1,\alpha} + v_{i-1}\left(1 - A_{i-2,\alpha}\right)\right]}{\varepsilon^{*}_{i-1} + \left(\varepsilon^{*}_{i} - \varepsilon^{*}_{i-1}\right)\left(A_{i-1,\alpha} - v_{i-1} A_{i-2,\alpha}\right)} \tag{3.10}$$

where i = 2,...., n-2; and variables $A_{i-1,\alpha}$ and $A_{i-2,\alpha}$ are defined by equation 3.7 and 3.8.

having obtained the effective permittivity $\overline{\varepsilon^{*}_{i-1,\alpha}}$ of particle, the induced dipole moment $\chi_{\alpha}(\omega)$ could be calculated by substituting this effective permittivity value into equation 3.11.

$$\chi_{\alpha}(\omega)=\frac{\overline{\varepsilon^{*}_{1\alpha}}-\varepsilon^{*}_{0}}{\left(\overline{\varepsilon^{*}_{1\alpha}}-\varepsilon^{*}_{0}\right)A_{0\alpha}+\varepsilon^{*}_{0}} \qquad \alpha=x,y \qquad (3.11)$$

After the induced dipole moment of the model was known, the stationary angular velocity of rotation about the z-axis for the ellipsoidal model could be calculated. The procedure for this calculation is as follows:

$$V_{c}=\frac{4\pi\cdot a_{0}b_{0}c_{0}}{3} \qquad (3.12)$$

where V_c is the volume of the multishell ellipsoid, a_0, b_0 and c_0 are the outermost shell radii of the model.

$$R_{f}=2V_{c}\eta\left[\frac{\left(a_{0}^{2}+b_{0}^{2}\right)}{\left(a_{0}^{2}A_{0x}+b_{0}^{2}A_{0y}\right)}\right] \qquad (3.13)$$

where η is the viscosity of the external medium; A_{0x} and A_{0y} are defined by equations 3.7 and 3.8.

$$\omega_{c}=0.5\varepsilon_{0}\left(\frac{V_{c}}{R_{f}}\right)\left\{\mathrm{Im}\left[\chi_{x}(\omega)+\chi_{y}(\omega)\right]\right\}E_{0}^{2} \qquad (3.14)$$

where ω_c is the stationary angular velocity of rotation about the z-axis. E_0 is the external applied electric field. $\chi_x(\omega)$ and $\chi_y(\omega)$ are the induced dipole moments of the ellipsoidal particle (equation 3.11). Once the stationary angular velocity of the tested latex bead sample had been calculated, the angular velocity results could be compared with the experimental ROT data using the Nelder-Mead simplex algorithm.

Therefore, these equations of the ellipsoidal model were applied into the analytic program of ellipsoidal model to perform the analysis. The flow chart applying these equations is shown below:

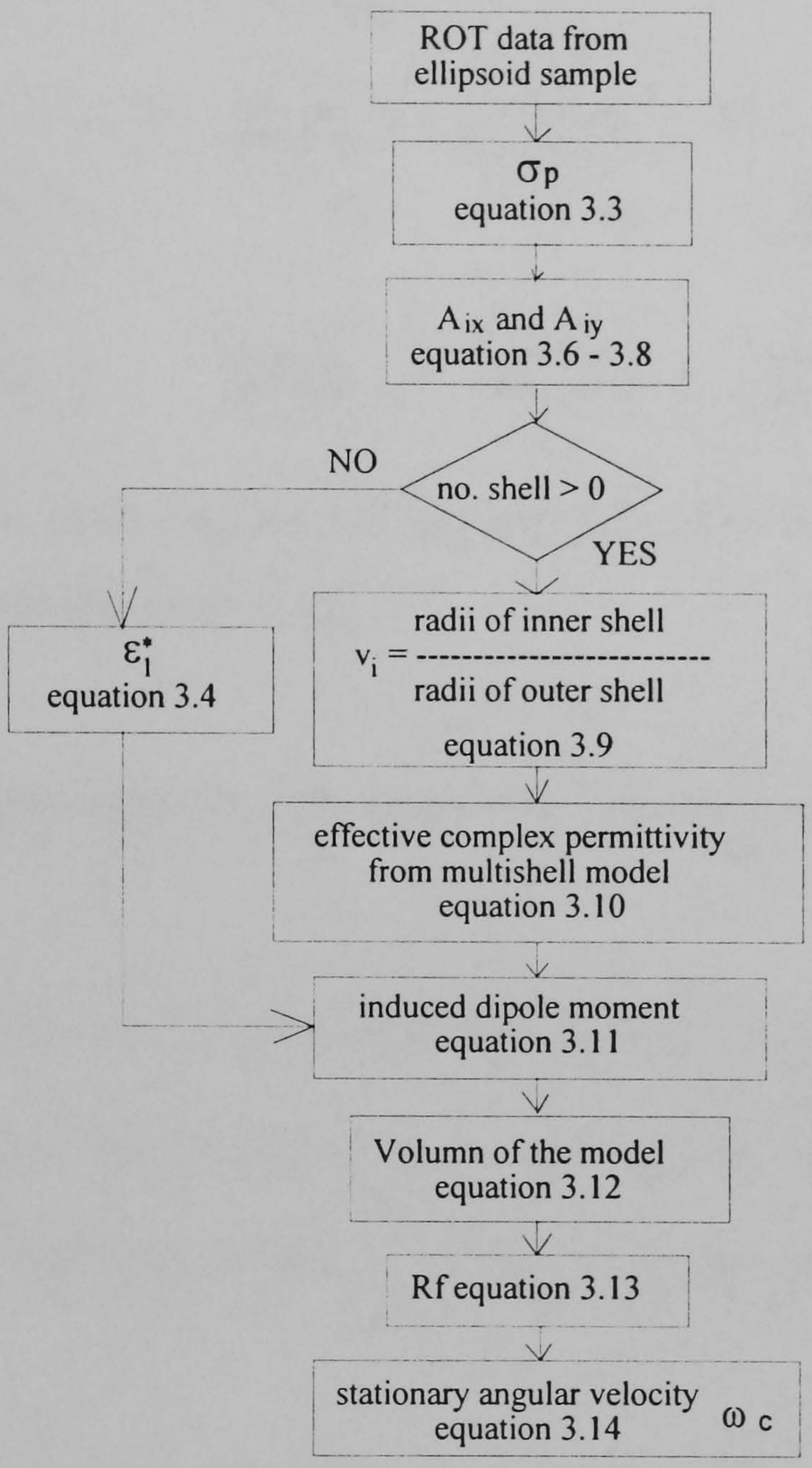

Figure 3.7 Flow chart diagram for ellipsoidal multi-shell in the computing analysis

This program could analyse ROT data with the DEP "cross-over" frequency data included, or ROT data alone, or dielectrophoresis data with or without the DEP crossing over frequency data. The particular routine for analysis could be chosen before the analysis was started, using the following procedure

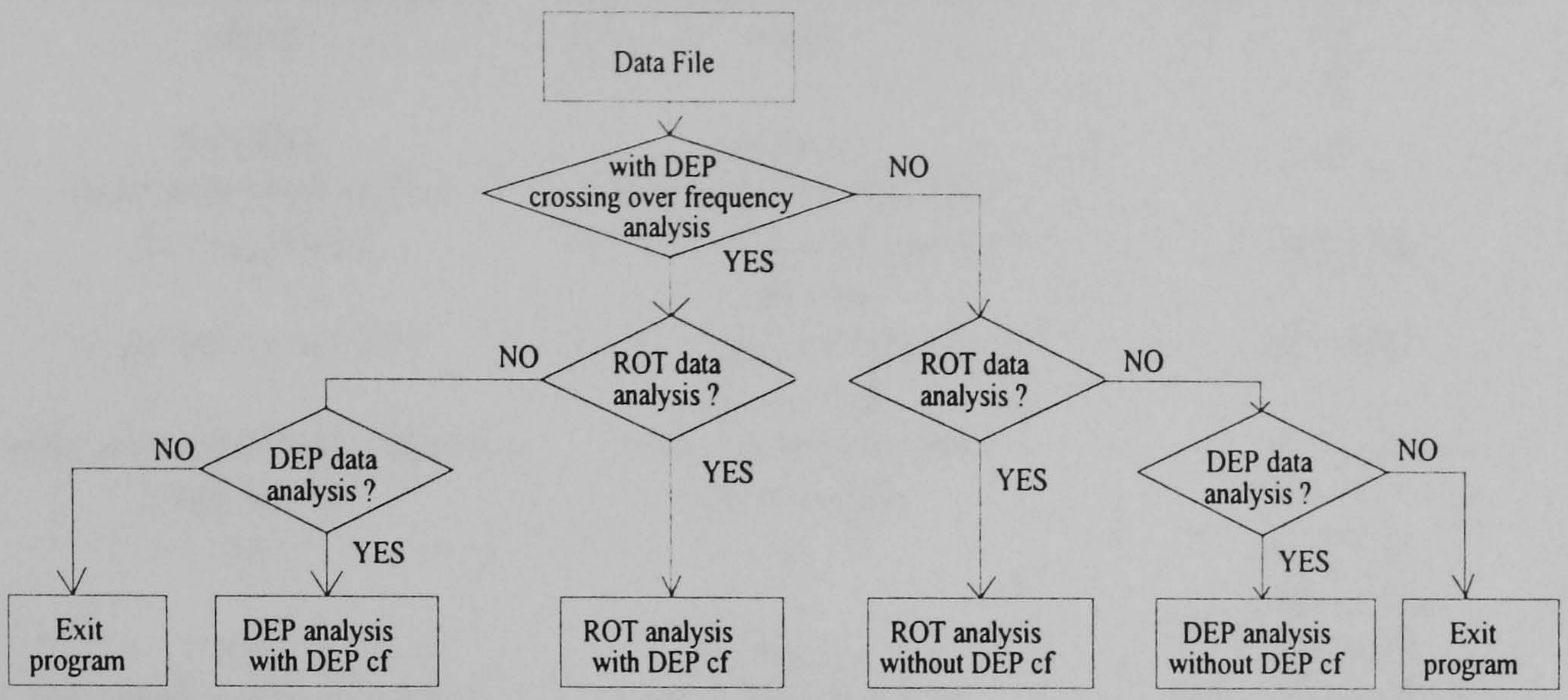

Figure 3.8 Flow chart diagram for the classification of data analysis in the ellipsoidal shell model.

3.2.5 *Data programs for the ellipsoidal dielectric shell model*

The matrix data file array for the ellipsoidal shell model program was very similar to the data file for the spherical multishell model program. The matrix arrays of this data file for the ellipsoidal model are shown in Table 3.2.

The variables A, T, α and the surface conductance Ks (see equation 3.3) were employed in the ellipsoidal particle data file, and used to calculate the effective conductivity value of the latex bead. Variables A and T were stored in row number {(ns+1)+2}, and α and Ks were stored in row [(ns + 1) + 3], where ns was the number of shells of the model.

Table 3.2 A data spread sheet for the analytical program of the ellipsoidal dielectric multi-shell model.

ns: (no. of shell)	Temperature	Crossover frequency
r0(x): outermost shell radius	r0(y): outermost shell radius	E: peak to peak voltage
r1(x)	r1(y)	0
..	..	0
r(ns)(x): innermost shell radius	r(ns)(y): innermost shell radius	0
A: magnitude	T: mean characteristic time constant	(0,1,2,3)
α: power factor of T	Ks: surface conductance of latex bead	(0,1,2,3)
ep0: outermost shell relative permittivity	sb(0): outermost shell conductivity	(0,1,2,3)
e1	s1	(0,1,2,3)
..	..	(0,1,2,3)
e(ns)	s(ns)	(0,1,2,3)
em: relative permittivity of the suspending medium	sm: conductivity of suspending medium at 100kHz	EL: scaling factor
f1: experimental frequency	dep1: DEP data	rot1: ROT data
f2	dep2	rot2
..	..	..
fn	depn	rotn

If the DEP "cross-over" frequency experiment had not been performed, the value 'NaN' ("not a number" value) was entered in the 3rd column of the 1st row. The program would then omit the DEP cross-over frequency analysis. The radii of the x-axis was stored in the first column of the matrix, from row 2 to row {ns+2}. The radii of the y-axis were given in the second column of the same row matrix. The radii designation commenced from the outermost shell to the innermost shell. The relative permittivity and conductivity of the suspending medium were entered in the first and second column of row number {2(ns+1)+4} respectively. The scaling factor for the analysis was located in the third column of the same row, whilst the experimental data occupied rows {2.(ns+1)+5} onwards. In the first column of this section was stored the frequency input values. This array structure was similar to the data program for the spherical shell model. The experimental ROT data was located in the third column of the matrix of table 3.2, whilst in the second column was stored the dielectrophoresis experimental data. If no DEP data was available, the 'NaN' variable was entered into the second column of this matrix. Because this matrix could be used to analyse DEP data on its own, then "NaN" could also be entered in the ROT data column if such experimental data had not been obtained.

3.2.6 *The testing computing program for the Nelder-Mead simplex algorithm in the ellipsoidal dielectric shell model*

The flow chart and the algorithm of this testing program were exactly the same as the testing program for the spherical multishell model program (see section 3.2.3). The only difference of this analytic program was based on the ellipsoidal multishell model rather than the spherical multishell model.

3.3 Results and Discussion

3.3.1 *Spherical dielectric single shell model*

3.3.1.1 *Iteration of all 5 dielectric parameters without the presence of DEP crossing over frequency data*

Data analysis was performed by the spherical shell model program and repeated 100 times successively with different sets of dielectric variables that were generated randomly by a computer. The simulated DEP cross-over frequency point was not provided to the analysis. Different amounts of noise level was introduced into the simulated ROT data. It was generated as a function of Gaussian noise. The amount of the noise level incremented from 0%, 3%, 5% and 10% as the function of the magnitude of the simulated ROT data. Also there were two other groups of ROT data tested. The first set of the data contained 17 ROT data points throughout the whole spectrum. The second set contained 37 data points. The results for both of these data sets are shown in figure 3.9.

When there are 17 ROT data points in the spectra, the accuracy level of the internal (cytoplasmic) permittivity was at 100%. The acceptable margin of the accuracy level was 10% of variation from the true value. The accuracy level of the internal permittivity maintained at 100% as noise level increased from 0% to 10%. The accuracy level of the scaling factor fluctuated between 88% and 93% as the amount of noise increased within the spectrum. The accuracy levels for both of the internal (cytoplasmic) conductivity and the membrane permittivity fluctuated between 38% and 52% as the noise level increased from 0% to 10%. Lastly, the accuracy level of the membrane conductivity decreased from 20% to 12% as the noise level increased from 0% to 10% within the ROT spectrum.

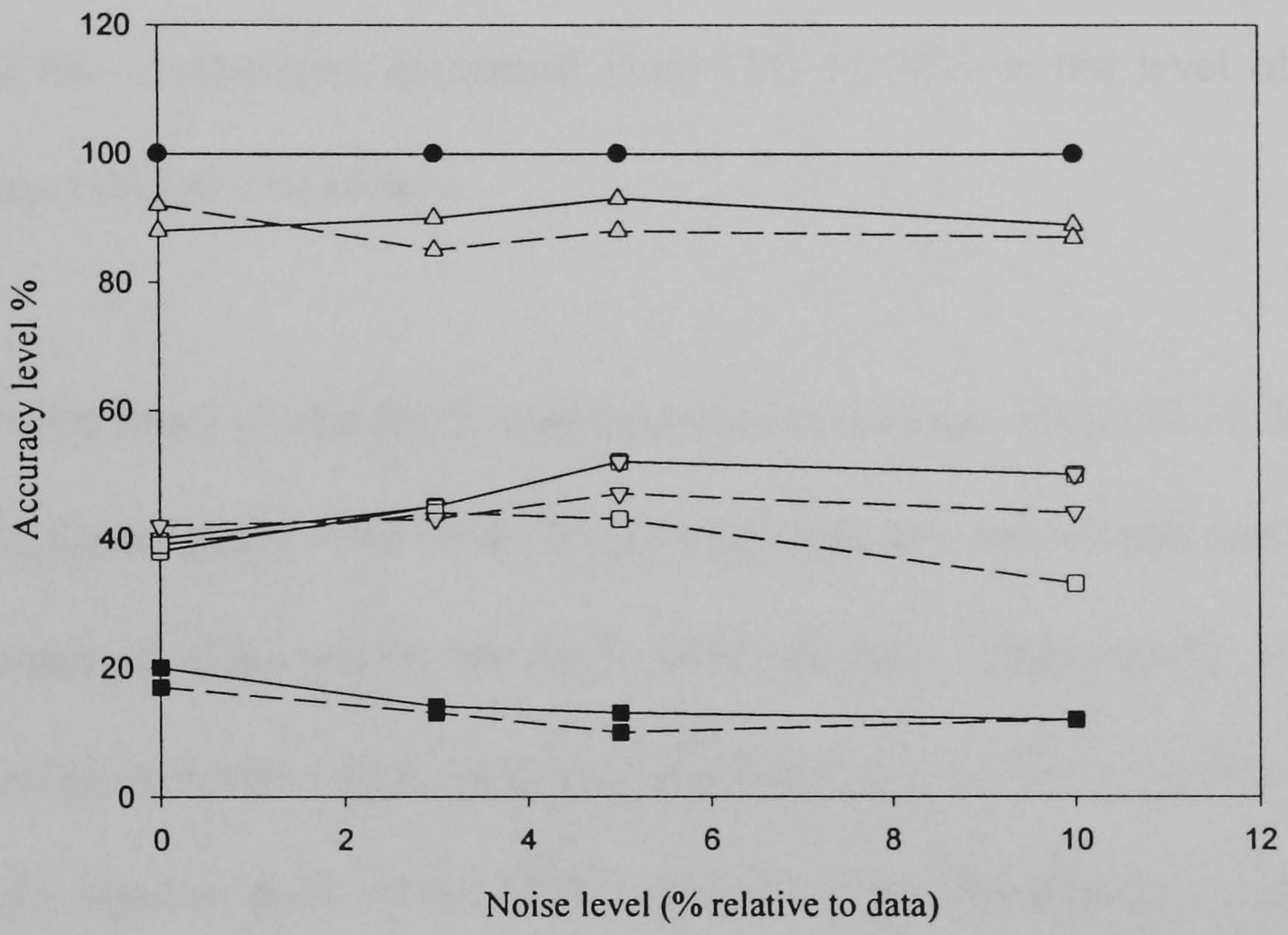

Figure 3.9 The results of accuracy level for each parameter were derived from a single spherical shell model, as a function of noise in the ROT spectrum. There were 17 ROT data points (___), 37 ROT data points (---), with no DEP crossing over frequency data. The parameters were the internal permittivity●, internal conductivity □, membrane permittivity ∇, membrane conductivity ■, and scaling factor Δ.

In the cases of the spectrum with 37 ROT data points, the accuracy level of the internal permittivity remained at 100% as noise level increased from 0% to 10%. The accuracy level of the scaling factor fell from 92% to 87%, as the noise level increased from 0% to 10%. The accuracy level of the membrane permittivity fluctuated between 42% and 47% as noise level increased. The accuracy level of the internal conductivity fluctuated from 44% to 33% as the level of noise increased. Lastly, the accuracy level of the membrane conductivity decreased from 17% to 12% as the level of noise increased with the ROT data.

In the situation of the ROT spectrum that contained either 17 or 37 data points, the accuracy level of the internal permittivity was not affected by the increment of noise within the ROT spectrum data. This was because the internal permittivity value could alter the frequency and the magnitude of the co-field rotation peak of the ROT spectrum quite significantly. Also, the internal permittivity value had the largest value amongst the dielectric variables of the spherical single shell model. Therefore the accuracy level of the other dielectric variables, such as internal conductivity and the membrane permittivity, were overshadowed by the domination of the internal permittivity value. The accuracy levels of these two variables were not as good as that of the internal permittivity and they fluctuated at around 40% to 47%. Fortunately, the Nelder-Mead simplex algorithm is very tolerant of noise in the function values [5]. Therefore the deterioration in the accuracy level for most of the dielectric variables were minimal as noise level increased. Also, the accuracy level of the scaling factor decreased slightly from 92% to 87% as the level of noise increased, because the scaling factor was the major parameter that dominated the change in the magnitude of the ROT spectrum significantly. On the contrary, the accuracy level of the membrane conductivity had the poorest results because the anti-field rotation peak of the ROT spectrum was dominated by the membrane permittivity values. The membrane conductivity value would start to influence the anti-field ROT peak when it would be larger than $1\mu S.m^{-1}$. Thus, this might explain the poor result of the accuracy level of the membrane conductivity.

Furthermore, the accuracy levels of most variables were improved in the ROT spectrum with more ROT data points when the noise was absent in the spectrum (Figure 3.9). However, as the noise was introduced into the ROT spectrum, the accuracy levels of the variables deteriorated further as the number of ROT data increased within the spectrum. It was possible that the level of noise increased in proportion to the increment of ROT data point within the spectrum. In any case, the accuracy level was not affected greatly due to this effect.

3.3.1.2 *Iteration of all 5 dielectric parameters with the presence of DEP crossing over frequency data*

A similar data analysis was performed also by the spherical shell model program and was repeated 100 times successively with different sets of dielectric variables that were generated randomly by a computer. The simulated DEP cross-over frequency point was provided for this data analysis. In the situation where the test was carried out with 17 ROT data points, the accuracy level of the internal permittivity was slightly reduced and was still maintained above 95% under the influence of 10% noise present (Figure 3.10). The accuracy level of the scaling factor fluctuated between 93% and 87% throughout the whole analysis. Unfortunately, the accuracy level of the internal conductivity was reduced slightly in comparison with the ROT analysis without the presence of DEP cross-over frequency data. Its accuracy level altered between 46% to 36% as the noise level increased.

By incorporating the DEP cross-over frequency data with the ROT analysis the accuracy level of the membrane permittivity was improved by 30%. The accuracy level of the membrane permittivity varied between 66% and 54% throughout this analysis. Also, the accuracy level of the membrane conductivity improved by more than 90% when compared with the ROT analysis without the DEP data. The accuracy level of the membrane conductivity ranged between 28% and 38% throughout this analysis.

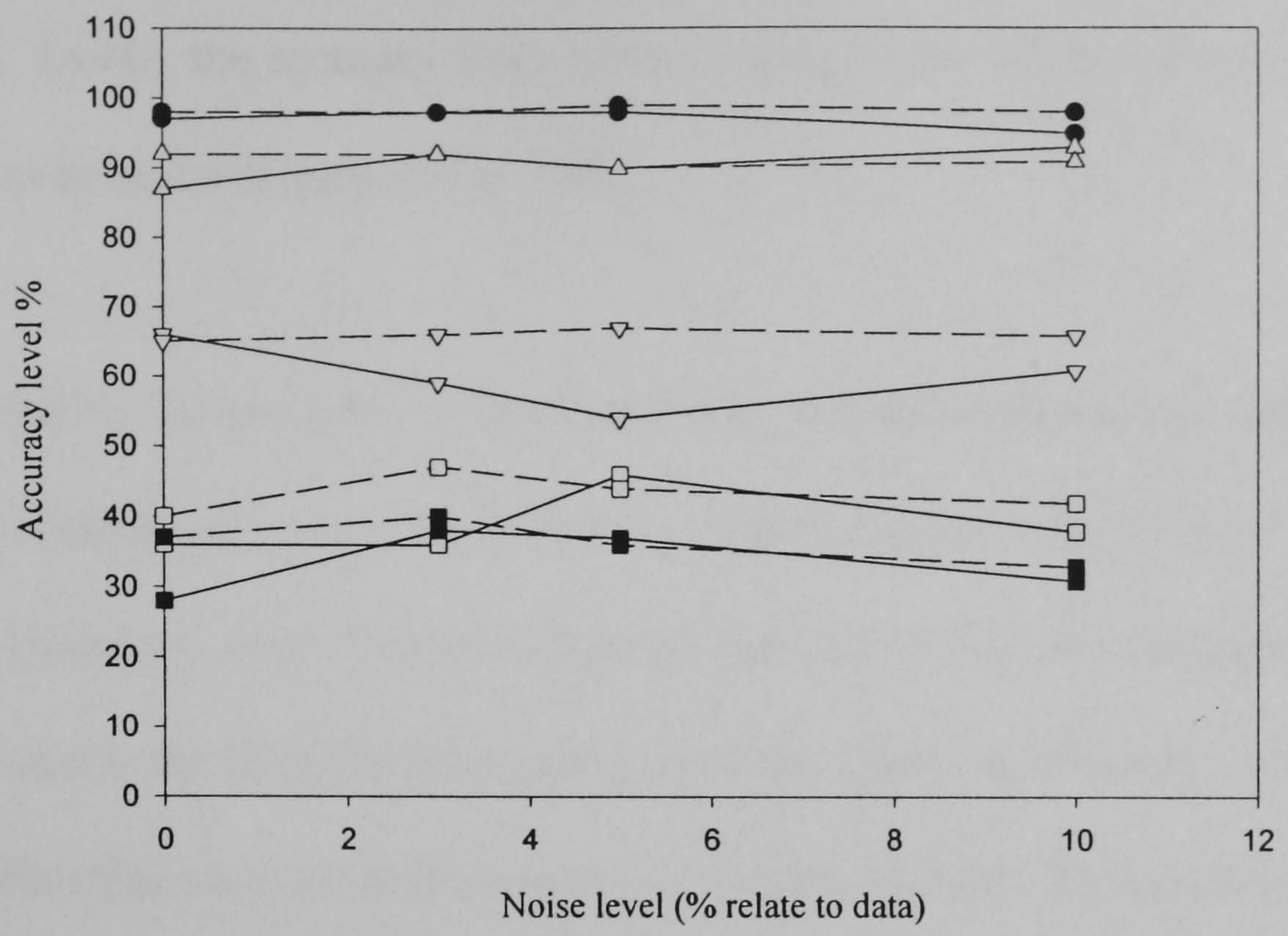

Figure 3.10 Accuracy level results for each parameter derived from a single spherical shell model, as a function of noise in the ROT spectrum. There were 17 ROT data points (___), 37 ROT data point (---), with DEP cross-over frequency data. The parameters were the internal permittivity ●, internal conductivity □, membrane permittivity ∇, membrane conductivity ■, and scaling factor Δ.

When the analysis was made with 37 ROT data points, there was marginal improvement of the accuracy levels for the test variables (Figure 3.10). The accuracy level of the internal permittivity varied between 99% and 98% throughout this analysis as the noise level increased, whilst the accuracy level of internal conductivity fluctuated between 47% to 40%. The accuracy level of the membrane permittivity ranged between 67% and 65% throughout the analysis as noise increased, whilst the accuracy level of the membrane conductivity was reduced from 40% to 33% as the noise level increased to 10%. Lastly, the accuracy level of the scaling factor reduced from 92% to 90% as noise level increased to 10%.

In general, the accuracy of the membrane dielectric parameters improved quite significantly when the ROT data was augmented with the DEP cross-over frequency data. This was because the DEP cross-over frequency data represented the REAL component part of the Clausius-Mossotti factor that described the complex dielectric response of the sample. The real part of the Clausius-Mossotti factor could be used to interpret the membrane capacitance value of the test sample [6]. The anti-field ROT spectrum represented the imaginary part of the Clausius-Mossotti factor that described the membrane dielectric variables. Hence, both real and imaginary parts of the membrane dielectric variables were provided and the accuracy levels of membrane variables could be improved. When the experimental ROT data was augmented with the experimental DEP cross-over frequency data, the accuracy of the analysed results for the membrane dielectric variables was improvided quite significantly. However, the accuracy level for the internal conductivity of the sample was reduced by about 10% (Comparing ROT data without DEP cross-over frequency data, see figure 3.9 and 3.10).

3.3.1.3 *Iteration of 4 dielectric parameters without the presence of DEP crossing over frequency data*

The internal permittivity variable was kept as a constant, globe variable, during this analysis procedure. Thus, the internal permittivity variable was not included in the self-iteration process using the Nelder-Mead simplex algorithm. The variables that were employed for self-iteration were the scaling factor, the internal conductivity, the membrane permittivity and its conductivity. The ROT spectra were presented with 17 ROT data points and without the presence of the DEP cross-over frequency data. The summary of this analysis is shown in figure 3.11.

The accuracy level of the internal conductivity improved by more than 50% compared with the previous analysis described in section 3.3.1.1 (ROT analysis with 5 changeable variables instead of 4). The accuracy level of the internal conductivity fluctuated between 98% and 93% when the noise level increased from 0% to 5%, and then decreased gradually from 93% to 64% as the noise level increased from 5% to 10%. The accuracy level of the membrane permittivity was improved by almost 100% compared with the analysis in section 3.3.1.1, and varied between 98% and 95% when the noise level increased from 0% to 5%, falling from 97% to 69% as the noise level increased from 5% to 10%. The accuracy level of the membrane conductivity was improved by almost 2 to 4 times, decreasing gradually from 94% to 58%, then from 58% to 44% and eventually to 23%, when the noise level increased from 0% to 3%, 5% and lastly to 10%, respectively. The accuracy level of the scaling factor was not affected seriously by incremental addition noise, fluctuating between 97% and 94% throughout the analysis.

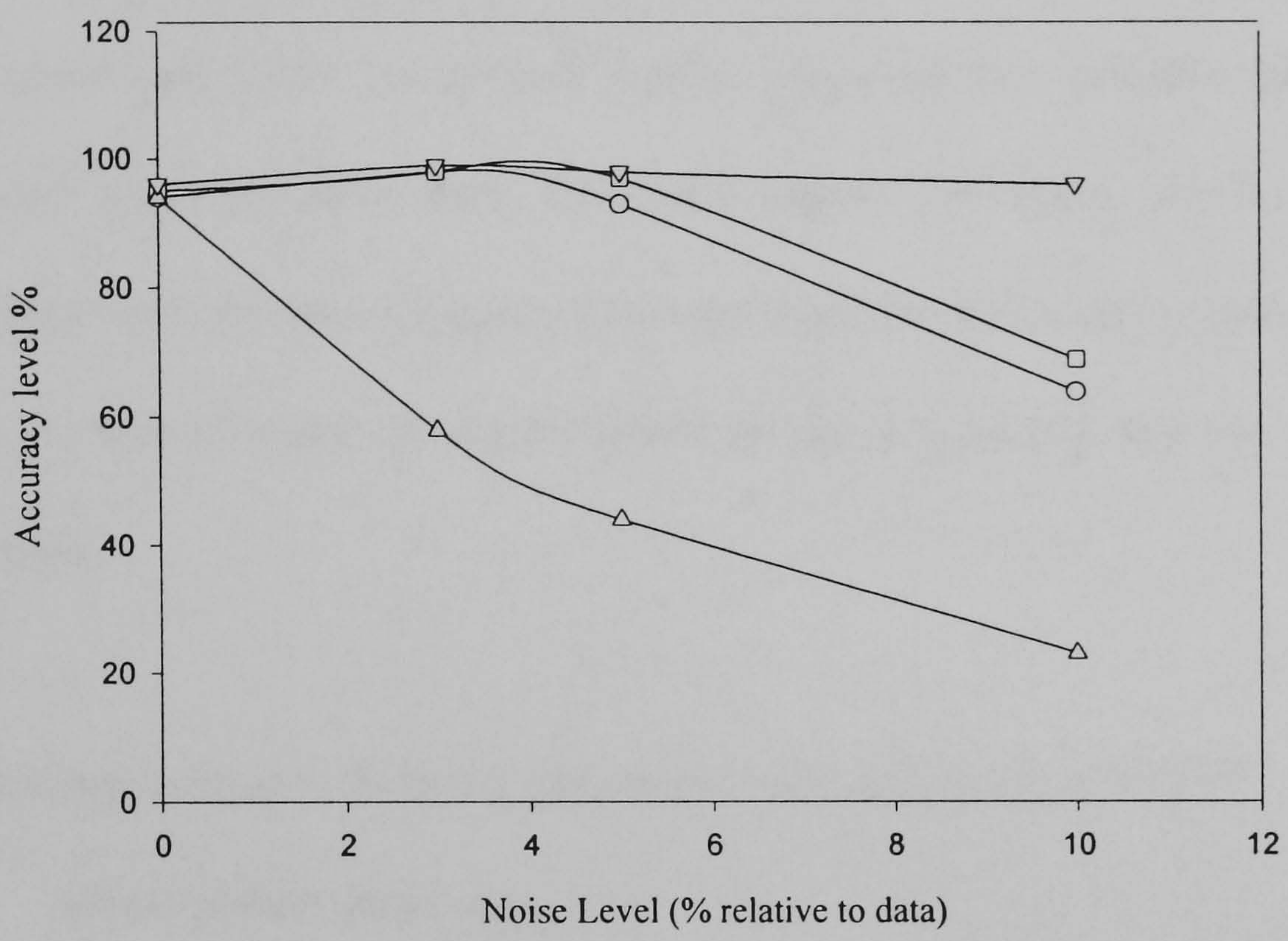

Figure 3.11 Accuracy levels for each parameter derived from a single spherical shell model, as a function of noise in the ROT spectrum. There were 17 ROT data points without DEP cross-over frequency data. The parameters were the internal conductivity O, membrane permittivity □, membrane conductivity Δ, and scaling factor ∇.

From figure 3.11, the accuracy levels for most of the major dielectric parameters from the single shell model were not seriously affect by noise. The explanations could be as follows. The Nelder-Mead simplex algorithm was very tolerant of noise from the experimental data to be analysed. Also, the FMINS function of the MATLAB program can only analyse a maximum amount of five variables and deliver the results quite accurately in an analysis. Four variables were altered by the FMINS function in this investigation, hence this analysis was within the safe tolerance margin for the MATLAB program. Also, the internal permittivity variable was one of the most dominant factor in the shell model, and since this variable was kept constant and excluded from the self-iteration procedure, all the other dielectric variables became more dominant when the self-iteration proceeded. This in turn provided an improvement of the accuracy levels for all the variables.

3.3.1.4 *Iteration of 4 dielectric parameters with the presence of DEP crossing over frequency data*

This took the form of a similar analysis to that described in the previous section 3.3.1.3. The only difference was that the DEP cross-over frequency data was included with the ROT data. The summary of this investigation is given in figure 3.12.

The accuracy level of the internal conductivity decreased slowly from 94% to 91% when the noise level increased from 0% to 5%, reducing gradually from 91% to 75% as noise increased from 5% to 10%.

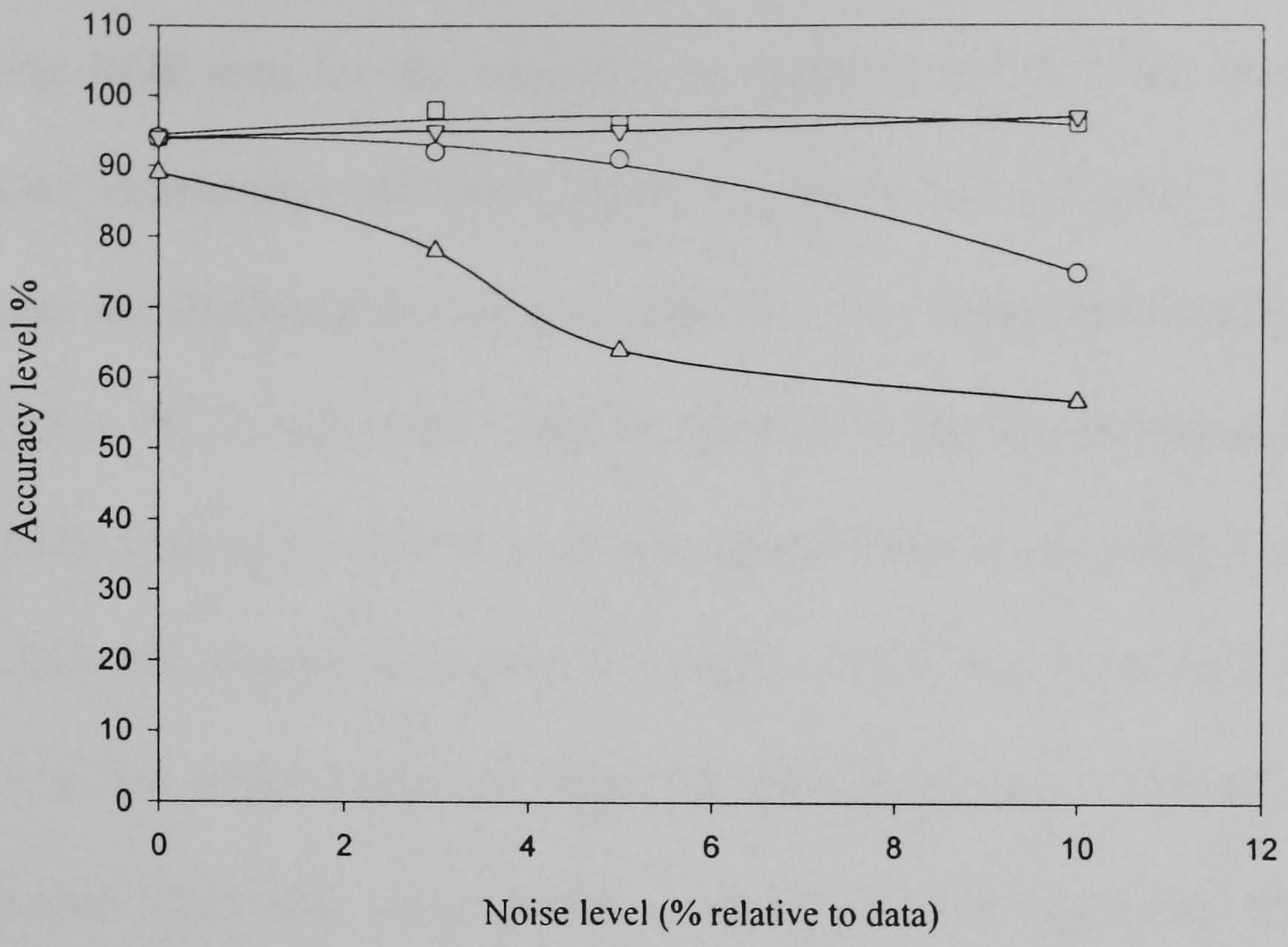

Figure 3.12 Accuracy level results for each parameter derived from a single spherical shell model, as a function of noise in the ROT spectrum. There were 17 ROT data points with DEP cross-over frequency data. The parameters were the internal conductivity O, membrane permittivity □, membrane conductivity Δ, and scaling factor ∇.

The accuracy level of the membrane permittivity fluctuated between 98% and 94% throughout the whole analysis, whilst that for the membrane conductivity decreased gradually from 89%, to 78%, then to 64% and eventually to 57% as noise increased from 0%, 3%, 5% and then to 10%, respectively. Comparing these results with the analysis in section 3.3.1.2, it can be seen that the accuracy level for all of the dielectric variables were improved by about 100% or more. The accuracy level of the scaling factor fluctuated between 97% and 94% as noise increased and this represents only a slight improvement.

In the situation where the DEP cross-over frequency data point was included with the ROT data for the analysis, the accuracy levels of all changeable variables became less influenced by the presence of noise (Figure 3.11, 3.12). This can be explained by the fact that only four changeable variables are required to be altered by the FMINS function in the Nelder-Mead simplex algorithm, leading to an improved analytical ability of the FMINS function [7]. Also, the internal permittivity variable was one of the most dominant factors in the shell model and since this variable became a constant it was withdrawn from the self-iteration procedure. All the other dielectric variables thus became more dominant during the self-iteration procedure. Lastly, the real part of the Clausius-Mossotti factor is related to the membrane dielectric properties is given by the DEP cross-over frequency data; the imaginary part was given by the anti-field ROT spectrum. Since both real and imaginary components of the dielectric variables of the sample were provided, this should theoretically improve the accuracy level for each dielectric variable, especially the membrane dielectric variables.

3.3.2 *Spherical dielectric three shell model*

A three shell model was employed to test the accuracy level for each variable as the noise level in the ROT spectrum increased. The permittivity of the innermost shell (nucleoplasm) and the intermediate shell (cytoplasm) were kept as constants with values of 80.36. Apart from these two parameters, all other variables were free to iterate. In the absence of noise, the accuracy of the scaling factor was 96% (Figure 3.13). The accuracy of the outermost membrane permittivity and conductivity were 96% and 84% respectively. The accuracy level of the intermediate shell (cytoplasmic) conductivity value was 81%, whilst the accuracy levels for the inner membrane permittivity and conductivity were 77% and 24% respectively. Lastly, the accuracy of innermost shell (nucleoplasm) conductivity was 77%.

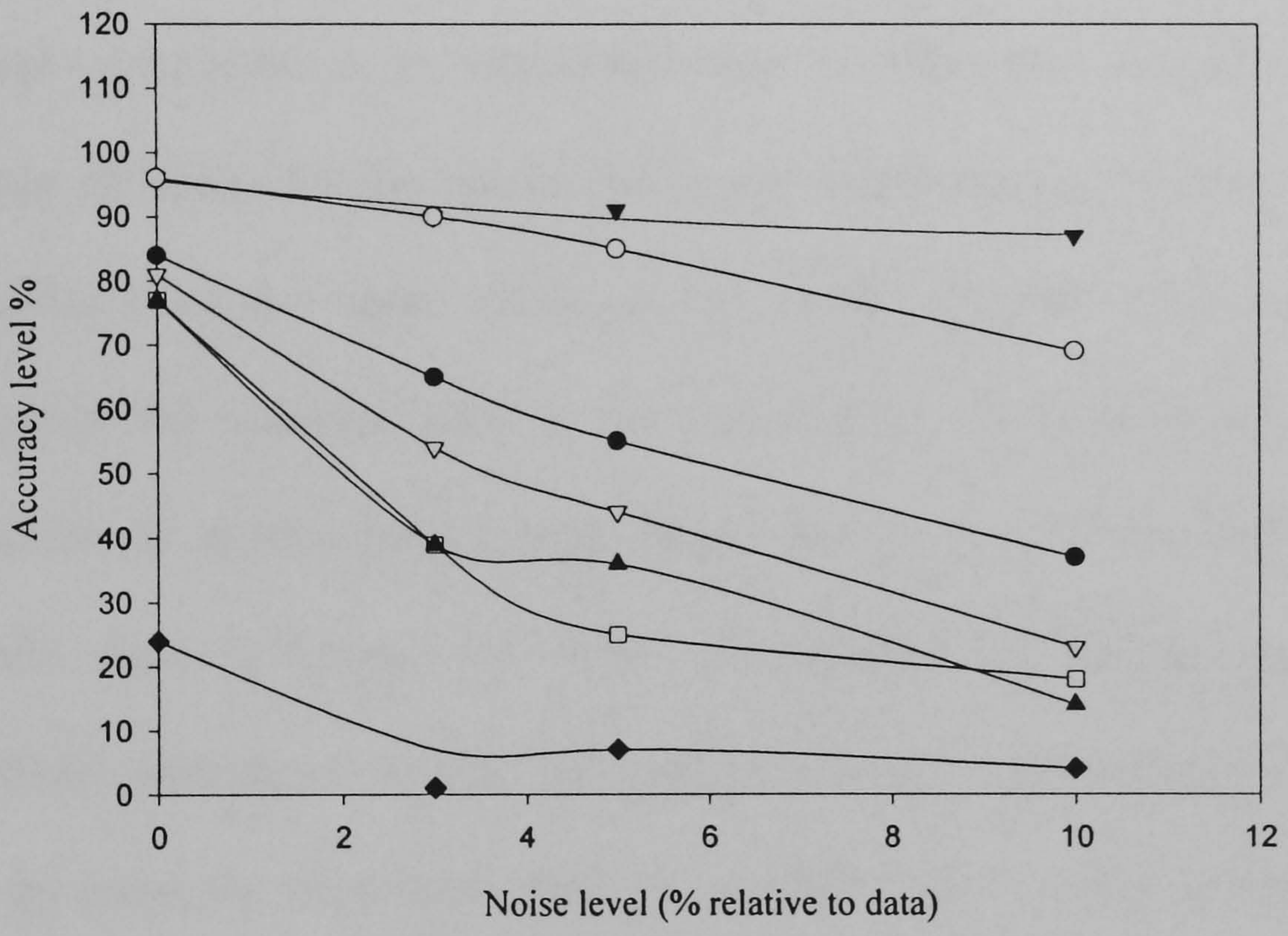

Figure 3.13 Accuracy level for each dielectric variable of the three shell model with increasing noise in the ROT spectrum.▼ : scaling factor; O: outer most membrane ; ● outer most conductivity ; ∇: intermediate medium conductivity ; □: inner membrane permittivity ; ◆: inner membrane conductivity ;▲: inner most medium conductivity.

As the noise level increased up to 10% relative to the ROT spectrum value, the accuracy for most of the parameters was reduced quite significantly. The accuracy level for the scaling factor was reduced to 87%, with the accuracy value for the outermost membrane permittivity and conductivity being reduced to 69% and 37%, respectively. Also, the accuracy value for the intermediate shell (cytoplasmic) conductivity was 23%, the accuracy levels of the inner membrane permittivity and conductivity were 18% and 4%, respectively, and the accuracy level for the innermost shell (nucleoplasmic) conductivity was 14%. These results might arise from two causes. First of all, the maximum number of variables for the MATLAB minimisation route 'FMINS' to cope with were normally five parameters, so that the maximum number of variables to be iterated had been exceeded [7]. Secondly, as the number of shells for the model increased, determination of the complex permittivity of the inner shells of the model became more involved. Therefore, the accuracy level of the parameters to be determined reduced progressively as they probed more deeply into the core of the shell model. Despite these problems, the major parameters such as the outermost membrane permittivity and the scaling factor could be determined reasonably well by using the three shell model to analyse some complex systems. As noise level decreases, the derived parameters for the outer shells become more reliable.

3.3.3 *Spherical dielectric five shell model*

In this analysis, the self-iteration procedure of the Nelder-Mead simplex algorithm became inoperative because of the complexity of the model. Also, the amount of the variables for self-iteration, exceeded the maximum that could be managed by MATLAB [7]. Unless the initial guessed variables were very closed to the true values of the test sample at the start of the analysis, the resultant values derived by the program would be neither reliable nor accurate.

3.3.4 *Ellipsoidal dielectric single shell model*

The ellipsoidal shell model program was used in the data analysis whilst was repeated 100 times successively with different sets of dielectric variables generated randomly by a computer. The results of the accuracy level for each variable determined by this investigation are shown in figure 3.14.

The accuracy level of the magnitude of characteristic time-constant A [3] was reduced from 42% to 25% as the level of noise increased from 0% to 10% within the ROT spectrum. The accuracy level of the characteristic time-constant T [3] fluctuated between 43% and 57% as the noise level increased from 0% to 5%, and eventually reduced to 33% as the noise increased to 10%. Both of the variables A and T were used to determined the frequency region of the low frequency ROT spectrum for the latex bead sample (see chapter 5). As the variable A increased or the variable T decreased, the low frequency ROT peak shifted towards the high frequency region. As the variable A decreased or variable T increased, the low frequency rotation peak would shift back to the low frequency region. Both of these variables changed neither the magnitude nor the width of the low frequency ROT spectrum. Since both variables contributed to the same function, it could introduce uncertainty to the model for the analysis and thus make it difficult to produce an unique solution. Thus, the Nelder-Mead simplex algorithm might have difficulties in determining the true values for both variables A and T, and might explain the poor accuracy results for these variables (Figure 3.14).

The variable α was used to determine the width of the low frequency ROT spectrum and the Nelder-Mead simplex algorithm was very sensitive to variations of this variable. The accuracy level of the variable α remained at 100% when the noise level increased from 0% to 3%, and it fell to 98% and eventually to 92% as the noise level of the ROT spectrum increased from 5% to 10%.

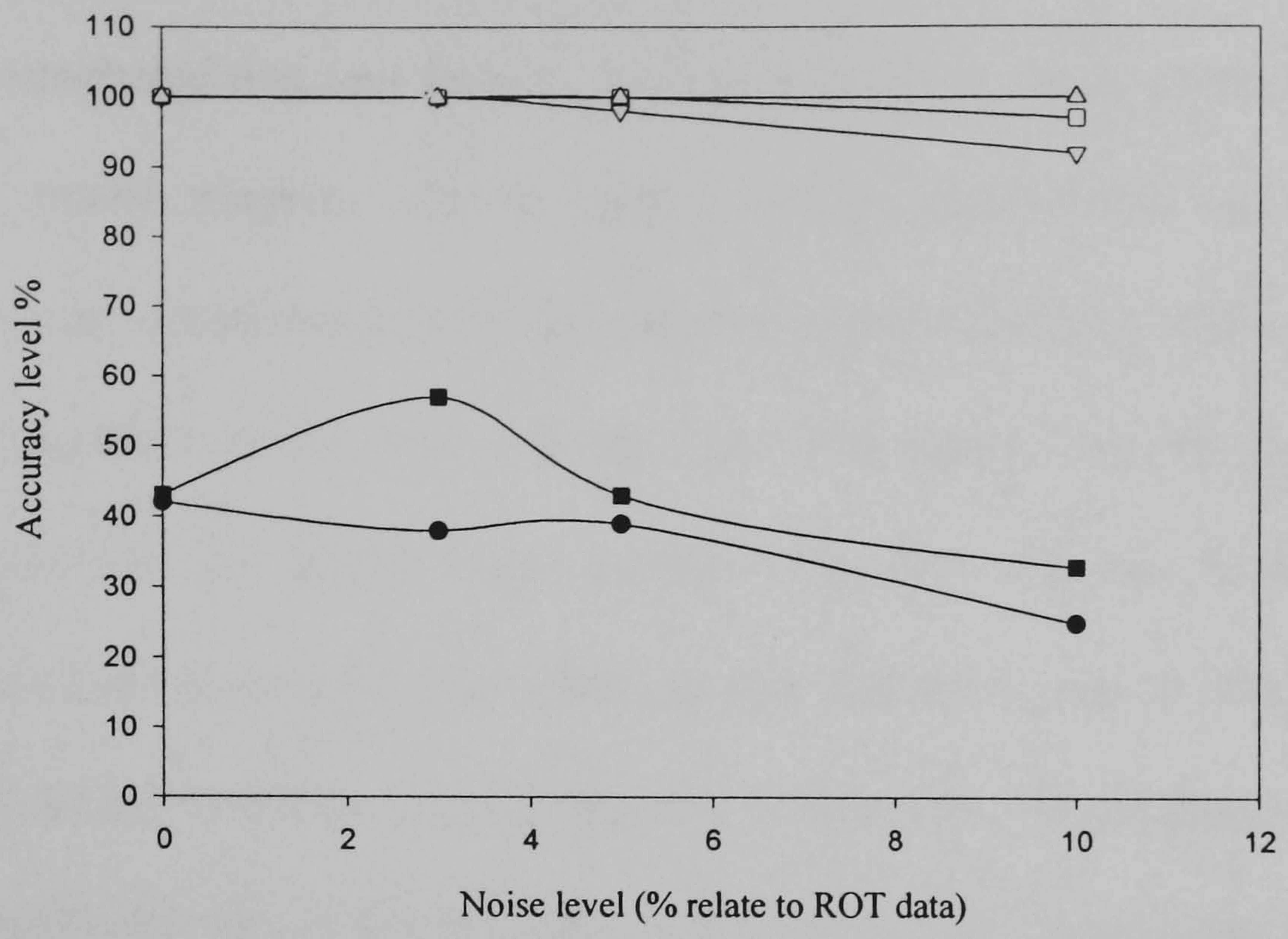

Figure 3.14 Accuracy level results for each variable derived from an ellipsoidal shell model, as a function of noise in the ROT spectrum. These parameters were: ● A the magnitude of characteristic dispersion [3], ■ T characteristic time-constant [3], ∇ variable α [3], □ Ks surface conductance of latex bead [3], Δ scaling factor (see equation 3.3).

The surface conductance was the only variable that changed the frequency value of the high frequency ROT peak. Thus, the Nelder-Mead simplex algorithm could determine the true value of the surface conductance very accurately. The accuracy level of the surface conductance was maintained at 100% as the level of noise increased from 0% to 5%. Eventually, it fell to 97% as the noise level increased to 10%. Finally, the scaling factor variable was very tolerant to the effect of noise within the ROT spectrum, and its accuracy level remained at 100% as the noise level increased from 0% to 10%.

3.4 Conclusion

It is concluded that four factors can determine the accuracy of the spherical shell model program. The complexity of the shell model is the most important consideration, with the simplest single shell model delivering the most accurate results from the analysis. The number of variables to be analysed by the Nelder-Mead simplex algorithm can also significantly influence the accuracy of the spherical shell model program for determining the dielectric variables. Five changeable variables are the maximum that can be used in the MATLAB program, so by reducing this number, the accuracy of the analytic program is improved considerably. Also, the internal permittivity variable is the most dominant factor within the spherical shell model. If this variable is known and kept as a constant, globe variable, during the analysis, the accuracy levels of the other dielectric parameters are improved very significantly. Lastly, the program gives more accurate results when the ROT analysis is augmented with the DEP cross-over frequency data.

For latex beads, the surface conductance, the scaling factor of the ROT spectrum and the variable α could be derived very accurately by using the ellipsoidal shell model program. However, the magnitude A and the characteristic time-constant T could not be determined very accurately.

The Nelder-Mead simplex algorithm was very tolerant of noise being added to the analysis data of these programs. In most cases, the accuracy levels of the dielectric variables were quite stable as the noise level increased to 5%, falling as the noise level was increased beyond this point.

3.5 References

1. Y. Huang, R. Hölzel, R. Pethig and X-B. Wang (1992) Differences in the AC electrodynamics of viable and non-viable yeast cells determined through combined dielectrophoresis and electrorotation studies, *Phys. Med. Biol.*, **37**, 7, 1499-1517

2. T. Kakutani, S. Shibatani and M. Sugai (1993) Electrorotation of non-spherical cells: theory for ellipsoidal cells an arbitrary number of shells *Bioelectrochemistry and Bioenergetics* **31** 131-145

3. X-F. Zhou, G. H. Markx, R. Pethig, I. M. Eastwood (1995) Differentiation of viable and non-viable bacterial biofilms using electrorotation, *Biochimica et Biophysica Acta* **1245** 85-93

4 J. A. Nelder and R. Mead (1964) A simplex method for function minimization, *The Computer Journal* 7 308-313

5. J. E. Dennis and D. J. Woods in (1987) *New Computing Environments: Microcomputers in Large-Scale Computing* (A. Wouk, ed.), Optimization on Microcomputers: The Nelder-Mead Simplex Algorithm, 116-122, **SIAM**

6. P. R. C. Gascoyne, J. Noshari, F. F. Becker and R. Pethig (1994) Use of Dielectrophoretic Collection Spectra for Characterizing Differences between Normal and Cancerous Cells, *IEEE Transaction on Industry Applications* **30**, 4, 829-834

7. MATLAB: High Performance Numeric Computation and Visualization Software, Reference Guide, *THE MATH WORKS Inc.*

3.7 Appendix

3.7.1 Appendix 3.1a

Spherical dielectric multi-shell model

```
%"Spherical dielectric multi-shell modelling program written by Ka Lok Chan"
%"GENERAL PURPOSE FITTING PROGRAM"
%Get ASCII file containing ROT experimental data
%3 columns of data such as
%initial guesses of permittivity and conductivity of
%membrane and encapsulated suspension
%  Frequency   medium conductivity   rotation data
%
%(no. of radius)=shell number of the model + 1
%Temp is the temperature of electrode chamber when experimentis carried out.
%Crossoverfrequency is the Crossing over frequency of particle in DEP experiment.
%  (no. of radius)  Temp  Crossoverfrequency
%      r2           d2     E    (r is measured radius of shell)
%      r4           d4     EL    (d is thickness of membrane)
%      ..           ..     0    (E is applied voltage)
%      r(nr)        d(nr)  0    (EL is the scaling factor)
%      .........................  (r2 is an intermost shell radius,
%                               r(nr) is an outermost shell radius)
%     maxlimit    minlimit  0    (maxlimit and minimium limit of medium permittivity)
%      .........................
%      e1          s1   (0,1,2,3) (e is relative
%      e2          s2   (0,1,2,3) permittivity)
%      ..          ..   (0,1,2,3) (s is conduct ivity)
%      e(nr)       s(nr) (0,1,2,3)
%      .........................
%      f1          s1     rot1
%      f2          s2     rot2
%      ..          ..     ..
%      fn          sn     rotn
%(0)s which is flags todeactivate all iteration process.
%(1)s activate permittivity(e) for iteration. (2)s activate
%conductivity(s) iteration only. (3)s activate all
%iteration.

%weighting factors on the rotation spectrum and the crossover frequency.
%if weighting factor of the crossover frequency is equal to 0,
%the fitting program will try to fit the ROT spectrum only.
%In normal condition, both weight factors are equal to 1.
%If fitting program is over emphasise on the crossover frequency
%and affect the accuracy on the fitting on the ROT spectrum,
%put "rotweight"=10 and "depweight"=1, it may put the weighting on the
%ROT spectrum in order to have a proper fitting.

rotweight=input('The rotation spectrum weighting factor=');
depweight=input('The crossover frequency weighting factor=');

%Input the rotation data file into this program.
%File will be taken from directory of 'c:\depdata\'
%then the input file will be evaluated and
%the size of the (matrix) file will be known by (n) rows and (cols) columns.
```

```
file=input('ROT data fileroot=','s');
fullfile=['c:\depdata\',file];
fullfile=[fullfile,'.dat'];
eval(['load ',fullfile]);
eval(['rotdat=',file]);
[n, cols]=size(rotdat);

rotsimdat=rotdat;

%no. amount of radius require for (n-1) shell model:
nr=rotsimdat(1,1);
Temp=rotsimdat(1,2);
CrossoverFrequency=rotsimdat(1,3);
fco=CrossoverFrequency*1000;
wfco=fco*2*pi;

%applied voltage(E) and scaling fractor(EL)
E=rotsimdat(2,3);
EL=rotsimdat(3,3);

%maximum and mininium limit of medium relative permittivity
%normally, it is from 78 to 82
maxlim=rotsimdat(2+nr/2,1);
minlim=rotsimdat(2+nr/2,2);

% radius for each shells and thickness of the membrane
%they are provided from the data file.
for rcount=2:2.0:nr,
   nr1=rcount./2;
   r(1,rcount)=rotsimdat(1+nr1, 1);
   d(1,rcount)=rotsimdat(1+nr1, 2);
   r(1,rcount-1)=r(1,rcount)-d(1,rcount);
end

%Volume of cell or vesicle
rexe=r(1,nr);
V=4/3*pi*(rexe)^3;

%relative permittivity and conductivity of each shells

eflagincrement=0;
eflagincrement2=0;
sflagincrement=0;
sflagincrement2=0;

%flag indicators for iteration is put in an array matrix (flag)
%Array matrix (evar) stores permittivity parameters for iteration.
%Array matrix (svar) stores conductivity parameters for iteration.
%Array matrix (eset) and (sset) store perm. and cond. parameters as constant values.

for flagcount=nr/2+2+1:nr/2+2+nr,
   flag(1,flagcount-nr/2-2)=rotsimdat(flagcount,3);
end

for flagcount=2+nr/2+1:2+nr/2+nr,
```

```
  if rotsimdat(flagcount,3)==3,
    eflagincrement=eflagincrement+1;
    sflagincrement=sflagincrement+1;
    evar(1,eflagincrement)=rotsimdat(flagcount,1);
    svar(1,sflagincrement)=rotsimdat(flagcount,2);
    eflag1(1,eflagincrement)=flagcount-nr/2-2;
    sflag1(1,sflagincrement)=flagcount-nr/2-2;

  elseif  rotsimdat(flagcount,3)==0,
    eflagincrement2=eflagincrement2+1;
    sflagincrement2=sflagincrement2+1;
    eset(1,eflagincrement2)=rotsimdat(flagcount,1);
    sset(1,sflagincrement2)=rotsimdat(flagcount,2);
    eflag2(1,eflagincrement2)=flagcount-nr/2-2;
    sflag2(1,sflagincrement2)=flagcount-nr/2-2;

  elseif  rotsimdat(flagcount,3)==1,
    eflagincrement=eflagincrement+1;
    sflagincrement2=sflagincrement2+1;
    evar(1,eflagincrement)=rotsimdat(flagcount,1);
    sset(1,sflagincrement2)=rotsimdat(flagcount,2);
    eflag1(1,eflagincrement)=flagcount-nr/2-2;
    sflag2(1,sflagincrement2)=flagcount-nr/2-2;

  elseif  rotsimdat(flagcount,3)==2,
    eflagincrement2=eflagincrement2+1;
    sflagincrement=sflagincrement+1;
    eset(1,eflagincrement2)=rotsimdat(flagcount,1);
    svar(1,sflagincrement)=rotsimdat(flagcount,2);
    sflag1(1,sflagincrement)=flagcount-nr/2-2;
    eflag2(1,eflagincrement2)=flagcount-nr/2-2;
  end
end

[evarn,evarcol]=size(evar);
enf1=evarcol;
enf2=nr-enf1;

[svarn,svarcol]=size(svar);
snf1=svarcol;
snf2=nr-snf1;

% relative permittivty of suspending medium
%em=80;
emjudge=3+nr/2;
if rotsimdat(emjudge,3)==2,
  em=eset(1,1);
elseif rotsimdat(emjudge,3)==3,
  em=evar(1,1);
end
%permittivity of free space
e0=8.825e-12;

%Generate the matrix ROTDATA for autofiting program

p1=nr/2+3+nr;
```

```
p2=nr/2+2+nr;

na=n-p2;

for p=p1:n;
   rotatdat(p-p2,1) = rotsimdat(p,1);
   rotatdat(p-p2,2) = rotsimdat(p,2);
   rotatdat(p-p2,3) = rotsimdat(p,3);
end


%frequency data point from the experiment
z1=rot90(rotatdat(:,1));
z2=z1;

% scale frequency to 2.pi*Hz and conductivity to S/m
wf=2000*pi;
rotatdat(:,2)=rotatdat(:,2).*1e-4;
rotatdat(:,1)=rotatdat(:,1).*wf;
w1=rot90(rotatdat(:,1));

%suspending medium conductivity
%sm=rot90(rotatdat(:,2));
sm=sum(rotatdat(:,2))/na;

%The following session is ROT simulation of best-fit graph

x1=logspace(-1,6);
x2=x1;
w2=x1.*wf;
lin=x1.*0;
[B,nf]=size(x1);

%curve fitting errors minimization logarithm

errsqu=0;
deperr=0;
rotparams=[EL evar svar];

global rotatdat r d eset sset eflag1 eflag2 sflag1 sflag2 enf1 enf2 snf1 snf2 V em e0 E nr nf
wfco fco errsqu deperr maxlim minlim rotweight depweight;

weight=1;
tracestatus=1;

nrotparams=fmins ('rotafitx',rotparams,5e20,tracestatus);

%After iteration, all permittivities values are put in matrix(e).
%All conductivities values are put in matrix(s).

EL=nrotparams(1);
for ememcount=1:enf1,
   ememcount1=eflag1(1,ememcount);
   e(1, ememcount1)=abs(nrotparams(1,1+ememcount));
end
for esetcount=1:enf2,
```

```
   esetcount1=eflag2(1,esetcount);
   e(1,esetcount1)=eset(1,esetcount);
end
for smemcount=1:snf1,
   smemcount1=sflag1(1,smemcount);
   s(1,smemcount1)=abs(nrotparams(1,1+enf1+smemcount));
end
for ssetcount=1:snf2,
   ssetcount1=sflag2(1,ssetcount);
   s(1,ssetcount1)=sset(1,ssetcount);
end

%complex permittivity of suspending mwedium

eme=em*e0-j*sm./w2;

%complex permittivity of each part of shell in term of
%matrix (er)
for rol=1:nr,
etemp=e(1,rol);
stemp=s(1,rol);
ertemp=etemp*e0-j*stemp./w2;
er(rol,1:nf)=ertemp;
end


%(n)-shells modelling

for Acm=1:nr-1,


   eu(Acm,1:nf)=(r(1,Acm+1)./r(1,Acm)).^3 -(er(Acm,1:nf)-
er(Acm+1,1:nf))./(er(Acm,:)+2.*er(Acm+1,:));


   etr(Acm,1:nf)=((r(1,Acm+1)./r(1,Acm)).^3+2.*(er(Acm,:)-
er(Acm+1,:))./(er(Acm,:)+2.*er(Acm+1,:)));

   ee(Acm,1:nf)=er(Acm+1,:).*etr(Acm,1:nf)./eu(Acm,1:nf);

   er(Acm+1,:)=ee(Acm,:);
   epe=ee(Acm,1:nf);
end

%cmf is Clasius Mossotti factor, y1 is ROT, df2 is DEP.

cmf=(epe-eme)./(epe+2.*eme);
dm=3*V*E*em*e0.*cmf;
DF=real(dm).*(norm(E).^2)./2*E;
RT=-imag(dm).*E;
y1=(EL^2).*(RT);
df2=(EL^2).*(DF);

%To limit the amplitude of DEP for the purpose of graph plotting.
%DEP plots as y2 in the graph.
mxr=max(rotatdat(:,3));
```

```
mxd=max(df2);

if  mxr < mxd
     sdf=mxd/mxr;
     y2=df2./sdf;
else

     y2=df2;
end

%Experimental frequency point for the plot
z3=z2;
y3=rot90(rotatdat(:,3));

%To display permittivities values matrix(e)
%and conductivities values matrix(s) in the graph,
%and in matlab editor as as well.
esca=";
ssca=";
for dply=1:nr,
   epst=['e',int2str(dply),'=',num2str(e(1,dply))];
   sps=['s',int2str(dply),'=',num2str(s(1,dply))];
   disp(epst);
   disp(sps);
   esca=[esca,sprintf('e%1.0f=%g ',dply,e(1,dply))];
   ssca=[ssca,sprintf('s%1.0f=%gS/m ',dply,s(1,dply))];
end

%To display radii values of the (liposome) model in the graph,
%and in matlab editor as as well.
rsca=";
for rcount=2:2.0:nr,
   nr1=rcount./2;
   rps=['r',int2str(nr1),'=',num2str(r(1,rcount))];
   disp(rps);
   rsca=[rsca,sprintf('r%1.0f=%gm ',nr1,r(1,rcount))];
end

%To display membrane surface per unit area capacitance values (e/d) in the graph,
%and in matlab editor as as well.
edsca=";
for edtm=2:2.0:nr,
   edtmem=edtm./2;
   edd(1,edtmem)=e0.*e(1,edtm)./d(1,edtm);
  edt=['abmcap',int2str(edtmem),'=',num2str(edd(1,edtmem))];
   disp(edt);
   edsca=[edsca,sprintf('abmcap%1.0f=%gF/m^2 ',edtmem,edd(1,edtmem))];
end

%To display those remained parameters in the graph
%and in matlab editor as as well.
a1=num2str(E);
a2=num2str(EL);
a3=num2str(Temp);
a4=num2str(CrossoverFrequency);
a5=num2str(sm);
```

```
da1=['Applied Voltage=',a1];
da2=['Scale=',a2];
da3=['Temp=',a3];
da4=['CrossoverFrequency=',a4];
da5=['SuspendingMedium cond.=',a5];
disp(da1);
disp(da2);
disp(da3);
disp(da4);
disp(da5);

%Plot graph

rshell=nr-1;
semilogx(x1,y1,x2,y2,z3,y3,'or',x1,lin,'-');
title1=(['Comparison of ROTATION Data with Best Fit of ',num2str(rshell),' Shell
Model']);
title2=(['Applied Voltage=',num2str(E),'V, EL=',num2str(EL),',
Temp=',num2str(Temp),'C, CrossoverFrequency=',num2str(CrossoverFrequency),'kHz ']);
title3=(['Suspending Medium Cond.=',num2str(sm),'S/m']);
text(0.25,1.0,title1,'sc');
text(0.1,0.95,title2,'sc');
text(0.12,0.9,esca,'sc');
text(0.12,0.85,ssca,'sc');
text(0.12,0.8,rsca,'sc');
text(0.12,0.75,edsca,'sc');
text(0.12,0.7,title3,'sc');
xlabel('Frequency, (kHz)');
ylabel('Initial ROTATION Velocity (/sec/V^2)');
grid;
```

3.7.2 Appendix 3.1b

```
%"Analytic spherical multi-shell model with Nelder-Mead simplex alogrithm wriiten by
%Ka Lok Chan"
%ITERATION FUNCTION FOR GENERAL PUTPOSE FITTING PROGRAM
function y=rotafitx(rotparams)

% ROTAFIT error function used for ROT surface fitting based
%on the n shells or unlimited number of shells
%       model of the cell
%
%       rotatdat is a matrix containing rot data in 3 columns:
%       [Angular frequency in Hz;   Conductivity in S/m;
%ROT rate]
%
%       rotparams contains the guesses:
%       [scalefactor;   Emembrane';   Smembrane]


global rotatdat r d eset sset eflag1 eflag2 sflag1 sflag2 enf1 enf2 snf1 snf2 V em e0 E nr nf
wfco fco errsqu deperr maxlim minlim rotweight depweight;
```

```
EL=abs(rotparams(1));
for ememcount=1:enf1,
   ememcount1=eflag1(1,ememcount);
   e(1,ememcount1)=abs(rotparams(1,1+ememcount));
end
for esetcount=1:enf2,
   esetcount1=eflag2(1,esetcount);
   e(1,esetcount1)=eset(1,esetcount);
end
for smemcount=1:snf1,
   smemcount1=sflag1(1,smemcount);
   s(1,smemcount1)=abs(rotparams(1,1+enf1+smemcount));
end
for ssetcount=1:snf2,
   ssetcount1=sflag2(1,ssetcount);
   s(1,ssetcount1)=sset(1,ssetcount);
end

[na, ncols]=size(rotatdat);
w=rot90(rotatdat(:,1));
data=rot90(rotatdat(:,3));

errsqu=0;


sm=sum(rotatdat(:,2)/na);

%
%if depweight>0,
%
%er is the complex permittivity of each shell.
%ercof is the complex permittivity of each shell at the crossover frequency point.
for rol=1:nr,
etemp=e(1,rol);
stemp=s(1,rol);
ertemp=etemp*e0-j*stemp./w ;
er(rol,1:na)=ertemp;
ercof=etemp*e0-j*stemp./wfco;
erdcof(rol,1)=ercof;
end


%complex permittivity of suspending medium at crossover frequency point

emcof=em*e0-j*sm/wfco;

%complex permittivity of vesicle or cell at crossover frequency

for Acf=1:nr-1,

eucof(Acf)=(r(1,Acf+1)./r(1,Acf))^3-(erdcof(Acf,1)-
erdcof(Acf+1,1))./(erdcof(Acf,1)+2*erdcof(Acf+1,1));

etrcof(Acf)=(r(1,Acf+1)./r(1,Acf))^3+2.*(erdcof(Acf,1)-
erdcof(Acf+1,1))./(erdcof(Acf,1)+2.*erdcof(Acf+1,1));
```

```
eecof(Acf)=erdcof(Acf+1,1).*etrcof(Acf)./eucof(Acf);
erdcof(Acf+1)=eecof(Acf);

end
epcof=eecof(Acf);
depco=real((epcof-emcof)/(epcof+2*emcof));
deperr=2e1*depweight*depco^2;

%end
%complex permittivity of suspending medium

eme=em*e0-j*sm./w;

%shells modelling

for Acm=1:nr-1,


   eu(Acm,1:na)=(r(1,Acm+1)./r(1,Acm)).^3 -(er(Acm,1:na)-
er(Acm+1,1:na))./(er(Acm,:)+2.*er(Acm+1,:));


   etr(Acm,1:na)=((r(1,Acm+1)./r(1,Acm)).^3+2.*(er(Acm,:)-
er(Acm+1,:))./(er(Acm,:)+2.*er(Acm+1,:)));

   ee(Acm,1:na)=er(Acm+1,:).*etr(Acm,1:na)./eu(Acm,1:na);

   er(Acm+1,:)=ee(Acm,:);
end
   epe=ee(Acm,1:na);

cmf=(epe-eme)./(epe+2.*eme);
dm=3*V*E*em*e0.*cmf;
DF=real(dm).*(norm(E).^2)./2*E;
RT=-imag(dm).*E;
rata=(EL^2).*(RT);

    err=rotweight*(data-rata);
    errsqu=(norm(err))^2;

nre=nr-1;
nre1=nr-3;
   for rol=1:2.0:nre1,
    if s(1,rol+2)>s(1,rol),
      errsqu=errsqu*10;
    elseif sm>s(1,nre),
      errsqu=errsqu*10;
    end
   end

y=errsqu+deperr;
```

3.7.3 Appendix 3.2a

Ellipsoidal dielectric shell model

```
%"Program written by Ka Lok Chan"
%"GENERAL PURPOSE FITTING PROGRAM FOR MULTISHELLED ELLIPSOID
%MODEL"
%Get ASCII file containing ROT experimental data
%3 columns of data such as
%initial guesses of permittivity and conductivity of
%membrane and encapsulated suspension
%   Frequency   dep data    rotation data
%     (Hz)
%
%(no. of shell) = no. of shells from the multishelled ellipsoid model + 1
%Temp is the temperature of electrode chamber when experimentis carried out.
%Crossoverfrequency is the experimental DEP Crossing over frequency of particle.
%In experiments of untreated latex beads, viscosity is referred to the
%aqueous suspending medium, viscosity of water
%   (no. of shell)  Temp   Crossoverfrequency
%       r0(x)      r0(y)     E     (r is measured radius of shell)
%       r1(x)      r1(y)     0     (r(x) is the radius component on x-axis)
%       r2(x)      r2(y)     0     (r(y) is the radius component on y-axis)
%       r3(x)      r3(y)     0     (E is applied voltage)
%        ..          ..      0
%     r(ns)(x)   r(ns)(y)    0     (r0(x,y) is an outermost shell radius)
%      ........................    (r(ns)(x,y) is an innermost shell radius)
%        A          T     (0,1,2,3) (magnitude and mean characteristic time constant)
%       alpha       Ks    (0,1,2,3) (Alpha is power factor of T,)
%      ........................        (Ks surface conductance of latex bead.)
%       epo       sb(o)   (0,1,2,3) (epo and sb(o): outermost shell relative permittivity and
%                                      outermost shell conductivity of latex bead.)
%       e1          s1    (0,1,2,3) (e(ns) is the innermost relative permittivity)
%       e2          s2    (0,1,2,3) (s1(ns)is the bulk conductivity of the latex bead. In 0 shell
%                                     case, sb(o) is the bulk conductivity of the bead.)
%       ..          ..    (0,1,2,3) (s is conductivity, Unit: S/cm)
%      e(ns)       s(ns)  (0,1,2,3) (EL is the scaling factor)
%      ........................
%       em          sm       EL     (em relative permittivity of the suspending medium.)
%      ........................     (sm conductivity of suspending medium at 100kHz.)
%       f1         dep1     rot1    (f1 to fn: frequencies for experiments)
%       f2         dep2     rot2    (DEP: DEP data)
%       ..          ..       ..     (rot: ROT data)
%       fn         depn     rotn
%(0)s which is flags to deactivate all iteration process.
%(1)s activate permittivity(e) for iteration. (2)s activate
%conductivity(s) iteration only. (3)s activate all
%iteration.

%Input the rotation data file into this program.
%File will be taken from directory of 'c:\depdata\'
%then the input file will be evaluated and
%the size of the (matrix) file will be known by (n) rows and (cols) columns.

file=input('ROT data fileroot=','s');
fullfile=['c:\depdata\',file];
```

```
fullfile=[fullfile,'.dat'];
eval(['load ',fullfile]);
eval(['rotdat=',file]);
[nrow, cols]=size(rotdat);

%To determine the therotrical analysis for ROT or DEP data

y=1;
n=0;
depd=input('DEP data to be analysed y/n =');
rotd=0;
if depd==n,

rotd=input('ROT data to be analysed y/n =');

end

%start to identify each parameters from the input file and
%to relocate the matrix

rotsimdat=rotdat;

%no. amount of radius (nr) require for (ns) shell ellipsoid model:
ns=rotsimdat(1,1);
nr=ns+1;

%use Temperature value to detemine the visocity of the suspending
%medium.  Visocity values vs Temp are from CRC Physics and Chemistry
%Handbook 72th edition.

Temp=rotsimdat(1,2);

Temp1=[0 1 2 3 4 5 6 7 8 9 10 11 12 13 14 15 16 17 18 19 20];
Temp2=[21 22 23 24 25 26 27 28 29 30 31 32 33 34 35 36 37 38 39 40];
Temp3=[41 42 43 44 45 46 47 48 49 50 51 52 53 54 55 56 57 58 59 60];
Temp4=[61 62 63 64 65 66 67 68 69 70 71 72 73 74 75 76 77 78 79 80];
Temp5=[81 82 83 84 85 86 87 88 89 90 91 92 93 94 95 96 97 98 99 100];
Tempv=[Temp1 Temp2 Temp3 Temp4 Temp5];

bv1=[1.787 1.728 1.671 1.618 1.567 1.519 1.412 1.428 1.386 1.346 1.307];
bv2=[1.271 1.235 1.202 1.169 1.139 1.109 1.081 1.053 1.027 1.002];
bv3=[0.9779 0.9548 .9325 .9111 .8904 .8705 .8513 .8327 .8148 .7975];
bv4=[.7808 .7647 .7491 .7340 .7194 .7052 .6915 .6783 .6654 .6529];
bv5=[.6408 .6291 .6178 .6067 .5960 .5856 .5755 .5656 .5561 .5468];
bv6=[.5378 .5290 .5204 .5121 .5040 .4961 .4884 .4809 .4736 .4665];
bv7=[.4596 .4528 .4462 .4398 .4335 .4278 .4213 .4155 .4098 .4042];
bv8=[.3987 .3934 .3882 .3831 .3781 .3732 .3684 .3638 .3592 .3547];
bv9=[.3503 .3460 .3418 .3377 .3337 .3297 .3259 .3221 .3184 .3147];
bv10=[.3111 .3076 .3042 .3008 .2975 .2942 .2911 .2879 .2849 .2818];
bv=[bv1 bv2 bv3 bv4 bv5 bv6 bv7 bv8 bv9 bv10];

for as=1:101,
  if Temp==Tempv(1,as),
    vis=bv(1,as);
  end
end
```

```
%Crossover frequency of DEP

fco=rotsimdat(1,3);
wfco=fco*2*pi;

%applied voltage(E) and scaling fractor(EL)
E=rotsimdat(2,3);
EL=rotsimdat(4+2*nr,3);


% radius for each shells for both x- and y-axis
%they are provided from the data file.
for rcount=1:1.0:nr,
   nr1=1+rcount;
   rx(1,rcount)=rotsimdat(nr1, 1);
   ry(1,rcount)=rotsimdat(nr1, 2);
end

%Volume of latex bead or cell; assuming ry=rz.
rxout=rx(1,1);
ryout=ry(1,1);
rzout=ry(1,1);
V=4/3*pi*(rxout*ryout*rzout);

%From paper Xiao-Feng Zhou et al BBA 1245(1995)85-93,
%parameters to calculate effective conductivity of latex bead.
%A, T magnitude and mean characteristic time-constant.
%From the same paper, alpha and Ks: surface conductance.

A=rotsimdat(2+nr,1);
T=rotsimdat(2+nr,2);
alpha=rotsimdat(3+nr,1);
Ks=rotsimdat(3+nr,2);

ksurfincrement1=0;
ksurfincrement2=0;

if rotsimdat(2+nr,3)==3,
   ksurfincrement1=ksurfincrement1+1;
   ksurfvar(1,ksurfincrement1)=A;
   ksurflag1(1,ksurfincrement1)=1;
   ksurfincrement1=ksurfincrement1+1;
   ksurfvar(1,ksurfincrement1)=T;
   ksurflag1(1,ksurfincrement1)=2;
elseif rotsimdat(2+nr,3)==0,
   ksurfincrement2=ksurfincrement2+1;
   ksurfset(1,ksurfincrement2)=A;
   ksutflag2(1,ksurfincrement2)=1;
   ksurfincrement2=ksurfincrement2+1;
   ksurfset(1,ksurfincrement2)=T;
   ksurflag2(1,ksurfincrement2)=2;
elseif rotsimdat(2+nr,3)==1,
   ksurfincrement1=ksurfincrement1+1;
   ksurfvar(1,ksurfincrement1)=A;
   ksurflag1(1,ksurfincrement1)=1;
```

```
  ksurfincrement2=ksurfincrement2+1;
  ksurfset(1,ksurfincrement2)=T;
  ksurflag2(1,ksurfincrement2)=2;
elseif rotsimdat(2+nr,3)==2,
  ksurfincrement2=ksurfincrement2+1;
  ksurfset(1,ksurfincrement2)=A;
  ksurflag2(1,ksurfincrement2)=1;
  ksurfincrement1=ksurfincrement1+1;
  ksurfvar(1,ksurfincrement1)=T;
  ksurflag1(1,ksurfincrement1)=2;
end


if rotsimdat(3+nr,3)==3,
  ksurfincrement1=ksurfincrement1+1;
  ksurfvar(1,ksurfincrement1)=alpha;
  ksurflag1(1,ksurfincrement1)=3;
  ksurfincrement1=ksurfincrement1+1;
  ksurfvar(1,ksurfincrement1)=Ks;
  ksurflag1(1,ksurfincrement1)=4;
elseif rotsimdat(3+nr,3)==0,
  ksurfincrement2=ksurfincrement2+1;
  ksurfset(1,ksurfincrement2)=alpha;
  ksurflag2(1,ksurfincrement2)=3;
  ksurfincrement2=ksurfincrement2+1;
  ksurfset(1,ksurfincrement2)=Ks;
  ksurflag2(1,ksurfincrement2)=4;
elseif rotsimdat(3+nr,3)==1,
  ksurfincrement1=ksurfincrement1+1;
  ksurfvar(1,ksurfincrement1)=alpha;
  ksurflag1(1,ksurfincrement1)=3;
  ksurfincrement2=ksurfincrement2+1;
  ksurfset(1,ksurfincrement2)=Ks;
  ksurflag2(1,ksurfincrement2)=4;
elseif rotsimdat(3+nr,3)==2,
  ksurfincrement2=ksurfincrement2+1;
  ksurfset(1,ksurfincrement2)=alpha;
  ksurflag2(1,ksurfincrement2)=3;
  ksurfincrement1=ksurfincrement1+1;
  ksurfvar(1,ksurfincrement1)=Ks;
  ksurflag1(1,ksurfincrement1)=4;
end

[ksurfn, ksurfcol]=size(ksurfvar);
ksurf1=ksurfcol;
ksurf2=4-ksurf1;

%relative permittivity and conductivity of each shells

eflagincrement=0;
eflagincrement2=0;
sflagincrement=0;
sflagincrement2=0;

%flag indicators for iteration would be put in an array matrix (flag)
%Array matrix (evar) stores permittivity parameters for iteration.
```

```
%Array matrix (svar) stores conductivity parameters for iteration.
%Array matrix (eset) and (sset) store perm. and cond. parameters as constant values.
%Array matrix (eflag1) indicates the location of each permittivity parameters to be iterated.
%Array matrix (eflag2) indicates the location of each permittivity parameters to stay as
constant.
%Array matrix (sflag1) indiactes the location of each conductivity parameters to be
iterated.
%Array matrix (sflag2) indiactes the location of each conductivity parameters to stay as
constant.

 for flagcount=nr+4:nr+3+nr,
   flag(1,flagcount-nr-3)=rotsimdat(flagcount,3);
end

for flagcount=nr+4:2+nr+3+nr,
   if rotsimdat(flagcount,3)==3,
      eflagincrement=eflagincrement+1;
      sflagincrement=sflagincrement+1;
      evar(1,eflagincrement)=rotsimdat(flagcount,1);
      svar(1,sflagincrement)=rotsimdat(flagcount,2);
      eflag1(1,eflagincrement)=flagcount-nr-3;
      sflag1(1,sflagincrement)=flagcount-nr-3;

   elseif rotsimdat(flagcount,3)==0,
      eflagincrement2=eflagincrement2+1;
      sflagincrement2=sflagincrement2+1;
      eset(1,eflagincrement2)=rotsimdat(flagcount,1);
      sset(1,sflagincrement2)=rotsimdat(flagcount,2);
      eflag2(1,eflagincrement2)=flagcount-nr-3;
      sflag2(1,sflagincrement2)=flagcount-nr-3;

   elseif rotsimdat(flagcount,3)==1,
      eflagincrement=eflagincrement+1;
      sflagincrement2=sflagincrement2+1;
      evar(1,eflagincrement)=rotsimdat(flagcount,1);
      sset(1,sflagincrement2)=rotsimdat(flagcount,2);
      eflag1(1,eflagincrement)=flagcount-nr-3;
      sflag2(1,sflagincrement2)=flagcount-nr-3;

   elseif rotsimdat(flagcount,3)==2,
      eflagincrement2=eflagincrement2+1;
      sflagincrement=sflagincrement+1;
      eset(1,eflagincrement2)=rotsimdat(flagcount,1);
      svar(1,sflagincrement)=rotsimdat(flagcount,2);
      sflag1(1,sflagincrement)=flagcount-nr-3;
      eflag2(1,eflagincrement2)=flagcount-nr-3;
   end
end

%To evaluate the amount of permittivity parameters to be iterated.

[evarn,evarcol]=size(evar);
enf1=evarcol;
enf2=nr-enf1;

%To evaluate the amount of conductivity parameters to be iterated.
```

```
[svarn,svarcol]=size(svar);
snf1=svarcol;
snf2=nr-snf1;

% relative permittivty of suspending medium
em=rotsimdat(4+nr*2,1);

% conductivity of suspending medium at 100kHz (in S/m)
smk=rotsimdat(4+nr*2,2);

%permittivity of free space
e0=8.825e-12;

%Generate the matrix ROTDATA or DEPDATA for autofiting program

p1=nr*2+5;
p2=nr*2+4;

na=nrow-p2;

for p=p1:nrow;
   rotatdat(p-p2,1) = rotsimdat(p,1);
   rotatdat(p-p2,2) = rotsimdat(p,2);
   rotatdat(p-p2,3) = rotsimdat(p,3);
end

%To sort out the order of the matrix for analysis.

for step1=na:-1:2,
 for step1=na:-1:2,
   step2=step1-1;
   if rotatdat(step1,1)>rotatdat(step2,1);

   tempera1=rotatdat(step1,1);
   rotatdat(step1,1)=rotatdat(step2,1);
   rotatdat(step2,1)=tempera1;

   tempera2=rotatdat(step1,2);
   rotatdat(step1,2)=rotatadat(step2,2);
   rotatdat(step2,2)=tempera2;

   tempera3=rotatdat(step1,3);
   rotatdat(step1,3)=rotatdat(step2,3);
   rotatdat(step2,3)=tempera3;

   elseif rotatdat(step1,1)<rotatdat(step2,1);
   end
 end
end

%frequency data point from the experiment

z1=rot90(rotatdat(:,1));

% scale frequency to 2.pi*Hz
```

```
wf=2*pi;
rotatdat(:,1)=rotatdat(:,1).*wf;
f=logspace(7,1,70);
w1=f.*wf;

if depd==1,

%experimental data points for dielectrophoresis
depdat=rotatdat(:,2);
z3=rot90(depdat);
z4=depdat;

elseif rotd==1,
%experimental data points for electrorotation:

rotdata=rotatdat(:,3);
z3=rot90(rotdata);
z4=rotdata;

end

%Deal to the problem in electrode polarisation effect at low frequency region.
%Derive correction factor "pf" by using polyfit to adjust rotation data with
%experimental conductance data

pff=[800e3 700e3 600e3 500e3 400e3 300e3 200e3 150e3 100e3 80e3 70e3 60e3...
    50e3 40e3 30e3 20e3 15e3 10e3 8e3 7e3 6e3 5e3 4e3 3e3 2e3 1.5e3 1e3...
    800 700 600 500 400 300 200 150 100];

bonesigma=[6.02 6.02 6.02 6.02 6.01 6.01 6.01 6.01 6.00 6.00 6.00 ...
        5.99 5.99 5.98 5.98 5.98 5.98 5.97 5.97 5.97 5.96 5.96 5.95...
        5.95 5.95 5.94 5.94 5.94 5.93 5.93 5.92 5.92 5.91 5.91 5.91 5.91].*1e-6;

pff=rot90(pff);
bonesigma=rot90(bonesigma);

bonesigma(:,1)=bonesigma(:,1)./max(bonesigma(:,1));

pfs=polyfit(log10(pff),bonesigma(:,1),6)

pfc=polyval(pfs,log10(z1));

pf=1./pfc;
pf=rot90(rot90(rot90(pf)));
z4=z4.*pf;


z2=rot90(z4);

%To creat a x-base line (lin) for the graph.
%w2 is not necessary, use w1 for calculation.

x1=logspace(0,7);
x2=x1;
w2=x1.*wf;
lin=x1.*0;
```

```
[B,nf]=size(x1);

%The following session is ROT simulation of best-fit graph

%curve fitting errors minimization logarithm

errsqu=0;
deperr=0;

rotparams=[EL evar svar ksurfvar];

global rotatdat rx ry rxout ryout vis eset sset depd rotd z4 ksurfset eflag1 eflag2 sflag1
sflag2 ksurflag1 ksurflag2 enf1 enf2 snf1 snf2 ksurf1 ksurf2 V em smk e0 w1 E nr ns nf Xx
Xy exr eyr Rf wfco deperr errsqu;

weight=1;
tracestatus=1;

nrotparams=fmins('ellipsof',rotparams,5e20,tracestatus);

%After iteration, all permittivities values are put in matrix(e).
%All conductivities values are put in matrix(s).

EL=nrotparams(1);
for ememcount=1:enf1,
   ememcount1=eflag1(1,ememcount);
   e(1, ememcount1)=abs(nrotparams(1,1+ememcount));
end
for esetcount=1:enf2,
   esetcount1=eflag2(1,esetcount);
   e(1,esetcount1)=eset(1,esetcount);
end
for smemcount=1:snf1,
   smemcount1=sflag1(1,smemcount);
   s(1,smemcount1)=abs(nrotparams(1,1+enf1+smemcount));
end
for ssetcount=1:snf2,
   ssetcount1=sflag2(1,ssetcount);
   s(1,ssetcount1)=sset(1,ssetcount);
end
for ksurfcountv=1:ksurf1,
   ksurfcountv1=ksurflag1(1,ksurfcountv);
   ksurface(1,ksurfcountv1)=abs(nrotparams(1,1+enf1+snf1+ksurfcountv));
end
for ksurfcounts=1:ksurf2,
   ksurfcounts1=ksurflag2(1,ksurfcounts);
   ksurface(1,ksurfcounts1)=ksurfset(1,ksurfcounts);
end

%ksurface=[A T alpha Ks]

nA=ksurface(1,1);
nT=ksurface(1,2);
nalpha=ksurface(1,3);
nKs =ksurface(1,4);
```

```
%complex permittivity of suspending medium

eme(1,:)=em*e0-j.*smk./w1(1,:);

%surface conductivity of latex bead under the influence of surface conductance.

sx=s;
sy=s;
spx=s(1,1)+(2*nKs)/rxout+nA./(1+(j.*w1.*nT).^nalpha);
spy=s(1,1)+(2*nKs)/ryout+nA./(1+(j.*w1.*nT).^nalpha);
sx=spx;
sy=spy;

%complex permittivity of each part of shell in term of matrix (er)
%From outermost shell parameters to innermost shell parameters.

for rol=1:nr,

etemp=e(1,rol);
sxtemp=sx(1,:);
sytemp=sy(1,:);
erxtemp=etemp*e0-j.*sxtemp./w1;
erytemp=etemp*e0-j.*sytemp./w1;
erx(rol,:)=erxtemp;
ery(rol,:)=erytemp;

end

%To determine the depolarizing factors of each shells along the x and y axis.
%From maximium outermost shell (radius) to the innermost shell (radius).

for POLAR=1:nr,
Qo(1,POLAR)=(rx(1,POLAR)./ry(1,POLAR));
Axu(1,POLAR)=((Qo(1,POLAR)./sqrt(Qo(1,POLAR).^2-
1)).*log(Qo(1,POLAR)+sqrt(Qo(1,POLAR).^2-1))-1);
Axd(1,POLAR)=(Qo(1,POLAR).^2-1);
Ax(1,POLAR)=Axu(1,POLAR)./Axd(1,POLAR);
Ay(1,POLAR)=(1-Ax(1,POLAR))./2;
end

%Ratio between x and y, z axis of each individual shell layers.
%From outermost shell radii to innermost shell radii.

if ns>0,

 for RAT=1:ns,

 v(1,RAT)=(rx(1,RAT).*(ry(1,RAT)).^2)./(rx(1,RAT+1).*(ry(1,RAT+1)).^2);

 end

%The effective complex permittivity (dielectric constant) in the x-axis of the ellipsoid
model.
% The calculation is from innermost shell parameters to outermost shell parameters.

 for CPR=ns:-1:1,
```

```
 EPXU(CPR,:)=erx(CPR,:)+(erx(CPR+1,:)-erx(CPR,:)).*(Ax(1,CPR+1)+v(1,CPR).*(1-
Ax(1,CPR)));
 EPXD(CPR,:)=erx(CPR,:)+(erx(CPR+1,:)-erx(CPR,:)).*(Ax(1,CPR+1)-
v(1,CPR).*Ax(1,CPR));
 eex(CPR,:)=erx(CPR,:).*(EPXU(CPR,:)./EPXD(CPR,:));
 erx(CPR,:)=eex(CPR,:);

 end

%Effective complex permittivity on the X-axis:

 exr=erx(1,:);

elseif ns==0,

 exr=erx;

end

%The effective complex permittivity (dielectric constant) in the y-axisof the ellipsoid
model.
%The calculation is from innermost shell parameters to outermost shell parameters.

if ns>0,

 for CPY=nr-1:-1:1,

 EPYU(CPY,:)=ery(CPY,:)+(ery(CPY+1,:)-ery(CPY,:)).*(Ay(1,CPY+1)+v(1,CPR).*(1-
Ay(1,CPY)));
 EPYD(CPY,:)=ery(CPY,:)+(ery(CPY+1,:)-ery(CPY,:)).*(Ay(1,CPY+1)-
v(1,CPY).*Ay(1,CPY));
 eey(CPY,:)=ery(CPY,:).*(EPYU(CPY,:)./EPYD(CPY,:));
 ery(CPY,:)=eey(CPY,:);

 end

%Effective complex permittivity on the Y-axis:

 eyr=ery(1,:);

elseif ns==0,

 eyr=ery;

end

%The X term from the modelin x-axis parameter:

Xx=(exr(1,:)-eme(1,:))./((exr(1,:)-eme(1,:)).*Ax(1,1)+eme(1,:));

%The X term from the model in y-axis parameter:

Xy=(eyr(1,:)-eme(1,:))./((eyr(1,:)-eme(1,:)).*Ay(1,1)+eme(1,:));
```

```
if rotd==1,
%The electrical torque <Tc> of the multishelled ellipsoid:

Tc=0.5.*V.*eme.*(imag(Xx)+imag(Xy)).*E^2;


%The Rf factor for the stationary angular velocity:

Rf=2.*V.*vis.*((rxout^2+ryout^2)./(rxout^2.*Ax(1,1)+ryout^2.*Ay(1,1)));

%The stationary angular velocity of the ellipsoid model:

wc=0.5.*(V./Rf).*em.*(imag(Xx)+imag(Xy)).*E^2;

wc=wc.*(-1).*EL;

elseif depd==1,

Depf=0.5.*(V./Rf).*em.*(real(Xx)+real(Xy)).*E^2.*EL;

wc=Depf;

end

semilogx(f,wc,z1,z2,'*',z1,z3,'o');

%To display permittivities values matrix(e)
%and conductivities values matrix(s) in the graph,
%and in matlab editor as as well.
esca='';
ssca='';
for dply=1:nr,
   epst=['e',int2str(dply),'=',num2str(e(1,dply))];
   sps=['s',int2str(dply),'=',num2str(s(1,dply))];
   disp(epst);
   disp(sps);
   esca=[esca,sprintf('e%1.0f=%g ',dply,e(1,dply))];
   ssca=[ssca,sprintf('s%1.0f=%gS/m ',dply,s(1,dply))];
end

%To display radii values of the ellipsical model in the graph,
%and in matlab editor as as well.(x parameter)
rxsca='';
for rcount=1:nr,
   nr1=rcount;
   rxps=['rx',int2str(nr1),'=',num2str(rx(1,rcount))];
   disp(rxps);
   rsca=[rxsca,sprintf('rx%1.0f=%gm ',nr1,rx(1,rcount))];
end


%To display radii values of the ellipsical model in the graph,
%and in matlab editor as as well.(y parameter)
rysca='';
for rcount=1:nr,
```

```
   nr1=rcount;
   ryps=['ry',int2str(nr1),'=',num2str(ry(1,rcount))];
   disp(ryps);
   rysca=[rysca,sprintf('ry%1.0f=%gm ',nr1,ry(1,rcount))];
end

%To display those remained parameters in the graph
%and in matlab editor as as well.
a1=num2str(E);
a2=num2str(EL);
a3=num2str(Temp);
a5=num2str(smk);
a6=num2str(ksurface(1,1));
a7=num2str(ksurface(1,2));
a8=num2str(ksurface(1,3));
a9=num2str(ksurface(1,4));
da1=['Applied Voltage=',a1];
da2=['Scale=',a2];
da3=['Temp=',a3];
da5=['SuspendingMedium cond.=',a5];
da6=['A=',a6];
da7=['T=',a7];
da8=['alpha=',a8];
da9=['Ks=',a9];
disp(da1);
disp(da2);
disp(da3);
disp(da5);
disp(da6);
disp(da7);
disp(da8);
disp(da9);

%Plot graph

rshell=nr-1;
title1=(['Comparison of ROTATION Data with Best Fit of ',num2str(rshell),' Shell
Model']);
title2=(['Applied Voltage=',num2str(E),'V, EL=',num2str(EL),',
Temp=',num2str(Temp),'C']);
title3=(['Suspending Medium Cond.=',num2str(smk),'S/m']);
%text(0.25,1.0,title1,'sc');
%text(0.1,0.95,title2,'sc');
%text(0.12,0.9,esca,'sc');
%text(0.12,0.85,ssca,'sc');
%text(0.12,0.8,rsca,'sc');
%text(0.12,0.75,edsca,'sc');
%text(0.12,0.7,title3,'sc');
xlabel('Frequency, (Hz)');
ylabel('ROTATION Velocity (/sec/V^2)');
%grid;
```

3.7.4 Appendix 3.2b

```
%"Program written by Ka Lok Chan Program "
%ITERATION FUNCTION FOR GENERAL PUTPOSE FITTING PROGRAM FOR
ELLIPSOIDAL MODEL
function y=ellipsof(rotparams)

% ROTAFIT error function used for ROT surface fitting based
%on the n shells or unlimited number of shells
%      model of the cell
%
%      rotatdat is a matrix containing rot data in 3 columns:
%      [Angular frequency in Hz;   Conductivity in S/m;   ROT rate]
%
%      rotparams contains the guesses:
%      [scalefactor;   Emembrane';   Smembrane]

global rotatdat rx ry rxout ryout vis eset sset depd rotd z4 ksurfset eflag1 eflag2 sflag1
sflag2 ksurflag1 ksurflag2 enf1 enf2 snf1 snf2 ksurf1 ksurf2 V em smk e0 w1 E nr ns nf Xx
Xy exr eyr Rf fco wfco deperr errsqu;

EL=abs(rotparams(1));
for ememcount=1:enf1,
   ememcount1=eflag1(1,ememcount);
   e(1,ememcount1)=abs(rotparams(1,1+ememcount));
end
for esetcount=1:enf2,
   esetcount1=eflag2(1,esetcount);
   e(1,esetcount1)=eset(1,esetcount);
end
for smemcount=1:snf1,
   smemcount1=sflag1(1,smemcount);
   s(1,smemcount1)=abs(rotparams(1,1+enf1+smemcount));
end
for ssetcount=1:snf2,
   ssetcount1=sflag2(1,ssetcount);
   s(1,ssetcount1)=sset(1,ssetcount);
end
for ksurfcountv=1:ksurf1,
   ksurfcountv1=ksurflag1(1,ksurfcountv);
   ksurface(1,ksurfcountv1)=abs(rotparams(1,1+enf1+snf1+ksurfcountv));
end
for ksurfcounts=1:ksurf2,
   ksurfcounts1=ksurflag2(1,ksurfcounts);
   ksurface(1,ksurfcounts1)=ksurfset(1,ksurfcounts);
end

%matrix for ksurface conductance parameters is reformed.
%ksurface=[A T alpha Ks]

A=ksurface(1,1);
T=ksurface(1,2);
alpha=ksurface(1,3);
Ks=ksurface(1,4);
```

```
[na, ncols]=size(rotatdat);
w=rot90(rotatdat(:,1));
data=rot90(z4);

errsqu=0;

%complex permittivity of suspending medium

eme(1,:)=em*e0-j.*smk./w(1,:);

%surface conductivity of latex bead under the influence of surface conductance.

sx=s;
sy=s;
spx=s(1,1)+(2*Ks)/rxout+A./(1+(j.*w.*T).^alpha);
spy=s(1,1)+(2*Ks)/ryout+A./(1+(j.*w.*T).^alpha);
sx=spx;
sy=spy;

%complex permittivity of each part of shell in term of matrix (er)
%From outermost shell parameters to innermost shell parameters.

for rol=1:nr,

etemp=e(1,rol);
sxtemp=sx(1,:);
sytemp=sy(1,:);
erxtemp=etemp*e0-j.*sxtemp./w;
erytemp=etemp*e0-j.*sytemp./w;
erx(rol,:)=erxtemp;
ery(rol,:)=erytemp;

end

%To determine the depolarizing factors of each shells along the x and y axis.
%From maximium outermost shell (radius) to the innermost shell (radius).


for POLAR=1:nr,

Qo(1,POLAR)=(rx(1,POLAR)./ry(1,POLAR));

Axu(1,POLAR)=((Qo(1,POLAR)./sqrt(Qo(1,POLAR).^2-
1)).*log(Qo(1,POLAR)+sqrt(Qo(1,POLAR).^2-1))-1);

Axd(1,POLAR)=(Qo(1,POLAR).^2-1);

Ax(1,POLAR)=Axu(1,POLAR)./Axd(1,POLAR);

Ay(1,POLAR)=(1-Ax(1,POLAR))./2;

end

%Ratio between x and y, z axis of each individual shell layers.
%From outermost shell radii to innermost shell radii.
```

```
if ns>0,

 for RAT=1:ns,
 v(1,RAT)=(rx(1,RAT).*(ry(1,RAT)).^2)./(rx(1,RAT+1).*(ry(1,RAT+1)).^2);
 end

%The effective complex permittivity (dielectric constant) in the x-axis of the ellipsoid
model.
% The calculation is from innermost shell parameters to outermost shell parameters.

 for CPR=nr-1:-1:1,

 EPXU(CPR,:)=erx(CPR,:)+(erx(CPR+1,:)-erx(CPR,:)).*(Ax(1,CPR+1)+v(1,CPR).*(1-
Ax(1,CPR)));

 EPXD(CPR,:)=erx(CPR,:)+(erx(CPR+1,:)-erx(CPR,:)).*(Ax(1,CPR+1)-
v(1,CPR).*Ax(1,CPR));

 eex(CPR,:)=erx(CPR,:).*(EPXU(CPR,:)./EPXD(CPR,:));

 erx(CPR,:)=eex(CPR,:);

 end

%Effective complex permittivity on the X-axis:

 exr=erx(1,:);
elseif ns==0,
 exr=erx;
end

%The effective complex permittivity (dielectric constant) in the y-axisof the ellipsoid
model.
%The calculation is from innermost shell parameters to outermost shell parameters.

if ns>0,

 for CPY=nr-1:-1:1,

 EPYU(CPY,:)=ery(CPY,:)+(ery(CPY+1,:)-ery(CPY,:)).*(Ay(1,CPY+1)+v(1,CPR).*(1-
Ay(1,CPY)));

 EPYD(CPY,:)=ery(CPY,:)+(ery(CPY+1,:)-ery(CPY,:)).*(Ay(1,CPY+1)-
v(1,CPY).*Ay(1,CPY));

 eey(CPY,:)=ery(CPY,:).*(EPYU(CPY,:)./EPYD(CPY,:));

 ery(CPY,:)=eey(CPY,:);

 end

%Effective complex permittivity on the Y-axis:

 eyr=ery(1,:);
elseif ns==0,
```

```
 eyr=ery;
end

%The X term from the model in x-axis parameter:

Xx=(exr(1,:)-eme(1,:))./((exr(1,:)-eme(1,:)).*Ax(1,1)+eme(1,:));

%The X term from the model in y-axis parameter:

Xy=(eyr(1,:)-eme(1,:))./((eyr(1,:)-eme(1,:)).*Ay(1,1)+eme(1,:));

if rotd==1,
%The electrical torque <Tc> of the multishelled ellipsoid:

%Tc=0.5.*V.*eme.*(imag(Xx)+imag(Xy)).*E^2.*EL;

%The Rf factor for the stationary angular velocity:

Rf=2.*V.*vis.*((rxout^2+ryout^2)./(rxout^2.*Ax(1,1)+ryout^2.*Ay(1,1)));

%The stationary angular velocity of the ellipsoid model:

wc=0.5.*(V./Rf).*em.*(imag(Xx)+imag(Xy)).*E^2;

wc=wc.*(-1).*EL;

elseif depd==1,

Depf=0.5.*(V./Rf).*em.*(real(Xx)+real(Xy)).*E^2.*EL;
wc=Depf;

end

rata=wc;

% To calculate the percentage of error between the experimental data and the simulated values.

   err=data-rata;
   errsqu=(norm(err))^2;

%To calculate the percentage of error in crossover frequency are as followed

if fco==NaN,
elseif fco>0,

%complex permittivity of suspending medium for crossover frequency

emefc=em*e0-j.*smk./wfco;

%surface conductivity of latex bead under the influence of surface conductance.
%crossover frequency

sx=s;
sy=s;
spxfc=s(1,1)+(2*Ks)/rxout+A./(1+(j.*wfco.*T).^alpha);
```

```
spyfc=s(1,1)+(2*Ks)/ryout+A./(1+(j.*wfco.*T).^alpha);
sxfc=spxfc;
syfc=spyfc;

%complex permittivity of each part of shell in term of matrix (er)
%From outermost shell parameters to innermost shell parameters.

for rol=1:nr,

etemp=e(1,rol);
sxtemp=sx(1,:);
sytemp=sy(1,:);
efxtemp=etemp*e0-j.*sxtemp./wfco;
efytemp=etemp*e0-j.*sytemp./wfco;
efx(rol,:)=efxtemp;
efy(rol,:)=efytemp;

end

%Ratio between x and y, z axis of each individual shell layers.
%From outermost shell radii to innermost shell radii.

if ns>0,

 for RAT=1:ns,

 v(1,RAT)=(rx(1,RAT).*(ry(1,RAT)).^2)./(rx(1,RAT+1).*(ry(1,RAT+1)).^2);

 end

%The effective complex permittivity (dielectric constant) in the x-axis of the ellipsoid
model.
% The calculation is from innermost shell parameters to outermost shell parameters.

 for CPR=nr-1:-1:1,

 EFXU(CPR,:)=efx(CPR,:)+(efx(CPR+1,:)-efx(CPR,:)).*(Ax(1,CPR+1)+v(1,CPR).*(1-
Ax(1,CPR)));
 EFXD(CPR,:)=efx(CPR,:)+(efx(CPR+1,:)-efx(CPR,:)).*(Ax(1,CPR+1)-
v(1,CPR).*Ax(1,CPR));
 eex(CPR,:)=efx(CPR,:).*(EFXU(CPR,:)./EFXD(CPR,:));
 efx(CPR,:)=eex(CPR,:);

 end

%Effective complex permittivity on the X-axis:

 exf=efx(1,:);

elseif ns==0,

 exf=efx;

end
```

```
%The effective complex permittivity (dielectric constant) in the y-axisof the ellipsoid
model.
%The calculation is from innermost shell parameters to outermost shell parameters.

if ns>0,

 for CPY=nr-1:-1:1,

 EFYU(CPY,:)=efy(CPY,:)+(efy(CPY+1,:)-efy(CPY,:)).*(Ay(1,CPY+1)+v(1,CPR).*(1-
Ay(1,CPY)));
 EFYD(CPY,:)=efy(CPY,:)+(efy(CPY+1,:)-efy(CPY,:)).*(Ay(1,CPY+1)-
v(1,CPY).*Ay(1,CPY));
 eey(CPY,:)=efy(CPY,:).*(EFYU(CPY,:)./EFYD(CPY,:));
 eFy(CPY,:)=eey(CPY,:);

 end

%Effective complex permittivity on the Y-axis:

 eyf=efy(1,:);
elseif ns==0,
 eyf=efy;
end

%The X term from the modelin x-axis parameter:

Fx=(efr(1,:)-emefc(1,:))./((efr(1,:)-emefc(1,:)).*Ax(1,1)+emefc(1,:));

%The X term from the model in y-axis parameter:

Fy=(efr(1,:)-emefc(1,:))./((efr(1,:)-emefc(1,:)).*Ay(1,1)+emefc(1,:));

%The dielectrophoretic force should be zero at crossover frequency point.

deperr=(real(Fx)+real(Fy)).^2;

end

y=errsqu+deperr;
```

3.7.5 Appendix 3.3a

Testing program for the rotation fitting program (Single spherical shell model)

```
%Repeatedly testing program for rotation fitting program
rand('uniform');
global e0 eg1 sg1 eg2 sg2 em smvalue r2 r1 rotatdat r d eset sset eflag1 eflag2 sflag1 sflag2
enf1 enf2 snf1 snf2 V em e0 E nr nf wfco fco errsqu deperr maxlim minlim depweight
rotweight;

depweight=1;
rotweight=1;
```

```
turn=input('number of turn to be run =');

for cycle=1:turn,

%from gensim.m program
% ROT data generation program
% r is the cytoplasmic radius. d is the membrance thickness.
% V is the cytoplasmic volumn.
%simmat is tha matrix to store variables and ROT data.

simmat=[];
simmat='';
yo=[];

%number of radii = number of shell + 1
nr=2;
simmat(1,1)=nr;

%temperture is 21C
simmat(1,2)=21;

r=2.8004e-6;
r2=r;
d=4.5E-09;
r1=r2-d;
V=4/3*pi*r^3;
k1=(r/(r-d))^3;

%initial guess of crossover frequency in kHz
cof=100;
cf=cof*1e3;

%location of outer radus in the matrix
simmat(2,1)=r2;
simmat(2,2)=d;

%maxlimit and minlimit of medium permittivity and their location
maxlimit=82;
minlimit=78;
mnloc=nr./2+2;
simmat(mnloc,1)=maxlimit;
simmat(mnloc,2)=minlimit;

% sg1 and eg1 are cytoplasmic conductivity and permittivity
% respectivity.

sga=0.0135+1.4565.*rand(1);
sg1=abs(sga);
ega=78+4.*rand(1);
eg1=abs(ega);

% location of internal permittivity and conductivity
%(80 instead of eg1) and 1.47 instead of sg1 as initial guesses
stloc=mnloc+1;
simmat(stloc,1)=80;
```

```
simmat(stloc,2)=1.47;
%flag to active iteration for (eg1) and sg2
simmat(stloc,3)=3;

% sg2 and eg2 are cytoplasmic membrane conductivity and
% permittivity respectivity.

sgb=2.1E-07+1.979e-5.*rand(1);
sg2=abs(sgb);
egb=1+9.*rand(1);
eg2=abs(egb);

%location of membrane permittivity and conductivity
%4 instead of eg2 and 2.1e-6 instead of sg2 as initial guesses
ndloc=mnloc+2;
simmat(ndloc,1)=4;
simmat(ndloc,2)=1.0e-5;
%flag to active iteration for eg2 and sg2
simmat(ndloc,3)=3;

% em is suspending medium permittivity and E is the scaling
% factor. e0 is permittivity of free space. EL is applied
% voltage.

em=80;
ELa=1e11+9e11.*rand(1);
EL=abs(ELa);
%EL=5e12;
e0=8.825E-12;
E=0.9;

%location of for scaling factor EL
%5e12 instead of EL as initial guess
simmat(2,3)=E;
simmat(3,3)=5e12;

%suspecting medium conductivity in S/m

smvalue=1.35e-2;
b=[1:17];
c=rot90(b./b);
sgm=smvalue.*c;
smdisp=135.*c;

%location of sm in the simmat matrix
rowsta=nr./2+2+nr+1;
rowend=nr./2+2+nr+17;
for rowrun=rowsta:rowend,
   smrow=rowrun-(nr./2+2+nr);
   simmat(rowrun,2)=smdisp(smrow,1);
end

%to calculate the crossover frequency value

cfparams=[cf];
```

```
tracestatus=1;

ncfparams=fmins('rcfover',cfparams,5e9,tracestatus);

%After iteration, crossover frequency value is generated

cf=ncfparams(1)


%position of crossover frequency
cfkHz=cf./1000;
simmat(1,3)=cfkHz;
% ROT simulation of best-fit graph
%logspace frequencies are originally in Hz,
%but in this contest, the frequencies values are in kHz.
x1=logspace(1,5,17);
%xg2 is in kHz.
xg2=x1;
x3=flipud(rot90(xg2));
w2=x3.*2000.*pi;
lin=x1.*0;


eg1r=eg1*e0-j*sg1./w2;
eg2r=eg2*e0-j*sg2./w2;
egme=em*e0-j*sgm./w2;


eg1u=(k1-(eg1r-eg2r)./(eg1r+2.*eg2r));
eg1e=eg2r.*(k1+2.*(eg1r-eg2r)./(eg1r+2.*eg2r))./eg1u;

egpe=eg1e;
cmf=(egpe-egme)./(egpe+2.*egme);
dm=3*V*E*em*e0.*cmf;
DF=real(dm).*(norm(E).^2)./2*E;
y2=(EL^2).*(DF);
RT=-imag(dm).*E;
y1=(EL^2).*(RT);

% This section determines whether noise is introduced to the ROT data or not!
%This does not give noise to the ROT data

%RTnos=y1;

%This section introduced noise to the ROT data.
%Gaussian noise distribution
rand('normal');
for corrupt=1:17;

% 3% noise given by (y1(corrupt,1)./33.33)*rand(1)
% 5% noise given by (y1(corrupt,1)./20)*rand(1)
% 10% noise giveb by (y1(corrupt,1)./10)*rand(1)

  RTnos(corrupt,1)=y1(corrupt,1)+(y1(corrupt,1)./10)*rand(1);
end
```

```
rand('uniform');
%values of ROT data, frequency points and their locations
rstart=nr./2+2+nr+1;
rotend=nr./2+2+nr+17;
for rotrun=rstart:rotend,
   rotrow=rotrun-(nr./2+2+nr);
    simmat(rotrun,1)=x3(rotrow,1);
    simmat(rotrun,3)=RTnos(rotrow,1);
end

%To store similated data in a data.dat file
trial(cycle,1)=eg1;
trial(cycle,2)=sg1;
trial(cycle,3)=eg2;
trial(cycle,4)=sg2;
trial(cycle,5)=EL;

save c:\depdata\tempdat.dat simmat /ascii

%From ROTFITX.M general purpose fitting program

[n, cols]=size(simmat);


rotsimdat=simmat;

%no. amount of radius require for (n-1) shell model:
nr=rotsimdat(1,1);
Temp=rotsimdat(1,2);
CrossoverFrequency=rotsimdat(1,3);
fco=CrossoverFrequency*1000;
wfco=fco*2*pi;

%applied voltage(E) and scaling fractor(EL)
E=rotsimdat(2,3);
EL=rotsimdat(3,3);

%maximum and mininium limit of medium relative permittivity
%normally, it is from 78 to 82
maxlim=rotsimdat(2+nr/2,1);
minlim=rotsimdat(2+nr/2,2);

% radius for each shells and thickness of the membrane
%they are provided from the data file.
for rcount=2:2.0:nr,
   nr1=rcount./2;
   r(1,rcount)=rotsimdat(1+nr1, 1);
   d(1,rcount)=rotsimdat(1+nr1, 2);
   r(1,rcount-1)=r(1,rcount)-d(1,rcount);
end

%Volume of cell or vesicle
rexe=r(1,nr);
V=4/3*pi*(rexe)^3

%relative permittivity and conductivity of each shells
```

```
eflagincrement=0;
eflagincrement2=0;
sflagincrement=0;
sflagincrement2=0;

%flag indicators for iteration is put in an array matrix (flag)
%Array matrix (evar) stores permittivity parameters for iteration.
%Array matrix (svar) stores conductivity parameters for iteration.
%Array matrix (eset) and (sset) store perm. and cond. parameters as constant values.

for flagcount=nr/2+2+1:nr/2+2+nr,
   flag(1,flagcount-nr/2-2)=rotsimdat(flagcount,3);
end

for flagcount=2+nr/2+1:2+nr/2+nr,
   if rotsimdat(flagcount,3)==3,
      eflagincrement=eflagincrement+1;
      sflagincrement=sflagincrement+1;
      evar(1,eflagincrement)=rotsimdat(flagcount,1);
      svar(1,sflagincrement)=rotsimdat(flagcount,2);
      eflag1(1,eflagincrement)=flagcount-nr/2-2;
      sflag1(1,sflagincrement)=flagcount-nr/2-2;

   elseif  rotsimdat(flagcount,3)==0,
      eflagincrement2=eflagincrement2+1;
      sflagincrement2=sflagincrement2+1;
      eset(1,eflagincrement2)=rotsimdat(flagcount,1);
      sset(1,sflagincrement2)=rotsimdat(flagcount,2);
      eflag2(1,eflagincrement2)=flagcount-nr/2-2;
      sflag2(1,sflagincrement2)=flagcount-nr/2-2;

   elseif  rotsimdat(flagcount,3)==1,
      eflagincrement=eflagincrement+1;
      sflagincrement2=sflagincrement2+1;
      evar(1,eflagincrement)=rotsimdat(flagcount,1);
      sset(1,sflagincrement2)=rotsimdat(flagcount,2);
      eflag1(1,eflagincrement)=flagcount-nr/2-2;
      sflag2(1,sflagincrement2)=flagcount-nr/2-2;

   elseif  rotsimdat(flagcount,3)==2,
      eflagincrement2=eflagincrement2+1;
      sflagincrement=sflagincrement+1;
      eset(1,eflagincrement2)=rotsimdat(flagcount,1);
      svar(1,sflagincrement)=rotsimdat(flagcount,2);
      sflag1(1,sflagincrement)=flagcount-nr/2-2;
      eflag2(1,eflagincrement2)=flagcount-nr/2-2;
   end
end

[evarn,evarcol]=size(evar);
enf1=evarcol;
enf2=nr-enf1;

[svarn,svarcol]=size(svar);
snf1=svarcol;
```

```
snf2=nr-snf1;

% relative permittivty of suspending medium
em=80;

%permittivity of free space
e0=8.825e-12;

%Generate the matrix ROTDATA for autofiting program

p1=nr/2+3+nr;
p2=nr/2+2+nr;

na=n-p2;

for p=p1:n;
   rotatdat(p-p2,1) = rotsimdat(p,1);
   rotatdat(p-p2,2) = rotsimdat(p,2);
   rotatdat(p-p2,3) = rotsimdat(p,3);
end


%frequency data point from the experiment
z1=rot90(rotatdat(:,1));
z2=z1;

% scale frequency to 2.pi*Hz and conductivity to S/m
wf=2000*pi;
rotatdat(:,2)=rotatdat(:,2).*1e-4;
rotatdat(:,1)=rotatdat(:,1).*wf;
w1=rot90(rotatdat(:,1));

%suspending medium conductivity
%sm=rot90(rotatdat(:,2));
sm=sum(rotatdat(:,2))/na;

%The following session is ROT simulation of best-fit graph

x1=logspace(0,6);
x2=x1;
w2=x1.*wf;
lin=x1.*0;
[B,nf]=size(x1);

%curve fitting errors minimization logarithm

errsqu=0;
deperr=0;
rotparams=[EL evar svar];


tracestatus=1;

nrotparams=fmins('rotafitx',rotparams,5e20,tracestatus);

%After iteration, all permittivities values are put in matrix(e).
```

```
%All conductivities values are put in matrix(s).

EL=abs(nrotparams(1));
for ememcount=1:enf1,
   ememcount1=eflag1(1,ememcount);
%   e(1, ememcount1)=abs(nrotparams(1,ememcount));
   e(1, ememcount1)=abs(nrotparams(1,1+ememcount));
end
for esetcount=1:enf2,
   esetcount1=eflag2(1,esetcount);
   e(1,esetcount1)=eset(1,esetcount);
end
for smemcount=1:snf1,
   smemcount1=sflag1(1,smemcount);
%   s(1,smemcount1)=abs(nrotparams(1,enf1+smemcount));
   s(1,smemcount1)=abs(nrotparams(1,1+enf1+smemcount));
end
for ssetcount=1:snf2,
   ssetcount1=sflag2(1,ssetcount);
   s(1,ssetcount1)=sset(1,ssetcount);
end

trial(cycle,6)=e(1,1);
trial(cycle,7)=s(1,1);
trial(cycle,8)=e(1,2);
trial(cycle,9)=s(1,2);
trial(cycle,10)=EL;
trial(cycle,11)=errsqu;
end
save c:\depdata\destiny.dat trial /ascii
```

3.7.6 Appendix 3.3b

```
function yo=rcfover(cfparams)

global e0 eg1 sg1 eg2 sg2 em smvalue r2 r1 rotatdat r d eset sset eflag1 eflag2 sflag1 sflag2
enf1 enf2 snf1 snf2 V em e0 E nr nf wfco fco errsqu deperr maxlim minlim depweight
rotweight;



% CROSSOVER error function is used to calculate the crossover frequency
% of the similated data.

cf=abs(cfparams(1));

cferrsqu=0;

% suspending medium complex permittivity
smd=smvalue;
emcf=em*e0-j*smd./(2*pi*cf);
```

```
%e1p is the complex permittivity of internal internal medium of vesicle
%e2p is the complex permittivity ot the vesicle's membrane

e1p=eg1*e0-j*sg1./(2*pi*cf);
e2p=eg2*e0-j*sg2./(2*pi*cf);

%ep is complex permittivity of partical. At the crossover frequency point,
% the real part of the Clausius-Mossotti factor (depco) is equal zero.
ep=e2p.*((r2./r1)^3+2.*(e1p-e2p)./(e1p+2.*e2p))./((r2./r1)^3-(e1p-e2p)./(e1p+2*e2p));
depcfo=real((ep-emcf)./(ep+2*emcf));
cferrsqu=depcfo^2;

end

yo=cferrsqu;
```

3.7.7 Appendix 3.4a

Testing program for ellipsoidal shell model

```
%Repeatedly testing program for rotation fitting program
rand('uniform');
global e0 eg1 sg1 eg2 sg2 em smvalue r2 r1 rotatdat r d eset sset eflag1 eflag2 sflag1 sflag2
enf1 enf2 snf1 snf2 V em e0 E nr nf wfco fco errsqu deperr maxlim minlim depweight
rotweight;

turn=input('number of turn to be run =');

for cycle=1:turn,

%from gensim.m program
% ROT data generation program
% r is the cytoplasmic radius. d is the membrance thickness.
% V is the cytoplasmic volumn.
%simmat is tha matrix to store variables and ROT data.

simmat=[];
simmat='';
yo=[];

%number of shell = number of radius - 1
nr=1;
ns=0;

%location of shell number in matrix
simmat(1,1)=ns;

%temperture is 21C
Temp=21;
simmat(1,2)=Temp;

%initial guess of crossover frequency in kHz
cof=NaN;
```

```
simmat(1,3)=cof;

%location of outer radus in the matrix
rx=3.00e-6;
ry=200e-6;
rxout=rx;
ryout=ry;
simmat(2,1)=rx;
simmat(2,2)=ry;

%Volume of latex bead or cell; assuming ry=rz.
rxout=rx;
ryout=ry;
rzout=ry;
reV=4/3*pi*(rxout*ryout*rzout);


%location of for scaling factor E

E=14.142;
simmat(2,3)=E;

%location of A, T, alpha and Ks

reA=0.001+0.01.*rand(1)+0.1.*rand(1)+1.*rand(1);
reT=0.001+0.01.*rand(1)+0.1.*rand(1)+1.*rand(1)+10.*rand(1);
simmat(3,1)=reA;
simmat(3,2)=reT;
simmat(3,3)=3;

realpha=0.7+0.2.*rand(1);
reKs=5e-10+3e-10.*rand(1);
simmat(4,1)=realpha;
simmat(4,2)=reKs;
simmat(4,3)=3;

% ep0 and sb(0) are latex bead bulk permittivity and conductivity
% respectivity. Also, locations of these ep(0) and sb(0) in the matrix

ep0=3.5;
sb0=10e-9;
simmat(5,1)=ep0;
simmat(5,2)=sb0;
simmat(5,3)=0;

%location of medium permittivity and conductivity

em=80;
smk=5.54e-4;
simmat(6,1)=em;
simmat(6,2)=smk;

e0=8.825E-12;

%EL as scaling factor.
%4.80e-6 instead of EL as initial guess
```

```
ELa=4.80e-6+4.80e-6.*rand(1);
EL=abs(ELa);

simmat(6,3)=EL;

b=[1:37];
c=rot90(b./b);

% ROT simulation of best-fit graph
%logspace frequencies are originally in Hz,
%but in this contest, the frequencies values are in Hz.
x1=logspace(2,6.7,37);
%xg2 is in Hz.
xg2=x1;
x3=rot90(rot90(xg2));
w2=x3.*2.*pi;
lin=x1.*0;

%use Temperature value to detemine the visocity of the suspending
%medium.  Visocity values vs Temp are from CRC Physics and Chemistry
%Handbook 72th edition.

Temp1=[0 1 2 3 4 5 6 7 8 9 10 11 12 13 14 15 16 17 18 19 20];
Temp2=[21 22 23 24 25 26 27 28 29 30 31 32 33 34 35 36 37 38 39 40];
Temp3=[41 42 43 44 45 46 47 48 49 50 51 52 53 54 55 56 57 58 59 60];
Temp4=[61 62 63 64 65 66 67 68 69 70 71 72 73 74 75 76 77 78 79 80];
Temp5=[81 82 83 84 85 86 87 88 89 90 91 92 93 94 95 96 97 98 99 100];
Tempv=[Temp1 Temp2 Temp3 Temp4 Temp5];

bv1=[1.787 1.728 1.671 1.618 1.567 1.519 1.412 1.428 1.386 1.346 1.307];
bv2=[1.271 1.235 1.202 1.169 1.139 1.109 1.081 1.053 1.027 1.002];
bv3=[0.9779 0.9548 .9325 .9111 .8904 .8705 .8513 .8327 .8148 .7975];
bv4=[.7808 .7647 .7491 .7340 .7194 .7052 .6915 .6783 .6654 .6529];
bv5=[.6408 .6291 .6178 .6067 .5960 .5856 .5755 .5656 .5561 .5468];
bv6=[.5378 .5290 .5204 .5121 .5040 .4961 .4884 .4809 .4736 .4665];
bv7=[.4596 .4528 .4462 .4398 .4335 .4278 .4213 .4155 .4098 .4042];
bv8=[.3987 .3934 .3882 .3831 .3781 .3732 .3684 .3638 .3592 .3547];
bv9=[.3503 .3460 .3418 .3377 .3337 .3297 .3259 .3221 .3184 .3147];
bv10=[.3111 .3076 .3042 .3008 .2975 .2942 .2911 .2879 .2849 .2818];
bv=[bv1 bv2 bv3 bv4 bv5 bv6 bv7 bv8 bv9 bv10];

for as=1:101,
   if Temp==Tempv(1,as),
      vis=bv(1,as);
   end
end

%complex permittivity of suspending medium

eme(1,:)=em*e0-j.*smk./w2(1,:);

%surface conductivity of latex bead under the influence of surface conductance.

sx=sb0;
sy=sb0;
spx=sb0+(2*reKs)/rxout+reA./(1+(j.*w2.*reT).^realpha);
```

```
spy=sb0+(2*reKs)/ryout+reA./(1+(j.*w2.*reT).^realpha);
sx=spx;
sy=spy;
%complex permittivity of each part of shell in term of matrix (er)
%From outermost shell parameters to innermost shell parameters.

for rol=1:nr,

etemp=ep0;
sxtemp=sx(1,:);
sytemp=sy(1,:);
erxtemp=etemp*e0-j.*sxtemp./w2;
erytemp=etemp*e0-j.*sytemp./w2;
erx(rol,:)=erxtemp;
ery(rol,:)=erytemp;

end



%To determine the depolarizing factors of each shells along the x and y axis.
%From maximium outermost shell (radius) to the innermost shell (radius).


for POLAR=1:nr,

Qo(1,POLAR)=(rx(1,POLAR)./ry(1,POLAR));

Axu(1,POLAR)=((Qo(1,POLAR)./sqrt(Qo(1,POLAR).^2-
1)).*log(Qo(1,POLAR)+sqrt(Qo(1,POLAR).^2-1))-1);

Axd(1,POLAR)=(Qo(1,POLAR).^2-1);

Ax(1,POLAR)=real(Axu(1,POLAR)./Axd(1,POLAR));

Ay(1,POLAR)=real((1-Ax(1,POLAR))./2);

end


%Ratio between x and y, z axis of each individual shell layers.
%From outermost shell radii to innermost shell radii.

if ns>0,

 for RAT=1:ns,

 v(1,RAT)=(rx(1,RAT).*(ry(1,RAT)).^2)./(rx(1,RAT+1).*(ry(1,RAT+1)).^2);

 end


%The effective complex permittivity (dielectric constant) in the x-axis of the ellipsoid
model.
% The calculation is from innermost shell parameters to outermost shell parameters.
```

```
 for CPR=ns:-1:1,

 EPXU(CPR,:)=erx(CPR,:)+(erx(CPR+1,:)-erx(CPR,:)).*(Ax(1,CPR+1)+v(1,CPR).*(1-
Ax(1,CPR)));
 EPXD(CPR,:)=erx(CPR,:)+(erx(CPR+1,:)-erx(CPR,:)).*(Ax(1,CPR+1)-
v(1,CPR).*Ax(1,CPR));
 eex(CPR,:)=erx(CPR,:).*(EPXU(CPR,:)./EPXD(CPR,:));
 erx(CPR,:)=eex(CPR,:);

 end

%Effective complex permittivity on the X-axis:

 exr=erx(1,:);

elseif ns==0,

 exr=erx;

end

%The effective complex permittivity (dielectric constant) in the y-axisof the ellipsoid
model.
%The calculation is from innermost shell parameters to outermost shell parameters.

if ns>0,

 for CPY=nr-1:-1:1,

 EPYU(CPY,:)=ery(CPY,:)+(ery(CPY+1,:)-ery(CPY,:)).*(Ay(1,CPY+1)+v(1,CPR).*(1-
Ay(1,CPY)));
 EPYD(CPY,:)=ery(CPY,:)+(ery(CPY+1,:)-ery(CPY,:)).*(Ay(1,CPY+1)-
v(1,CPY).*Ay(1,CPY));
 eey(CPY,:)=ery(CPY,:).*(EPYU(CPY,:)./EPYD(CPY,:));
 ery(CPY,:)=eey(CPY,:);

 end

%Effective complex permittivity on the Y-axis:

 eyr=ery(1,:);

elseif ns==0,

 eyr=ery;

end

%The X term from the modelin x-axis parameter:

Xx=(exr(1,:)-eme(1,:))./((exr(1,:)-eme(1,:)).*Ax(1,1)+eme(1,:));

%The X term from the model in y-axis parameter:

Xy=(eyr(1,:)-eme(1,:))./((eyr(1,:)-eme(1,:)).*Ay(1,1)+eme(1,:));
```

```
%To activate the ROT algorithm and calculate the rotation data.
%And to close the DEP algorithm.
rotd=1;
depd=0;

if rotd==1,
%The electrical torque <Tc> of the multishelled ellipsoid:

Tc=0.5.*V.*eme.*(imag(Xx)+imag(Xy)).*E^2;


%The Rf factor for the stationary angular velocity:

Rf=2.*reV.*vis.*((rxout^2+ryout^2)./(rxout^2.*Ax(1,1)+ryout^2.*Ay(1,1)));

%The stationary angular velocity of the ellipsoid model:

wc=0.5.*(reV./Rf).*em.*(imag(Xx)+imag(Xy)).*E^2;

wc=wc.*(-1).*EL;

elseif depd==1,

Depf=0.5.*(reV./Rf).*em.*(real(Xx)+real(Xy)).*E^2.*EL;

wc=Depf;

end



%RTnos=wc;

%Gaussian noise distribution
rand('normal');
for corrupt=1:37;
   RTnos(1,corrupt)=wc(1,corrupt)+(wc(1,corrupt)./10)*rand(1);
end
rand('uniform');
%values of ROT data, frequency points and their locations
rstart=4+2*nr+1;
rotend=4+2*nr+37;
for rotrun=rstart:rotend,
   rotrow=rotrun-(4+2*nr);
    simmat(rotrun,1)=x3(1,rotrow);
    simmat(rotrun,3)=RTnos(1,rotrow);
    simmat(rotrun,2)=NaN;
end

%To store similated data in a data.dat file
trial(cycle,1)=reA;
trial(cycle,2)=reT;
trial(cycle,3)=realpha;
trial(cycle,4)=reKs;
trial(cycle,5)=EL;
```

```
save c:\depdata\tempdat.dat simmat /ascii

%the size of the (matrix) file will be known by (n) rows and (cols) columns.

[nrow, cols]=size(simmat);

%To determine the therotrical analysis for ROT or DEP data

rotd=1;
depd=0;

%start to identify each parameters from the input file and
%to relocate the matrix

rotsimdat=simmat;

%no. amount of radius (nr) require for (ns) shell ellipsoid model:
ns=rotsimdat(1,1);
nr=ns+1;

%use Temperature value to detemine the visocity of the suspending
%medium.  Visocity values vs Temp are from CRC Physics and Chemistry
%Handbook 72th edition.

Temp=rotsimdat(1,2);

Temp1=[0 1 2 3 4 5 6 7 8 9 10 11 12 13 14 15 16 17 18 19 20];
Temp2=[21 22 23 24 25 26 27 28 29 30 31 32 33 34 35 36 37 38 39 40];
Temp3=[41 42 43 44 45 46 47 48 49 50 51 52 53 54 55 56 57 58 59 60];
Temp4=[61 62 63 64 65 66 67 68 69 70 71 72 73 74 75 76 77 78 79 80];
Temp5=[81 82 83 84 85 86 87 88 89 90 91 92 93 94 95 96 97 98 99 100];
Tempv=[Temp1 Temp2 Temp3 Temp4 Temp5];

bv1=[1.787 1.728 1.671 1.618 1.567 1.519 1.412 1.428 1.386 1.346 1.307];
bv2=[1.271 1.235 1.202 1.169 1.139 1.109 1.081 1.053 1.027 1.002];
bv3=[0.9779 0.9548 .9325 .9111 .8904 .8705 .8513 .8327 .8148 .7975];
bv4=[.7808 .7647 .7491 .7340 .7194 .7052 .6915 .6783 .6654 .6529];
bv5=[.6408 .6291 .6178 .6067 .5960 .5856 .5755 .5656 .5561 .5468];
bv6=[.5378 .5290 .5204 .5121 .5040 .4961 .4884 .4809 .4736 .4665];
bv7=[.4596 .4528 .4462 .4398 .4335 .4278 .4213 .4155 .4098 .4042];
bv8=[.3987 .3934 .3882 .3831 .3781 .3732 .3684 .3638 .3592 .3547];
bv9=[.3503 .3460 .3418 .3377 .3337 .3297 .3259 .3221 .3184 .3147];
bv10=[.3111 .3076 .3042 .3008 .2975 .2942 .2911 .2879 .2849 .2818];
bv=[bv1 bv2 bv3 bv4 bv5 bv6 bv7 bv8 bv9 bv10];

for as=1:101,
   if Temp==Tempv(1,as),
     vis=bv(1,as);
   end
end

%Crossover frequency of DEP

fco=rotsimdat(1,3);
wfco=fco*2*pi;
```

```
%applied voltage(E) and scaling fractor(EL)
E=rotsimdat(2,3);
EL=rotsimdat(4+2*nr,3);

% radius for each shells for both x- and y-axis
%they are provided from the data file.
for rcount=1:1.0:nr,
   nr1=1+rcount;
   rx(1,rcount)=rotsimdat(nr1, 1);
   ry(1,rcount)=rotsimdat(nr1, 2);
end

%Volume of latex bead or cell; assuming ry=rz.
rxout=rx(1,1);
ryout=ry(1,1);
rzout=ry(1,1);
V=4/3*pi*(rxout*ryout*rzout);

%From paper Xiao-Feng Zhou et al BBA 1245(1995)85-93,
%parameters to calculate effective conductivity of latex bead.
%A, T magnitude and mean characteristic time-constant.
%From the same paper, alpha and Ks: surface conductance.

A=rotsimdat(2+nr,1);
T=rotsimdat(2+nr,2);
alpha=rotsimdat(3+nr,1);
Ks=rotsimdat(3+nr,2);

ksurfincrement1=0;
ksurfincrement2=0;

if rotsimdat(2+nr,3)==3,
   ksurfincrement1=ksurfincrement1+1;
   ksurfvar(1,ksurfincrement1)=A;
   ksurflag1(1,ksurfincrement1)=1;
   ksurfincrement1=ksurfincrement1+1;
   ksurfvar(1,ksurfincrement1)=T;
   ksurflag1(1,ksurfincrement1)=2;
elseif rotsimdat(2+nr,3)==0,
   ksurfincrement2=ksurfincrement2+1;
   ksurfset(1,ksurfincrement2)=A;
   ksutflag2(1,ksurfincrement2)=1;
   ksurfincrement2=ksurfincrement2+1;
   ksurfset(1,ksurfincrement2)=T;
   ksurflag2(1,ksurfincrement2)=2;
elseif rotsimdat(2+nr,3)==1,
   ksurfincrement1=ksurfincrement1+1;
   ksurfvar(1,ksurfincrement1)=A;
   ksurflag1(1,ksurfincrement1)=1;
   ksurfincrement2=ksurfincrement2+1;
   ksurfset(1,ksurfincrement2)=T;
   ksurflag2(1,ksurfincrement2)=2;
elseif rotsimdat(2+nr,3)==2,
   ksurfincrement2=ksurfincrement2+1;
   ksurfset(1,ksurfincrement2)=A;
```

```
    ksurflag2(1,ksurfincrement2)=1;
    ksurfincrement1=ksurfincrement1+1;
    ksurfvar(1,ksurfincrement1)=T;
    ksurflag1(1,ksurfincrement1)=2;
end

if rotsimdat(3+nr,3)==3,
   ksurfincrement1=ksurfincrement1+1;
   ksurfvar(1,ksurfincrement1)=alpha;
   ksurflag1(1,ksurfincrement1)=3;
   ksurfincrement1=ksurfincrement1+1;
   ksurfvar(1,ksurfincrement1)=Ks;
   ksurflag1(1,ksurfincrement1)=4;
elseif rotsimdat(3+nr,3)==0,
   ksurfincrement2=ksurfincrement2+1;
   ksurfset(1,ksurfincrement2)=alpha;
   ksurflag2(1,ksurfincrement2)=3;
   ksurfincrement2=ksurfincrement2+1;
   ksurfset(1,ksurfincrement2)=Ks;
   ksurflag2(1,ksurfincrement2)=4;
elseif rotsimdat(3+nr,3)==1,
   ksurfincrement1=ksurfincrement1+1;
   ksurfvar(1,ksurfincrement1)=alpha;
   ksurflag1(1,ksurfincrement1)=3;
   ksurfincrement2=ksurfincrement2+1;
   ksurfset(1,ksurfincrement2)=Ks;
   ksurflag2(1,ksurfincrement2)=4;
elseif rotsimdat(3+nr,3)==2,
   ksurfincrement2=ksurfincrement2+1;
   ksurfset(1,ksurfincrement2)=alpha;
   ksurflag2(1,ksurfincrement2)=3;
   ksurfincrement1=ksurfincrement1+1;
   ksurfvar(1,ksurfincrement1)=Ks;
   ksurflag1(1,ksurfincrement1)=4;
end

[ksurfn, ksurfcol]=size(ksurfvar);
ksurf1=ksurfcol;
ksurf2=4-ksurf1;

%relative permittivity and conductivity of each shells

eflagincrement=0;
eflagincrement2=0;
sflagincrement=0;
sflagincrement2=0;

%flag indicators for iteration would be put in an array matrix (flag)
%Array matrix (evar) stores permittivity parameters for iteration.
%Array matrix (svar) stores conductivity parameters for iteration.
%Array matrix (eset) and (sset) store perm. and cond. parameters as constant values.
%Array matrix (eflag1) indicates the location of each permittivity parameters to be iterated.
%Array matrix (eflag2) indicates the location of each permittivity parameters to stay as
constant.
%Array matrix (sflag1) indiactes the location of each conductivity parameters to be
iterated.
```

```
%Array matrix (sflag2) indiactes the location of each conductivity parameters to stay as constant.


for flagcount=nr+4:nr+3+nr,
   flag(1,flagcount-nr-3)=rotsimdat(flagcount,3);
end

for flagcount=nr+4:2+nr+3+nr,
   if rotsimdat(flagcount,3)==3,
      eflagincrement=eflagincrement+1;
      sflagincrement=sflagincrement+1;
      evar(1,eflagincrement)=rotsimdat(flagcount,1);
      svar(1,sflagincrement)=rotsimdat(flagcount,2);
      eflag1(1,eflagincrement)=flagcount-nr-3;
      sflag1(1,sflagincrement)=flagcount-nr-3;

   elseif  rotsimdat(flagcount,3)==0,
      eflagincrement2=eflagincrement2+1;
      sflagincrement2=sflagincrement2+1;
      eset(1,eflagincrement2)=rotsimdat(flagcount,1);
      sset(1,sflagincrement2)=rotsimdat(flagcount,2);
      eflag2(1,eflagincrement2)=flagcount-nr-3;
      sflag2(1,sflagincrement2)=flagcount-nr-3;

   elseif  rotsimdat(flagcount,3)==1,
      eflagincrement=eflagincrement+1;
      sflagincrement2=sflagincrement2+1;
      evar(1,eflagincrement)=rotsimdat(flagcount,1);
      sset(1,sflagincrement2)=rotsimdat(flagcount,2);
      eflag1(1,eflagincrement)=flagcount-nr-3;
      sflag2(1,sflagincrement2)=flagcount-nr-3;

   elseif  rotsimdat(flagcount,3)==2,
      eflagincrement2=eflagincrement2+1;
      sflagincrement=sflagincrement+1;
      eset(1,eflagincrement2)=rotsimdat(flagcount,1);
      svar(1,sflagincrement)=rotsimdat(flagcount,2);
      sflag1(1,sflagincrement)=flagcount-nr-3;
      eflag2(1,eflagincrement2)=flagcount-nr-3;
   end
end

%To evaluate the amount of permittivity parameters to be iterated.

[evarn,evarcol]=size(evar);
enf1=evarcol;
enf2=nr-enf1;

%To evaluate the amount of conductivity parameters to be iterated.

[svarn,svarcol]=size(svar);
snf1=svarcol;
snf2=nr-snf1;

% relative permittivty of suspending medium
```

```
em=rotsimdat(4+nr*2,1);

% conductivity of suspending medium at 100kHz (in S/m)
smk=rotsimdat(4+nr*2,2);

%permittivity of free space
e0=8.825e-12;

%Generate the matrix ROTDATA or DEPDATA for autofiting program

p1=nr*2+5;
p2=nr*2+4;

na=nrow-p2;

for p=p1:nrow;
   rotatdat(p-p2,1) = rotsimdat(p,1);
   rotatdat(p-p2,2) = rotsimdat(p,2);
   rotatdat(p-p2,3) = rotsimdat(p,3);
end

%To sort out the order of the matrix for analysis.

for step1=na:-1:2,
 for step1=na:-1:2,
   step2=step1-1;
   if rotatdat(step1,1)>rotatdat(step2,1);

   tempera1=rotatdat(step1,1);
   rotatdat(step1,1)=rotatdat(step2,1);
   rotatdat(step2,1)=tempera1;

   tempera2=rotatdat(step1,2);
   rotatdat(step1,2)=rotatadat(step2,2);
   rotatdat(step2,2)=tempera2;

   tempera3=rotatdat(step1,3);
   rotatdat(step1,3)=rotatdat(step2,3);
   rotatdat(step2,3)=tempera3;

   elseif rotatdat(step1,1)<rotatdat(step2,1);
   end
 end
end

%frequency data point from the experiment

z1=rot90(rotatdat(:,1));

% scale frequency to 2.pi*Hz
wf=2*pi;
rotatdat(:,1)=rotatdat(:,1).*wf;
f=logspace(7,1,70);
w1=f.*wf;

if depd==1,
```

```
%experimental data points for dielectrophoresis
depdat=rotatdat(:,2);
z3=rot90(depdat);
z4=depdat;

elseif rotd==1,
%experimental data points for electrorotation:

rotdata=rotatdat(:,3);
z3=rot90(rotdata);
z4=rotdata;

end

%Deal to the problem in electrode polarisation effect at low frequency region.
%Derive correction factor "pf" by using polyfit to adjust rotation data with
%experimental conductance data

pff=[800e3 700e3 600e3 500e3 400e3 300e3 200e3 150e3 100e3 80e3 70e3 60e3...
    50e3 40e3 30e3 20e3 15e3 10e3 8e3 7e3 6e3 5e3 4e3 3e3 2e3 1.5e3 1e3...
    800 700 600 500 400 300 200 150 100];

bonesigma=[6.02 6.02 6.02 6.02 6.01 6.01 6.01 6.01 6.00 6.00 6.00 ...
        5.99 5.99 5.98 5.98 5.98 5.98 5.97 5.97 5.97 5.96 5.96 5.95...
        5.95 5.95 5.94 5.94 5.94 5.93 5.93 5.92 5.92 5.91 5.91 5.91 5.91].*1e-6;

pff=rot90(pff);
bonesigma=rot90(bonesigma);

bonesigma(:,1)=bonesigma(:,1)./max(bonesigma(:,1));

pfs=polyfit(log10(pff),bonesigma(:,1),6)

pfc=polyval(pfs,log10(z1));

pf=1./pfc;
pf=rot90(rot90(rot90(pf)));
z4=z4.*pf;

z2=rot90(z4);

%To creat a x-base line (lin) for the graph.
%w2 is not necessary, use w1 for calculation.

x1=logspace(0,7);
x2=x1;
w2=x1.*wf;
lin=x1.*0;
[B,nf]=size(x1);

%The following session is ROT simulation of best-fit graph

%curve fitting errors minimization logarithm

errsqu=0;
```

```
deperr=0;

rotparams=[EL evar svar ksurfvar];

global rotatdat rx ry rxout ryout vis eset sset depd rotd z4 ksurfset eflag1 eflag2 sflag1
sflag2 ksurflag1 ksurflag2 enf1 enf2 snf1 snf2 ksurf1 ksurf2 V em smk e0 w1 E nr ns nf Xx
Xy exr eyr Rf wfco deperr errsqu;

weight=1;
tracestatus=1;

nrotparams=fmins ('ellipsof',rotparams,5e20,tracestatus);

%After iteration, all permittivities values are put in matrix(e).
%All conductivities values are put in matrix(s).

EL=nrotparams(1);
for ememcount=1:enf1,
   ememcount1=eflag1(1,ememcount);
   e(1, ememcount1)=abs(nrotparams(1,1+ememcount));
end
for esetcount=1:enf2,
   esetcount1=eflag2(1,esetcount);
   e(1,esetcount1)=eset(1,esetcount);
end
for smemcount=1:snf1,
   smemcount1=sflag1(1,smemcount);
   s(1,smemcount1)=abs(nrotparams(1,1+enf1+smemcount));
end
for ssetcount=1:snf2,
   ssetcount1=sflag2(1,ssetcount);
   s(1,ssetcount1)=sset(1,ssetcount);
end
for ksurfcountv=1:ksurf1,
   ksurfcountv1=ksurflag1(1,ksurfcountv);
   ksurface(1,ksurfcountv1)=abs(nrotparams(1,1+enf1+snf1+ksurfcountv));
end
for ksurfcounts=1:ksurf2,
   ksurfcounts1=ksurflag2(1,ksurfcounts);
   ksurface(1,ksurfcounts1)=ksurfset(1,ksurfcounts);
end

nA=ksurface(1,1);
nT=ksurface(1,2);
nalpha=ksurface(1,3);
nKs=ksurface(1,4);

trial(cycle,6)=nA;
trial(cycle,7)=nT;
trial(cycle,8)=nalpha;
trial(cycle,9)=nKs;
trial(cycle,10)=EL;
trial(cycle,11)=errsqu;
end
save c:\depdata\destiny.dat trial /ascii
```

Chapter 4

VERIFICATION OF DIELECTRIC SHELL THEORIES BY DIELECTROPHORETIC AND ELECTROROTATIONAL STUDIES OF SYNTHETIC VESICLES

4.1 Introduction

In order to interpret dielectrophoresis (DEP) and electrorotation (ROT) data, as well as derive meaningful physical characteristics of the cells, an appropriate dielectric model is required. Generally, as discussed in chapter 2 and 3, shell models have been applied for this purpose. Using such a dielectric model to fit ROT spectral data is analogous to using an equivalent circuit to model a complicated impedance network. However, there is no guarantee that the equivalent circuit bears any physical correspondence to the real network. Therefore the fact that a shell model fits ROT or DEP data does not ensure that the parameters derived from it have a true correspondence with the cellular structure. One way of testing whether such a correspondence exists is to make measurements on simple particles whose physical characteristics can be manipulated and are thoroughly characterised. Liposomes are analogous structures to multi-shell dielectric models and are ideal test particles for this purpose. Indeed, Wicher and Gündel have made comparisons between the known physical properties of multi- and oligolamellar vesicles and the parameters derived from fitting one and two shell dielectric models to ROT and dielectric data [1, 2, 3]. However, the thickness of the vesicle membranes was poorly characterised. Recently, several advances have been made in the analytical methods that can be applied to fitting experimental data to dielectric shell models [4]. In this study, unilamellar, oligolamellar, and multilamellar 1,2-Dioleoyl-sn-Glycero-3-Phosphocholine (DOPC) vesicles of different sizes have been synthesised using the giant vesicle method [5, 6] and investigated by ROT and DEP. Fluorescence microscopy, flow cytometry and electron spin resonance of spin probes were used to characterise the vesicle morphology and membrane properties. A general purpose, recursive algorithm was used to analyse the dielectric properties of the various types of vesicles based on appropriate dielectric shell models. Through simulations, the confidence levels that can be assigned to parameters derived through application of simple shell models were estimated. As a result it was confirmed that electrorotation allows accurate determinations to be made of the dielectric properties of the outermost membrane of liposomes as well as indicating the level of complexity of the shells and internal compartments. We also demonstrate that under typical experimental conditions, ROT data cannot be analysed to yield unique solutions for the liposome dielectric parameters without additional data such as that provided by DEP.

4.2 Materials and Experimental Methods

4.2.1 *Synthesis of Vesicles*

In order to investigate particles whose size approximated mammalian cells, the giant vesicle method [5, 6] was used to produce vesicles with sizes ranging between 2μm to 15μm in radius. 2ml of 20mg/ml DOPC (Avanti Polar Lipids) was mixed in a scintillation vial with 1ml of 4mg/ml cholesterol (Sigma) in chloroform, 5.0μl of 2.5mg/ml N-(3-sulfopropyl)-4-(p-didecylamino-styryl) pyridinium salt (Di10ASP-PS) (a fluorescent dye obtained from Molecular Probes) in ethanol, and 30μl of 0.39mg/ml 5-doxyl-stearate (5-DS) (Sigma, St Louis) in ethanol (a spin label). Solvents were removed from the lipid mixture by rotary evaporation in a 40°C water bath under a gentle stream of nitrogen gas, which eliminated oxidation effects of atmospheric oxygen. After 30 minutes, films of phospholipid that were free of chloroform odour formed on the sides and bottom of the scintillation vial. 10ml of Percoll (Pharmacia BioProcess Technology) containing 150mM Sodium Chloride, 20mM HEPES, and 5mM EDTA (Sigma) was gently layered onto the film. After 24 hours undisturbed incubation at 37°C, the lamellae of the phospholipids had detached from the glass surface to form free-floating lipid globules. Giant vesicles [5, 6] were formed by gently drawing the suspension in and out of a Pasteur pipette several times over the course of a few seconds.

Vesicles produced by this technique contained a medium that was conductive (1.47 Sm^{-1} at $21°C$), contained EDTA to capture divalent ions such as Ca^{2+} and Mg^{2+} ions that can cause aggregation effects amongst vesicles [6] as well as transition metals that can catalyse lipid oxidation, and had a density of 1.143g/ml. This stock suspension of vesicles was found to be capable of storage at 4°C for up to 20 days.

4.2.2 *Fluorescence microscopy*

The lipophilic fluorescent dye Di1OASP-PS (λ_{ex} =496nm and λ_{em} =614nm) was used as a fluorescent probe in order to visualise the conformation and concentration of lipids in each vesicle. Since this dye became evenly distributed throughout phospholipid layers of all vesicles, the intensity of emission under fluorescence microscopy could be used to investigate the uniformity of membrane layers in the vesicles, distinguish between unilamellar and multiply-stacked lamellae [6], and discriminate between unilamellar vesicles and those containing multiple compartments. For gross characterisation of samples and the determination of particle size and lipid content distributions, stock vesicle suspensions were investigated on an Analyser (Becton-Dickinson) flow cytometer to provide scatter plots of lipid content *versus* vesicle volume, following a ten fold dilution with physiological saline.

4.2.3 *Electron Spin Resonance*

The stock vesicle preparation was diluted 1:10 with 5% mannitol in order that the vesicle density exceeded that of their suspending medium (see section 4.6.1). Following centrifugation for 4500g-minutes at 4°C, pelletted vesicle samples were transferred to 50μ*l* capillary tubes and investigated in a Varian E-109 EPR spectrometer over the temperature range 5°C to 45°C at 5°C increments. Spectra of the 5-DS incorporated in the lipid phase were acquired and the rigidity parameter S was analysed, by computer [7].

4.2.4 *Electrorotation (ROT) and Dielectrophoresis (DEP) Measurements*

Just prior to ROT and DEP measurements, the stock vesicle preparation was diluted one hundred fold with a 5% mannitol solution to produce a suspension containing approximately 10^6 vesicles/ml of radius > 2.5μm dispersed in an isotonic medium of conductivity $13mS.m^{-1}$ and density 1.14g/ml. In this way, the vesicles were introduced into an environment that was significantly less dense, and had a much lower conductivity, than their internal medium and in which they suffered no osmotic stress to their membranes.

ROT measurements were conducted in a flow-through chamber whose lower surface comprised a polynomial electrode array [8] of 400μ*m* tip-to-tip spacing of gold-on-glass construction. The four electrodes of the array were energised with sinusoidal signals in phase quadrature that produced an essentially homogeneous rotating electric field in the central region of the array [9]. Following injection of a new sample, vesicles settled almost immediately because of their high density value. Rotation measurements were then taken over the frequency range 500Hz to 150MHz at four points per decade for vesicles that lay within 65μm of the geometrical centre of the array and that were at least three diameters from any neighbour. Experimental data points were taken at frequencies chosen in random order. These procedures ensured that measurements were taken on vesicles in the most homogeneous region of the applied field, that vesicles did not move significantly because of lateral motion due to circular dielectrophoretic forces [10], that they were not subjected to particle-particle interactions, and that systematic errors caused by time-dependent changes [11] in the vesicle were avoided. The temperature of the measurement chamber was maintained at 21±0.1°C by a massive platform (1.5cm thick × 7cm × 10cm brass block) through which fluid heat exchanger could be circulated. The apparatus was mounted on a Diaphot (Nikon) inverted microscope, and vesicle rotation rates were timed by stopwatch with the aid of video-enhanced microscopy.

In order to show that the rate of ion leakage through the vesicle membranes did not seriously affect the conductivity of the supporting or encapsulated media, the frequency at which the DEP response changed polarity was determined for each individual vesicle, before and after measurement of the ROT spectrum. In most cases in which cholesterol was present in the lipid, there was little or no change in the DEP crossover frequency. This can be used as confirmation [12, 13, 14] that the rate of ion leakage through the vesicle membrane was insufficient to affect the physical experimental conditions or compromise the accuracy and reliability of the ROT data.

4.3 *ROT data analysis methods*

A dielectric shell model that closely resembled the physical appearance of each vesicle in terms of physical dimensions and the number of compartments was used to analyse each ROT spectrum [15] by applying a curve fitting method based on the Nelder-Mead simplex optimisation procedure [16] provided by MATLAB [The MathWorks, Inc]. This procedure minimised the error function

$$Min\left\{\sum_i\left[R_{sim}(f_i)-R_{\exp}(f_i)\right]^2+W*\mathrm{Re}^2\left(f_{CM_{fitted}}(f_c)\right)\right\} \qquad (4.1)$$

for the i frequency points f in the experimental ROT spectrum R_{exp}. A general purpose, recursive algorithm (Chapter 3) was developed to generate the ROT spectrum R_{sim} based on dielectric parameter estimates for the appropriate multi-shell model [4]. W represents the weight given in the minimisation procedure to the real part of the Clausius-Mossotti factor $\mathrm{Re}\left(f_{CM_{fitted}}(f_c)\right)$ (which has a value of zero when the DEP force vanishes at the crossover frequency f_c) calculated from the dielectric parameters used to simulate R_{sim}.

We investigated how accurately this curve fitting procedure was able to recover dielectric parameters from idealised ROT spectra. This was accomplished by using the computer to generate sets, each of 100 spectra with Gaussian noise of up to 10% RMS added, to fit each of these simulated spectra by the method described above, and then to analyse statistically the recovered dielectric parameter sets in terms of the data sets used to generate the spectra. This was done both with and without the DEP crossover frequency constraint ($W \neq 0$ and $W=0$, respectively) in the analysis in order to assess the importance of this analysis approach.

In all analyses at $21^{\circ}C$, the measured value of the suspending medium conductivity was provided and the relative permittivity values for the internal and external aqueous media were fixed at 80.36 [17]. Furthermore, the measured radii of all shells were provided explicitly to the optimisation algorithm. Thus for the single shell model, the iterated parameters in the minimisations were: the membrane dielectric properties σ_{mem} and ε_{mem}; the internal conductivity σ_{int}; and the scaling factor k which took into account factors in the experimental environment that influenced the vesicle rotation rate, including the field strength, the suspension viscosity and the friction between the vesicle and the substrate. For each membrane and its resulting medium compartment that was added to the dielectric model, three additional parameters were iterated, namely the two new membrane dielectric properties and the conductivity of the new compartment.

4.4 Results

4.4.1 *Vesicle Properties*

The preparations using the giant vesicle method were heterogeneous, but typically 30-40% of the vesicles present had radii in excess of 2.5μm and were characterisable by our ROT procedure. Radii of unilamellar vesicles were as high as about 10μm; whilst those for multilamellar vesicles with multiple compartments were as large as 12μm.

4.4.2 *Fluorescence microscopy*

The fluorescent probe Di1OASP-PS allowed different types of vesicles to be distinguished and the amount of phospholipid present in the membranes of each to be visualised. As shown in figure 4.1, the vesicles had a wide variety of structural forms including those with a single compartment and an unilamellar membrane (figure 4.1a), a single compartment and a multilamellar membrane (figure 4.1b), two or more compartments (figure 4.1c), and more complex combinations of these characteristics (figure 4.1d). There was no dominant form, and in addition to vesicles many residual globules (containing little enclosed aqueous medium) from the initial suspension of the lipid film were present.

parameters were iterated, namely the two new membrane dielectric properties and the conductivity of the new compartment.

4.4 Results

4.4.1 *Vesicle Properties*

The preparations using the giant vesicle method were heterogeneous, but typically 30-40% of the vesicles present had radii in excess of 2.5μm and were characterisable by our ROT procedure. Radii of unilamellar vesicles were as high as about $10\mu m$; whilst those for multilamellar vesicles with multiple compartments were as large as $12\mu m$.

4.4.2 *Fluorescence microscopy*

The fluorescent probe Di1OASP-PS allowed different types of vesicles to be distinguished and the amount of phospholipid present in the membranes of each to be visualised. As shown in figure 4.1, the vesicles had a wide variety of structural forms including those with a single compartment and an unilamellar membrane (figure 4.1a), a single compartment and a multilamellar membrane (figure 4.1b), two or more compartments (figure 4.1c), and more complex combinations of these characteristics (figure 4.1d). There was no dominant form, and in addition to vesicles many residual globules (containing little enclosed aqueous medium) from the initial suspension of the lipid film were present.

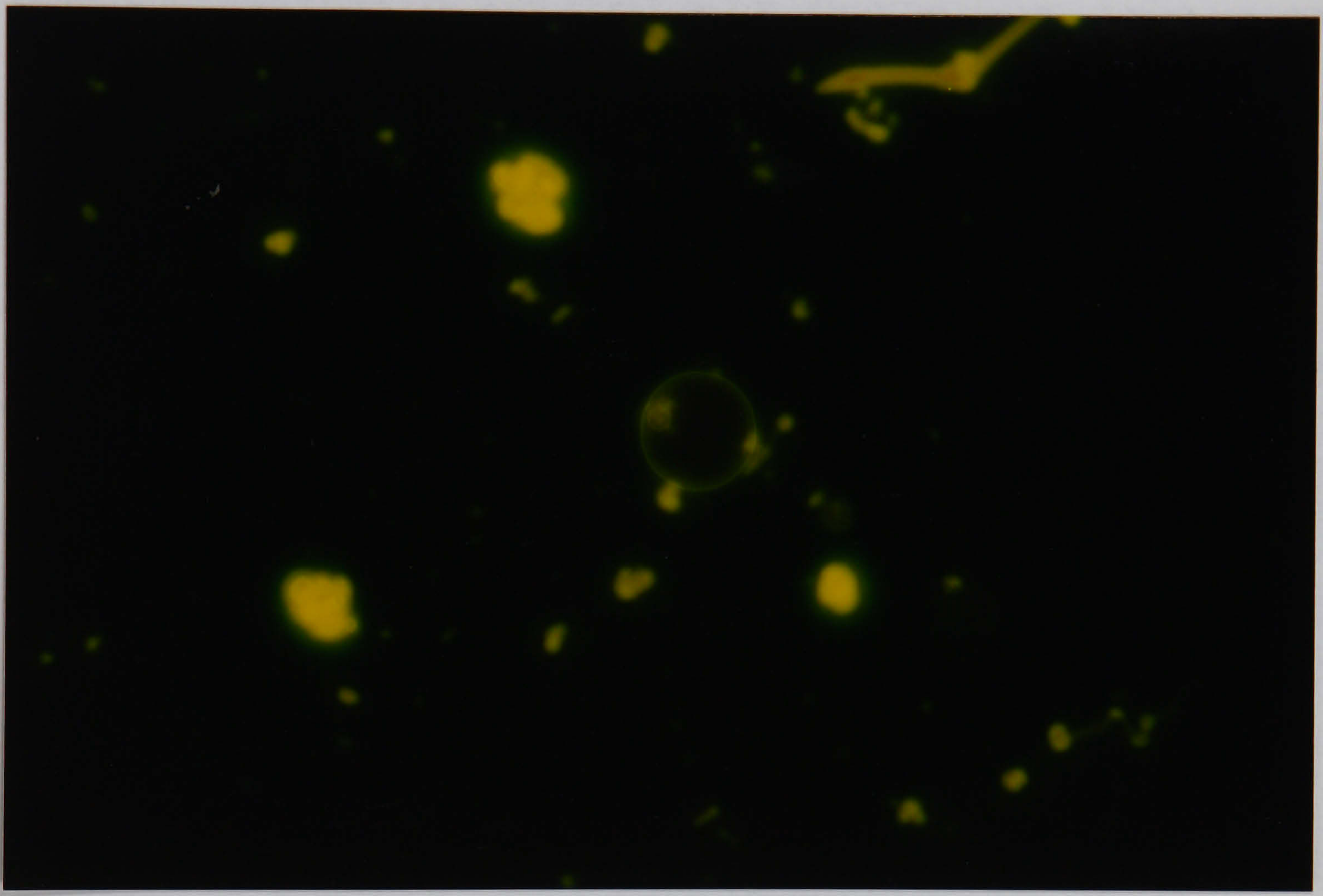

Figure 4.1a This is a single compartment and unilamellar membrane vesicle. This photograph, as well as the others in this series was taken by fluorescence microscopy.

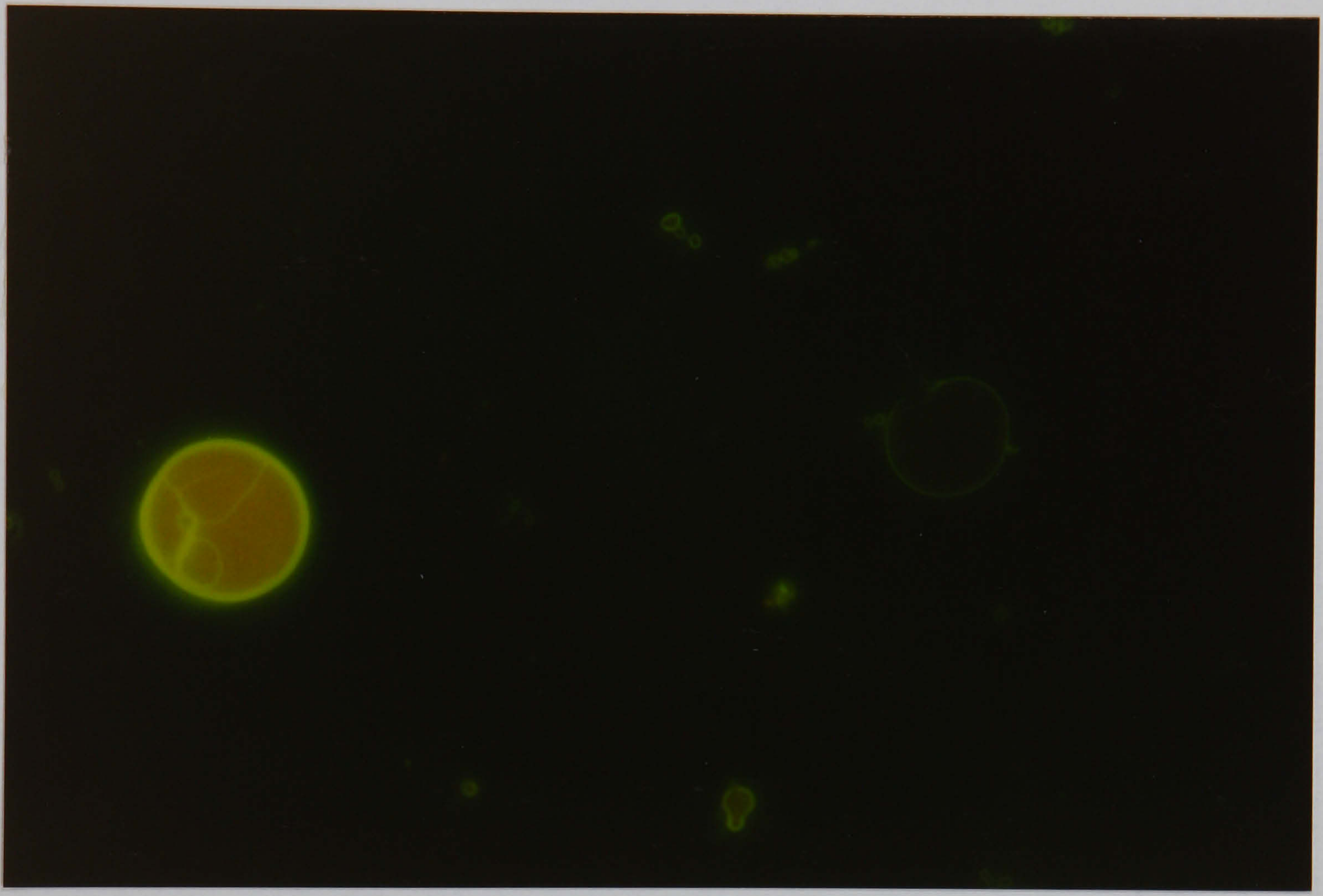

Figure 4.1b This vesicle is a multilamellar vesicle with single compartment.

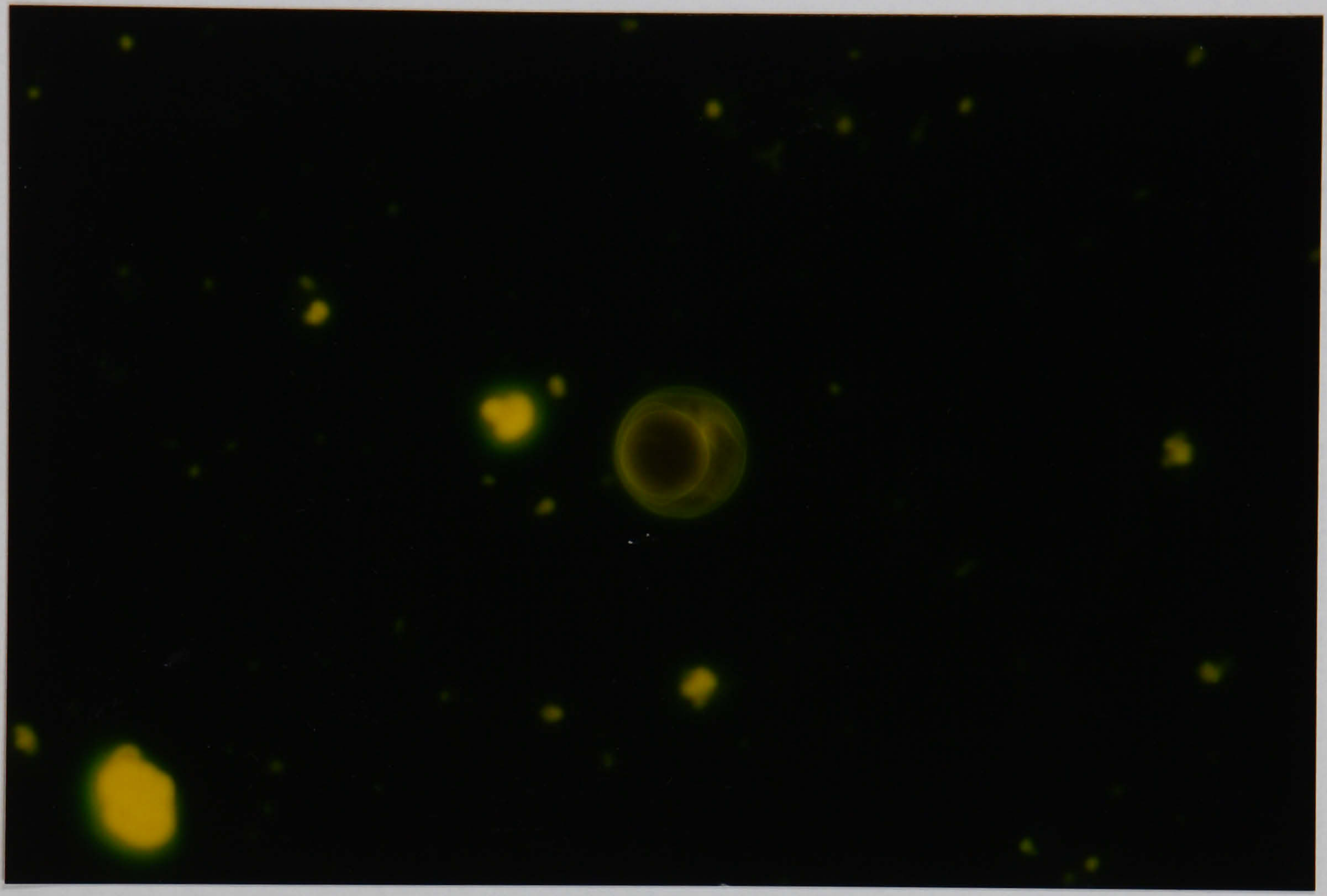

Figure 4.1c This is an oligolamellar vesicle which has two or more compartments.

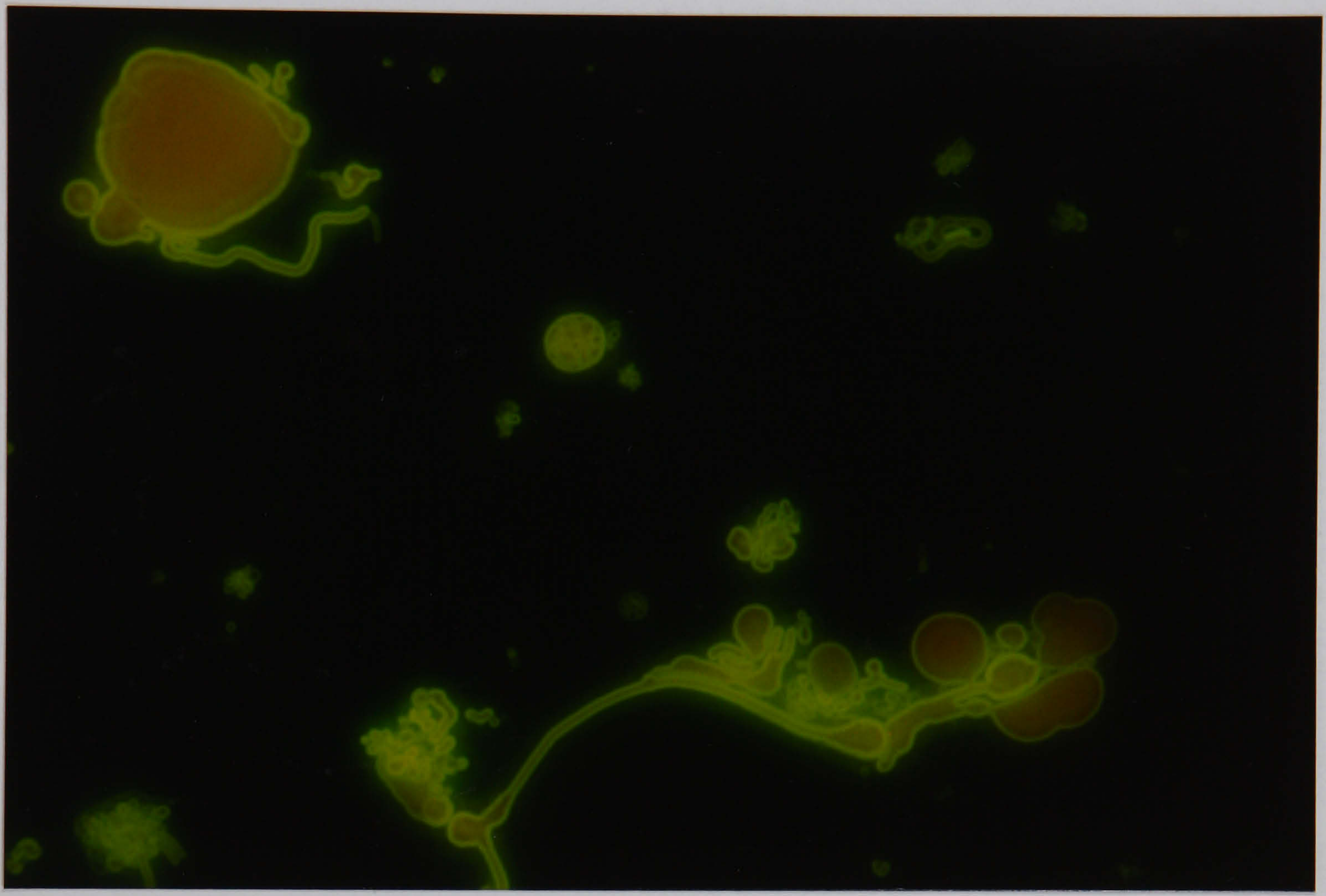

Figure 4.1d At the middle of this photo is a multi-vesicular liposomes which has a very complex structure.

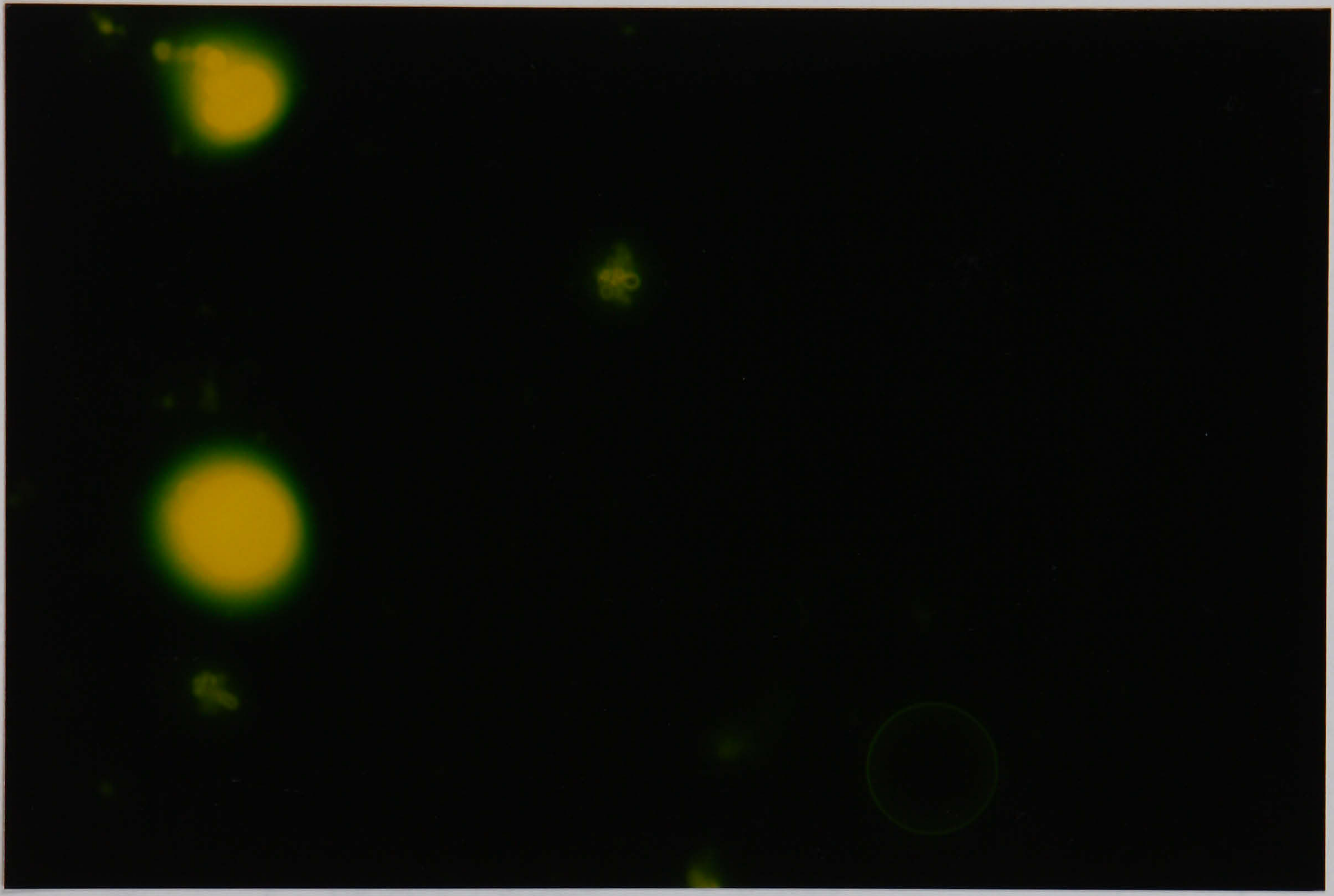

Figure 4.1e This is a multilamellar vesicle with many layers of lamellae underneath the first layer of membrane.

4.4.3 *Flow cytometry*

Figure 4.2 shows a typical scatter plot of lipid content (as gauged by Di1OASP-PS fluorescence) versus vesicle volume (determined by both light scattering and Coulter method). Two interesting features are apparent:

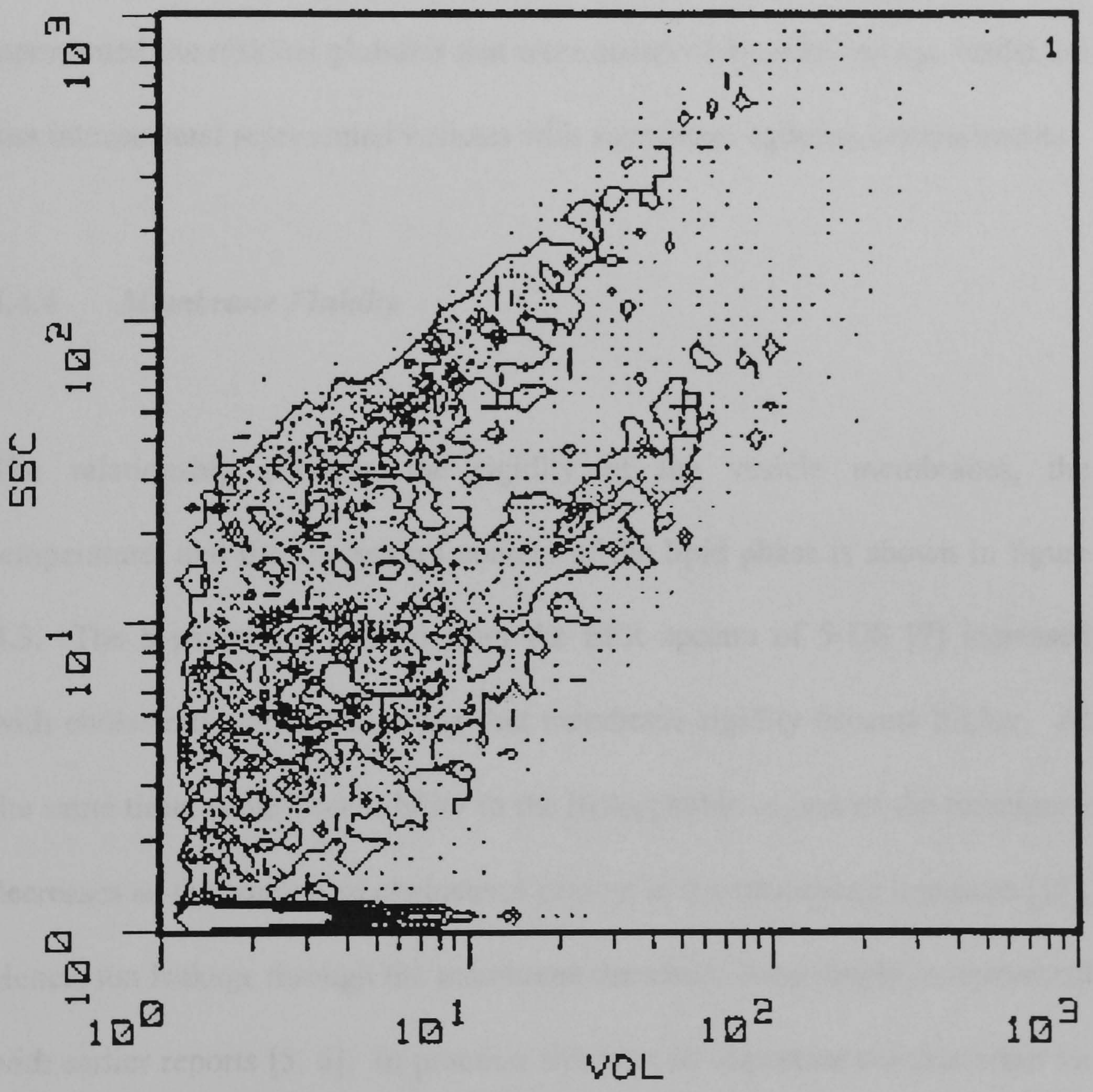

Figure 4.2 A typical scatter plot of vesicles' lipid content obtained using the flow cytometry technique.

1) The lipid content of a vesicle is directly proportional to its volume, as evidenced by the linear relationship with slope=1 between these parameters. A linear relationship with slope=2/3 would be expected if the lipid content mirrored the surface area of the vesicles; and,

2) There appear to be two distinct classes of vesicles present, as evidenced by the two parallel bands separated by an order of magnitude in lipid fluorescence. It is likely that the band having the more intense fluorescence represented the residual globules that were observed by microscopy, whilst the less intense band represented vesicles with significant aqueous compartments.

4.4.4 *Membrane Fluidity*

The relationship between the rigidity of the vesicle membranes, the temperature, and the cholesterol content of the lipid phase is shown in figure 4.3. The S-parameter derived from the EPR spectra of 5-DS [7] increased with cholesterol content showing that membrane rigidity became higher. At the same time, water accessibility to the hydrophobic region of the membrane decreases as the amount of cholesterol present in the membrane increases [18]. Hence, ion leakage through the membrane decreased accordingly in agreement with earlier reports [5, 6]. In practice, this was an important consideration for ROT measurements because the most information is available from ROT spectra when the internal conductivity of the vesicle compartment is much higher than the conductivity of the medium in which the vesicle is suspended.

Maintaining a high ion concentration gradient across the vesicle membrane for a sufficiently long period of time to complete ROT spectral measurements proved to be difficult in the absence of cholesterol. For this reason, all the ROT experiments reported here were undertaken on vesicles whose lipid contained 10% cholesterol.

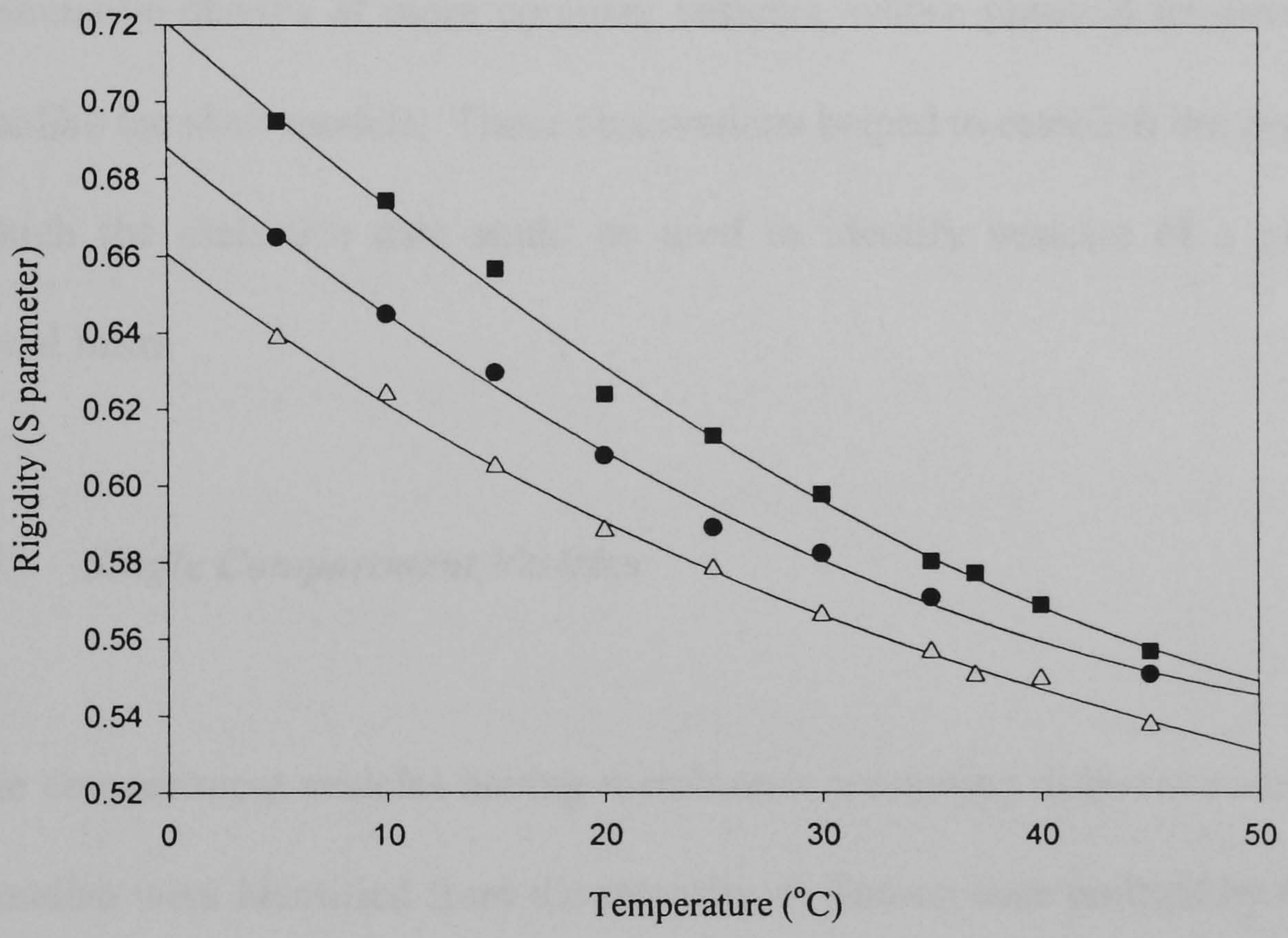

Figure 4.3 As temperature increased, the EPR derived S-parameter values of DOPC phospholipids decreased, indicating that the phospholipid layer membranes were getting more fluid. Δ: membrane without cholesterol present.

●: membrane with cholesterol of ratio 1:10 by weight present in the membrane.

■: membrane with cholesterol of ratio 1:5 by weight present in the membrane.

The rigidity of the membrane increased in proportion to the percentage of cholesterol present in the membrane

4.4.5 *Rotation Spectra*

From the many forms of vesicles present in the samples made by the giant vesicle method, ROT spectra of only the simplest morphological classes that most closely resembled 1, 3 and 5 shell dielectric models were measured. In addition, examination was made of the ROT characteristics of some representative classes of more complex vesicles, whose physical appearance was unlike the shell models. These observations helped to establish the degree to which the dielectric data could be used to identify vesicles of a given physical form.

4.4.5.1 *Single Compartment Vesicles*

Single compartment vesicles having membranes containing different numbers of lamellae were identified from the intensity of fluorescence emitted by their lipid phases. The single compartment vesicle form is most appropriately described by the single shell dielectric model, and in applying that model for analysis it was sought to determine whether the expected correlation was observed between the thickness of the membrane and its capacitance. Typical ROT spectra obtained for such vesicles, together with the best fit of the single shell model, are shown in figure 4.4. Crossover frequencies and ROT peak frequencies varied by more than an order of magnitude between the vesicles having the thinnest and thickest membranes examined. The optimisation procedure applied for the analysis of the ROT spectra allowed for the estimation of the specific membrane capacitance C_{mem} rather than ε_{mem} directly (see Chapter 2). It was also possible to estimate the membrane capacitance of single compartment vesicles using the single shell dielectric model and the DEP crossover frequency measurement alone using the relationship

$$C_m \approx \frac{\sigma_s}{R\pi \ \sqrt{2} f_{co}} \tag{4.2}$$

providing the membrane conductivity is sufficiently low that its influence on the crossover frequency f_{co} can be ignored [14] (see chapter 2). Here σ_s is the conductivity of the supporting medium and R is the radius of the vesicle. Table 4.1 summarises the capacitance values determined for single-compartment vesicles having membranes of different thicknesses as determined both from parameter optimisation of the entire ROT spectra and the DEP crossover frequency values. Membrane conductivity values derived from the optimisation analysis were very low, typically below 10^{-6} S/m.

Table 4.1: Summary of membrane capacitance values of vesicles analysed by the one shell dielectric model (see Ch. 2). The relative permittivity of the entire membrane phase is assumed to be 3.09 (see discussion).

Vesicle type	*number of vesicles measured*	*mean C_{mem} from ROT ($mF.m^{-2}$)*	*mean C_{mem} from DEP ($mF.m^{-2}$)*	*mean membrane thickness (nm)*	*closest integral no. of bilayers*
A	*16*	*6.48*	*6.98*	*4.07*	*1*
B	*6*	*3.66*	*3.78*	*7.55*	*2*
C	*2*	*1.98*	*2.13*	*13.9*	*4*
D	*2*	*1.60*	*1.71*	*17.4*	*5*
E	*1*	*0.62*	*0.61*	*45.3*	*12*
F	*3*	*13.6*	*15.3*		*1*

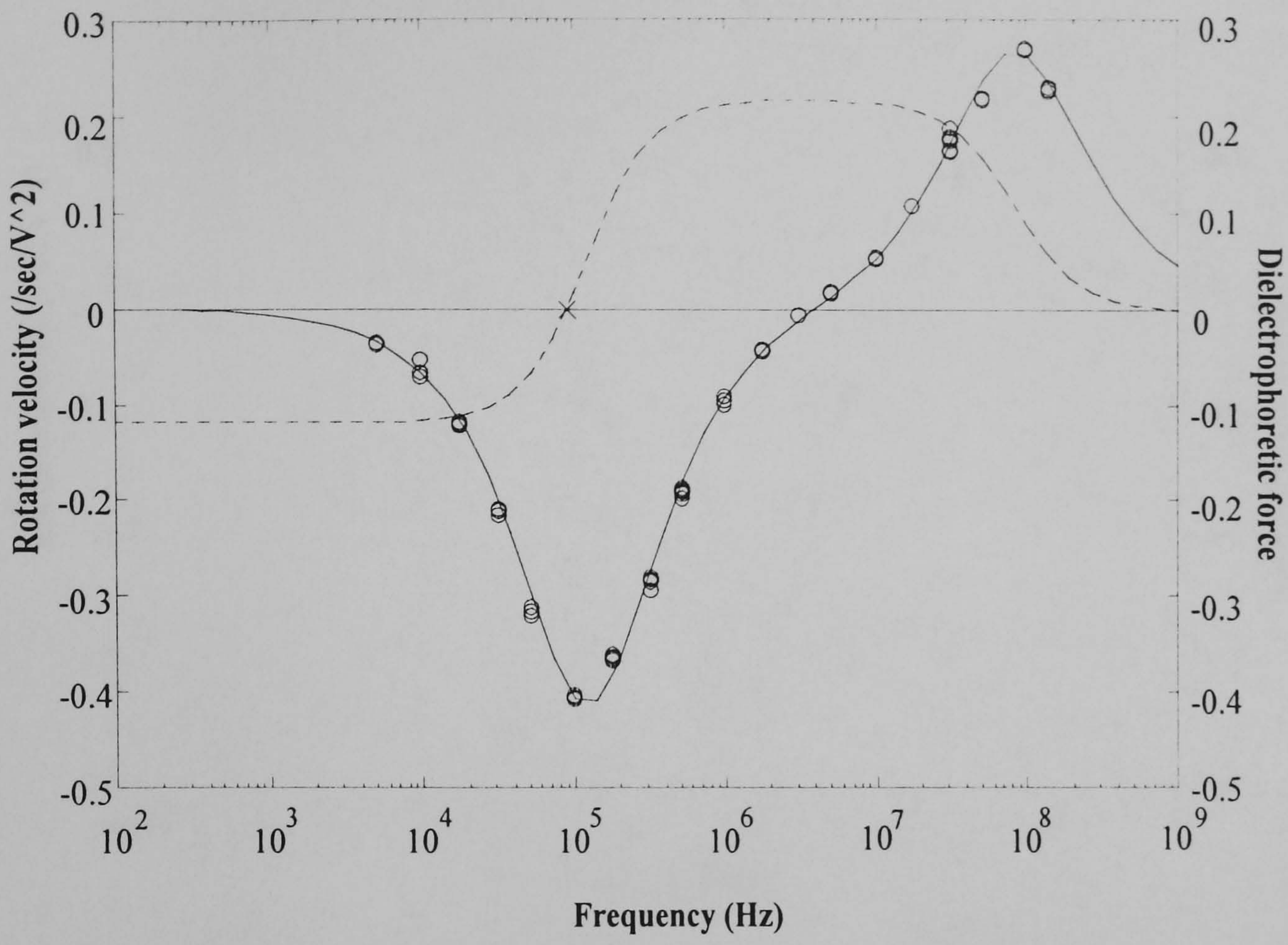

Figure 4.4a A typical ROT spectrum (solid line) for unilamellar vesicle (Figure 4.1a). "O": ROT experimental data of rotation (ROT) spectrum. "X": experimental data for DEP crossing over frequency. The DEP theoretical spectrum is shown as the dotted line. Experimental temperature is 21°C.

By single shell model: Membrane :

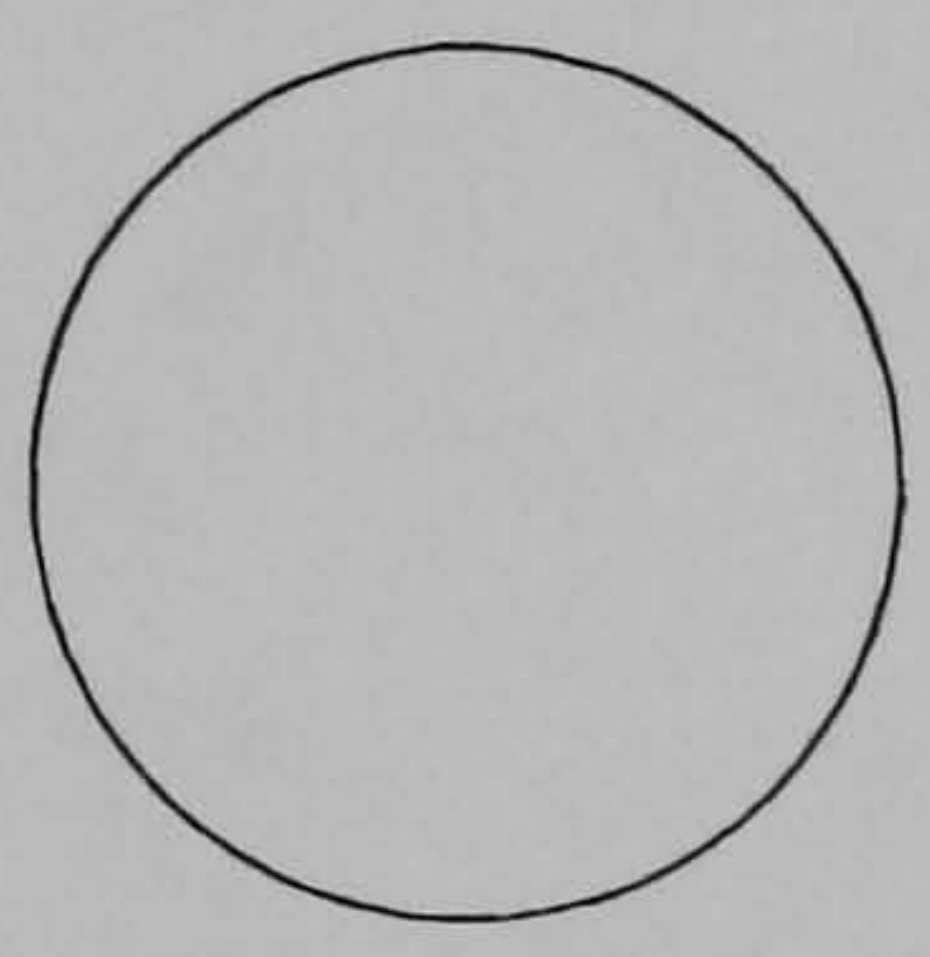

permittivity = 2.98

conductivity < 1×10^{-9} Sm^{-1}

thickness = 4.5nm

Encapsulated medium :

permittivity = 80.14

conductivity = 1.069 Sm^{-1}

Suspending medium:

permittivity = 80.14

conductivity = 12.45 $m.Sm^{-1}$

Vesicle

radius = 5.25μm

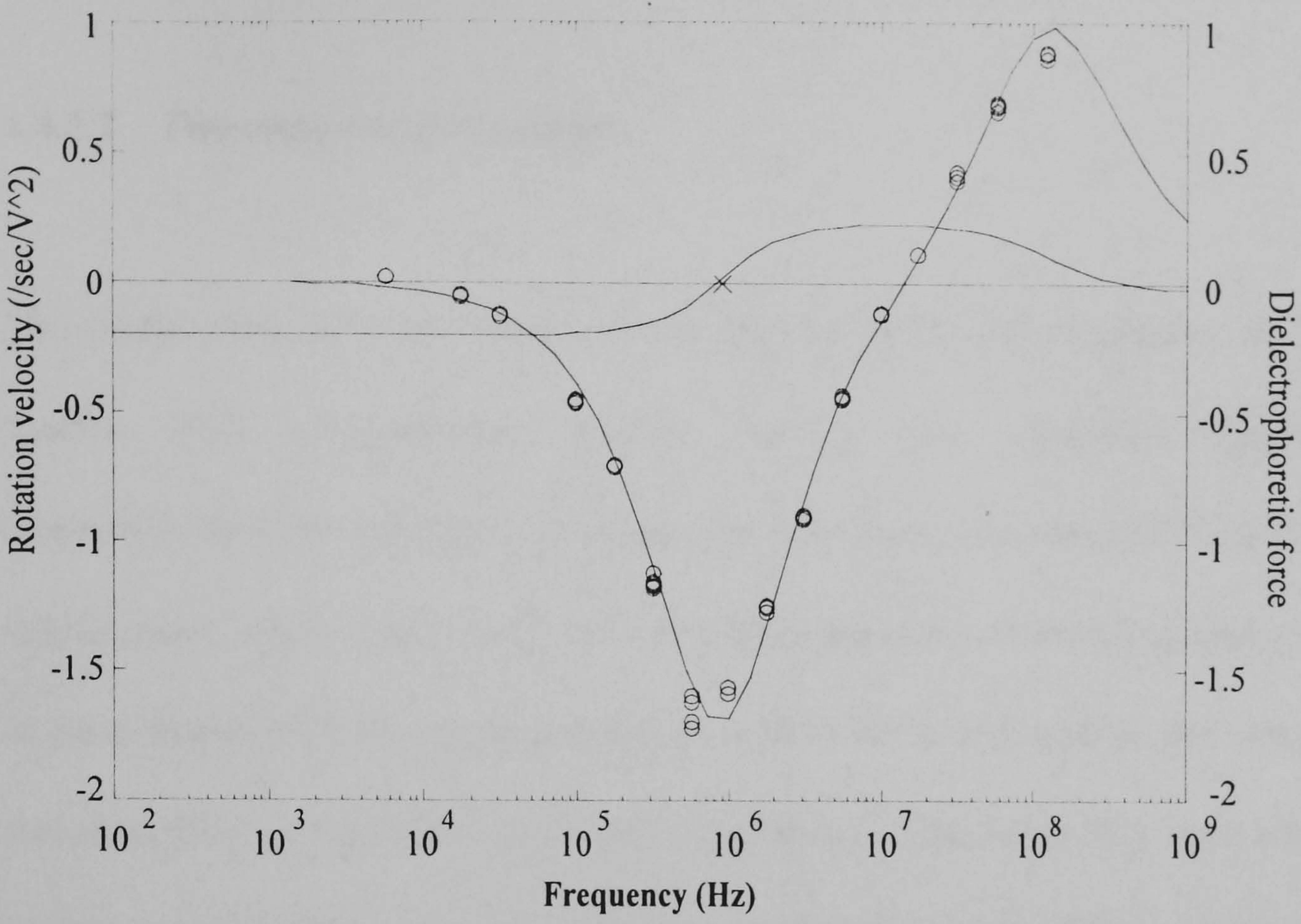

Figure 4.4b A typical ROT spectrum (solid line) for a multilamelllar vesicle with a single encapsulated medium compartment (Figure 4.1b). "O":ROT experimental data. It has been fitted by single shell model. "X": experimental data for DEP crossing over frequency. The DEP theoretical spectrum is shown as dotted line. Experimental temperature is 21°C.

By single shell model: Membrane :

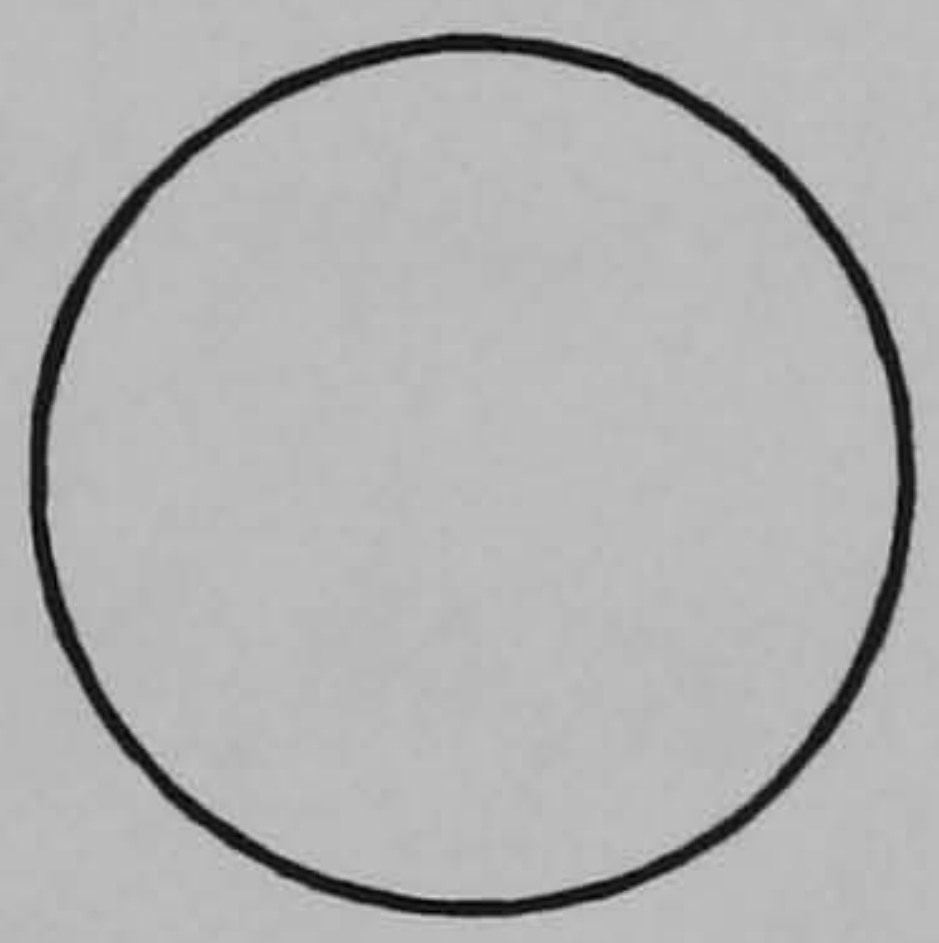

capacitance = 0.621 m.Fm^{-1}

thickness = 45nm

permittivity = 3.166

conductivity <1×10^{-9} Sm^{-1}

encapsulated medium:

permittivity = 80.4

conductivity = 1.375Sm^{-1}

suspending medium :

permittivity = 80.4

conductivity = 13.55 m.Sm^{-1}

Vesicle:

radius = 5.64μm

4.4.5.2 *Two compartment vesicles*

The single shell dielectric model was unable to fit the more complex ROT spectra from oligolamellar vesicles having two separate medium compartments if the innermost compartment was larger than about 30% of the vesicle outer radius. In general, such vesicles had a wider dielectric dispersion in the anti-field rotation region and these could be fitted with a three shell (two membrane) dielectric model as shown in Figure 4.5. The lower frequency side of the antifield ROT peak was dominated by the properties of the outermost membrane, while the innermost membrane influenced the width of the antifield peak and the position of the crossover frequency.

Computer simulations showed that the accuracy that could be obtained for derived dielectric parameters from the optimisation procedure fell with increasing distance into the vesicle as shown in Figure 4.8. Thus the outermost membrane parameters could be derived more accurately that the corresponding parameters for the innermost membrane.

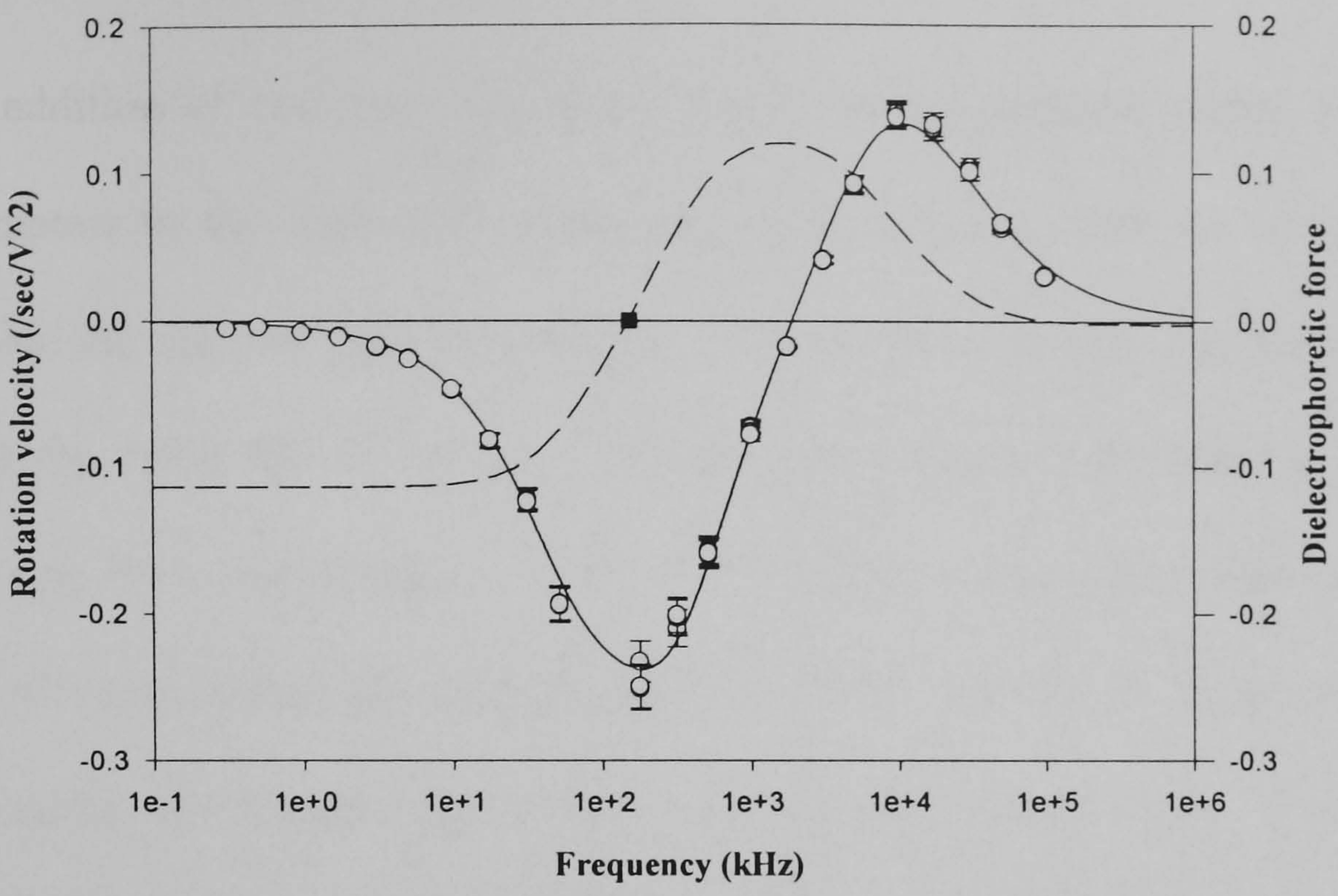

Figure 4.5 Typical ROT spectrum for an oligolamellar vesicle with two encapsulated medium compartments (Figure 4.1c). The solid line "_" is a theoretical fitting of the ROT experimental data "O". "■" is an experimental DEP crossing over frequency point. The "_ _" is a theoretical fitting for the experimental DEP crossing over frequency. The experimental temperature was 30°C.

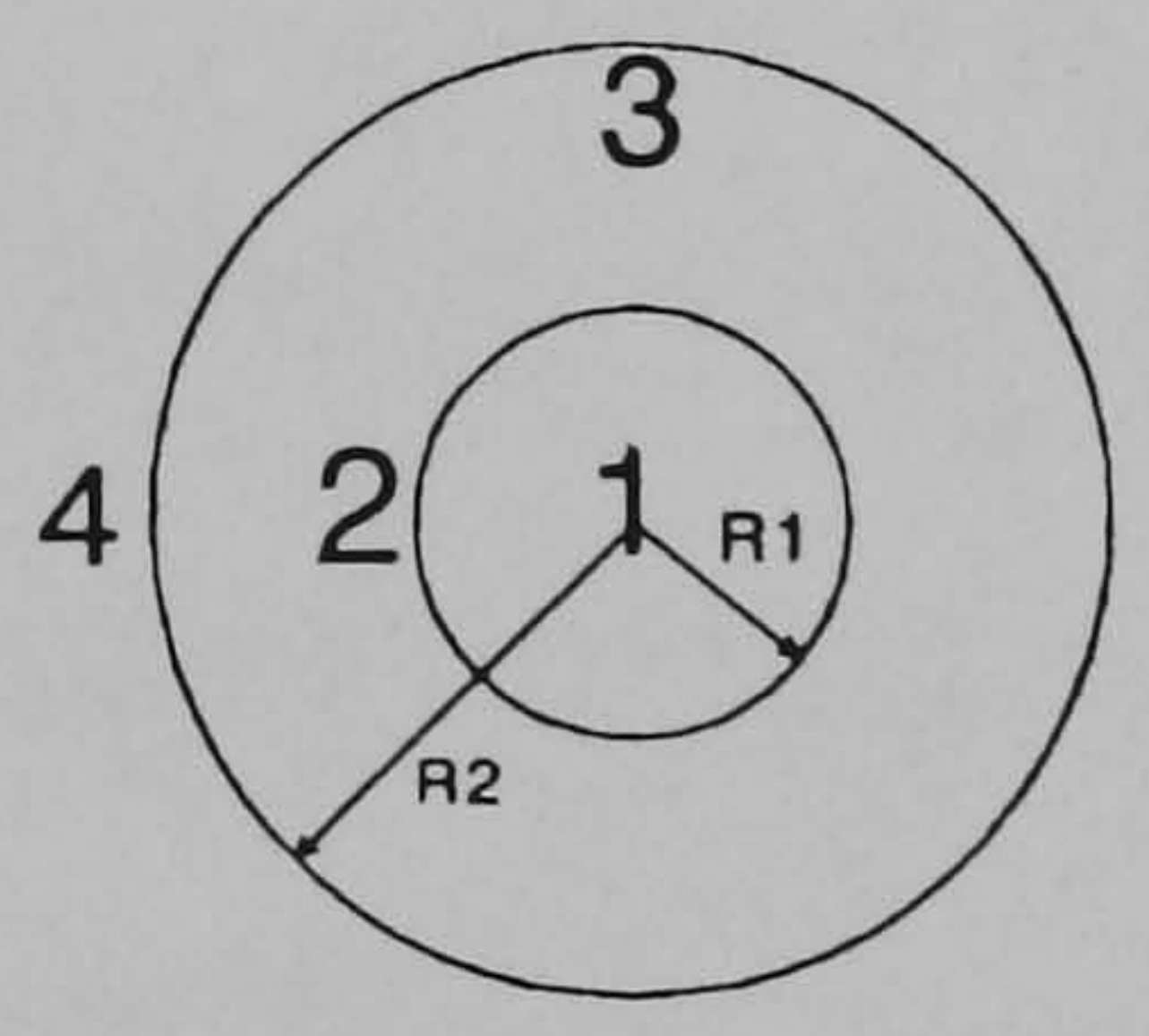

Inner vesicle:
radius R1 = 3.8μm
Outer vesicle:
radius R2 = 5.5μm

1: Innermost medium: permittivity = 77.1
conductivity = 212.3 mS.m^{-1}

2: Innermost membrane:
capacitance = 9.84 mF.m^{-1}
conductivity = 5.2×10^{-7}Sm^{-1}

3: Intermediate medium:
permittivity = 77.1
conductivity = 55.99 mS.m^{-1}

4: Outermost membrane :
capacitance = 5.61 mF.m^{-1}
conductivity = 6.8×10^{-8} Sm^{-1}

Suspending medium:
permittivity = 77.1
conductivity = 17.33 mS.m^{-1}

4.4.5.3 *More complex vesicles*

The addition of each new concentric membrane compartment added 3 new parameters to the dielectric model, as discussed earlier, and the computer simulations showed that the accuracy with which each new parameter set could be fitted fell off rapidly. Nevertheless, Figure 4.6 shows a ROT spectrum for a multilamellar vesicle with multiple compartments that can be clearly distinguished in its form from the ROT spectra of more simple unilamellar and oligolamellar vesicles (see Figures 4.4 and 4.5). A model having five shells (3 membranes) was the minimum complexity that was able to give a reasonable fit to this data, showing that while accurate parameters could not be derived for the inner dielectric properties, such complex vesicles could nevertheless be distinguished from simpler ones.

It was also possible to detect folding of the outermost membrane in both simple and complex vesicles. Such membrane folding resulted in much higher capacitance values that could be accounted for by a single smooth bilayer. For example, the ROT spectrum of the single compartment vesicle class F in Table 4.1 has a mean membrane capacitance of approximately 14.4 mF/m^2 because of a high degree of membrane folding that was readily apparent by microscopy. Similar effects were seen in multilamellar vesicles whose outermost membrane capacitance values were as high as $33.15 mF.m^{-2}$.

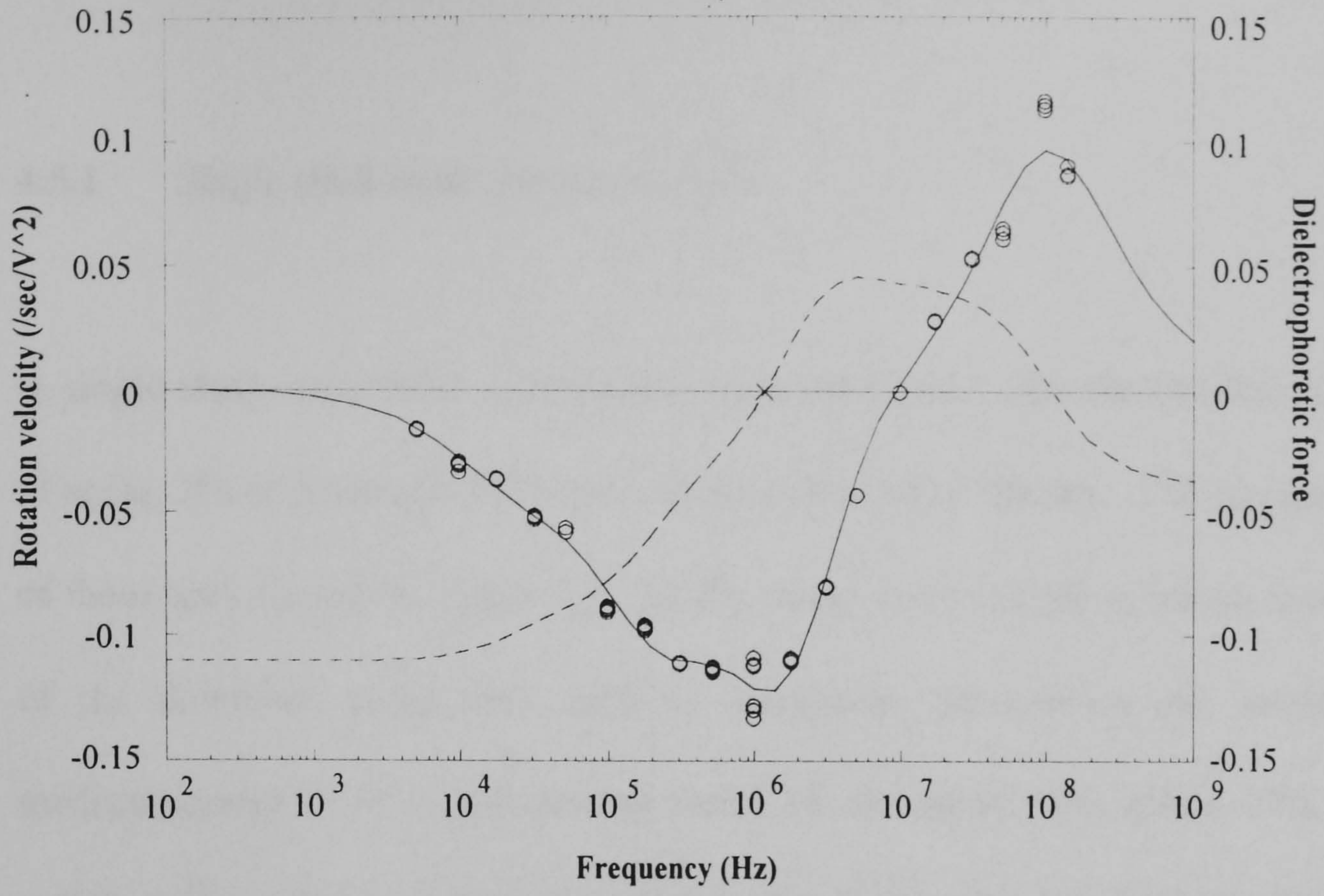

Figure 4.6 This is a spectrum from a complex multilamellar vesicle system (Figure 4.1e). The solid line "___" is the theoretical fitting of the the ROT experimental data "O". The dotted line "- - -" is the fitting of the DEP crossing over frequency data point "X". The experimental temperature is 21°C.

Five shell model:

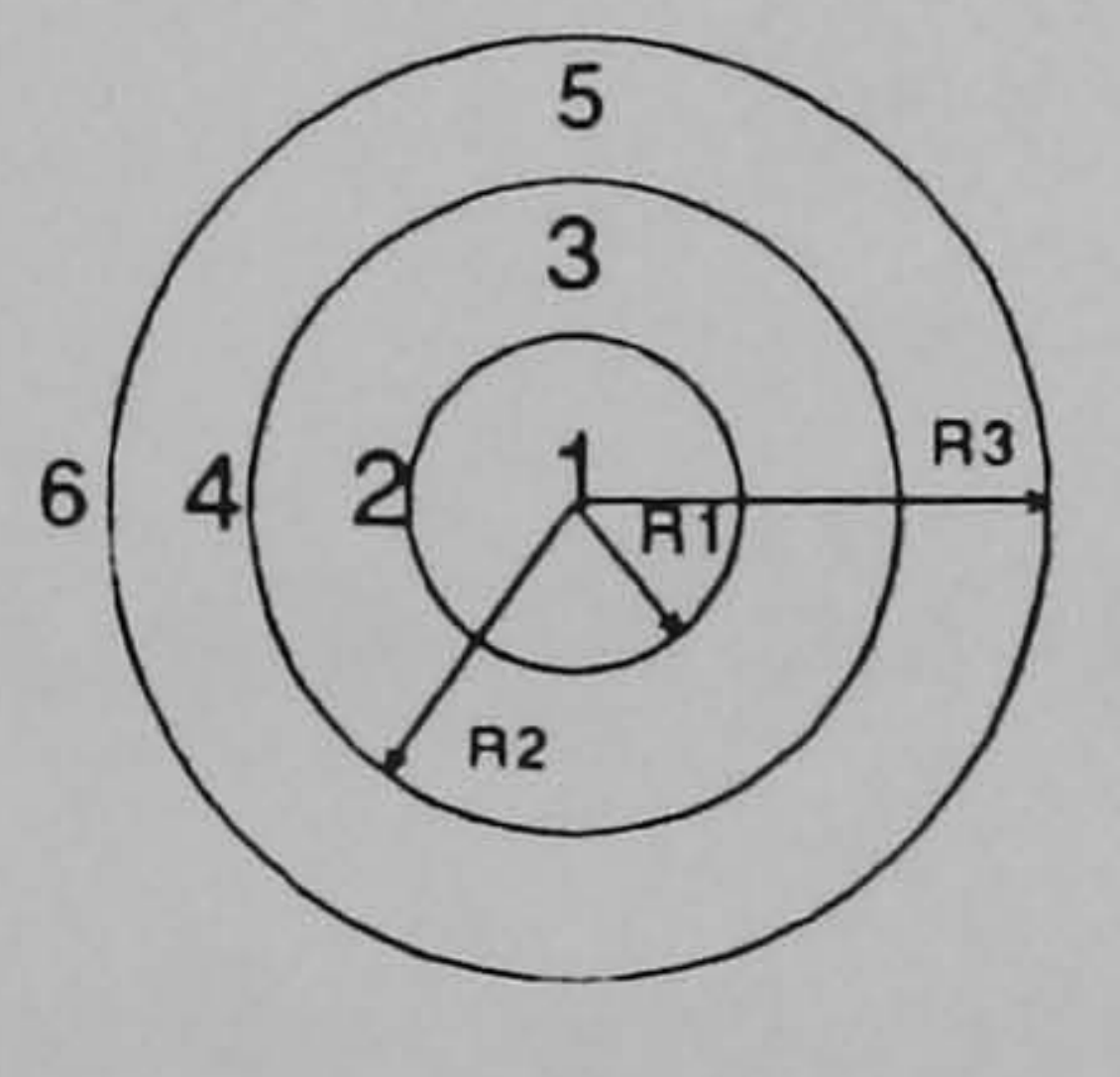

1: Innermost medium: permittivity = 80.4
conductivity = 0.8998 Sm^{-1}

2: innermost membrane: capacitance = 0.1824 mF.m^{-2}
conductivity = 2.62×10^{-5} Sm^{-1}

3: intermediate medium: permittivity = 80.4
conductivity = 17.83 mS.m^{-1}

4: intermediate membrane:capacitance=0.8127mF.m^{-2}
conductivity = 9.62×10^{-6} Sm^{-1}

5: outermost medium: permittivity = 80.4
conductivity = 17.83 mS.m^{-1}

6: outermost membrane: capacitance = 33.1 mF.m^{-2}
conductivity = 1.9×10^{-5} Sm^{-1}

Radii of:
Innermost vesicle:
R1 = 8.5μm
Intermediate vesicle
R2 = 10μm
Outermost vesicle:
R3 = 11.8μm

4.5 Results of Testing Shell Model Programs

4.5.1 *Single shell model fitting analysis*

In single shell cases, ROT spectra have been introduced with 0% of noise, 3% of noise, 5% of noise and 10% of noise present in ROT spectra. The summary of these tests shown in Figure 4.7. In 0% noise situation, the accuracy levels of the dominant parameters such as membrane permittivity e2, internal medium conductivity s1 and scaling factor EL are all at 94% within 10% of variation from the true value, the accuracy level of membrane conductivity s2 is 89% within 10% variation from the true value. For the same noise level, membrane permittivity achieved a result with 88% in perfect accuracy with no deviation; 90% for the scaling factor, 86% for medium conductivity and 87% for membrane conductivity with perfect accuracy.

As noise level increases to 10% relative to the value of a ROT spectrum, accuracy for the membrane conductivity has fallen down to 57% with standard deviation of 0.1403. The internal medium conductivity has fallen down to 75% with 0.05421 as standard deviation whereas the accuracy levels for the membrane permittivity and scaling factor have remained at 96% and 97%, respectively. The standard deviation of membrane permittivity and scaling factor are 0.00288 and 0.00281 respectively. From this analysis, the derived values of membrane permittivity and other major parameters, which are obtained from this single shell model, prove to be very reliable and very much closer to its true value even with noise present in the data.

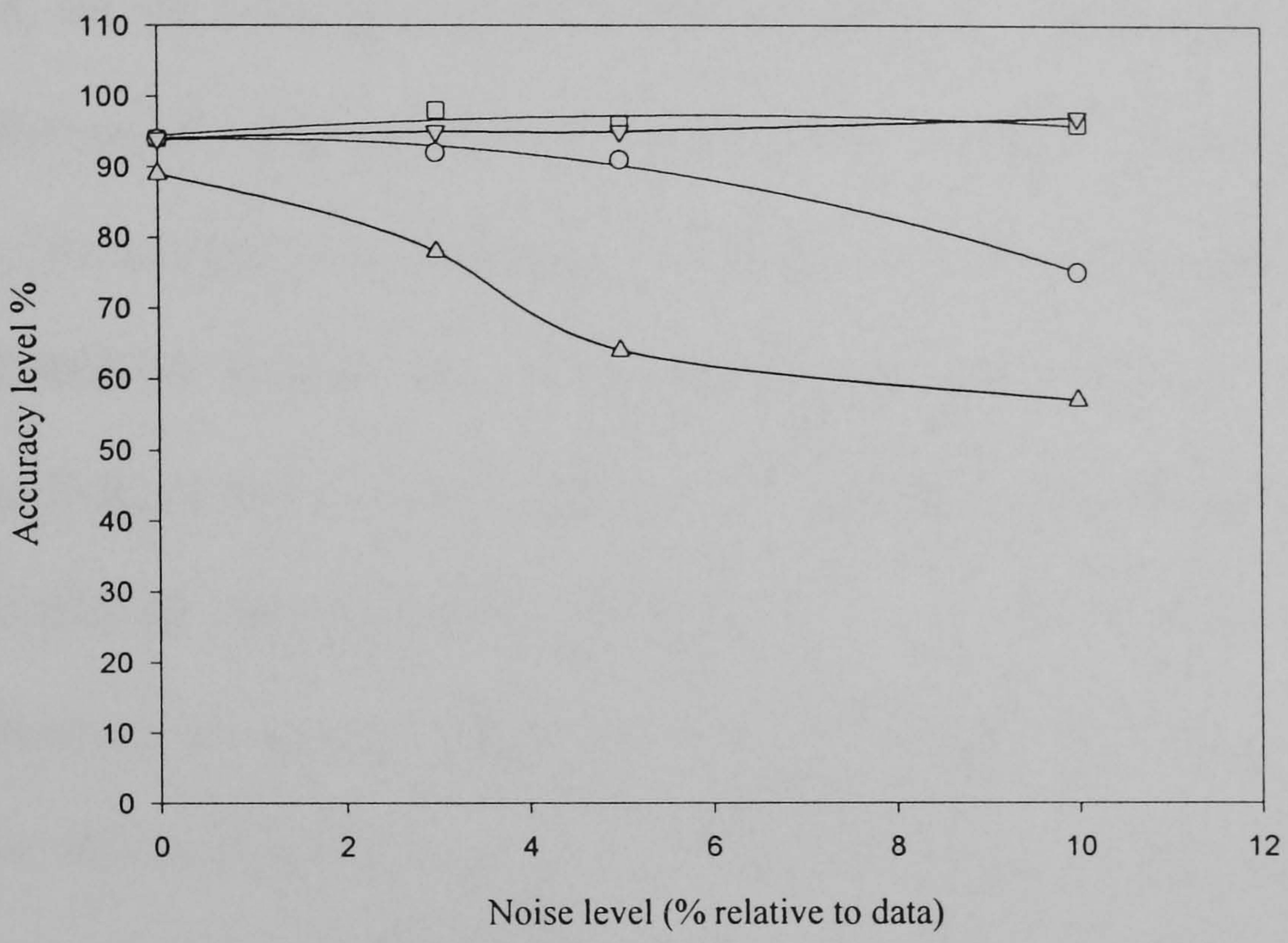

Figure 4.7 Accuracy level results for each parameter derived from a single shell model, as a function of noise in the ROT spectrum.

□ membrane relative permittivity e2.

∇ scaling factor EL.

○ internal conductivity s1.

Δ membrane conductivity s2.

4.5.2 *Three shell model fitting analysis*

In the case of the three shell model, the accuracy level for each parameter decreases as the percentage of noise in the ROT spectrum increases. In this analysis, the permittivity of encapsulated mediums e1 and e3 have been kept at 80.36, for the same reason as the previous analysis. Apart from these two parameters, all other parameters have been free to iterate. In the absence of noise, the accuracy of the scaling factor EL is 96% with a standard deviation of 0.0008459 (Figure 4.8). The accuracies of the outermost membrane permittivity e4 and conductivity s4 are 96% and 84%, with standard deviations of 0.002514 and 0.009874, respectively. The intermediate medium conductivity s3 accuracy value is 81% with standard deviation of 0.00362, whilst the accuracy levels for the inner membrane permittivity e2 and conductivity s2 are 77% and 24%, with standard deviations of 0.009502 and 0.04125, respectively. Lastly, the accuracy of innermost medium conductivity is 77% with a standard deviation of 0.00776.

As added noise increases up to 10% relative to the ROT spectrum value, the accuracy for most of the parameters has been reduced quite significantly. The accuracy level for the scaling factor has reduced to 87%, with the accuracy value for the outermost membrane permittivity and conductivity being reduced to 69% and 37%, respectively. Also, the accuracy value for the intermediate medium conductivity is 23%, the accuracy values of the inner membrane permittivity and conductivity are 18% and 4%, respectively, and the accuracy level for the innermost medium conductivity is 14%. These results may arise from two causes. The first is that the maximum number of parameters for the MATLAB minimisation route to cope with are normally five parameters so that the maximum number of parameters to be iterated has been exceeded. Secondly, as the number of shells for the model increases, determination of the complex permittivity of the inner shells of the model become more involved. Therefore, the accuracy level of the parameters to be determined reduce progressively as they go deeper into the core of the shell model.

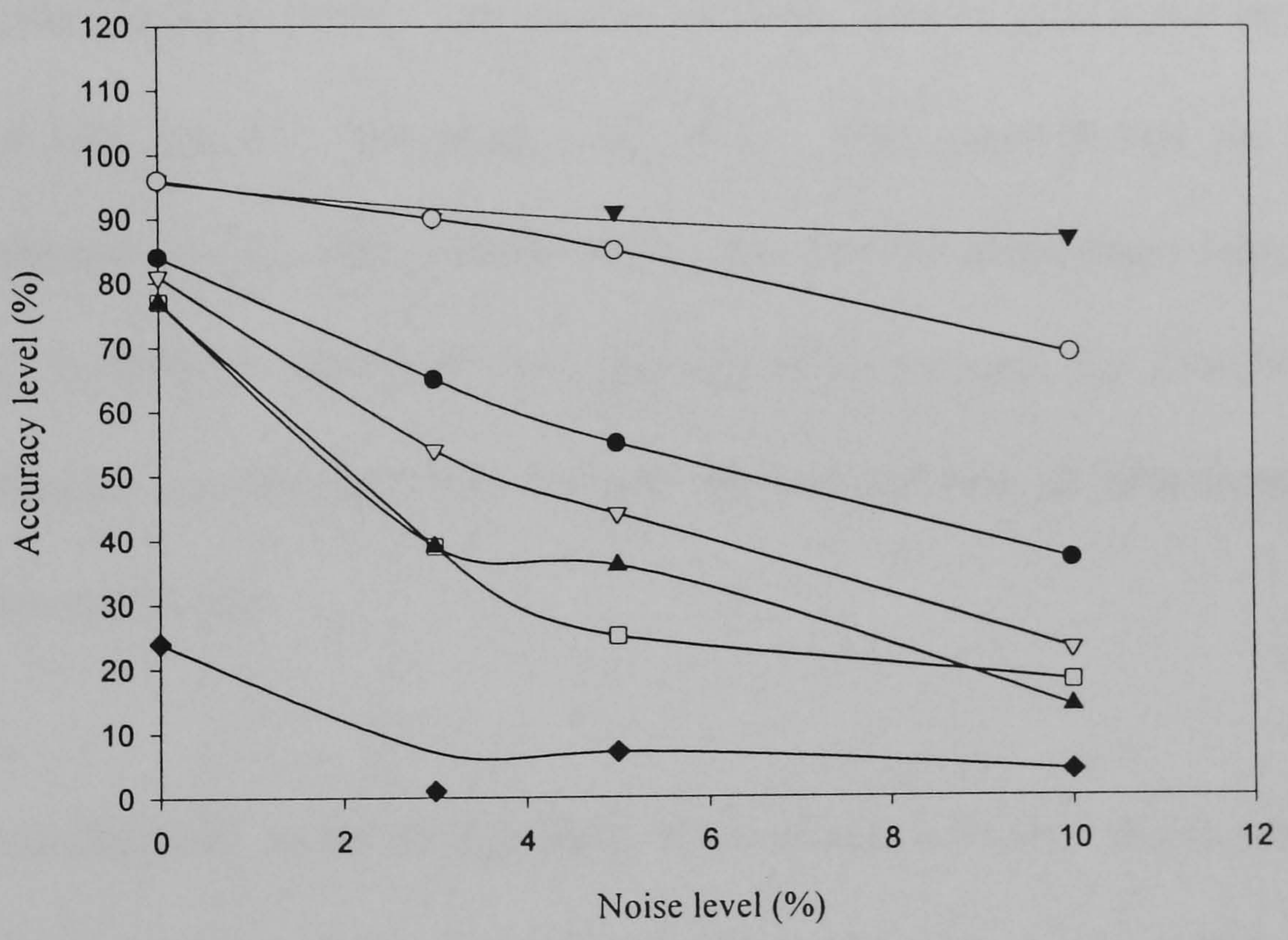

Figure 4.8 Accuracy level for each parameter of the three shell model with increasing noise in the ROT spectrum. ▼ : scaling factot EL; O: outer most membrane permittivity e4; ● outer most membrane conductivity s4; ∇: intermediate medium conductivity s3; □: inner membrane permittivity e2; ◆: inner membrane conductivity s2; ▲ : inner most medium conductivity s1.

Despite these problems, the major parameters such as the outermost membrane permittivity and the scaling factor can be determined reasonably well by using the three shell model to analyse some complex systems. As noise level decreases, the derived parameters for the outer shells become more reliable.

4.6 Discussion

4.6.1 *Vesicle Synthesis*

The phospholipid DOPC was used to form the vesicle membrane because it has a low transition temperature of $-4^{\circ}C$. This ensured that the vesicle membranes are physically stable in the experimental temperature region from $13^{\circ}C$ to $40^{\circ}C$. Cholesterol was introduced to decrease the fluidity of the membrane. In addition, this reduced the leakage rate of ions through the membrane [5, 6].

The conductivity of the encapsulated medium was $1.47Sm^{-1}$ which was about 100 times higher than that of the suspending medium, which had a conductivity of about $13mS.m^{-1}$. Using this high conductivity value for the encapsulated medium ensured that the interfacial dielectric dispersion to take place at a high frequency value, so that both co-field rotation and positive dielectrophoresis could be measured at the high frequency region.

Percoll has a high density value (1.129g/ml) and was introduced to the medium to be encapsulated. This allowed the vesicles to be centrifuged. During experiments, it also resulted in the vesicles settling on top of the electrode in less than about one minute. If vesicles were made in the absence of percoll, they did not settle on top of the electrode and remained evenly suspended in the medium.

4.6.2 *DEP Crossing Over Frequency for Unilamellar Vesicles*

The values of crossover frequency decreased as the unilamellar vesicle's radius increased (Figure 4.9), which is in good agreement with the theoretical prediction (equation(4.2)), since the membrane surface area of a vesicle and its effective capacitance increases with the vesicle radius. Base on this fact, the specific membrane capacitance of vesicles can be determined using the technique of Gascoyne et al [12, 13, 14]. The crossover frequency values of vesicles are plotted against the divided product of the suspending medium against their radii values (Figure 4.9), and the gradient of this graph divided by the product of $\left(\pi\sqrt{2}\right)$ provides the membrane capacitance value $7.26mF.m^{-2}$. By averaging all the membrane capacitance results for unilamellar vesicles, the mean capacitance value was $6.98mF.m^{-2}$ (Table 4.1).

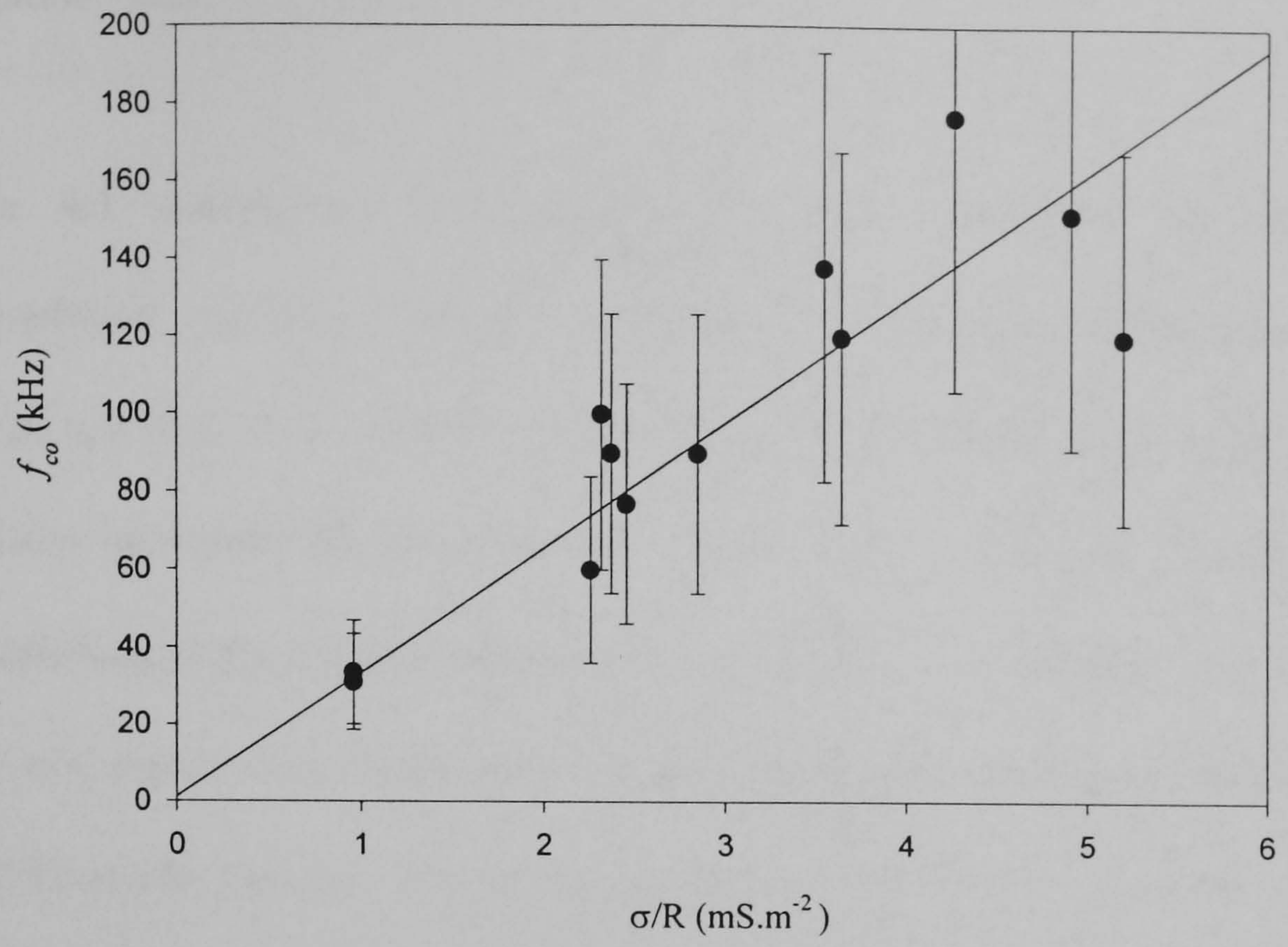

Figure 4.9 The gradient of this graph provides a value of $7.26mF.m^{-2}$ for the membrane capacitance (equation 4.2).

4.6.3 *Electrorotation results*

The hydrocarbon region of DOPC lipid bilayers is 2.7nm thick [19] and its relative permittivity can be taken as 2.25 [17]. Electrically, this capacitance appears in series with a contribution from the phospholipid head group region of the membrane that is 1.1nm thick [19] and has a relative permittivity between that of the hydrocarbon region and bulk water. Taking this permittivity value as 40, we derive an effective permittivity for the 3.8nm thick membrane of 3.09 (see chapter 2,appendix). The thickness *d* of each vesicle membrane can then be calculated from the relationship $d=\varepsilon_0\varepsilon_{mem.effective}/C_{mem}$.

Table 4.1 summarises the capacitance values determined for single-compartment vesicles having membranes of different thicknesses as determined both from parameter optimisation of the entire ROT spectra and the DEP crossover frequency values. While we did not have facilities to accurately quantify the fluorescent emission from the vesicle lipids (and hence their true membrane thicknesses), an estimate of the approximate thickness could be made visually. The membrane thickness calculated according to the above dielectric arguments are also shown in the table together with the closest corresponding integral multiple of a single 3.8nm phospholipid bilayer. A good correspondence was obtained between the dielectrically and visually determined thicknesses.

From the results of fluorescence microscopy, it was evident that some vesicles had more lipid content than others (ie the unilamellar vesicles, Figure 4.1a) because of the higher intensity of the fluorescence (Figure 4.1b). The membrane of second type of vesicles were multilamellar in nature [6, 20]. From Figure 4.4b, the multilamellar vesicle had an anti-field rotational peak and DEP crossing over frequency both at 900kHz. The radius of the vesicle was $5.64\,\mu m$. The membrane capacitance was 0.621mF.m^{-2} and the membrane conductivity was $2.7\times10^{-15}Sm^{-1}$. The inner encapsulated medium conductivity and permittivity were $1.38Sm^{-1}$ and 80.4 respectively. The suspending medium conductivity and permittivity were 13.55mS.m^{-1} and 80.4 respectively.

In figure 4.4a, the unilamellar vesicle had an anti-field rotational peak at about 110kHz with the DEP crossing over frequency at 90kHz. The radius of this vesicle was $5.25\mu m$. The membrane capacitance was $5.85mF.m^{-2}$, the membrane conductivity was $1.28\times10^{-16}Sm^{-1}$. The inner encapsulated medium conductivity and the permittivity were $1.07Sm^{-1}$ and 80.14 respectively. The suspending conductivity was $12.45mS.m^{-1}$.

The anti-field rotational peak of the ROT spectrum of the multilamellar vesicle was about one decade higher than the ROT spectrum of the unilamellar vesicle, as shown in figure 4.4. The crossover frequencies were consistent with the ROT spectra in both cases. By using the dielectric shell model to fit the ROT data of this type of vesicle, the membrane capacitance of the unilamellar vesicle was about 10 times higher than the capacitance of the multilamellar vesicle. From the theory given in chapter 2 (equation 2.81 and appendix), the membrane thickness of the vesicle can be analysed. From table 4.1, the membrane thickness of the multilamellar vesicle (Figure 4.4) is $45.3\pm0.7nm$ with the hydrocarbon core thickness of $31\pm0.7nm$; and the membrane thickness of the unilamellar vesicle is $4.1\pm0.1nm$ with the thickness of hydrocarbon core as $3\pm0.1nm$. The membrane conductivities of both the unilamellar and the multilamellar vesicles were very low. In the fitting program, a membrane conductivity below $1\times10^{-7}Sm^{-1}$ had very little effect on the ROT spectrum. This indicated that the membranes of these vesicles were very non-conductive. The original conductivity of the inner encapsulated medium was $1.47Sm^{-1}$. The conductivities of both the inner encapsulated media were slightly less than their original values. This suggests that a small number of ions had leaked out through the membrane from these vesicles. Since the conductivity values of the inner encapsulated medium of both unilamellar and multilamellar vesicles are close to each other, their co-field rotational peaks were in the same frequency region, which was about 100MHz.

4.6.3.1 *Single Shell Modelling*

From table 4.1, for vesicle type A, the mean specific membrane capacitance of unilamellar vesicles from the ROT and DEP crossing over frequency measurement was equal to $6.48mF.m^{-2}$. The mean specific membrane capacitance of unilamellar vesicles from DEP crossing over frequency measurement alone was equal to $6.98mF.m^{-2}$. From the ROT spectra, the dielectric expression in terms of the imaginary component of the Clausius-Mossotti factor was obtained [4,21,22]. The results from DEP crossing over frequency were the expression for the real component of the Clausius-Mossotti factor [4,21,22]. By comparing the mean specific capacitance values from the

ROT spectra and DEP crossing over frequency result, there was between 7.2% to 7.7% in difference. This indicated that the results between ROT and DEP were consistent with each other. On the other hand, the specific membrane capacitance for the solvent free di-(18:1)-lecithin is $7.21 \pm 0.21 mF.m^{-2}$ [23]. The specific membrane capacitance for lecithin with $2.8nm$ as the hydrocarbon core thickness was $6.82 \pm 0.014 mF.m^{-2}$ at $21°C$ [11]. The hydrocarbon core thickness of DOPC of a single bilayer was $2.8nm$ [19]. Both of these measurements were made using the black lipid membrane (BLM) capacitance. The results from ROT and DEP were in good agreement with these BLM measurements [11,23,24].

The effective capacitance value of the multilamellar vesicle with single medium compartment (Figure 4.4) was twelve times less than the capacitance value of the solvent free di-(18:1)-lecithin BLM. This may result from the difference in membrane thickness, due to the bilayer stacking in mutlilamellar vesicles.

Since a phospholipid bilayer consists of a hydrocarbon hydrophobic region sandwiched between two phosphate head group hydrophilic regions, it may be appropriate to include the dielectric properties of these two regions in order to calculate the total bilayer thickness of a DOPC vesicle. Based on the experimental membrane capacitance values of DOPC vesicles, the thickness of the vesicle membrane could be calculated by using the parallel plate capacitor equation:

$$C_{mem} = \frac{\varepsilon_o \varepsilon_r A}{d} \tag{4.3}$$

$$C_{spe.mem} = \frac{C_{mem}}{A} = \frac{\varepsilon_o \varepsilon_r}{d} \tag{4.4}$$

where C_{mem} is the membrane capacitance, ε_o is the relative permittivity of free space ($8.8543 \times 10^{-12} Fm^{-1}$), ε_r is the relative permittivity of the vesicle's membrane and d is the membrane thickness. $C_{spe.mem}$ is the specific membrane capacitance per unit effective surface area A. Relative permittivity values of both the hydrocarbon and phosphate head group at different temperatures could be calculated using the well known Lorentz formulation for a dielectric (equation 2.81 from Chapter2). Using equation A(5) in Chapter2, appendix, the thickness of the hydrocarbon region could also be calculated. The total bilayer thickness could then be found by the addition of the thickness of phosphate head group (A(6) in Chapter2, Appendix) which was within the bilayer region. The relative permittivity of the hydrocarbon chain was chosen to be 2.25 at $23°C$. This is the relative permittivity of Parawax [17]. This value is considered to be more suitable than the value for oleic acid of 2.46 at $20°C$ [17] because the hydrocarbon region of phospholipids does not contain a free proton from the acid, which would increase the permittivity value. In this analysis, the bilayer thickness of the phosphate head group was kept at $1.1nm$ [25] and unchanged throughout all the different temperatures. The mean membrane thickness of the bilayer membrane was $4.07 \pm 0.09nm$ (Table 4.1).

By comparing with known data of X-ray scattering measurements [19], the unilamellae membrane thickness of dioleoyl-phosphatidyl choline is $3.8 \pm 0.1nm$ with the thickness of hydrocarbon region being $2.7 \pm 0.1nm$ at $20^\circ C$. The thickness of the phosphate head group region is $1.1nm$ [19]. At the same time, the results of this investigation is also consistent with the rms GMO membrane thickness of $3.6nm$ at $20^\circ C$, which was measured using the quasi-elastic light scattering method by Crawford and Earnshaw in 1986 [25].

In the case of unilamellar vesicles, the mean thickness of the hydrocarbon region from this analysis is higher than the bilayer thickness of the hydrocarbon region of pure phosphatedyl choline [19]. This may suggest that there are some unwanted solvent residues, such as chloroform trapped inside the hyphobic region. Therefore, this can explain why the mean specfic membrane capacitance value from the ROT and DEP measurements was slightly low compared with the solvent free di-(18:1)-lecithin specific membrane capacitance value [23]. It is because the bilayer thickness has increased due to organic solvent content.

From the results obtained for the oligolamellar vesicles with single medium compartment (Table 4.1), vesicle type B, their membrane thickness is twice the value of the unilamellar vesicles and solvent free di-(18-1)-lecithin bilayer membrane. This suggests that these types of vesicle were double bilayer membrane in nature [6]. The same principles were applied for a single layer membrane with four and five layer of bilayer present in the membrane (Table

4.1), vesicles typies C and D. From the analysed results of the multilamellar vesicles with single medium compartment (Figure 4.4), the membrane thickness is twelve times larger than the bilayer membrane thickness, $3.8 \pm 0.1nm$ [19]. This suggests that this multilamellar vesicle contained 12 layers of bilayer membrane. On the other hand, the mean bilayer hydrocarbon thickness of these oligolamellar and multilamellar vesicles (Table 4.1) are less than the bilayer hydrocarbon thickness of solvent free phosphatedyl choline. This agrees with the observation of Lis et al in 1982 [20]. If there is some ionic solution that has been encapsulated between the phosphate head group of each lamellae layers, the hydrocarbon region can be compressed by the pressure from this ionic solvent. This will cause the hydrocarbon region to reduce in thickness. The limiting thickness for DOPC bilayer maximally hydrated in water is $3.2nm$ [20]. The bilayer thicknesses of oligolamellar and multilamellar vesicles are all between $3.8nm$ and $3.2nm$. Therefore, the values for the membrane thickness are in good agreements amongst these reports.

At the same time, co-field rotation has also been observed in the low frequency region (below 1kHz) for mutlilamellar vesicle with single medium compartment (Figure 4.4). This agrees with the observation by Wicher *et al* [1, 2, 3]. There is the possibility that an α-dielectric dispersion has been induced by proton ions, which interact with the membrane surface of the multilamellar vesicle [1] in the low frequency region. The pH of the suspending medium is 7.1 ± 0.05. Since this causes the membrane surface of a multilamellar vesicle to behave as conductive matter with a conductivity value higher than that of the suspending medium, co-field rotation would take place from this α-dispersion. However, co-field rotation has not been found in unilamellar vesicles and the single shell oligolamellar vesicle. On the other hand, membrane properties such as membrane thickness of vesicles and the amount of bilayers present in the membrane can be determined by using the membrane capacitance values. Also, the ROT spectra of multilamellar vesicles can be fitted by the theoretical description of the dielectric (multi-)shell model. These results contradict the assumptions of D. Wicher and J. Gündel in 1989 [2].

4.6.3.2 *Three Shell Model Fitting*

For frequencies below the "cross-over" frequency, most of the applied electric field is dropped across the outermost membrane layer of the vesicle. The applied electric field does not penetrate through this outermost membrane at low frequencies. Therefore, the electro-rotation spectrum is dominated by the dielectric properties of the outermost membrane in the low frequency region (Figure 4.5).

As the frequency of the applied field increases, the dielectric relaxation of the outermost membrane takes place. This allows the applied field to penetrate through this outermost membrane, increases the amount of voltage drop across the inner membrane, and influences the net dielectric dispersion of the vesicle as a whole. As the frequency increases from the low frequency region, the anti-field rotation gradually becomes influenced by the dielectric dispersions of the outermost and the inner membrane layers. Therefore, the anti-field rotation becomes broader after the DEP crossing over frequency has occurred. In this frequency region, more or less the same amount of voltage is dropped across the inner membrane and the outer membrane of the vesicle.

At the co-field rotation region, dielectric dispersions of both the intermediate medium and the inner membrane layer takes place under the exposure of the applied electric field. Both of the inner and outer membranes are short-circuited at this high frequency region. Therefore, the co-field rotation spectrum will be the product of the dielectric dispersions of the intermediate, innermost medium and the remnant of the anti-field rotation from the inner membrane. However, the DEP crossing over frequency is manifested from the inner membrane of the vesicle if the conductivity value of the intermediate medium is low or close to the value of the surrounding medium conductivity. This is because the effective dipole moment would be too weak to allow the positive DEP to take place. Otherwise, the DEP crossing over frequency is manifested by the domination of the dielectric properties of the outermost membrane of the vesicle.

4.6.3.3 *Five Shell Modelling Fitting*

When a five shell model is applied for analysis, a vesicle normally contains three separate membrane layers with two medium compartments, or it would be a more complex system which cannot be fitted by a three shell model. The anti-field ROT spectrum is much wider than any spectra of oligolamellar vesicles with two medium compartments (Figure 4.5), and the sequence of the dielectric dispersion to take place is similar to the oligolamellar vesicle of the three shell model. The five shell model can effectively become an equivalent circuit for analysis on complex systems, such as a more complicated multilamellar vesicle or even multi-veiscular liposomes. If a five shell model is inadequate to analysis a more complex system, the number of shell layers on the model can be added to compensate the complexity of the system, eg multilamellar vesicle.

4.6.4 Time variation control experiment

In this experiment, an oligolamellar vesicle with a single compartment was measured four times repeatedly by ROT and DEP crossing over frequency, over a period of six hours (Figure 4.10). As the time of the experiments progressed, the membrane conductivity of the vesicle increased slightly (Table 4.2). There was a possibility that the vesicle had gathered ions from the suspending medium which would increase the membrane conductivity value. On the other hand, the suspending medium inside the electrorotation chamber could have evaporated graduately over the long period of time of the experiments. This could increase the viscosity value of the suspending medium. Consequently, the magnitude of the ROT spectra of the same vesicle became reduced as time increased (Figure 4.10). This phenomenon had been shown by the reduction of the scaling factor.

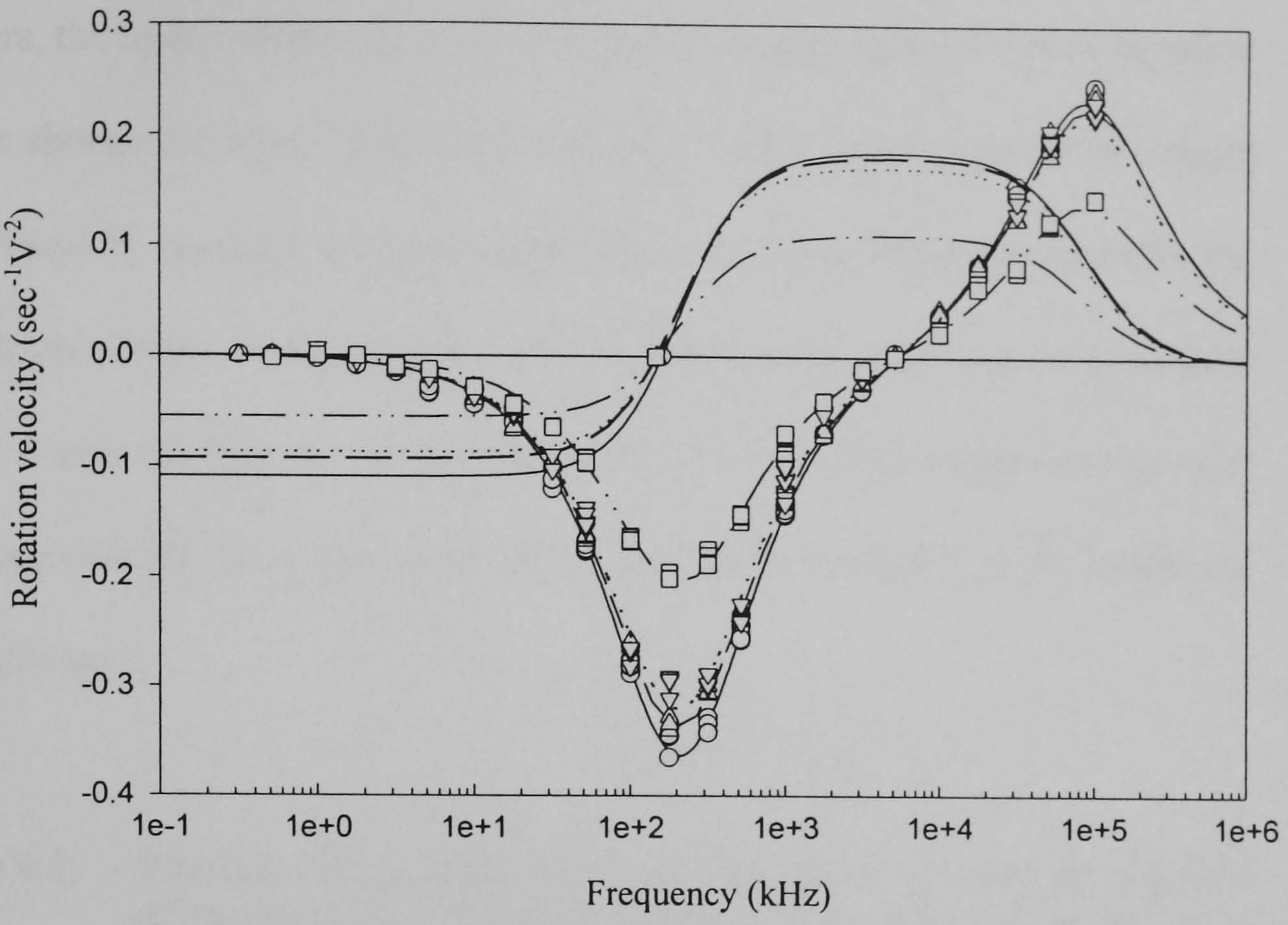

Figure 4.10 Time valuation experiments: as time increased, magnitude of both ROT and DEP spectra decreased gradually. ROT and DEP spectra with solid line "_" represented the 1st experiment to be taken. Line "_ _" represented the 2nd experiment, 1.5 hours after the 1st experiment. Line "....." represented the 3rd experiment, 3.5 hours after the 1st one. Line "_.._" represented the 4th experiment, 5.75 hours after the first one. Symbol O, Δ, ∇ and □ are DEP crossing over frequency points and the ROT data respectively for the 1st ,2nd, 3rd and last experiments.

At the same time, the encapsulated medium conductivity of the vesicle had decreased very slightly. This indicated that a small number of ions had leaked out through the lamellae membrane from the vesicle. Also, the membrane capacitance had increased very slightly as time for the experiments increased. There was a possibility that a small amount of medium had diffused into the hydrophilic region between two unilamellar layers of the membrane. As the medium solvent penetrated between the phosphate head groups of these bilayers, the hydrocarbon chain of the hydrophobic group would be compassed and be shorten in length [20]. Consequently, the overall membrane thickness contributed by the lipid layer would be reduced. Thus, this might increase the overall membrane relative permittivity and hence the membrane capacitance value. Never the less, the vesicles proved to provide quite stable samples over long periods of time for both ROT and DEP crossing over frequency experiments.

Table 4.2: Summary of analysed results for the same vesicle over a period of specific time. Internal permittivity assumed to be 80.36 at 21°C.

Procedure of time from the 1st experiment (hours)	**Crossing over frequency (kHz)**	**membrane capacitance** ($mF.m^{-2}$)	**membrane conductivity** (Sm^{-1})	**internal conductivity** (Sm^{-1})	**scaling factor**
0	160	3.17	8.48×10^{-8}	1.09	9.7×10^{11}
1.5	155	3.24	4.612×10^{-7}	1.10	9.3×10^{11}
3.5	149	3.34	1.021×10^{-6}	1.06	9.3×10^{11}
5.75	146	3.38	1.142×10^{-6}	1.05	7.47×10^{11}

4.6.5 Temperature variation control experiment

In this experiment, various samples of vesicles were measured by ROT and DEP crossing over frequency through the temperature range from about $10°C$

to 40° C (Figure 4.11). As temperature increased, this also increased the conductivity value of the surrounding medium and the encapsulated medium inside the vesicle [17]. This raised the DEP crossing over frequency of a vesicle [12].

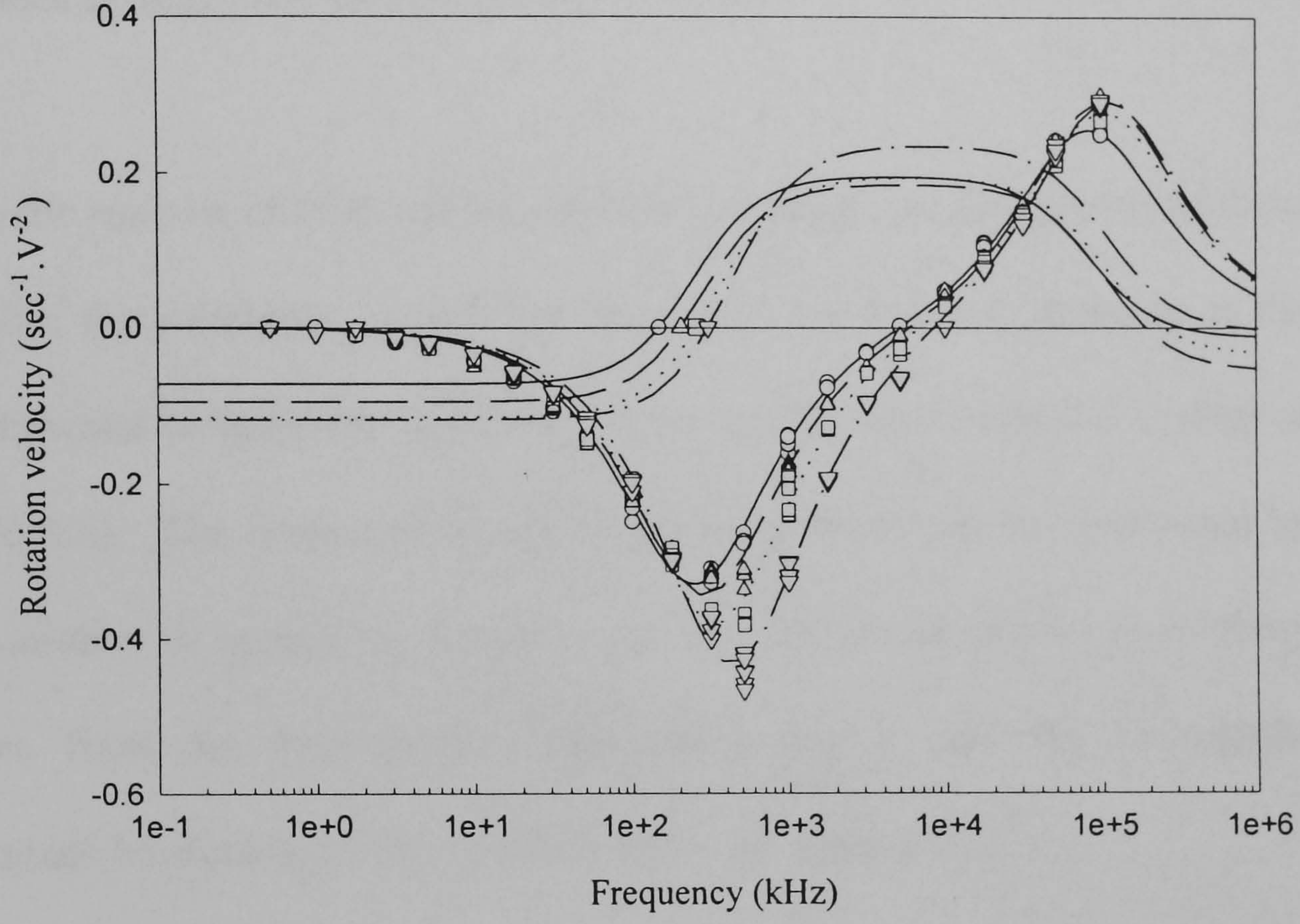

Figure 4.11 Measurements of ROT and DEP for a vesicle at $21^{\circ}C$, $30^{\circ}C$, $15.6^{\circ}C$ to $40^{\circ}C$. Solid line '_' and 'o' represents theoretical fitting and data points at $15.6^{\circ}C$. Dash line '--' and 'Δ' for values of $21^{\circ}C$. Doted line '...' and '□' for values of $30^{\circ}C$ and dashed doted line '-.-' and '∇' for values of $40^{\circ}C$.

From equation (4.2), the DEP crossing over frequency f_{co} is proportional to the conductivity of the surrounding medium σ_s. C_m and r are the membrane capacitance and the radius of the vesicle respectively. At the same time, an increment on conductivity value of the surrounding medium causes the dielectric dispersion of the vesicle to occur at a higher frequency. Thus, the peaks of anti-field and co-field rotations migrate to the high frequency region. On the other hand, the viscosity of the surrounding medium decreases as the temperature of the medium increases [17]. This phenomenon will reduce the frictional force from the medium, so that the rotational speed of the vesicle increases in magnitude as temperature increases.

From the analysis of ROT spectra and DEP crossing over frequencies of these vesicles, the membrane capacitance of vesicles are found to decrease as the experimental temperature increases. These results agree with the finding of White [26]. The change of the membrane capacitance can be contributed by the variation in membrane thickness and the changes of relative permittivity values from the hydrophobic hydrocarbon region and the hydrophilic phosphate head group of the membrane layer of vesicles.

From measurements of electron spin labelling (EPR) experiment, bilayer membrane fluidity measurements has been carried out at different positions of the hydrophobic hydrocarbon chains by using 5-doxyl sterate, 12-doxyl sterate and 16-doxyl sterate. Figure 4.12 shows that this membrane increases in fluidity from position 5 to position 16 of the hydrocarbon chains. As temperature increases, the inner part of the lipid bilayer is getting more fluid than the outer part.

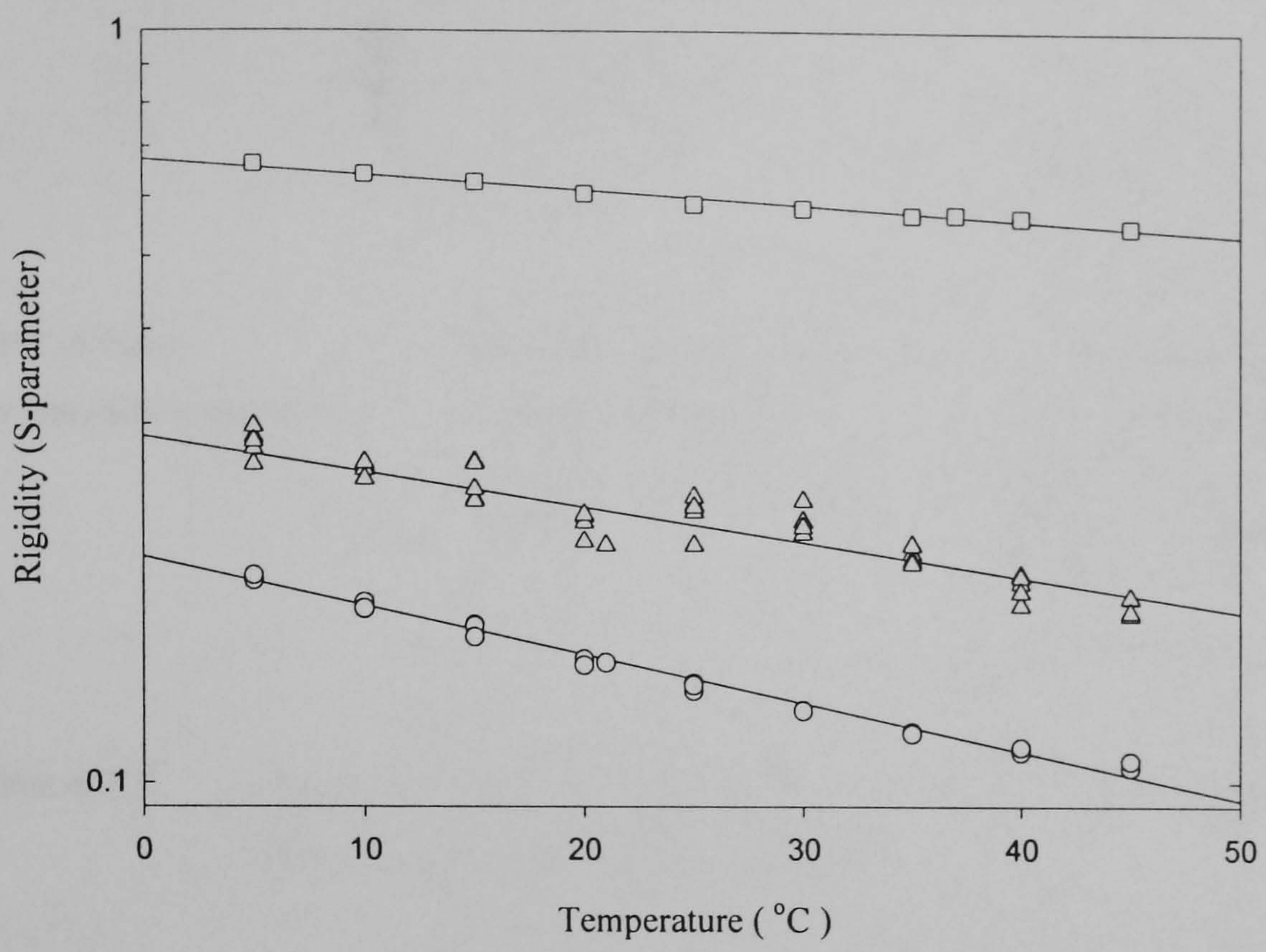

Figure 4.12 Fluidity of lipid membrane varies with temperature. In hydrocarbon chains, position 16(o) is more fluid than position 12(Δ) and position 5 (□).

This is because the hydrocarbon chains increasingly absorbed more thermal energy with increasing temperature. This finding might suggest that the hydrocarbon chains move in a larger volume of space as the temperature increases. Thus, lipid bilayers have to swell up in the longitudinal direction in order to provide the volume for hydrocarbon chains to rotate (Figure 4.13). On the other hand, the presence of cholesterol restrains the lipid bilayers for planar direction movement [6]. Thus there is only small amount in changes for vesicles' radii through out the whole experiment.

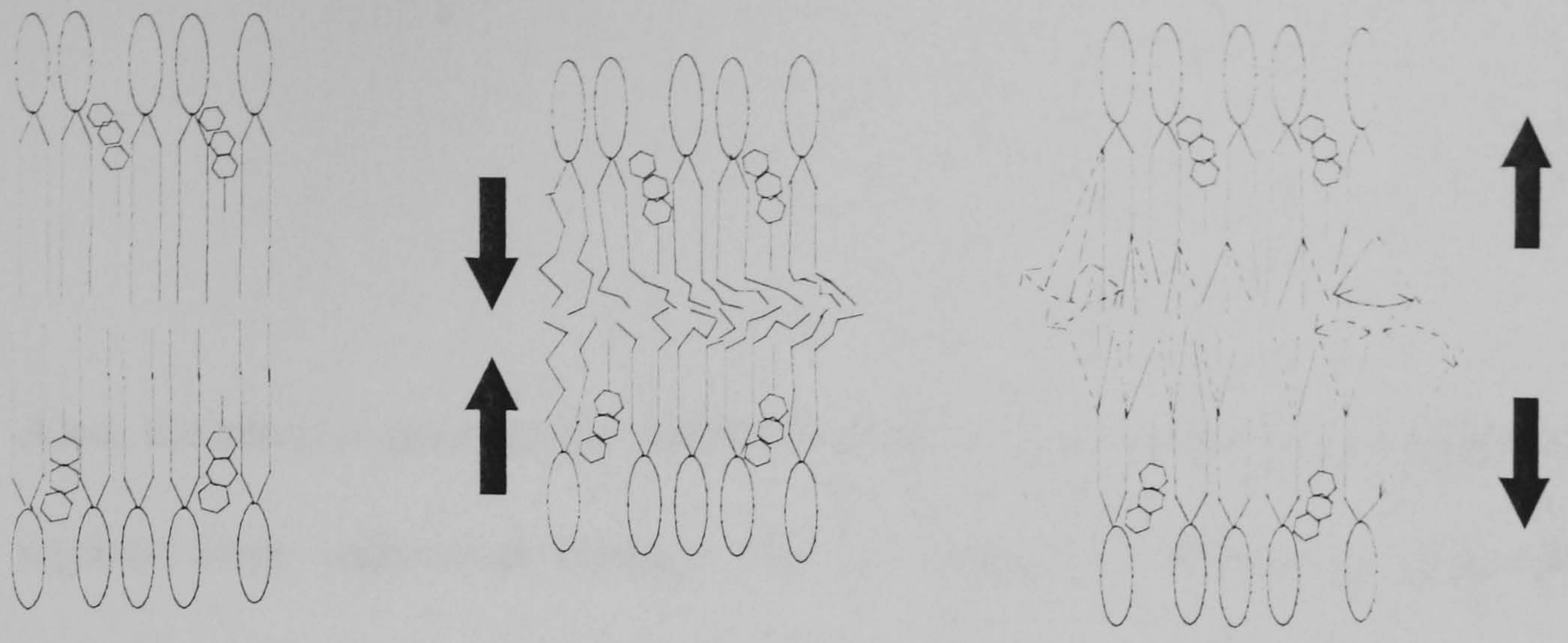

"Solid" Gel Phase
Below transition temperature

Gel to Liquid crystalline state
At transition temperature
membrane thickness decreases

"Fluid" Liquid crystalline state
Above transition temperature
membrane swells up by fluctuation movement of hydrocarbon chains

Membrane thickness increases

Figure 4.13 Changes of membrane thickness in phospholipids bilayer with cholesterol from gel state to liquid crystalline state.

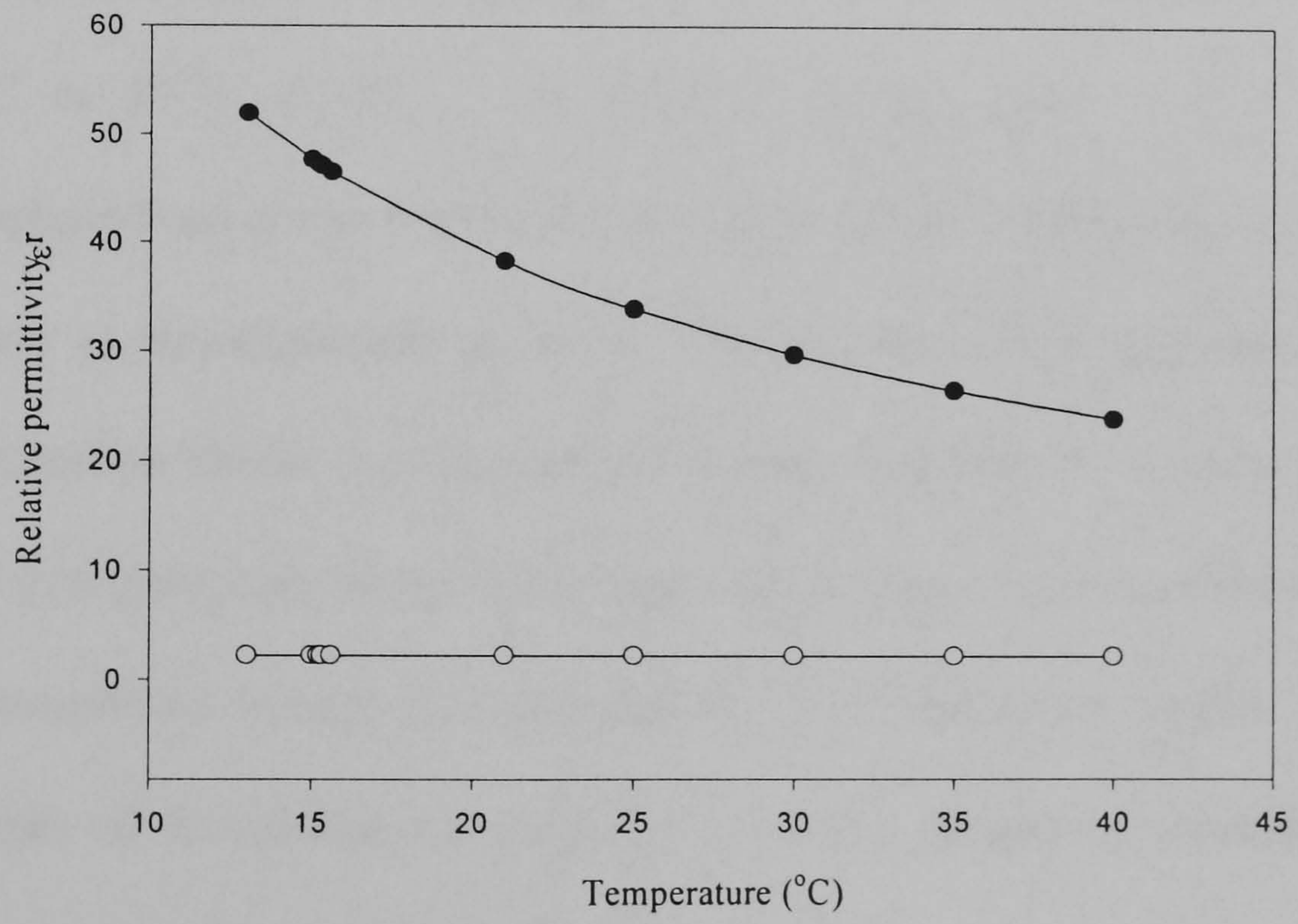

Figure 4.14 As temperature increases, the relative permittivity of phosphate head group (•) of DOPC had decreased significantly compared with the relative permittivity of the hydrocarbon region (o) of DOPC.

Also, the relative permittivity values for both of hydrophilic and hydrophobic regions were calculated through out the temperature range by using the Lorentz dielectric formulation [27] (Chapter2). The alteration of these relative permittivity values are shown in figure 4.14.

At the same time, the refractive index of hydrocarbon region is 1.438 [26] which gives the high frequency permittivity ε_∞ as 2.07 (chapter2: Appendix B). Based on the Lorentz formulation, the relative permttivity ε_s of the hydrocarbon region has changed very slightly, 2.26 at $13°C$ to 2.24 at $40°C$. The relative permittivity of phosphate head group has changed from 51.93 at $13°C$ to 23.98 at $40°C$. In terms of an RC network, the hydrophilic phosphate head group region and the hydrophobic hydrocarbon chain region behave as two capacitors in series. Because the relative permittivity of the hydrocarbon chains is comparatively smaller than that of the polar phosphate head group throughout the whole temperature range, the overall capacitance of the membrane bilayer is dominated by the hydrocarbon chains. Thus, the changes of membrane capacitance are closely related to variations of the hydrocarbon chain thicknesses in the membrane.

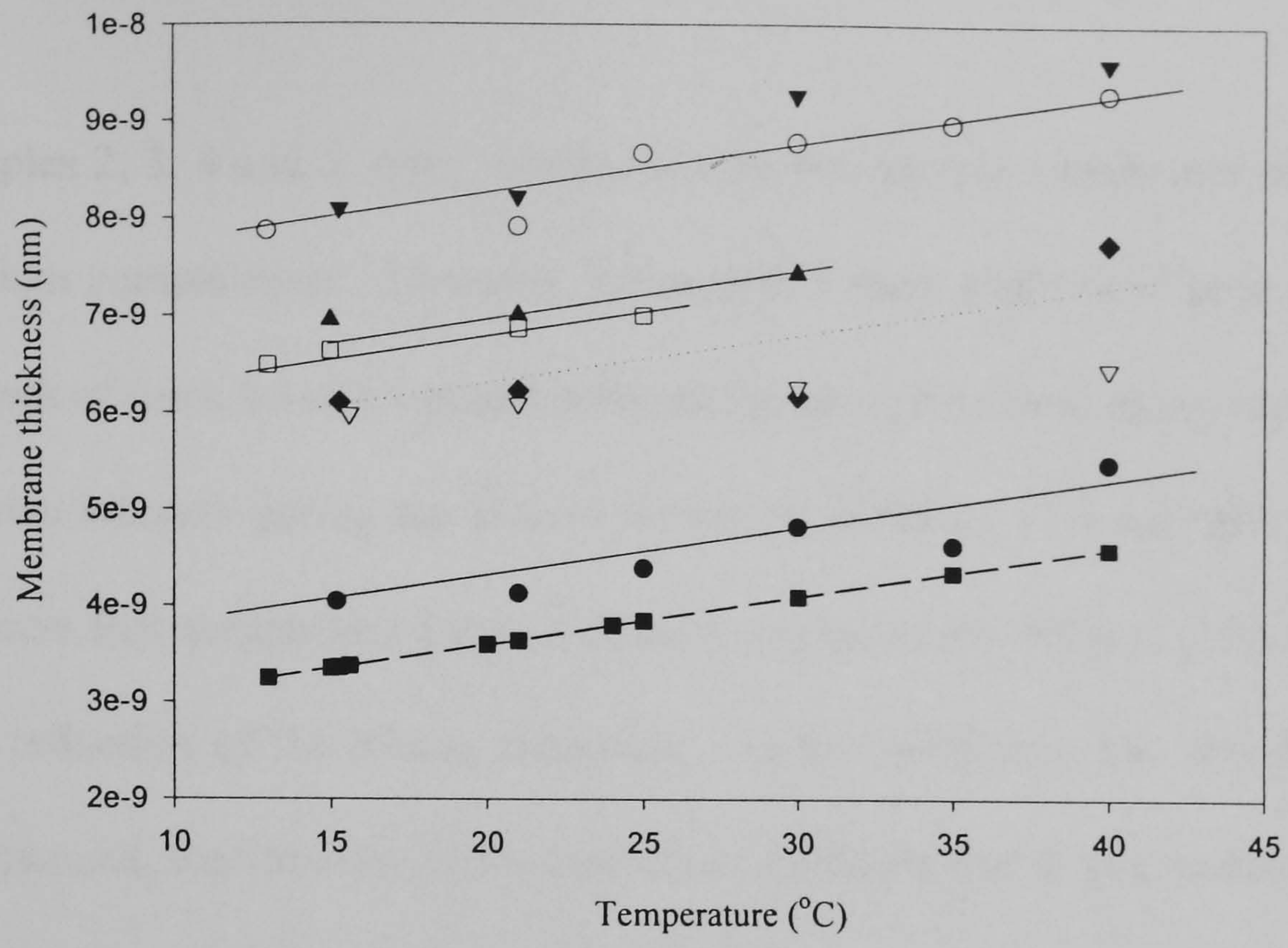

Figure 4.15 ■ represents the membrane thickness changes of glycerol monooleate (GMO) using quasi-elastic light scattering by Crawford and Earnshaw. All remaining data are for DOPC obtained by ROT and DEP. ● sample 1, a single unilamellar membrane. ∇ is sample 2; ♦ sample 3; □ sample 4; ▲ sample 5; O sample 6 and ▼ sample 7, which all have two layers of unilamellar membrane.

The membrane thickness d_m of each vesicle can be calculated (Figure 4.15) by using these relative permittivity values and membrane capacitance measurements, derived from the ROT data as described in chapter 2 (appendix A). Samples 2 to 7 are single medium compartment vesicles with two bilayers membrane. Apart from sample 2, the rates of change in membrane thicknesses of all these vesicles vs temperature are consistent with the results of Crawford and Earnshaw in 1986 [25] obtained using the quasi-elastic light scattering technique to monitor the GMO membrane thickness of solvent free BLM.

Samples 2, 3, 4 and 5, were vesicles having two bilayer membranes with one medium compartment. However, for sample 2 there might have been a small amount of ionic solvent trapped between the phosphate head group regions of the two bilayers during the vesicle formation process. This will give rise to pressure that compresses the hydrocarbon region of the bilayers [20], leading to a reduction of the bilayer thickness. As the membrane has already been compressed, the variation of the membrane thickness due to temperature effect will be less dominant, and could explain the results obtained for sample 2, shown in figure 4.15. The thickness of sample 3 is very close to sample 2. Thus, the step function increase in thickness at around $40^{\circ}C$ may have resulted from expulsion of the ionic solvent trapped between the two lamella.

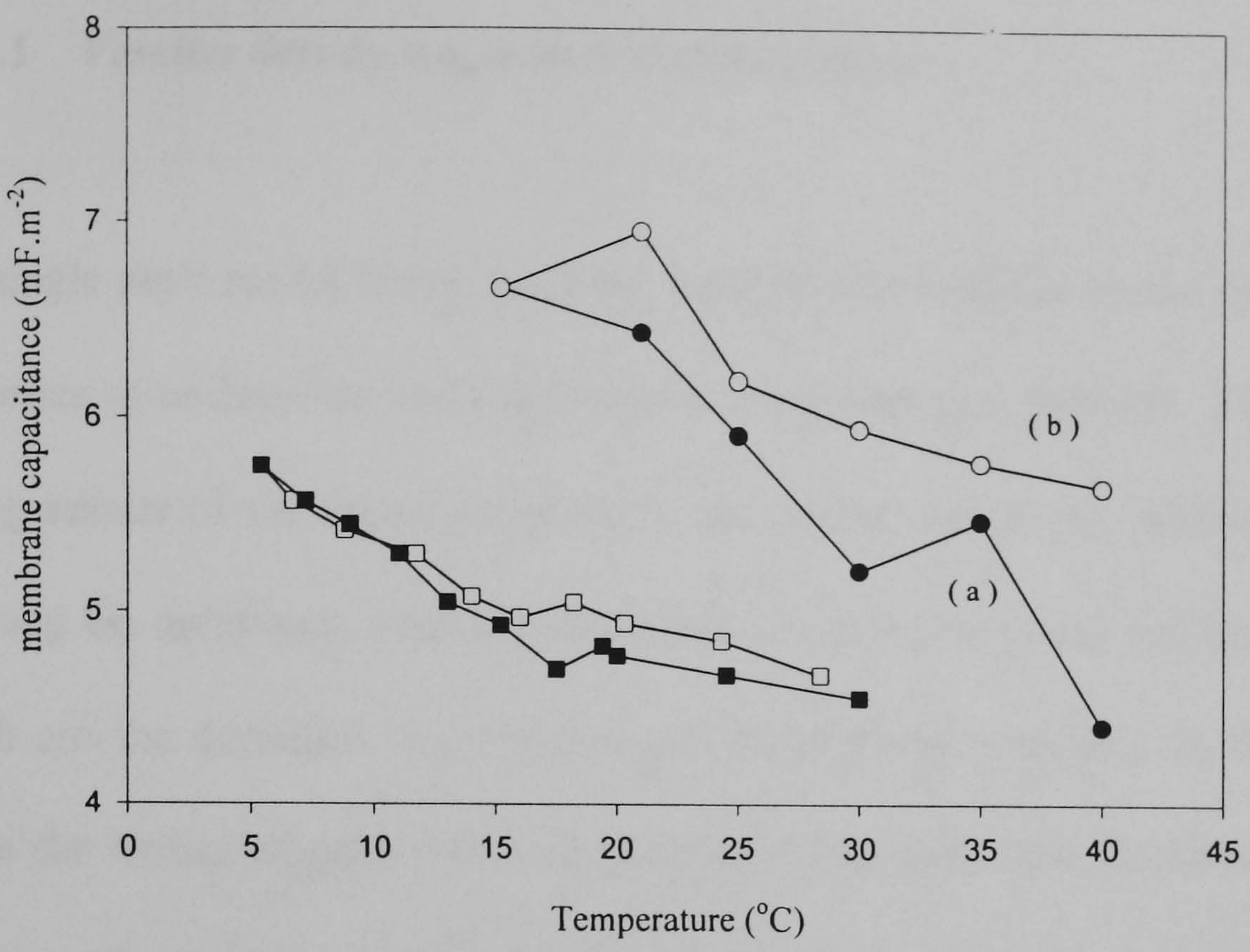

Figure 4.16 Membrane capacitance of DOPC sample 1 as a function of temperature. ● represents the cooling process for the vesicle. ○ represents the warming process of the vesicle after the cooling process. ■ and □ are of the cooling and re-warming process data respectively, on glycerol monooleate (GMO) black lipids membrane from White [26].

For the case of sample 1, it was cooled down from $40^\circ C$ to $15^\circ C$ in a controlled manner while ROT measurements were taken, and then re-heated again up to $40^\circ C$. From these observations for sample 1, a hystersis process was revealed as shown in figure 4.16. From the deduced capacitance values of this sample (Figure 4.16), the results are in good agreement with the hysteresis phenomena of GMO observed by White in 1975 [26].

4.6.6 Dielectric Shell Modelling Fitting

4.6.6.1 *Vesciles data by single shell model analysis*

The single shell model fitting has been used for the analysis on the dielectric properties of unilamellar and single medium compartment vesicles. From the testing results of the fitting program, it has proved that it can achieve good accuracy on membrane permittivity, internal conductivity and scaling factor which are the dominant dielectric properties of those vesicles. In the case where the fitting algorithm fits the synthetic data with 10% Gaussian noise presence, the overall confident level for dominant dielectric properties are fallen to between 75% and 96%.

The percentage of confident limit of membrane permittivity in the former case is up to 96%. The percentage of confident limit of internal conductivity is up to 75% and the percentage of confident limit of scaling factor is up to 97%. The confident limit for less dominant factors, such as membrane conductivity is poor if the value of the membrane conductivity is low compared with the suspending medium conductivity. If membrane conductivity is about four decades less than the medium conductivity, its influence to the interpretation of the experimental data would be overshadowed by the membrane permittivity and the medium conductivity. If the true scaling factor value for the analysis on the ROT data is known within a limited range, the confident limit of the membrane conductivity and other parameters can be improve quite significantly.

In normal experimental conditions, the noise present within good experimental data will be far less than 3% in Gaussian distribution. Therefore the confident level for the interpretions of dielectric properties of vesicles would be much higher than the confident level of synthetic data with 10% Gaussian noise presence.

4.6.6.2 *Vesicles data by three shell model analysis*

Three shell model fitting algorithm can be used as a tool to fit experimental data from a more complicated concentric system. In this case, obligolamellar vesicles and liposome with two membrane layers have been fitted by this algorithm. From figure 4.5, the ROT data has a wide β dispersion [3] which has been revealed as the anti-field rotation spectrum. This may suggest that there is more than one shell of membrane layer present in order to contribute this complex dispersion. This complex dispersion can be the summation of dielectric relaxations from two separate individual membrane layers and their intermediate encapsulated medium which superimposes on each others. By using fluorescent microscopy, these liposomes are shown to be obligolamellar vesicles which have two concentric membrane layers and two medium compartment (figure 4.1c). In this situation, single shell fitting algorithm is not possible to fit the ROT data from such liposomes because of their complexity.

By testing the accuracy of each parameter, the scaling factor is the most accurate parameter that can be given by this three shell model. This is followed by the outermost membrane dielectric parameters. As the analysis goes further into the inner core of this model, the accuracy of each parameters falls graduately. In the situation of 0% noise present, accuracies of most dielectric parameters are at around 77% or above, but the innermost membrane conductivity has fallen down to 24%. This is because the inner most membrane conductivity parameter has one of the smallest values of all the parameters. On the other hand, the analysis of dielectric properties are becoming more complex as it goes deeper into the core of the shell model. Also, this analysis has exceeded the maximum amount of the parameters to be determined by the MATLAB minimisation route. Therefore, the accuracy of most parameters have fallen quite seriously as noise has begun to affect the ROT data. Especially, the inner most membrane conductivity is the worst to be affected.

In the measurements of obligolamellar vesicles, ROT experimental data can be very reliable if there is not leakage of ions through the membrane of the vesicle. Thus the analysed parameters using the three shell model can be quite accurate. However, the accuracy of the analysed parameters can be seriously affected as the problem of ions leakage enlarges.

4.6.6.3 *Vesicle data using five shell model fitting*

The five shell model was used to analyse the more complex systems, such as the multilamellar vesicles with multi medium compartments in figure 4.1d and the multi-vesicular liposome in figure 4.1e. The ROT spectrum of a mutli-lamellar vesicle is shown in figure 4.6. In this model fitting, the problem of this analysis is the same as that of the three shell modelling fitting. If the number of dielectric parameters to be analysed can be reduced to five, the accuracy of the determined dielectric properties can be increased to the situation of the single shell model. However all the true values of the noniterated parameters have to be known before the analysis is initiated.

4.7 Conclusion

By using ROT and DEP crossing over frequency measurements, vesicles are used as simple non-conductive spheres with known internal dielectric properties to test the dielectric multi-shell model. Dielectric properties of vesicles in both simple and complex form can be analysed and obtained very accurately.

From flow cytometry analysis, two main groups of vesicles are to be found. They differ by the lipids present in the membrane, having either low or high lipid concentrations. In the case of low lipid concentration, vesicles are unilamelle and oligolamelle in nature. In the case of high lipid concentration, vesicles are multi-lamelle in nature. For unilamellar, oligolamellar and multilamellar vesicles with a single medium compartment, they can be analysed by using a single shell model. The amount of lipids bilayer in the membrane of vesicles can be determined by their membrane capacitance values and a known membrane thickness. Oligolamellar and multilamellar vesicles with more than one medium compartment present cannot be fitted by the single shell model. Oligolamellar vesicles with two separate medium compartments present can be fitted by a three shell model (figure 4.5). In the case of multi-lamellar vesicles with multi-medium compartments present, more shells are required in the model. For each extra membrane, two additional shells are required in the model. For example, a vesicle with three separate membranes can be fitted by using a five shell model (figure 4.6). Once the ROT data of any kind of vesicle is fitted by its required shell modelling, any increase in the number of shells included would not help or alter the original best fit data.

Variation of experimental temperature can change the dielectric properties of vesicles. From these experiments, the value of membrane capacitance decreased with increment in temperature. It is caused mainly by the increments of membrane thickness in the hydrophobic region. At the same time, the relative permittivity of the membrane and the medium are also decreased with the increment of temperature.

In conclusion, ROT and DEP crossing over frequency analysis can detect dielectric properties of various types of vesicle very accurately. Thus, these technique have been shown to be good analytical tools to analyse cellular structure of biological cells, in conjunction with the application of the dielectric multi-shell model.

4.8 Reference

1. D. Wicher, J. Gündel (1989)Existence of a low-frequency limit for electrorotation experiments, *Studia Biophysica* **134** 3 223-226

2. D. Wicher and J. Gündel (1989) Electrorotation of multi- and oligolamellar lipsomes, *Bioelectrochemsitry and Bioenergetics* **21** 279-288

3. D. Wicher, J. Gündel, H. Matthies (1986) Measuring chamber with extended applications of the electrorotation. α- and β-dispersion of lipsomes, *Studia Biophysica* **115** 51-58

4. Y. Huang, R. Hölzel, R. Pethig and X. B. Wang (1992) Differences in the AC electrodynamics of viable and non-viable yeast cells determined through combined dielectrophoresis and electrorotation studies, *Phys. Med. Biol.* **37** 7 1499-1517

5. J. P. Reeves and R. M. Dowben (1969) Formation and properties of thin-walled phospholipid vesicles, *J. Cell Physiol.* **73** 49-60

6. R. R. C. New *Liposomes a practical approach* (1990) IRL Press at Oxford University Press 23-27

7. L. M. Gordon and C. C. Curtain (1988) Alan R. Liss, Inc. *Methods for Studying Membrane Fluidity* 25-88

8. Y.Huang and R. Pethig (1991) Electrode design for negatibe dielectrophoresis, *Meas. Sci. Technol.* **2** 1142-1146

9. M. P. Hughes, R. Pethig and X. B. Wang (1995) Dielectrophoretic forces on particles in travelling electric fields, *J. Phys. D: Appl. Phys.* **28** 1-9

10. M. P. Hughes, X-B. Wang, F. F. Becker, P. R. C. Gascoyne and R. Pethig (1994) Computer-aided analyses of electric fields used in electrorotation studies, *J. Phys. D: Appl. Phys.* **27** 1564-1570

11. R. Fettiplace, D. M. Andrews and D. A. Haydon (1971) The thickness, composition and structure of some lipids bilayers and natural membranes, *J. Membran Biol* **5** 277-296

12. P. R.C. Gascoyne, R. Pethig, J. P.H. Burt and F. F. Becker (1993) Membrane changes accompanying the induced differentiation of Friend murine erythroleukemia cells studied by dielectrophoresis, *Biochimica et Biophysica Acta* **1149** 119-126

13. P. R.C. Gascoyne, Y. Huang, R. Pethig, J. Vykoukal and F. F. Becker (1992) Dielectrophoretic separation of mammalian cells studied by computerized image analysis, *Meas. Sci. Technol.* **3** 439-445

14. P. R.C. Gascoyne, J. Noshari, F. F. Becker and R. Pethig (1994) Use of dielectrophoretic collection spectra for characterizing differences

between normal and cancerous cells, *IEEE Transaction on Industry Applications,* **30**, 4, 829-834

15. A. Irimajiri, T. Hanai and A. Inouye (1979) A dielectric theory of "multi-stratified shell" model with its application to a lymphoma cell. *J. Theor. Biol.* **78** 251-269

16. J. E. Dennis and D. J. Woods in *New Computing Environments: Microcomputers in Large-Scale Computing* (A. Wouk, ed.), 116-122, SIAM

17. R. C. Weast and M. J. Astle (1982) *CRC Handbook of Chemistry and Physics 62nd edition 1981-1982* CRC Press

18. A. Kusumi, W. K. Subczynski, M. Pasenkiewicz-Gierula, J. S. Hyde and H. Merkle (1985) Spin-label studies on phosphatidylcholine-cholesterol membranes-effects of alkyl chain-length and unsaturation in the fluid phase, *Biochimica et Biophysica Acta* **854** 307-317

19. B. A. Lewis and D. M. Engelman (1983) Lipid bilayer thickness varies linearly with acyl chain length phosphatidylcholine vesicles, *J.Mol. Biol.* **166** 211-217

20. L. J. Lis, M. McAlister, N. Fuller, R. P. Rand and V. A. Parsegian (1982) Interactions between neutral phospholipid bilayer membranes, *Biophysical Journal* **37** 657-666

21. X. B. Wang, R. Pethig and T. B. Jones (1992) Relationship of dielectrophoretic and electrorotational behaviour exhibited by polarised particles, *J. Phys. D. : Appl. Phys.* **25** 905-912

22. X. B. Wang, Y. Huang, R. Hölzel, J. P. H. Burt and R. Pethig (1993) Theoretical and experimental investigations of the interdependence of the dielectric, dielectrophoretic and electrorotational behaviour of colloidal particles, *J. Phys. D. :Appl. Phys.* **26** 312-322

23. R. Benz, O. Frohlich, P. Lauger and M. Montal (1975) Electrical capacity of black lipid films and of lipid bilayers made from monolayers, *Biochim. Biophys. Acta* **394** 323-334

24. T. Hanai, D. A. Haydon and J. Taylor, (1965) Polar group orientation and the electrical properties of lecithin bimolecular leaflets, *J. Theoret. Biol.* **9** 278-296

25. G. E.Crawford and J. C. Earnshaw (1989) Phase transitions in monoglyceride bilayers: A Light Scattering Study, *Biophysical Journal* **49** 869-889

26. S. H. White (1975) Phase transitions in planar bilayer membranes, *Biophysical Journal* **15** 95-117

27. R. E. Pagano, R. J. Cherry and D. Chapman (1973) Phase transitions and heterogeneity in lipid bilayers, *Science* **181** 557-559

Abbreviations
DOPC = 1,2-Dioleoyl-sn-Glycero-3-Phosphocholine
Di1OASP-PS = N-(3-sulfopropyl)-4-(p-didecylamino-styryl) pyridinium inner salt
5-DS = 5-doxyl-stearate

DEP Crossing over Frequency Measurements

At the DEP crossing over frequency, the DEP force acting on the vesicle is effectively zero, since the real component of the Clausius-Mossotti factor equals zero. The DEP crossing over frequency f_{co} is directly proportional to the conductivity of the suspending medium σ_s and inversely proportional to membrane capacitance C_m of the vesicle [12].

$$f_{co} = \frac{\sigma_s}{r\pi\sqrt{2}C_m} \qquad (2)$$

Using this equation, the membrane capacitance value of the vesicle could be calculated, and the mean membrane capacitance of unilamellar vesicles was found to be $6.98mFm^{-2}$. The average bilayer capacitance for all vesicles with various amounts of bilayer present in the single membrane layers was equal to $7.37mFm^{-2}$ (Table 4.1).

Chapter 5

Electrorotational Studies of Latex beads with Bound Oligonucleotides

5.1 Introduction

The objective of the work described in this chapter was to investigate the feasibility of using electrorotation for determining DNA sequences. The basic concept is that binding oligonucleotides of known sequence to the surface of latex beads, and by monitoring any changes of their electrorotation characteristics to determining whether these bound oligonucleotides have complexed to complimentary DNA single strands. As such it could provide a new and exciting possibility to study oligonucleotides and DNA molecules with the aid of the polymerase chain reaction (PCR) [1], so that DNA molecules with different molecular sequence can be detected by electrorotation technology.

The method is rather similar to the use of latex beads to study the dielectric properties of biofilms, and the effect upon them of biocides [2], as well as for the monitoring of toxic micro-organism in water [3]. In this study, oligonucleotides were chemically bonded to the carboxyl groups of the carboxylated latex beads (Bangs Laboratories) by using 1-ethyl-3-(3-dimethylpropyl) carbondiimide (EDC) (Sigma) [4, 5].

5.2 Material and Experimental methods

5.2.1 *Preparation sequence of latex beads for electrorotation experiments*

Ellipsoidal latex beads (Bangs Laboratories) approximately 6×4×4μm in size were used in these experiments. The rotation rate of these beads can easily be detected in electrorotation experiments because of this geometry. Before the experiment, 50μl of beads (10% in weight from the stock sample) were suspended in 1ml of 0.01% diluted strength of standard buffer Phosphate buffer saline PBS (Sigma) in an eppendorf tube. The eppendorf tube had been coated with water repellent Sigma-coat (Sigma) which prevented the latex beads adhering to the inner surface of the eppendorf tube. Then latex beads were washed 3 times by centrifugation (6500rpm for 10 minutes by micro-centrifuge. Once the washing procedure was completed, latex beads were resuspended in 1ml of 0.01% PBS solution.

5.2.2 *Preparation of oligonucleotide sequence for electrorotation experiment*

In this investigation, three sets of different oligonucleotide samples were examined. The first and second samples, primer 1 and primer 2 were gifts from Dr C. A. O'Neill of the University of Leeds, Biochemistry Department. The third sample M13/pUC, (primer 3) was kindly donated by Dr S. Assinder, University of Wales, Bangor, Biochemistry Department. Primer 1 and primer 2 are both twenty-one bases long single stranded oligonucleotide. The primer 1 DNA sequence is (-CAGCTGGCGGCCGTCGAGGCG-), and the DNA sequence of primer 2 is (-TACTACGTCGCCATCTTCCTC-). The concentration of both primers solution are 20μMol. The primer 3 is seventeen bases long single stranded oligonucleotide. The DNA sequence is (-GTAAAACGACGGCCAGT-). The concentration of this primer is 0.82μMol.

The concentration of all these primers was diluted to 300nM, which is a suitable concentration for the covalent binding between the Carboxylated groups of latex beads and the 5th base from the end of the primers [4]. Due to the pro-degradation nature of the DNA molecules, samples were kept at $-20° C$ in a freezer. Unfortunately, single stranded oligonucleotide form coils to become double stranded oligonucleotide. Therefore, heat shock of the primer is required before the binding of the primers to the surface of carboxylated latex bead. The heat treatment reverts the oligonucleotide back into the single stranded format. Heat shock treatment is described in figure 5.1.

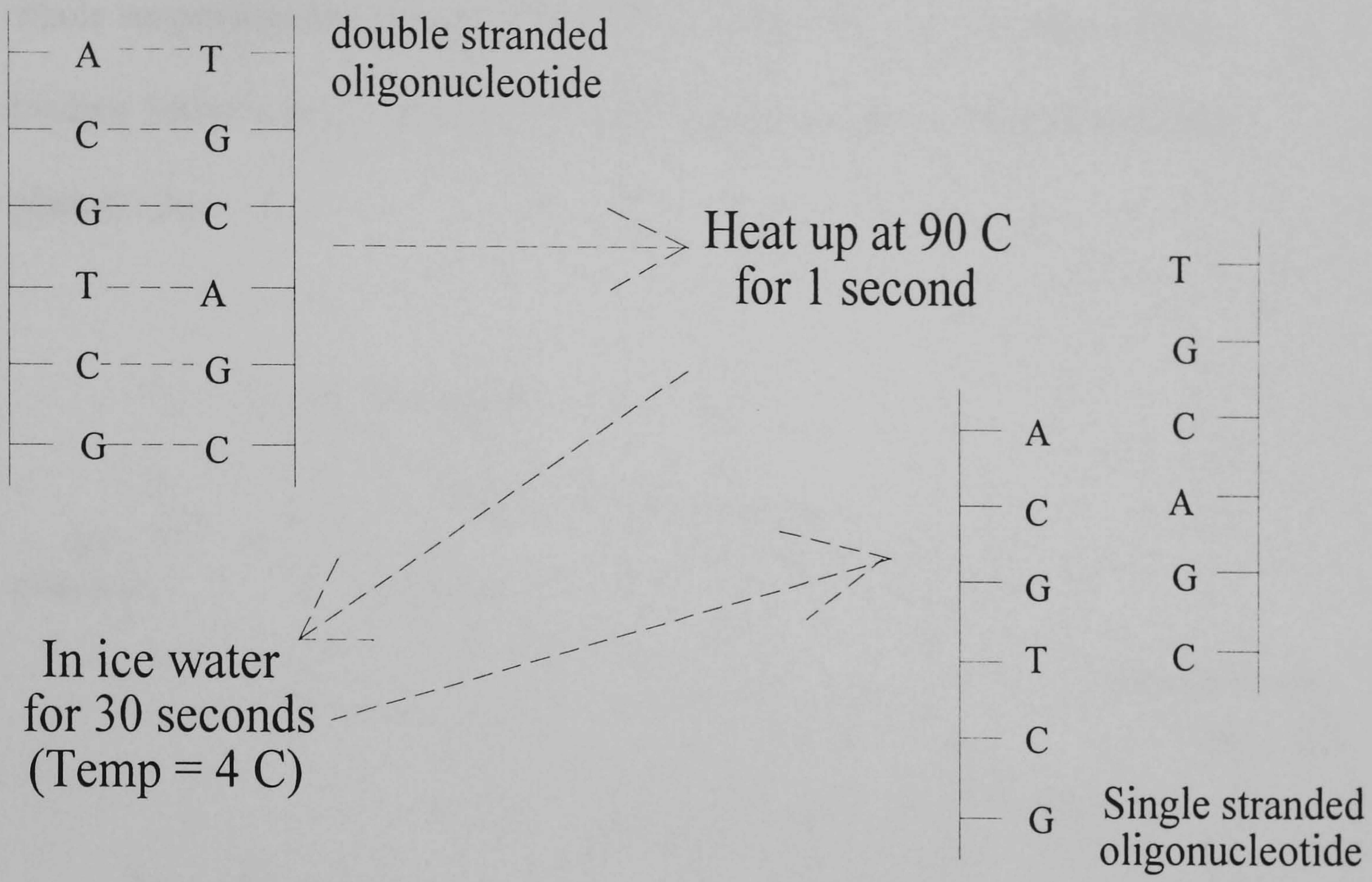

Figure 5.1 Double stranded oligonucleotide is heated at 90°C for 1 second. Then, sample is immediately put into ice-water for about 30 seconds. The hydrogen bonding between base groups is disrupted and single stranded oligonucleotides are formed.

Before the primers are bound onto the surface of carboxylated latex beads, they were washed as described previously. Also, the Sigma coated eppendorf tubes were soaked for 30 minutes in Marvel (Chivers & Sons Ltd) artifical milk solution, as a protein blocker. This prevented adhesion of oligonucleotide and latex beads to the surface of the tube. The concentration of this protein blocker was 5g in 100ml of 1/10,000 PBS. After the washing procedure was completed, the latex beads were resuspended in 1ml of 0.1M EDC [3, 4]. The EDC solution was adjusted to pH 7 or slightly below. Next, 50µl of 300nM oligonucleotide primer was added to the latex beads. The whole suspension was incubated at 50°C for three hours to allow the covalent binding between those primers and carboxylated groups of latex bead to take place (Figure 5.2).

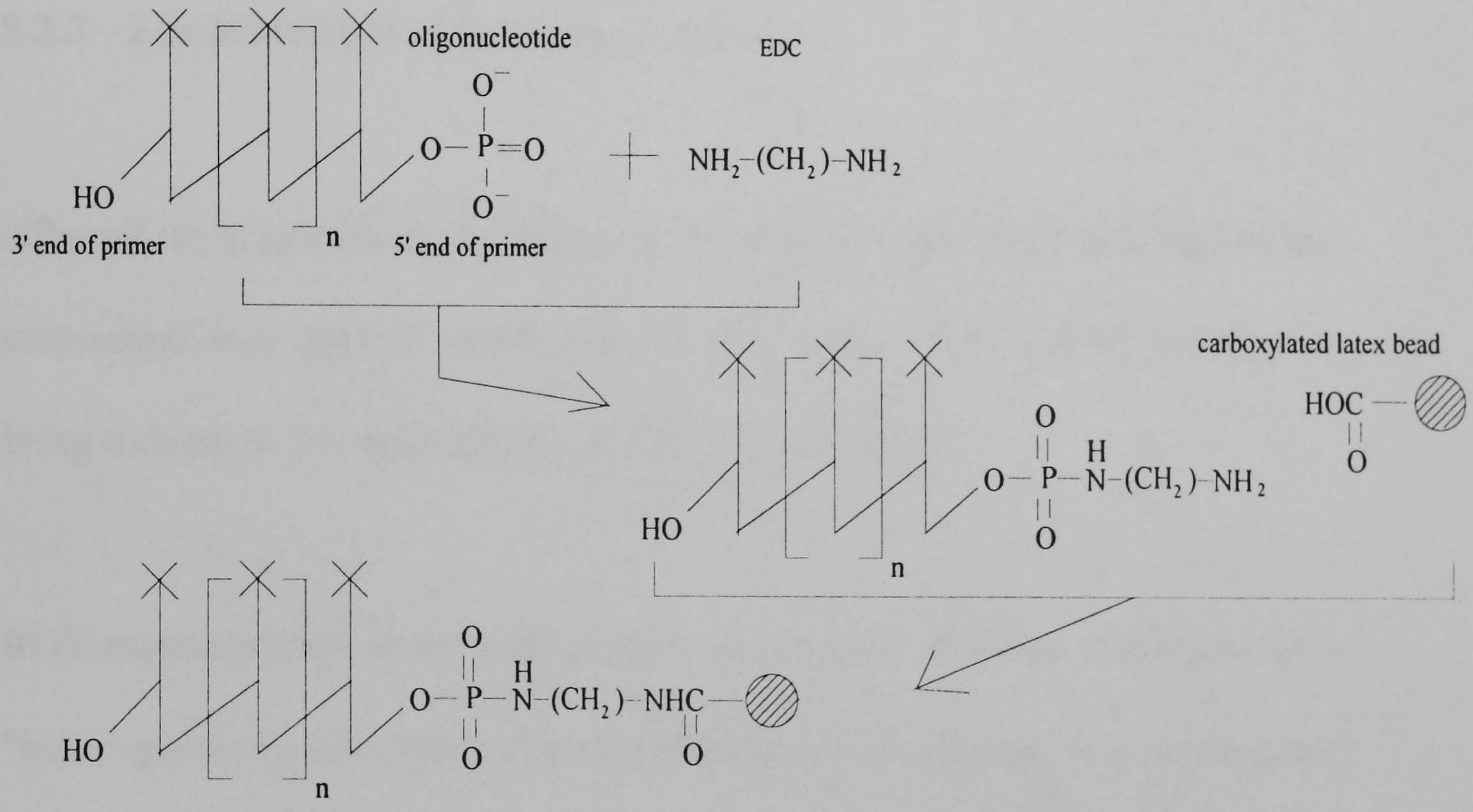

Figure 5.2 The phosphate group of the 5th base end of the oligonucleotide reacts with EDC to form covalent bonding. Then the remaining amide group binds to the carboxyl group of the latex bead. Reaction time of the whole process is 3 hours at 50°C.

After the incubation period was completed, sample of latex beads were washed by centrifugation. Next, the sample was resuspended in the Marvel solution and left for a further two hours at room temperature. The protein blocker reacted with all the unbound sites on the beads. Therefore, only the primer will be bound to the surface of the beads.

Before all these preparations, both containers and suspending media were autoclaved to remove contamination that might corrupt samples for these experiments.

5.2.3 *Electrorotation (ROT) Measurements*

After all the preparations and washing procedures were completed, 50μl of the suspension was diluted further into another 1ml of 0.01% PBS solution to bring it down to the right dilution for ROT experiments.

ROT measurements were conducted in an enclosed chamber comprised of a "bone" geometry electrode array of 400μm tip-to-tip spacing of gold-on-glass construction. The four electrodes of the array were energised by sinusoidal signals in quadrature that produced an essentially homogeneous rotating electric field in the central region of the array [6]. Once samples were placed in the ROT chamber, rotation measurements were then taken over the frequency range 100Hz to 5MHz at ten points per decade for beads that lay within 65μm of the geometrical centre of the array and that were at least three diameters from any neighbour. Experimental data points were obtained, conmencing at the highest frequency of 5MHz. Since latex beads had been washed extensively, there was a minimal amount of ions present that would leak into the suspending medium and alter the experimental results. Also, measurements were taken in the most homogeneous region of the applied field to ensure that latex beads did not move significantly as a result of lateral motion due to circular dielectrophoretic forces [7]. Thus they were not subjected to particle-particle interactions, also, systemic errors caused by time-dependent changes of latex beads were avoided. Experiments were carried out using a Labophot-2 (Nikon) microscope, and vesicle rotation rates were timed by stopwatch with the aid of video microscopy.

5.2.4 *ROT data correction from electrode polarisation effects by conductivity measurements of suspending medium*

Electrode polarisation effects become more dominant as the electric field frequency approaches the dc condition. Hence, the magnitude of the electrical field imposed on the test beads steadily decreases. This effect would manifest itself as a reduction in the measured solution conductance as the applied voltage frequency was reduced below around 10kHz. Thus, conductivity measurements using the bone electrode were carried out using a Hewlett-Packard 4192A impedance analyser from 5MHz to 100Hz. By using the high frequency asymptotic conductance value obtained using the bone electrodes, a correction factor for electrorotation data was calculated by using the *polyfit and polyval* function routines in MATLAB (The Math Works, Inc) (Figure 5.4).

5.2.5 *ROT data analysis methods*

Since latex beads are ellipsoidal in shape, a spherical dielectric shell model [8] was not appropriate for the data analysis in this investigation. Thus an ellipsoidal shell model [9] has been used in this analysis. Also, the surface charge of the latex beads contributes significantly to the low frequency region of a ROT spectrum (frequency below 10kHz). Therefore an equation to describe the surface charge effect of latex beads (equation 5.1) [2, 10] is also required. It was added to the ellipsoidal model in order to interpret the dielectric properties of the beads (see chapter two for details).

$$\sigma_p = \sigma_b + \frac{2K_s}{r} + \frac{A}{1+(j\omega T)^{\alpha}} \qquad (5.1)$$

where σ_p is effective conductivity of the latex bead, σ_b is the bulk conductivity of the bead. K_s is the surface conductance of the bead. A and T were the magnitude and mean characteristic time constant respectively, and α was a variable to describe the experimental curve fitting [2].

The dielectric ellipsoidal shell model closely resembled the physical appearance of the latex beads. Each ROT spectrum was analysed by a curve fitting method based on the Nelder-Mead simplex optimisation procedure [11] provided by MATLAB [The Math Works, Inc]. This procedure minimised the error function

$$Min\left\{\sum_i\left[R_{sim}(fi)-R_{\exp}(fi)\right]^2\right\} \quad (5.2)$$

for the i frequency points f in the experimental ROT spectrum R_{exp}.

In all analyses, the measured value of the suspending medium conductivity was provided. The relative permittivity and the viscosity values were fixed to the relative temperature at which the experiment was conducted. The internal permittivity and bulk conductivity of beads were fixed at $3.5\varepsilon_o$ and 10nS.m^{-1} respectively [2]. Furthermore, the radii of latex beads were homogeneous and were obtained from the manufacturer's data sheet. Thus, for the single shell model, the iterated parameters in the minimisation were: the surface conductance K_s; the defined magnitude A; the mean characteristic time constant T and the curve fitting α. Also included was the scaling factor k, which took into account factors in the experimental environment that influenced the latex bead rotation rate, including the field strength and the friction between the latex bead and the substrate.

5.3 Results

5.3.1 Electrode polarisation effect on the bone electrode

Electrode polarisation effects are contributed to by water molecules and small ions such as Na$^+$ and K$^+$ ions to form a boundary layer between the electrode and the suspension. This layer is called the Helmholtz Plane or the Stern layer [12]. According to the Gouy-Chapman model [12], which describes the electrode-electrolyte interface as a diffusion of charges from the electrode boundary into the bulk electrolyte solution, the potential profile of this diffusion mechanism is governed by an equation of the form:

$$\psi_x = \psi_o e^{-\mu x} \tag{5.3}$$

where ψ_x is the potential at a distance x from the Helmholtz plane into the suspension, ψ_o is the potential at the Helmholtz plane, x is the distance from the Helmholtz plane into the suspension, μ is a constant value and μ^{-1} can be considered the effective thickness of the ionic cloud, the Stern layer [12].

$$\mu^{-1} = \left(\frac{\varepsilon_o \varepsilon_r kT}{8\pi n_o Z^2 e_o^2} \right)^{\frac{1}{2}} \tag{5.4}$$

where k is Boltzmann's constant, T is the absolute temperature in Kelvin, n_o is the ionic concentration (ion dm^{-3}), Z is the valency of the ion and e_o is the electronic charge (1.621×10^{-19} C). From equation 5.4, the thickness of the Stern layer μ^{-1} increases as the concentration of ions n_o is decreased. This leads to the decrement in value for the constant μ. According to equation 5.3, the potential ψ_x increases as the value of μ is decreased. Therefore, this may indicate that the electrode polarisation effect could become less dominant. Thus, a higher electric potential which will be dropped within the suspension. This could explain the minimal reduction in the conductance values of 0.01%

PBS which was measured at 21°C (Figure 5.3). Meanwhile, the Stern layer thickness μ^{-1} decreases as the temperature decreases. Hence, from equation 5.3 the potential ψ_x decreases, and the electrode polarisation effects starts to dominate. This effect was manifested in the conductance measurements at 4°C (Figure 5.3).

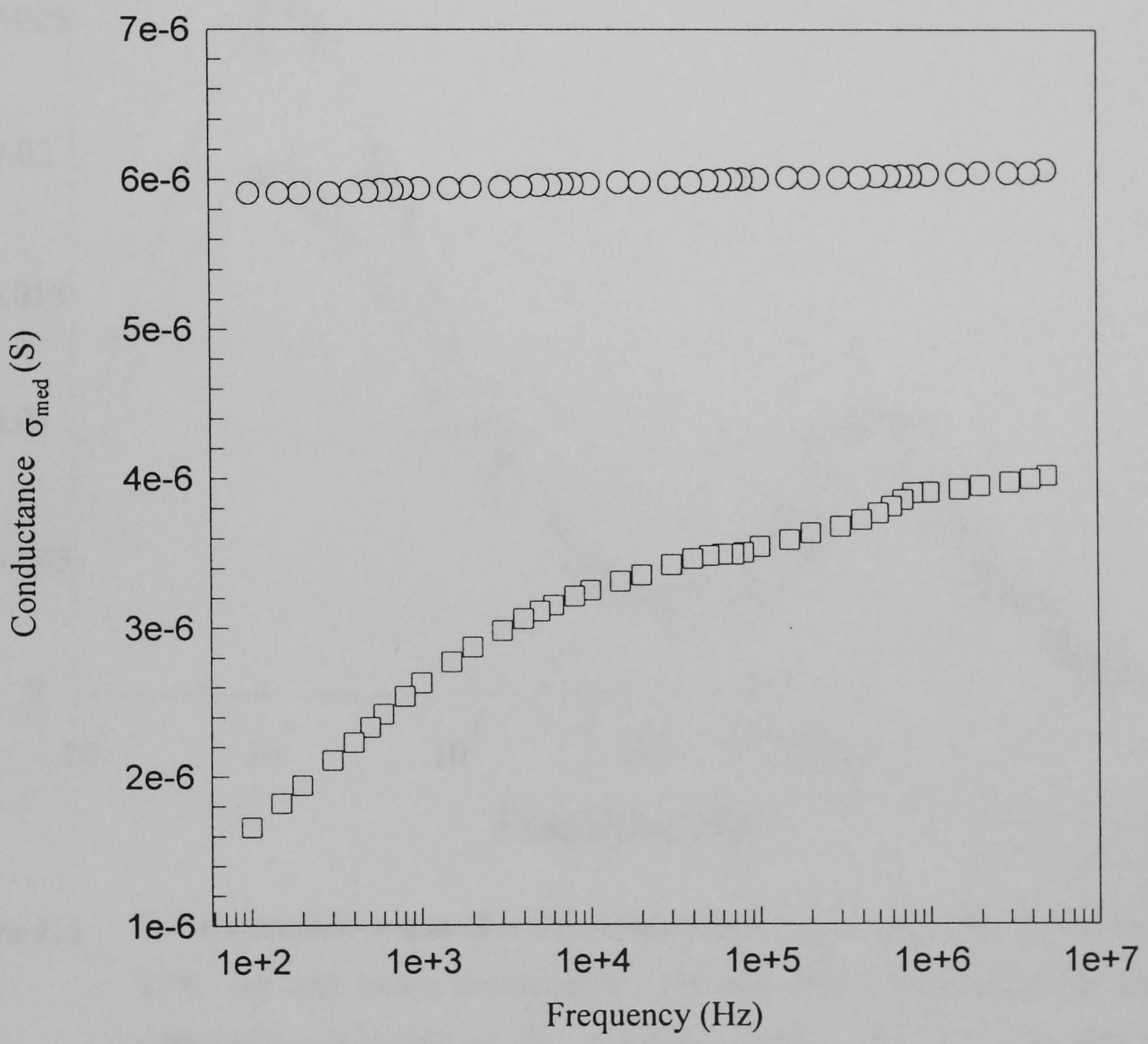

Figure 5.3 Conductance measurements of 0.01% PBS by using the bone electrode. Measurement was conducted at 21°C (○) and at 4°C (☐).

5.3.2 *Characterisation of untreated latex beads*

Carboxylated latex beads were analysed by ROT methods in order to characterise their rotation responses. The experiments were conducted at the temperature of 21°C and 10°C (Figure 5.4).

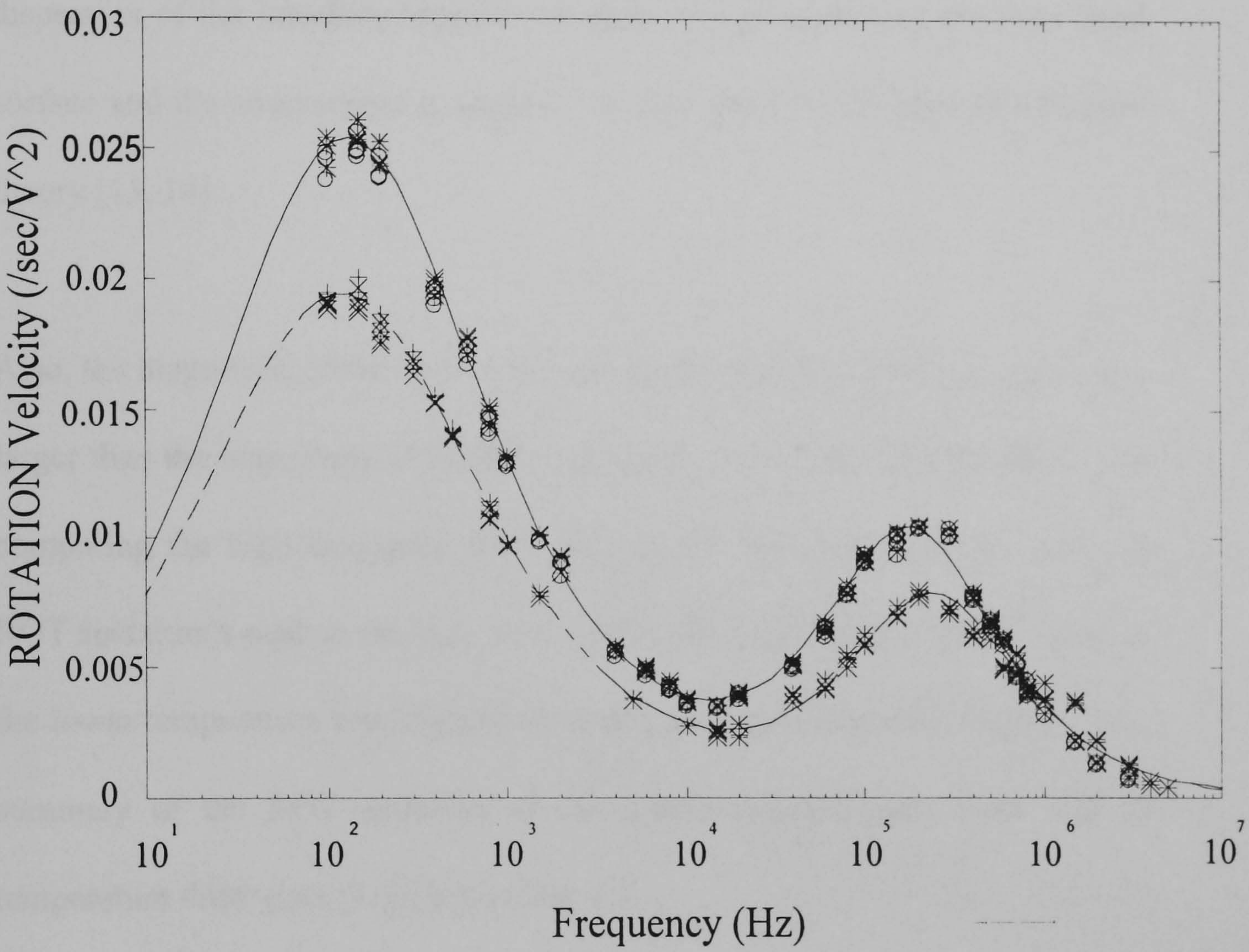

Figure 5.4 The electrorotation data of a carboxylated latex beads in 0.01% PBS medium. At 21°C, (o) data before compensation, (*) data after compensation for electrode polarisation, solid line is the theoretical fitting. At 10°C (X) data before compensation, (+) data after compensation for electrode polarisation, dotted line is the theoretical fitting. Best fit data for bead at 21°C are: A= 0.798; T= 3.34; α = 0.73; surface conductance Ks = $6.32 \times 10^{-10} Sm^{-1}$; medium conductivity $\sigma_{med} = 8.16 \times 10^{-4} Sm^{-1}$.

Best fit data for bead at 10°C are: A= 2.27; T= 13.66; α= 0.75; Ks = $5.12 \times 10^{-10} Sm^{-1}$; $\sigma_{med} = 6.296 \times 10^{-4} Sm^{-1}$

For both temperatures, there were two co-field rotation peaks. The first co-field rotation peak appeared at around 100-200Hz; the second peak at around 200kHz. The low frequency rotation peak can be attributed to the dielectric dispersion of the counterions that surrounded the surface of the latex bead [12]. The second rotation peak, at the high frequency is due to the dielectric dispersion of the interface between the dielectric properties of the latex bead surface and the counterions in medium, as described by the Maxwell-Wagner theory [13, 14].

Also, the magnitude of the ROT spectrum at the lower temperature region was larger than the magnitude of the ROT spectrum at the higher temperature. By comparing the high frequency ROT peak at the lower temperature with the ROT spectrum's peak at the high temperature, the high frequency ROT peak at the lower temperature was slightly shifted to the lower frequency region. The summary of the ROT response of these carboxylated latex beads due to temperature difference is given by table 5.1.

Table 5.1 Summary of ROT response of carboxylated latex beads at 10°C and 21°C. In both conditions, the relative permittivity of latex beads were kept at $3.5\varepsilon_o$, and the bulk conductivity at $10nS.m^{-1}$ [2].

Temp (°C)	A	T	α	K_s (Sm^{-1})	σ_{med} (Sm^{-1})	Scale	low freq. peak (Hz)	high freq. peak (Hz)
21	1.92×10^{-3} to 1.96	2.09×10^{-3} to 11.12	0.765	5.12×10^{-10}	7.15×10^{-4}	9.14×10^{-6}	100 to 200	150×10^3 to 200×10^3
10	0.32 to 8.001	0.46 to 29.33	0.78	5.04×10^{-10}	5.54×10^{-4}	1.77×10^{-5}	50 to 200	150×10^3 to 200×10^3

5.3.2 *Carboxylated latex beads treated with 1-ethyl-3-(3-dimethylpropyl) carbodiimde (EDC)*

After carboxylated latex beads were treated by EDC for three hours at 50°C, they (EDC-treated beads) were suspended into 0.01% PBS for ROT experiments. For all EDC-treated beads only one single rotation peak at around 600kHz could be recorded in the whole ROT spectrum (Figure 5.5). Below 80kHz, EDC-treated beads became very adhesive to the glass surface of the electrode chamber. Thus there was no rotation to be recorded. The summary of the ROT response for EDC-treated beads is shown in table 5.2.

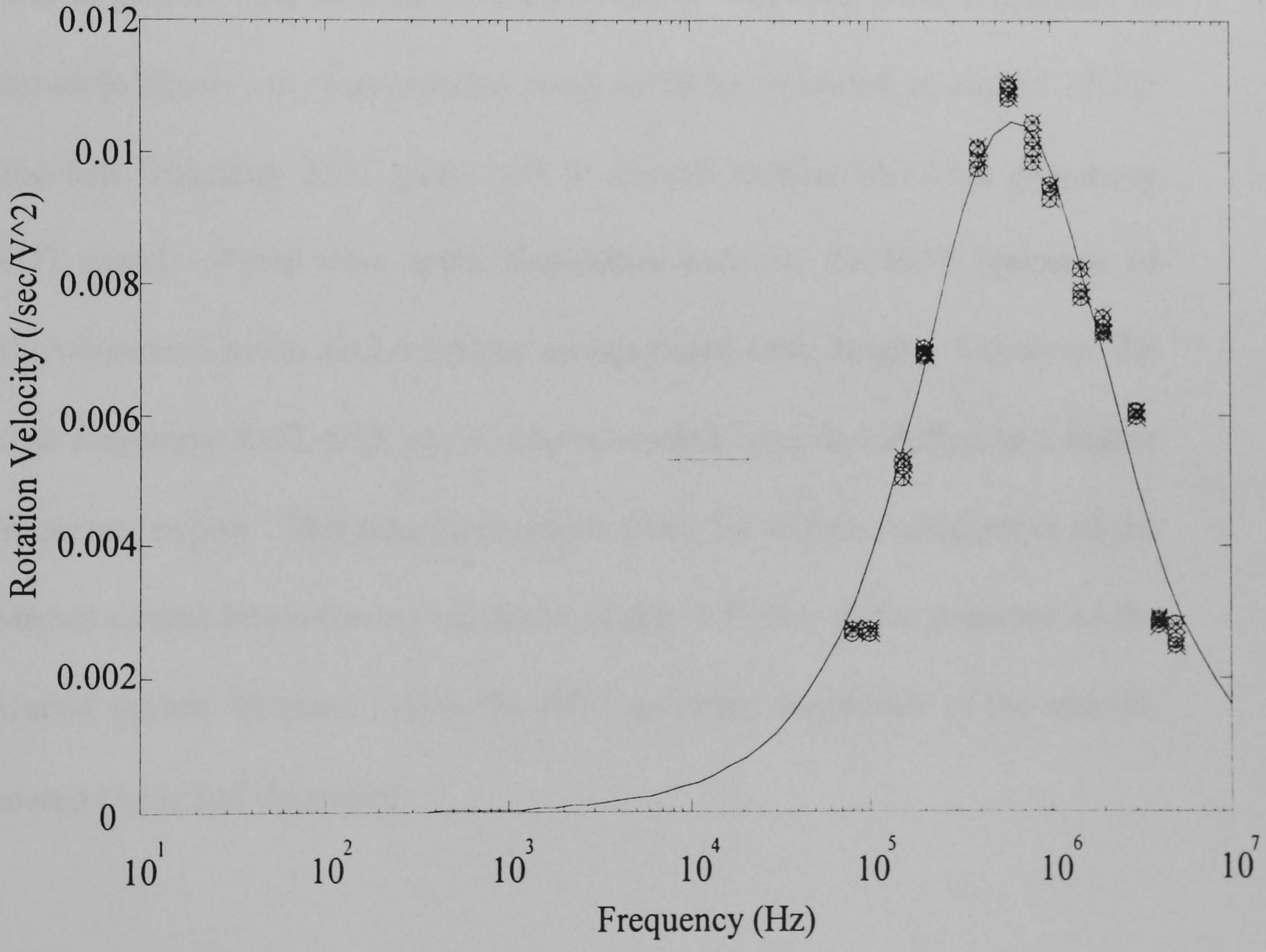

Figure 5.5 ROT response of carboxylated latex bead after the treatment of EDC. The surface conductance was $6.26 \times 10^{-9} Sm^{-1}$. There was no rotation response below 10kHz in the ROT experiment. The suspending medium conductivity was $5.54 \times 10^{-4} Sm^{-1}$ (0.01% PBS).

Table 5.2 Summary of ROT response for EDC-treated beads. The relative permittivity of latex beads were kept at $3.5\varepsilon_o$ and the bulk conductivity at $10nS.m^{-1}$ [5].

Temp (°C)	A	T	α	K_s (Sm^{-1})	σ_{med} (Sm^{-1})	Scale	high freq. peak (Hz)
21	1.3	2.06	4.52	5.36×10^{-9}	5.54×10^{-4}	3.28×10^{-6}	600×10^{3}

5.3.3 *Marvel protein blocker coated latex beads*

After the previous treatment, EDC-treated beads were coated with artificial milk as protein blocker (Marvel-coated beads). The typical ROT response is shown in figure 5.6. Two rotation peaks could be measured, at around 100Hz (the low frequency ROT peak) and at around 250kHz (the high frequency ROT peak). There were some similarities between the ROT spectrum of Marvel-coated beads and untreated carboxylated latex beads. However, the high frequency ROT peak of the Marvel-coated bead had shifted to a higher frequency region. This may have results from the surface conductance of the Marvel-coated beads having increased (Table 5.3) due to the presence of the Marvel protein blockers. Also, the ROT spectrum magnitude of the Marvel-coated beads had decreased.

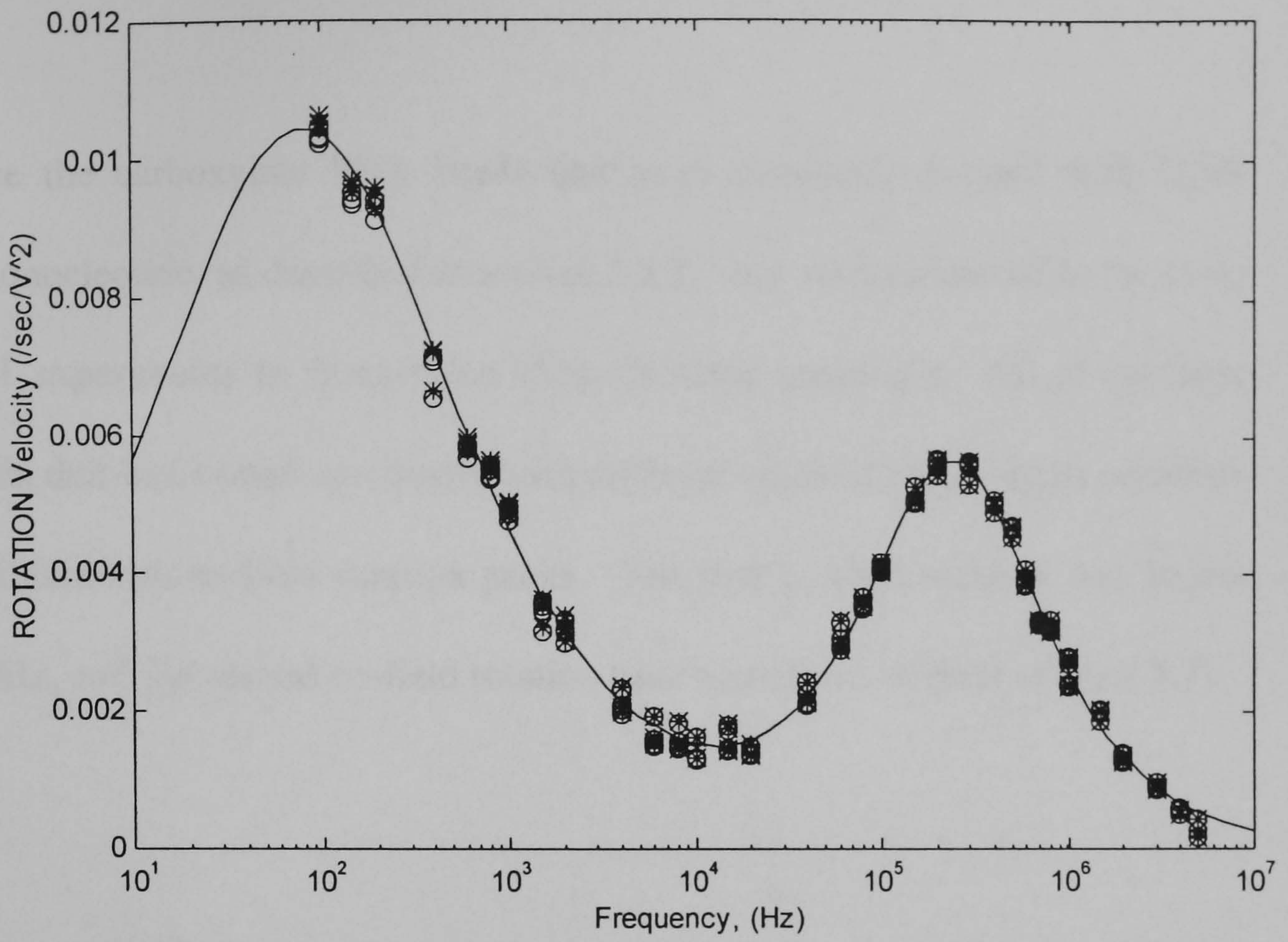

Figure 5.6 Typical ROT response of EDC-treated beads followed by coating with protein blocker (Marvel artificial milk). At 18°C, (o) data before compensation, (*) data after compensation for electrode polarisation, solid line is the theoretical fitting. As best fitted data: $A = 1.26 \times 10^{-2}$; $T = 2.13 \times 10^{-2}$; $\alpha = 7.28$; $K_s = 6.91 \times 10^{-10}\, Sm^{-1}$; $\sigma_{med} = 8.16 \times 10^{-4}\, Sm^{-1}$

Table 5.3 Summary of ROT response for Marvel-coated beads. The relative permittivity of latex beads were kept at $3.5\varepsilon_0$ and the bulk conductivity at $10nS.m^{-1}$ [2].

A	T	α	K_s (Sm^{-1})	σ_{med} (Sm^{-1})	Scale	Low freq. peak (Hz)	High freq. peak (kHz)
1.79×10^{-2}	2.46×10^{-2}	0.73	75×10^{-10}	8.16×10^{-4}	4.16×10^{-6}	100	250×10^3

5.3.4 *Latex beads bound covalently with DNA oligonucleotide*

Once the carboxylate latex beads had been covalently bonded with DNA oligonucleotide, as described in section 5.2.2, they were subjected to the same ROT experiments to characterise their dielectric properties. All of the latex beads that had bound covalently with different types of DNA oligonucleotide exhibited two co-field rotation peaks. The first co-field rotation was below 200Hz, and the second co-field rotation peak was above 400kHz (Figure 5.7).

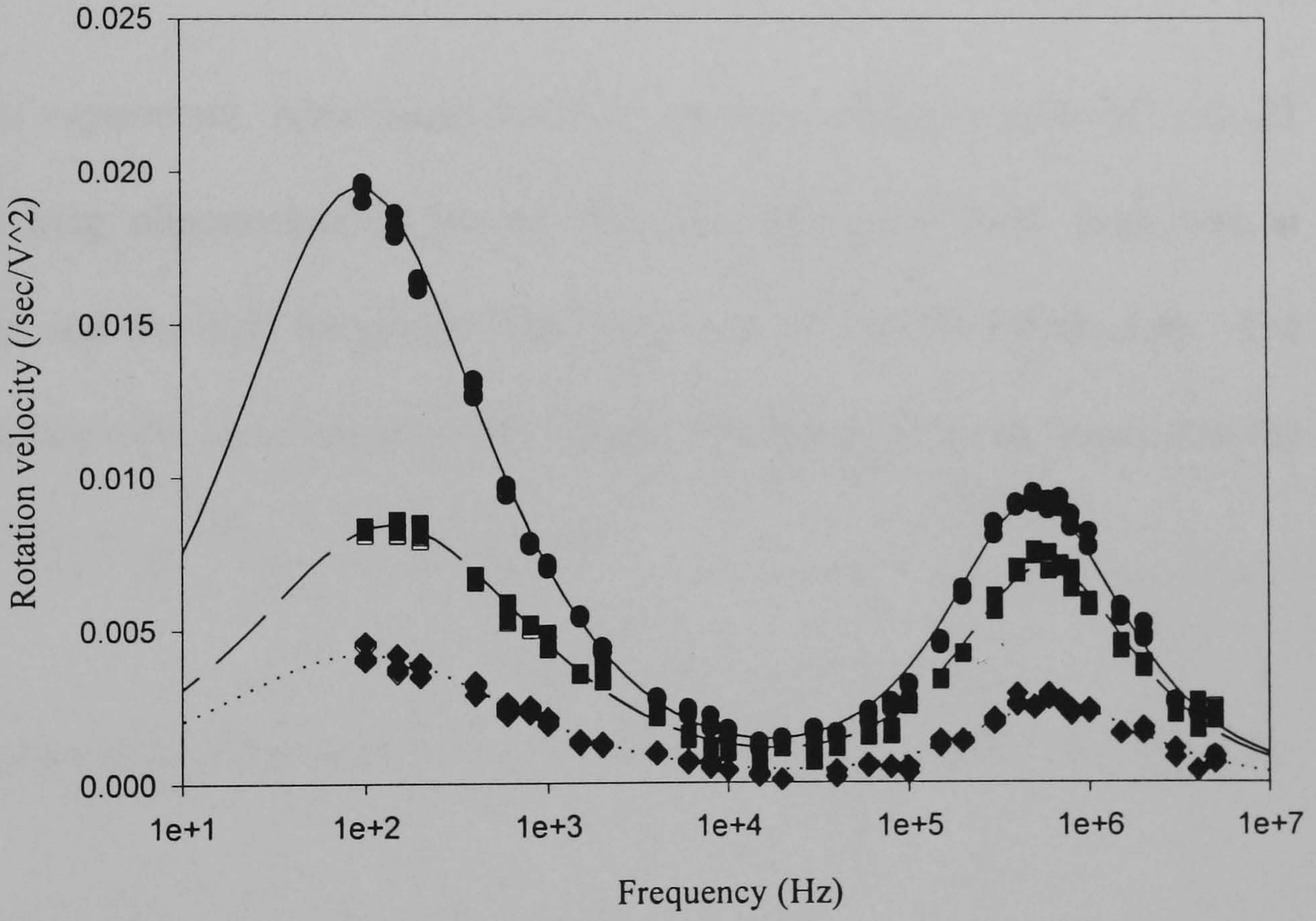

Figure 5.7 ROT spectra for DNA oligonucleotide: 21 bases long primer (21-mer), GC rich: ○ ROT data, ● after compensation of electrode polarisation, solid line is the theoretical fitting. 21 bases long primer (21-mer), AT rich: □ ROT data; ■ after compensation , dashed line is the theoretical fitting. 17 bases long primer: ◊ ROT data, ◆ data after compensation, dotted line is the theoretical fitting.

Table 5.4 ROT response for different types of DNA oligonucleotide.

Primer	**Temp (°C)**	**A**	**T**	**α**	**K_s (S)**	**σ_{med} (Sm^{-1})**	**Low freq. peak (Hz)**	**High freq. peak (Hz)**
21-mer (GC-rich)	19	3.313	4.613	0.802	1.61×10^{-9}	1.69×10^{-3}	100	500×10^3
21-mer (AT-rich)	18	0.019	0.00395	0.747	1.6×10^{-9}	1.99×10^{-3}	~150	600×10^3
17-mer M13/pUC	19	0.072	0.039	0.746	2.15×10^{-9}	1.89×10^{-3}	100-150	600×10^3 to 700×10^3

5.3.4.1 *Latex beads covalently bound with GC rich oligonucleotide (primer 1)*

In this experiment, latex beads had been bound covalently with GC rich 21 bases long oligonucleotide primer. The low frequency ROT peak was at 100Hz and the high frequency ROT peak was at 500kHz (Table 5.4). The magnitude of the low frequency ROT peak was about two times larger than the high frequency ROT peak (Figure 5.7).

5.3.2.3 *Latex beads bound covalently with AT rich oligonucleotide (primer 2)*

In this experiment, latex beads had been bound covalently with AT rich 21 bases long oligonucleotide primers. The low frequency ROT peak was at about 150Hz and the high frequency ROT peak was 600kHz (Table 5.4). The magnitude of both these were almost the same (Figure 5.7).

5.3.2.4 *Latex beads bound covalently with 17 bases long oligonucleotide primer (M13/pUC)*

In this experiment, latex beads had bound covalently with the 17 bases long oligonucleotide primer. The low frequency peak was at about 100Hz and the high frequency one at around 600kHz to 700kHz (Table 5.4). The magnitude of the low frequency ROT peak was about 1.4 times larger than the magnitude of the high frequency ROT peak.

5.4 Discussion

5.4.1 ***Temperature effect on carboxylate latex beads***

From table 5.1, variables A, T and α represent the ROT response of the lower frequency rotation peak. All of their values increased as the temperature was reduced. As the variable α increases, the magnitude of the lower frequency rotation peak increases. At the same time, the frequency of this rotation peak is moving further to a lower frequency region (see chapter 2). Since the surface ionic group of the carboxylate latex bead is composed of caboxylic acid (COOH) (Figure 5.2), ions such as Na^+ and K^+ can be attracted to them from the medium. This ionic cloud can cover the whole surface of the latex bead. These ions might form a double layer or a Stern layer on the surface of the bead. According to equation 5.4 of the Gouy-Chapman model, the thickness of the Stern layer, or the double layer starts to fall as temperature decreases. This ionic double layer will act effectively as a capacitor covering the whole surface of the bead, so has the thickness of this Stern layer decreases, its effective capacitance increases. Because the relaxation time of this double layer capacitance increases, the alpha dispersion will correspondingly take place at a lower frequency (Table 5.1).

Also, the surface conductance of latex beads has decreased as the temperature has decreased. In terms of the Clausius-Mossotti factor [10] (equation 5.5), the magnitude of the ROT spectrum should decrease as temperature decreases.

$$f\left(\varepsilon_2^*,\varepsilon_1^*\right)=\frac{\varepsilon_2^*-\varepsilon_1^*}{\varepsilon_2^*+2\varepsilon_1^*}=\frac{\sigma_2^*-\sigma_1^*}{\sigma_2^*+2\sigma_1^*} \qquad (5.5)$$

The factor $f\left(\varepsilon_2^*,\varepsilon_1^*\right)$ is the complex Clausius-Mossotti term, σ_2^* is the complex conductivity of the latex bead and σ_1^* is the complex conductivity of the suspending medium. The conductivity of the suspending medium also decreases with the decrement of temperature. At 10°C, the ratio of the surface conductance and the suspending medium conductivity (K_s/σ_{med}) is equal to 9.09×10^{-7} whereas the ratio (K_s/σ_{med}) at 21°C is 7.16×10^{-7}. Thus the effective conductivity of the bead at 10°C appears to be more conductive than the effective conductivity at 21°C (equation 5.6).

$$\left(\frac{\sigma_2^*-\sigma_1^*}{\sigma_2^*+2\sigma_1^*}\right)_{10^\circ C}>\left(\frac{\sigma_2^*-\sigma_1^*}{\sigma_2^*+2\sigma_1^*}\right)_{21^\circ C} \qquad (5.6)$$

Thus, the value of Clausius-Mossotti factor for latex bead at 10°C is larger than the value at 21°C. Hence, the magnitude of the ROT spectrum at low temperature is higher than the magnitude of the ROT spectrum at the higher temperature.

5.4.2 *Carboxylate latex bead being treated by 1-ethyl-3-(3-dimethylpropyl) carbodiimide*

Once carboxylate latex beads had been treated by EDC, the carboxyl ionic group of the bead become covalently bonded with an amide group from the EDC (Figure 5.8). Thus the ionic group which is on the surface of the beads becomes more conductive, and the high frequency ROT peak has shifted from 200kHz to 600kHz. The surface conductance of these EDC-treated beads has increased by one decade in magnitude (Table 5.2) in comparison with the surface conductance values of untreated latex beads (Table 5.1). Since the ionic groups of the glass surface of the electrode have negative charge, the hydrogen ions from the amide group may be attracted to the glass. This could explain why the EDC-treated beads become very adhesive to the surface of the electrode chamber at the low frequency region. Thus, the values of A and T have no meaning to describe the ROT data. The value of α has increased to 4.5, this has actually merged the low frequency ROT peak to the high frequency ROT peak.

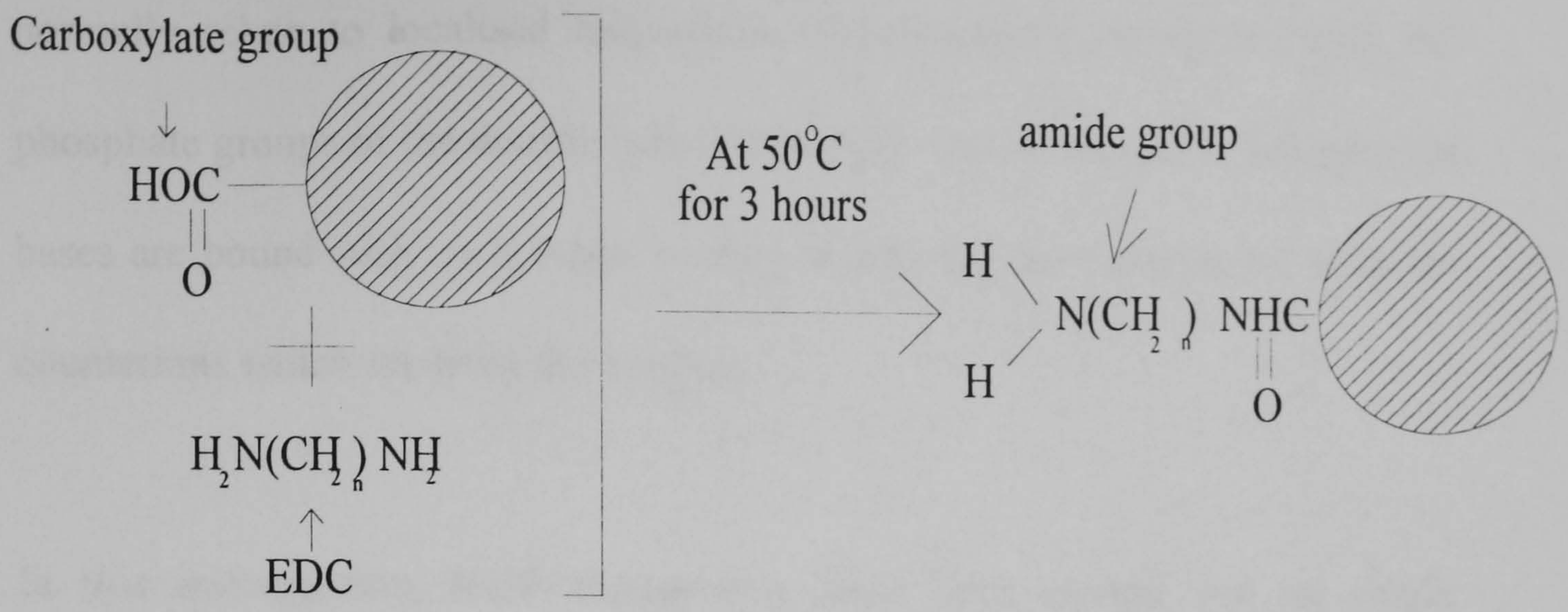

Figure 5.8 Carboxylate latex beads are treated with 1-ethyl-3-(3-dimethylpropyl) carbodiimide. The surface ionic group of beads have changed into amide ions.

5.4.3 *Effect of Marvel protein blockers on Carboxylate latex beads*

From table 5.3, the ROT response of Marvel-coated latex beads are very similar to the ROT response of untreated latex beads. The only difference between these beads is that the surface conductance of the Marvel-coated bead is slightly higher than that of the untreated beads (see Table 5.1 and 5.3).

5.4.4 *Comparison of latex beads with different types of oligonucleotide*

For each different strand of DNA oligonucleotide, phosphate groups act as their backbone skeleton and nitrogenous bases such as Adenine A, Guanine G, Thymine T, and Cytosine C as their building blocks. In conventional dielectric studies of DNA, measurements have normally been performed on double stranded DNA with helical structure. The dielectric responses normally relate to localised relaxations of counterions associated with the phosphate groups of the double helix DNA [15]. In this situation, nitrogenous bases are bound with each other, so they would not have interacted with the counterions which are from the medium.

In this investigation, ROT experiments have been carried out on single stranded oligonucleotide. Thus, the nitrogenous bases of the oligonucleotide are exposed to the counterions of the medium.

For nitrogenous bases, each Adenine and Thymine consists of two hydrogen bonding sites in which, A and T can form hydrogen bonding with each other [16]. Also, each Cytosine and Guanine consists of three hydrogen bonding sites in which, C and G can form hydrogen bonds with each other [16]. These hydrogen bonding available sites are basically lone pairs of electrons from oxygen atoms, amide groups ions and nitrogen ions with negative charge. Therefore, the GC rich 21 bases long primer has 59 available sites for forming hydrogen bonds. The AT rich 21 bases long primer has 53 available sites for forming hydrogen bonds. The primer M13/pUC 17 bases long primer has 43 available sites for hydrogen bonds. Since the conductivity of oligonucleotide strands is related to the presence of these hydrogen bonding sites, the conductivity of each strand of oligonucleotide is determined by the amount of hydrogen bonding sites per base length, namely the ratio between the amount of the hydrogen bonding sites and the amount of nitrogenous bases in each oligonucleotide. These ratio values for primer1, 2 and M13/pUC are given in table 5.5.

Table 5.5 Ratio of amount of hydrogen bonding sites per base length of each different type o oligonucleotide and their ratio of high and low frequency ROT peak.

Primer	no. hydrogen bonds / bases length	magnitude of low freq. peak / magnitude of high freq. peak
1 (GC rich 21-mer)	2.81	2.1
2 (AT rich 21-mer)	2.52	1.08
M13/pUC (17-mer)	2.53	1.43

Since hydrogen bonds of oligonucleotides have the ability to attract others ion groups, charged molecules with water molecules from the suspension of the medium. These ions can hop between the bases group of the oligonucleotide strand and act as conductance elements [17]. This can indicate that these primers have been surrounded by a large cloud of ions and have shielded these primers away from the medium solution. Since Primer 1 (GC rich 21-mer) has the largest amount of hydrogen bonds sites per base length. This means that primer 1 will have the largest α-dispersion amongst all primers samples. Figure 5.7 has shown that primer 1 has the largest magnitude of low frequency ROT peak, and the largest ratio of low and high frequency ROT peak height (Table 5.5). This finding is also supported by the values of the variables A, T and α obtained from the theoretical fitting (Table 5.4), which are the largest amongst the rest of the primer samples. The ratio of the high and low frequency ROT peak for both primer 2 (AT rich 21-mer) and primer M13/pUC are relatively small compared with primer 1 (Table 5.5). Therefore it is possible to identify different strands of oligonucleotide with different combination of nitrogenous bases. Firstly, it is from the difference of their α-dispersion and the β-dispersion, which are manifested as the low and high frequency rotation peaks respectively(Figure 5.7). Secondly, it is from the ratio between the amount of hydrogen bonding available sites and the amount of bases present. Thirdly, the values of A, T and α can be determined by using the ellipsoidal model. However, there have been only a limited amount of ROT data for oligonucleotides to support this finding, further investigations in this subject are crucial and more ROT experiments are required.

The surface conductance of primer 1 (GC rich 21-mer) is slightly higher than primer 2 (AT rich 21-mer) (Table 5.4). This agrees with the amount of hydrogen bonding sites present. However the surface conductance of primer M13/pUC, 17 bases long oligonucloetide is larger than the surface conductance value of the (GC rich 21-mer) primer 1 (Table 5.4). Since the base length of both primer1 and primer2 are longer than the 17-mer M13/pUC primer. Therefore it is possible that some nitrogenous bases such as Cytosine, Guanine and Thymine of the longer chain primer have bound covalently with the amide groups from the surface of bead, when the treatment with 1-ethyl -3-(3-dimethylpropyl) carbondiimide (EDC) took place (Figure 5.9).

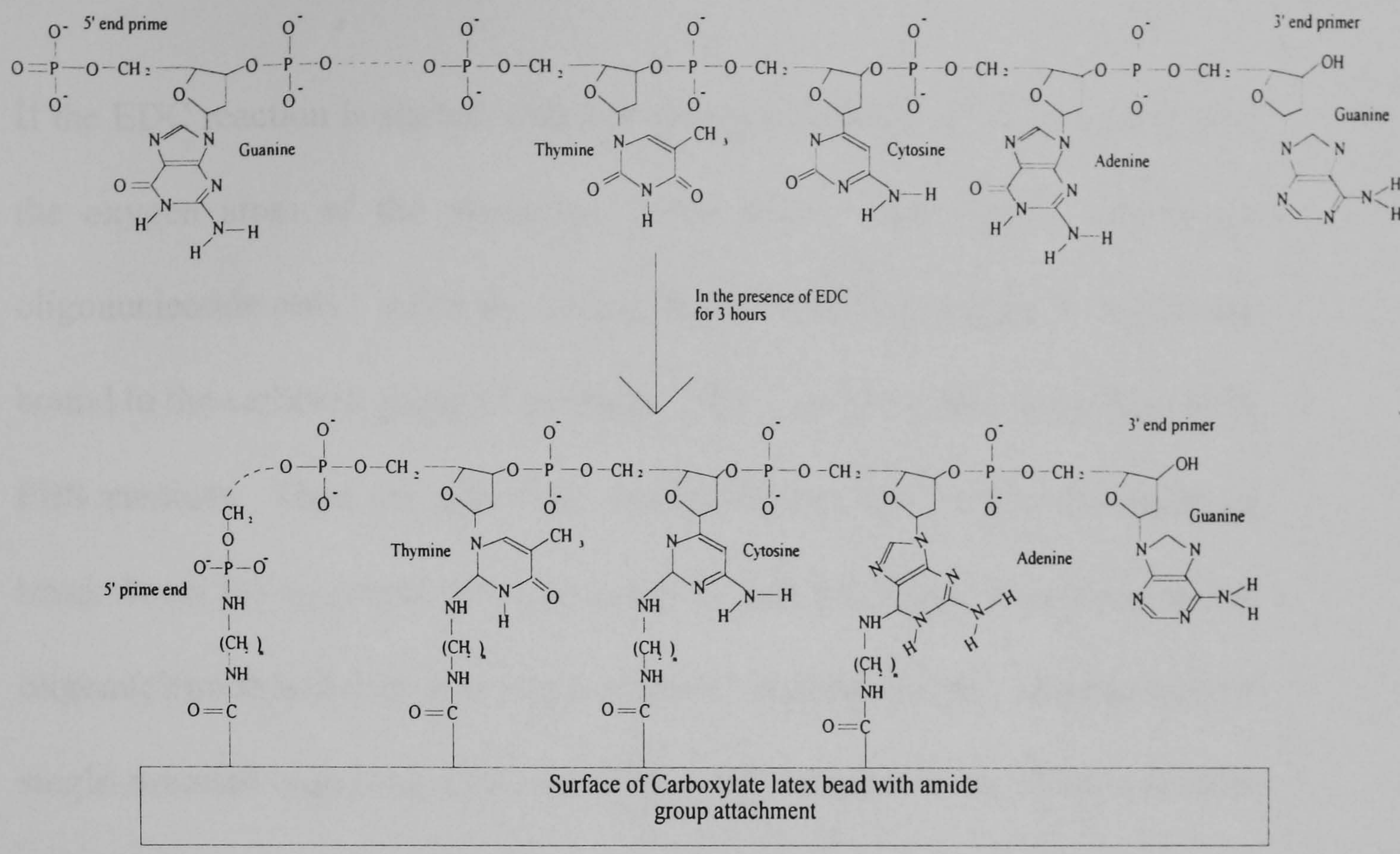

Figure 5.9 Nitrogenous bases such as Thymine, Cytosine and Adenine might bind with amide ions from the surface of the EDC-treated bead.

Since these bases contain the an oxygen lone pair that is very similar to the 5' end of the single stranded oligonucleotide, it is possible to form covalent bonding with carboxyl group of beads through EDC. Therefore, some of these longer base length primers might partially lie flat onto the surface of beads. This can explain the closeness of the high frequency ROT peaks amongst these primers (Table 5.4), (Figure 5.7). It is because the dielectric properties of the surface of these beads become similar as the longer base length oligonucleotides are shortened. At the same time, some of the hydrogen bonding sites have been used up by forming covalent bonds with amide ions. The amounts of hydrogen bonding sites for ions to hop round the oligonucleotide are limited. Therefore this might lead to the decrement in surface conductance values of these long base length oligonucleotide samples.

If the EDC reaction is started with a double strand DNA, EDC will react with the oxygen atom of the phosphate group that is from the 5' end of the oligonucleotide only. After the double stranded oligonucleotide is covalently bound to the carboxyl group of the bead, EDC can be washed away by 0.01% PBS medium. Then the pH of the suspension can alter to become acidic to break down the hydrogen bonding between each base pair. Double stranded oligonucleotide will turn into single stranded oligonucleotide. After excessive single stranded oligonucleotide are washed off, those remain oligonucleotide that has binded to the surface of beads are available for PCR to take place (Figure 5.10).

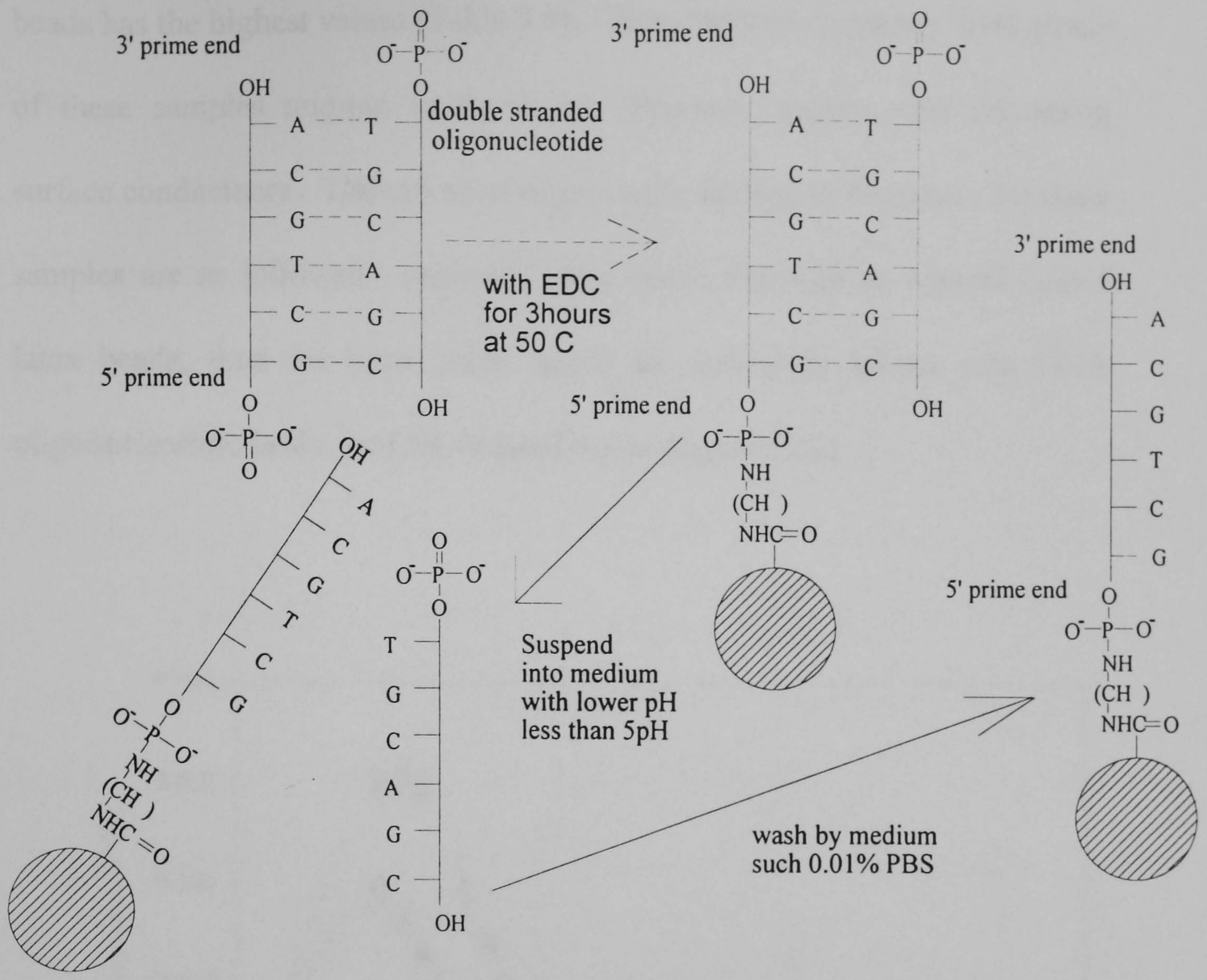

Figure 5.10 Uses double stranded oligonucleotide for binding with Carboxylate latex beads. Hydrogen bonding sites of oligonucleotide can be protected. Hence PCR reaction for oligonucleotide with DNA molecules in a medium is possible.

5.4.5 *Importance of this investigation*

In this investigation, ROT experiments have been carried out with different types of samples that have been described above. Their ROT responses were all different one to another (Figure 5.11) because of their difference in surface conductance values. The surface conductance of untreated latex beads has the lowest value (Table 5.1) whilst the surface conductance of the EDC-treated beads has the highest values (Table 5.3). Thus, the high frequency ROT peaks of these samples migrate to the higher frequency region with increasing surface conductance. The orders of migration to the higher frequency for these samples are as followed: untreated latex beads followed by Marvel coated latex beads; then the latex beads which are covalently bound with DNA oligonucleotide; lastly the EDC-treated beads (Figure 5.11).

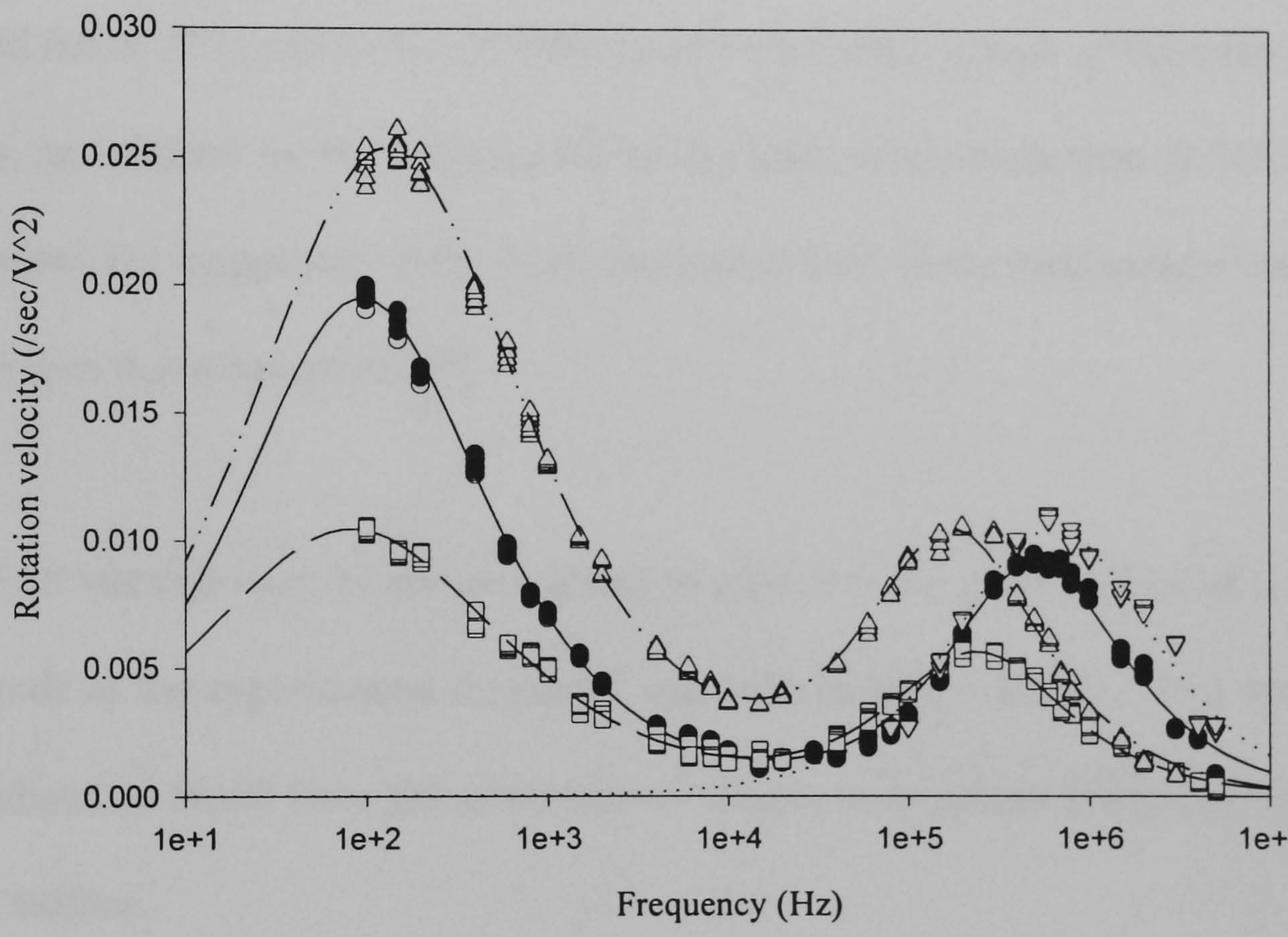

Figure 5.11 Latex beads with DNA oligonucletide: ROT experimental data ●, theoretical fitting (___) solid line. Latex bead coated with Marvel protein blocker: ROT data □, theoretical fitting (---) dashed line. EDC treated latex bead: ROT data ∇, theoretical fitting (...) dotted line. Untreated latex bead: ROT data Δ, theoretical fitting (-..-) dashed-dotted-dotted-dashed line. ROT experiments of all these samples were carried out in 0.01% PBS as the suspending medium.

5.5 Conclusion

In this investigation, ROT experiments have been performed on untreated latex beads, latex beads which have undergone EDC treatment, latex beads which have been coated with Marvel artificial milk as protein blockers, and latex beads which have been bound covalently with different types of DNA oligonucleotides. In the untreated bead cases, ROT experiments have been carried out at 21°C and 10°C. At 10°C the effective conductance of these latex beads, as reflected by the Clausius-Mossotti factor, were larger than at 21°C. Therefore, the magnitude of the ROT obtained at 10°C lower temperature was larger than that obtained at 21°C.

The EDC-treated latex beads were found to adhere to the glass surface of the electrode as the experimental frequency was reduced below 80kHz. This was considered to result from the attraction of surface ionic amide groups of the glass surface.

Different types of DNA oligonucleotide can possibly be identified by the amount of hydrogen bonding available sites of its nitrogenous bases. These nitrogenous bases group can alter the surface conductance and the α-relaxation of DNA oligonucleotide bound beads. Consequently, the ratio of the magnitude of the low frequency ROT peak and the high frequency ROT peak will be altered for different types of oligonucleotide attachments.

Oligonucleotide coated beads could be identified using electrorotation from other types of beads namely, untreated latex beads, EDC-treated beads and Marvel coated beads. Thus DNA oligonucleotide bound beads can be isolated and different types of oligonucleotides can be classified by their different ROT responses. Once different types of oligonucleotides are identified by ROT technique, they are possible to be used in PCR reaction for DNA analysis. The DNA oligonucleotide bound latex beads can be hybridised with the desirable DNA molecules that are in the medium used for the PCR reaction. If this PCR process is successful, new ways of investigating DNA molecules will be explored.

5.6 Reference

1. B. A. White (1993) *Methods in Molecular Biology: PCR Protocols Current Methods and Applications* **15**

2. X. F. Zhou, G. H. Markx, R. Pethig, I. M. Eastwood (1995) Differentiation of viable and non-viable bacterial biofilms using electrorotation, *Biochimica et Biophysica Acta* **1245** 85-93

3. J.P.H. Burt, K. L. Chan, D. Dawson, A. Parton, R. Pethig (1996) Assays for microbial contamination and DNA analysis based on electrorotation, *Ann. Biol. Clin.* **54** 253-257

4. S. S. Ghosh and G. F. Musso (1987) Covalent attachment of oligonucleotides to solid supports, *Nucleic Acid Research* **15** 13 5353-5372

5. A. Parton (1994) *Private communication: Methods of Detecting or Quantitating Nucleic Acids and of Producing Labelled Immobilised Nucleic Acids*

6. M. P. Hughes, R. Pethig and X. B. Wang (1995) Dielectrophoretic forces on particles in travelling electric fields, *J. Phys. D: Appl. Phys.* **28** 1-9

7. M. P. Hughes, X-B. Wang, F. F. Becker, P. R. C. Gascoyne and R. Pethig (1994) Computer-aided analyses of electric fields used in electrorotation studies, *J. Phys. D: Appl. Phys.* **27** 1564-1570

8. Y. Huang, R. Hölzel, R. Pethig and X-B. Wang (1992) Differences in the AC electrodynamics of viable and non-viable yeast cells determined through combined dielectrophoresis and electrorotation studies, *Phys. Med. Biol.* **37** 7 1499-1517

9. T. Kakutani, S. Shibatani and M. Sugai (1993) Electrorotation of non-spherical cells: theory for ellipsoidal cells with an arbitrary number of cells, *Bioelectrochemistry and Bioenergetics* **31** 131-145

10. W. M. Arnold, H. P. Schwan and U. Zimmermann (1987) Surface Conductance and Other Properties of Latex Particles Measured by Electrorotation, *Journal of Physical Chemistry* **91** 5093-5098

11. J. E. Dennis and D. J. Woods in (1987) *New Computing Environments: Microcomputers in Large-Scale Computing* (A. Wouk, ed.), Optimization on Microcomputers: The Nelder-Mead Simplex Algorithm, 116-122, **SIAM**

12. J. O'M. Bockris and A. K. N. Reddy (1977) *Modern Electrochemistry vol.2* 728-738, Plenum Press, New York

13. E. H. Grant, R. J. Sheppard and G. P. South (1978) *Dielectric behaviour of Biological molecules in solution,* Oxford University Press

14. R. Pethig, (1979) *Dielectric and Electronic Properties of Biological Materials,* J. Wiley and sons, Chichester

15. R. S. Lee and S. Bone (1996) Time domain reflectometry techniques used as an analytical tool to investigate water molecules bound to solid-state deoxyribonucleic acid (DNA), *Faraday Discuss.*, **103**, 103/16

16. E. Alcamo *Fundamentals of Microbiology, Fourth edition,* 42-50, The Benjamin/Cummings Publishing Company, Inc.

17. R. Pethig (1988) Dielectric studies of proton transport in proteins, *Ferroelectrics* **86** 31-39

Chapter six

Conclusion

In this work, a number of different types of experiments and analyses have been carried out with the aim of determining the accuracy of results that the electrorotation experiment technique can give. Also, the further expansion of this analytical technique was performed on DNA oligonucleotides with the aim of identifying the oligonucleotides with different nitrogenous base sequences depending on their dielectric properties. The feasibility of the electrorotation technique can extend from the analysis of the samples that are in the size in biological cells (larger than few μm in diameter), to samples that are of much smaller scale (in nm region). Furthermore, the computer analytic programs based on the dielectric spherical or ellipsoidal shell models theories were developed to analyse the dielectric properties of the biological or artificial particles. Tests of the accuracy analysis for these programs have been performed. The aim of this work was to determine the accuracy and reliability of the resultant variables that are given by computer analysis. The results of analysis can be summarised as follows:

In the case of the analytic spherical shell model program, it is concluded that four factors can determine its accuracy. The complexity of the shell model is the most important consideration, with the simplest single shell model delivering the most accurate results from the analysis. The number of variables to be altered in the Nelder-Mead simplex algorithm can significantly influence the accuracy of the spherical shell model program for determining the dielectric variables. Five changeable variables are the maximum that can be used in the MATLAB program, so by reducing this number, the accuracy of the analytic program is improved considerably. Also, the internal permittivity variable is the most dominant variable within the spherical shell model. If the value of this internal permittivity is known and kept as a constant during the analysis, the accuracy levels of all other dielectric parameters are improved very significantly. Lastly, the program achieves more accurate results when the ROT analysis is augmented with the DEP "cross-over" frequency data.

The ellipsoidal shell model gives very accurate values on:

(1) the surface conductance of the tested sample, latex beads or latex beads that are covalently bound with DNA oligonucleotide,

(2) the scaling factor of the ROT spectrum and

(3) the variable α that determines the width of the low frequency ROT spectrum. However, the magnitude A and the characteristic time-constant T of equation (3.3) on page 81 cannot be derived very accurately by this ellipsoidal shell model program.

The Nelder-Mead simplex algorithm that was used in these programs was very tolerant of noise being added to the analysis data. In most cases, the accuracy levels of the dielectric variables were quite stable as the noise level increased to 5%, falling as the noise level rose beyond this point.

By using ROT, and DEP cross-over frequency measurements, vesicles were used as simple non-conductive spheres with known internal dielectric properties to test the dielectric multi-shell model. Dielectric properties of vesicles in both simple and complex form were analysed.

From flow cytometry analysis, two main groups of vesicles were found to be formed. They differ by the lipids present in the membrane, having either low or high lipid concentrations. In the case of low lipid concentration, vesicles are unilamelle and oligolamelle in nature. In the case of high lipid concentration, vesicles are multi-lamelle in nature. For unilamellar, oligolamellar and multilamellar vesicles with a single medium compartment, they can be analysed by using a single shell model. The amount of lipids bilayer in the membrane of vesicles can be determined by their membrane capacitance values and a known membrane thickness. Oligolamellar and multilamellar vesicles with more than one medium compartment present cannot be fitted by the single shell model. Oligolamellar vesicles with two separate medium compartments present can be fitted by a three shell model. In the case of multi-lamellar vesicles with multi-medium compartments present, more shells are required in the model. For each extra membrane, two additional shells are required. For example, a vesicle with three separate membranes can be fitted by using a five shell model. Once the ROT data of any kind of vesicle is fitted by its required shell modelling, any increase in the number of shells included would not help or alter the original best fit data.

Variation of experimental temperature can change the dielectric properties of vesicles. From these experiments, the value of membrane capacitance decreased with increase in temperature, an effect assumed to be caused mainly by the increment of membrane thickness in the hydrophobic region. At the same time, the relative permittivity of the membrane and the medium also decreased with increase of temperature.

It is concluded from the vesicles experiments, that ROT and DEP cross-over frequency analysis can determine the dielectric properties of various types of vesicle very accurately. Thus, these have been shown to be good analytical tools to analyse the cellular structure of biological cells, in conjunction with the application of the dielectric multi-shell model.

In the investigation of DNA oligonucleotides, ROT experiments have been performed on untreated latex beads, latex beads which have undergone EDC treatment, latex beads which have been coated with Marvel artificial milk as protein blockers, and latex beads which have been bound covalently with different types of DNA oligonucleotides. In the untreated bead cases, ROT experiments have been carried out at 21°C and 10°C. At 10°C the effective conductance of these latex beads, as reflected by the Clausius-Mossotti factor, was larger than at 21°C. Therefore, the magnitude of the ROT obtained at a 10°C lower temperature was larger than that obtained at 21°C.

The EDC-treated latex beads were found to adhere to the glass surface of the electrode as the experimental frequency was reduced below 80kHz. This was considered to result from attraction by the surface ionic amide groups of the glass surface.

Different types of DNA oligonucleotide can possibly be identified by the number of hydrogen bonding sites of its nitrogenous bases. Different bases can lead to differences of the surface conductance and the α-relaxation of DNA oligonucleotide bound beads. Consequently, the ratio of the magnitude of the low frequency ROT peak and the high frequency ROT peak will be altered for different types of oligonucleotide attachments.

Oligonucleotide coated beads could be identified using electrorotation from other types of beads, namely, untreated latex beads, EDC-treated beads and Marvel coated beads. Thus beads have different oligonucleotides bound to their surfaces can be classified by their different ROT responses. Once different types of oligonucleotides are identified by ROT technique, they might possibly be used in the PCR reaction for DNA analysis. The DNA oligonucleotide bound latex beads can be hybridised with the desirable DNA molecules that are in the medium used for the PCR reaction. If this PCR process is successful, new ways of investigating DNA molecules will be explored.

Publications Resulting From This Work

K. L. Chan (1994) Verification of Dielectric Shell Theories by Dielectrophoretic and Electrorotational Studies of Synthetic Vesicles, *Biophysical Journal,* **Program and Abstracts**, A383 (Th-Pos 140)

J. P. H. Burt, K. L. Chan, D. Dawson, A. Parton and R. Pethig (1996) Assays for microbial contamination and DNA analysis based on electrorotation, *Ann. Biol. Clin.,* **54** 253-257

In preparation:

K. L. Chan, P. R. C. Gascoyne, F. F. Becker and R. Pethig, Dielectrophoresis and electrorotation of lipsomes: Verification of Dielectric Multishell Model for Cells.